Measuring the Gap and Investigating Non-equilibrium in the BEC-BCS Crossover

Dissertation
zur
Erlangung des Doktorgrades (Dr. rer. nat.)
der
Mathematisch-Naturwissenschaftlichen Fakultät
der
Rheinischen Friedrich-Wilhelms-Universität Bonn

vorgelegt von

Timothy Joseph Harrison
aus
London, Großbritannien

Bonn 2017

Angefertigt mit Genehmigung der Mathematisch-Naturwissenschaftlichen
Fakultät der Rheinischen Friedrich-Wilhelms-Universität Bonn

1. Gutachter: Prof. Dr. Michael Köhl

2. Gutachter: Prof. Dr. Dieter Meschede

Tag der Promotion: 27.06.2017

Erscheinungsjahr: 2017

Abstract

This thesis presents a new Bose-Fermi mixture quantum gas experiment that has been used to measure the gap over the BEC-BCS crossover and investigate the non-equilibrium dynamics of a superfluid in response to a quench of the interaction strength. Bosonic ^{23}Na sympathetically cools fermionic ^{6}Li in an optically plugged magnetic trap before transferring the atoms to an optical dipole trap. The broad Feshbach resonance of ^{6}Li is then used to tune the scattering length and by entering the strongly interacting regime, very efficient evaporation can be performed. Bose-Einstein condensation of molecules with over 5×10^6 ^{6}Li atoms per spin state has been observed and temperatures $T/T_F = 0.07 \pm 0.02$ have been achieved. The broad Feshbach resonance of ^{6}Li can then be used to bring the atoms into the BCS regime, where long range Cooper pairs of opposite spin and momentum form a superfluid state, or into the universality regime, where the scattering length diverges and the system obeys universal laws.

A technique was developed whereby the population of one component of the superfluid was continuously modulated with a specific frequency. Theoretical studies show that this excitation couples to the amplitude/Higgs mode of the superfluid order parameter, which should have a resonance frequency at twice the gap value. By measuring the response of the condensate fraction at various modulation frequencies, a measure of the gap in the BEC-BCS crossover could be extracted. The measured gap value was found to be in agreement with the mean-field theory calculations and quantum Monte Carlo simulations.

Extending the same method, it was possible to rapidly change one of the components of a superfluid to a different third component. The inversion was performed in less than 50 µs, faster than the dynamical gap time and quasiparticle relaxation time. This provides an excellent realization of the fast quenches of the interaction strength that have been intensely investigated theoretically. By quenching a strongly interacting superfluid to much weaker interactions, the decay of the order parameter was studied. During these non-equilibrium dynamics, evidence of a revival of the order parameter has been observed at longer time scales for weak quenches. Additionally, a weakly interacting normal mixture above the critical temperature can be quenched to interaction strengths where, in equilibrium, a superfluid should be present. The emergence of the order parameter was measured as a function of time and was found to be faster for weak quenches into the BCS regime than for larger quenches into unitarity.

for Jack Myers

Acknowledgements

Firstly, I would like to thank my supervisor Professor Michael Köhl for his continued guidance, support and encouragement throughout my PhD. He has always been available, interested and willing to help in the laboratory, providing new ideas and suggestions. Importantly, he also encouraged me to try measurements, techniques and ideas even when our opinions differed!

When we arrived in Bonn, we began building a new experiment in an empty room that has now become known as the *Humphry Lab*. Building this new quantum gas experiment has been a challenging but extremely rewarding experience and would not have been possible without the help and collaboration of Alexandra Behrle and Kuiyi Gao. We have spent many long days (and nights) together in the lab and I thank them both for all the help they have given me throughout the last years. Our new PhD student Martin Link has rapidly learned how to operate the experiment and is already contributing greatly to the current investigations. It is nice to know that the future of the experiment is in safe hands.

Over the course of my PhD, I have had the wonderful opportunity to work with several students who have helped with the Humphry experiment. I would like to thank Christoph Linse, Mohammadali Salari, Justas Andrijauskas, Maximilian Zawierucha and Till Leuteritz. The evidence of their achievements is how much of their projects are still fully operational within the experiment today. I would also like to thank Andreas Kell, who is currently building the lattice laser system for his Masters thesis. I must specifically thank Daniel Pertot and Akos Hoffman for all the incredible help they have given me in debugging, repairing and building electronics in the lab.

Beyond the direct team I have worked with, there is the excellent wider research group who have always been available to help and socialize. I spent many fun weekends in the lab with Jonathan Silver and Tim Ballance as we soon discovered the lab was the best place for us to meet before getting food on Sundays. I would also like to thank the members

of the Fermi experiment: Luke Miller, Eugenio Cocchi, Jan Drewes, Jeffrey Chan, Nicola Wurz, Marcell Gall, Daniel Pertot and Ferdinand Brennecke. Of course, I must also thank the ion-trapping team (where I began with my Masters thesis in Cambridge): Leonardo Carcagni, Jonathan Silver, Tim Ballance, Kilian Kluge, Robert Maiwald and Hendrik Meyer. Our group administrator, Tina Naggert, has also provided continued support with all aspects of life in the research group.

Finally, I would like to thank the many Physics teachers I have had throughout my education, including David Smith from Highgate school. Specifically, I would like to thank Prof. Chris Hanniff and Prof. Richard Stibbs from the University of Cambridge. Their supervisions not only challenged me in Physics and Mathematics, but also taught me how to ask (and sometimes attempt to answer) hard questions.

Contents

Chapter 1

Introduction

Erwin Schrödinger wrote, in his 1946 seminar lectures on statistical thermodynamics [1], that whilst '*the region of noticeable gas degeneration is by no means outside the reach of experiment... the densities are so high and the temperatures so low... that the Van der Waals corrections are bound to coalesce with the possible effects of degeneration, and there is little prospect of ever being able to separate the two kinds of effect*'. The techniques of laser cooling atomic gases, first proposed in 1975 [2] and developed through the 1980s (1997 Nobel prize Phillips, Cohen-Tannoudji and Chu [3–5]), meant that temperatures, and importantly densities, much lower than those considered by Schrödinger became possible. Throughout the 1980s and 1990s, new techniques to trap and cool atoms were developed and refined including: the Zeeman slower [6] using the scattering force from laser radiation to slow an atomic beam; the magneto-optical trap [7], which takes advantage of radiation pressure to confine and cool atoms; magnetic traps [8], which take advantage of the finite magnetic moment of hyperfine states to create a conservative trapping potential; and evaporative cooling [9] first implemented for experiments with cryogenic hydrogen, whereby the highest energy atoms are selectively removed, leaving the system to re-equilibrate at a lower temperature. All of these techniques were implemented in the experiment described in this thesis. During the 1990s, several groups were attempting to observe degeneracy of bosons in the formation of a Bose-Einstein condensate (BEC) in these dilute, low-temperature atomic gases, as originally predicted in the works of Bose and Einstein [10]. With the improvement of techniques, the phase-space density of the atomic gas steadily increased and eventually, in 1995, several research groups observed Bose-Einstein condensation using different alkali atoms [11–13]. What was perhaps seen to be a race to realize a century old prediction, rapidly developed into a well-established research field which has had diverse implications in the field of condensed matter [14] and

even particle physics [15] and astrophysics [16, 17].

All matter is composed of elementary fermions and it did not take long before research groups attempted to cool atomic isotopes that were composite fermions. Quantum statistics lead to fundamental differences between bosons and fermions at low energies. Notably, Pauli's exclusion principle prevents fermions from occupying the same quantum state such that collisions between identical fermions are suppressed and the gas is unable to thermalize, making traditional cooling methods ineffective. However, by using a mixture of different hyperfine levels, where the distinguishable states could interact with each other and thermalize, the first realisation of a degenerate Fermi gas [18] was achieved. An alternative method, known as sympathetic cooling, evaporates a bosonic isotope in the presence of the Fermi gas. Collisions bring the Fermi gas into equilibrium with the bosons with the added advantage that the number of fermions does not have to be reduced during the process. The first experiments using sympathetic cooling of fermions [19, 20] produced degenerate Fermi gases with large atom numbers and also opened the possibility of studying mixture experiments involving simultaneously degenerate Bose and Fermi gases.

An interacting ensemble of either fermions or bosons can undergo a phase transition to a superfluid state characterized by a coherent flow without dissipation. Pioneering work by Kamerlingh Onnes in 1908 cooled liquid helium to less than 2.17 K [21] and gave some of the first evidence of superfluidity. Soon after this, Onnes discovered superconductivity [22, 23] by observing that a sample of mercury was able to conduct electricity without any dissipation when cooled to 4.2 K. These experiments provided the first evidence for quantum mechanics on a macroscopic scale. After the simple two-fluid model by London [24, 25], the 1957 Bardeen-Cooper-Schrieffer (BCS) theory of superconductivity [26], where weakly interacting fermions with opposite spin and momentum form s-wave pairs that condense in a superconducting ground state, successfully explained many features of the experiments in superconductivity. However, many recently developed superconductors cannot be understood by conventional BCS theory, including superconductivity in cuprates [27] and superfluid helium-3 [28]. These states are now believed to have fermion pairs with higher angular momentum symmetry [29] in two-dimensional planes [30] and strong interactions [31]. However, these unconventional superconductors are still not fully understood theoretically.

An important advantage of ultracold atomic gases is the ability to fine-tune the parameters of the system such as density, temperature, trap geometries, interactions and dimensions. In contrast, solid state systems often have these parameters fixed by the material under

investigation. Notably, the scattering length, which determines the interaction strength, can be tuned with the magnetic field by using Feshbach resonances [32]. Across the resonance the system changes from repulsive to attractive interactions, crossing the unitarity regime in between where the scattering length diverges. Far on the weakly attractive side of the resonance, the system behaves like the ideal BCS superfluid discussed above. Far on the other side of the resonance, the fermions form bound states of dimers that interact repulsively, and are composite bosons which can condense. In the unitarity regime, the many-body system has strong interactions that cannot be treated perturbatively, making the system difficult to model theoretically, although universal scaling laws can be formulated [33–36]. The unitarity regime has a superfluid state with the highest known critical temperature, which is of great relevance to the unconventional high-temperature superconductors where strong interactions are known to play an important role. Fermi gases across a Feshbach resonance provide an ideal system for investigating fermionic superfluidity with varying interactions across the so-called BEC-BCS crossover. Several key experiments on the BEC-BCS crossover are listed in Table 1.1.

This thesis describes the construction of a new ultracold quantum gas mixture experiment using bosonic ^{23}Na and fermionic ^{6}Li. A collimated atomic beam of both species is decelerated using a Zeeman slower and collected in a dual-species magneto-optical trap. Both species are then magnetically transported and the ^{23}Na atoms are evaporatively cooled in a plugged quadrupole magnetic trap, sympathetically cooling the ^{6}Li before transferring to a dipole trap. Currently, we do not use the bosonic ^{23}Na in investigations but only as the *refrigerator* with which to cool the fermions. With the ^{6}Li fermions in the dipole trap, a spin mixture is prepared and by applying a magnetic field, the Feshbach resonances can be used to explore the BEC-BCS crossover. The system is able to produce a BEC of ^{23}Na in the magnetic trap with 1×10^7 atoms without ^{6}Li present. The large ^{23}Na reservoir means large ^{6}Li numbers are also achievable and after evaporation in the dipole trap on the Feshbach resonance, we have made pure molecular BECs of ^{6}Li with over 5×10^6 atoms per spin state, comparable to the highest numbers that have been achieved so far. The construction and implementation of the experiment system took approximately two and a half years and now runs 24 hours per day producing a degenerate gas approximately every 20 seconds. Due to the large superfluids we could produce in our experiment and the exceptionally broad Feshbach resonance of ^{6}Li, we focused on how the quantum system responds to a modulation or sudden change in the interaction strength.

The phase transition to a superfluid is associated with the occurence of off-diagonal long

Table 1.1: A selection of papers investigating the BEC-BCS crossover with Fermi gases.

Research Group	Species	Reference (year)	Topic
Thomas, Duke	^{6}Li	[37] (2002)	Strongly interacting system
		[38] (2005)	Heat capacity
Jin, Colorado	^{40}K	[39] (2004)	Pair condensation (rapid ramp)
		[40] (2006)	Energy and unitarity
		[41] (2008)	Photoemission spectroscopy
Ketterle, MIT	^{6}Li	[42] (2004)	Pair condensation (rapid ramp)
		[43, 44] (2005,2007)	Observation of vortices
		[45] (2006)	Imbalanced spin population
Salomon, ENS Paris	^{6}Li	[46] (2003)	Interaction energy measurement
		[47] (2004)	Pair condensation
Hulet, Rice	^{6}Li	[48] (2005)	Molecular spectroscopy
		[49] (2007)	Imbalanced spin population
Grimm, Innsbruck	^{6}Li	[50] (2004)	RF spectroscopy
		[51, 52] (2004,2007)	Collective excitations
		[53] (2012)	Polarons
Esslinger, ETH	^{6}Li	[54] (2007)	Transport
Köhl, Cambridge	^{40}K	[55](2011)	Pairing gap (2D)
		[56] (2012)	Polarons (2D)
		[57] (2012)	Viscosity (2D)
Zwierlein, MIT	^{6}Li	[58] (2011)	Spin transport
		[59] (2013)	Solitons
Inguscio, LENS	^{6}Li	[60] (2015)	Josephson effect
Moritz, Hamburg	^{6}Li	[61] (2015)	Critical velocity
Jochim, Heidelberg	^{6}Li	[62, 63] (2015,2016)	Two-dimensional

range order [64] characterized by a complex order parameter, Δ. Since the superfluid is composed of Cooper pairs, to remove a particle from the system a pair must be broken, costing energy. Hence, the single-particle excitation spectrum of a superfluid has a gap, with a finite energy for zero momentum excitations. Most properties of the superfluid can be characterized in terms of the order parameter and the gap, which are equivalent in the BCS regime. An important question is how the superfluid responds to a change in the order parameter, away from its equilibrium value. Early papers considered small deviations from equilibrium [65, 66] with an important result in 1974 by Volkov and Kogan [67], who showed that, if the order parameter was perturbed in the BCS limit, it would undergo power-law-decaying oscillations with frequency $2\Delta/\hbar$. There was little investigation of this topic until the experiments on Fermi gases in the BEC-BCS crossover reignited interest in quenches of the order parameter, which could be attempted by changing the interaction strength. Barankov, Levitov and Spivak [68], encouraged by recent experiments at MIT [42], studied a sudden turn-on of the pairing interaction and showed it could lead to oscillations between the normal and superfluid state. This work also clarified the different time scales of the dynamics for a quench in terms of the quasiparticle relaxation time ($\hbar E_F/\Delta^2$) and dynamical gap time ($\hbar/\Delta$), requiring the turn-on time to be faster than these time scales.

In the years that followed, several developments and generalisations were made to include, for example, quenches from BEC to BCS regimes [69]; finite temperature effects [70]; and long time dynamics [71]. In 2015, Yuzbashyan et al. [72] wrote an encyclopedic paper summarizing the theoretical findings of quenches in BEC-BCS crossover superfluids. In this paper they characterize the quenches in a *phase diagram* of three different regimes depending on the initial and final Δ. Depending on the regime, the order parameter either decays to zero exponentially, goes to a non-zero constant as a power-law possibly with damped oscillations, or oscillates persistently. Stringari et al. [73] proposed using the oscillations as a method for measuring the gap in the BEC-BCS crossover, even providing details of how it could be experimentally implemented with different quenches or a driven modulation in the scattering length. Despite the vast body of theoretical work spanning nearly five decades, very few cold atom experiments have investigated the non-equilibrium dynamics by quenching the order parameter. Experiments at MIT [74] investigated the formation dynamics of the superfluid by modulating the magnetic field on the Feshbach resonance, and thus changing the interaction strength. However, the timescale of this modulation was several orders of magnitude slower than those discussed above.

So far, there has been a serious experimental limit, namely that Faraday's law makes it

difficult to rapidly change a magnetic field, resulting in large induced voltages and eddy currents. Even with the low-inductance coils in our experiment it is not possible to modulate or turn off the field at time scales $\sim \hbar/\Delta$ or $\hbar/E_F$. We have implemented a unique method, taking advantage of the several Feshbach resonances between different hyperfine states of ^{6}Li and the ability to rapidly change the hyperfine state using a radiofrequency (RF) pulse on time scales $\lesssim \hbar/\Delta$ and $\hbar/E_F$. By using the RF not as a preparation tool or probing method, but rather as a mechanism to drive the system's interaction strength, we are able to perform quenches similar to those discussed in the theory papers above. By preparing a two-component superfluid in the two lowest hyperfine states, we can rapidly transfer one component to a third state (π pulse), with which there is a significantly different interaction strength. Furthermore, the superfluid can be continuously driven (Rabi oscillations), modulating the atoms in a coherent linear combination of the different states. By driving the modulation at different frequencies, we can measure if the final order parameter has any resonance due to collective modes, in an experiment qualitatively similar to the mechanism discussed in [73]. Using this method, we have measured the gap in the BEC-BCS crossover, showing good agreement with recent theoretical calculations [75, 76]. Furthermore, by transferring the entire population of one component, the scattering length is rapidly changed and the evolution of the superfluid state can be monitored in time. After the quench, the system is far from equilibrium and depending on the direction of the quench we can monitor the vanishing or emergence of long range order and quantum correlations. These non-equilibrium dynamics are of great theoretical interest and are related to several fundamental and long-standing questions in physics regarding equilibration and thermalization of quantum-many body systems [77, 78]. For example, the evolution and formation of quantum correlations is still under much investigation [79]. For specific quenches that lead to a phase characterized by spontaneous symmetry breaking, Kibble and Zurek [80, 81] predicted the formation of topological defects, which are thought to be responsible for structured domain formation in the early universe. Furthermore, recent experiments have used pulsed lasers to drive systems out of equilibrium to induce superconductivity at high temperatures [82, 83], showing that non-equilibrium dynamics can lead to complex phenomena.

It is interesting that the oscillations in the order parameter, which may persist for specific quench conditions, are related to the collective amplitude mode of the order parameter. This amplitude mode, often called the Higgs mode, was first investigated in the context of superconductors by Littlewood and Varma [84], where it was shown that a process analogous to the Anderson-Higgs mechanism [85] was possible, with the role of Lorentz invariance provided by the particle-hole symmetry in the BCS Hamiltonian. The Higgs

mode has been observed with bosons in a two-dimensional lattice [86] and in several solid state systems [87–89], but has not yet been observed in Fermi gases. Preliminary results from theoretical work performed in the group of Corinna Kollath, in collaboration with our experiment, have shown that the modulation we perform should indeed excite the Higgs mode of the Fermi superfluid. The Higgs mode is of vital importance in the standard model of particle physics and is a fundamental collective mode in quantum many-body systems, with the existence of the Higgs mode deeply related to the concept of spontaneous symmetry breaking. The dynamics and damping of the Higgs mode in the BEC-BCS crossover is still under much theoretical investigation [90–92].

This thesis aims to give a complete description of the new experiment we have constructed and to describe two investigations we have performed with the new quantum gas system. In Chapter 2 the basic theoretical background necessary for understanding the experiment is provided. Chapter 3 describes the experimental setup including an overview of the vacuum chamber, laser systems, the different magnetic, radio frequency and microwave frequency coils and their electronic configurations. In Chapter 4 the experimental sequence is described from the hot atomic beam to the optical pumping, which prepares the atoms in the correct hyperfine states for the magnetic trap. Chapter 5 continues the experimental sequence from the magnetic transport and evaporation of ^{23}Na to the evaporation of ^{6}Li in the dipole trap to produce a molecular BEC of ^{6}Li. Before performing investigations, several properties, such as the trap frequencies, atom number and magnetic field, need to be characterized and calibrated. These measurements are described in Chapter 6. Chapter 7 shows the results of the first investigation where the spectral gap was measured in the BEC-BCS crossover by exciting a collective mode using a continuous RF drive. Chapter 8 shows the results of the second investigation where the superfluid was quenched rapidly by changing one of the spin components to a different state using a short RF pulse. This leads to a rapid change in the scattering length, and the evolution of the resultant non-equilibrium superfluid can be monitored. Chapter 9 summarizes the thesis and considers future investigations that could be performed.

Chapter 2

Theory

This section gives an overview of the relevant theory to describe ultracold quantum gases of bosons and fermions, highlighting the differences between the two. Section 2.1 describes the thermodynamics and quantum statistics for bosons and fermions. In Section 2.2 basic scattering theory is discussed with the aim of understanding the physics behind the broad Feshbach resonance of ^{6}Li used in the experiment. In Section 2.3 an overview of the BEC-BCS crossover is presented. Some specific theoretical discussions associated with experimental techniques or the investigations performed will be discussed later in the relevant sections of this thesis.

This theory section does not aim to provide complete derivations of all results, which would be beyond the scope of this thesis[1].

2.1 Bosons and Fermions

All particles are either bosons or fermions depending on whether they have integer or half-integer spin, respectively. The symmetry of the wave function of a system of identical particles depends dramatically on whether the particles are bosonic or fermionic. The wave function of a system of fermions is antisymmetric with respect to the interchange of two identical particles, whereas the bosonic wave function is symmetric under the same exchange. These symmetry properties have profound consequences in differentiating the physics of bosons and fermions, notably in the formulation of Pauli's Exclusion Principle

[1] I would recommend the following text-books or reviews for a more complete discussion of specific topics: [93] (Review of Fermi gases), [94] (detailed review of Feshbach resonances), [95] (detailed textbook of quantum mechanics and atomic physics) and [96] (broad textbook focused on quantum gases).

which states that no two identical fermions can simultaneously occupy the same quantum state. For bosons, however, there is no such requirement, with an arbitrary number of bosons able to occupy the same quantum state. How this will affect the physics of the system becomes clear when we write down the grand partition function, $\mathcal{Z}_{\mathbf{k}}$, of a quantum state $\mathbf{k}$, for an ideal gas of identical bosons or fermions:

$$\mathcal{Z}_{\mathbf{k}} = \begin{cases} \sum_{n=0}^{\infty} \left(\mathrm{e}^{-\beta(\epsilon_{\mathbf{k}}-\mu)}\right)^n = \frac{1}{1-\mathrm{e}^{-\beta(\epsilon_{\mathbf{k}}-\mu)}} & \text{(bosons)} \\ \sum_{n=0}^{1} \left(\mathrm{e}^{-\beta(\epsilon_{\mathbf{k}}-\mu)}\right)^n = 1 + \mathrm{e}^{-\beta(\epsilon_{\mathbf{k}}-\mu)} & \text{(fermions)} \end{cases} \tag{2.1}$$

where $\beta = \frac{1}{\mathrm{k_B}T}$ is the inverse temperature parameter, μ is the chemical potential, $\epsilon_{\mathbf{k}}$ is the energy of the state $\mathbf{k}$ and n is a dummy variable representing the possible occupancy levels of the state $\mathbf{k}$. The limits of the summation in Eq. (2.1) encapsulate Pauli's Exclusion Principle with an arbitrary number of bosons able to occupy a state, whereas there can be at most one fermion in a given state. From $\mathcal{Z}_{\mathbf{k}}$ we can write down the grand potential, $\Phi_{\mathbf{k}}$, from which all thermodynamic properties can be derived.

$$\Phi_{\mathbf{k}} = -\mathrm{k_B}T \ln\left(\mathcal{Z}_{\mathbf{k}}\right) = \begin{cases} -\mathrm{k_B}T \ln\left(\frac{1}{1-\mathrm{e}^{-\beta(\epsilon_{\mathbf{k}}-\mu)}}\right) & \text{(bosons)} \\ -\mathrm{k_B}T \ln\left(1 + \mathrm{e}^{-\beta(\epsilon_{\mathbf{k}}-\mu)}\right) & \text{(fermions)} \end{cases} \tag{2.2}$$

The average occupancy $n_{\mathbf{k}}$ of the state $\mathbf{k}$ can be derived from Eq. (2.2) using $n_{\mathbf{k}} = \left(-\frac{\partial \Phi_{\mathbf{k}}}{\partial \mu}\right)_{T,V}$, giving:

$$n_{\mathbf{k}} = \begin{cases} \frac{1}{\mathrm{e}^{\beta(\epsilon_{\mathbf{k}}-\mu)}-1} & \text{(bosons)} \\ \frac{1}{\mathrm{e}^{\beta(\epsilon_{\mathbf{k}}-\mu)}+1} & \text{(fermions)} \end{cases} \tag{2.3}$$

In Eq. (2.3) the difference in the occupancy probability of a given state is made clear by the sign of the ± 1 in the denominator. If the exponential term $\beta\left(\epsilon_{\mathbf{k}} - \mu\right) \gg 1$ then contributions from $n > 1$ are negligible and Eqs. (2.1) to (2.3) approach the limits of a classical ideal gas. For the exponent term to meet this condition for all values of $\epsilon_{\mathbf{k}}$, μ must be large and negative[1]. The difference in average occupancy for bosons, fermions and a classical gas is shown in Fig. 2.1. In order to derive properties of the system all states $\mathbf{k}$ must be summed over. It is often convenient to introduce a density of states, $g(\epsilon)$, to convert this sum into an integral, such that if we sum a function $f(\epsilon)$ over all

[1]Note that this condition is not simply the high temperature limit, however, we will show shortly that in the high temperature limit classical, bosonic and fermionic gases all have large negative chemical potentials and hence converge to the classical ideal gas equations.

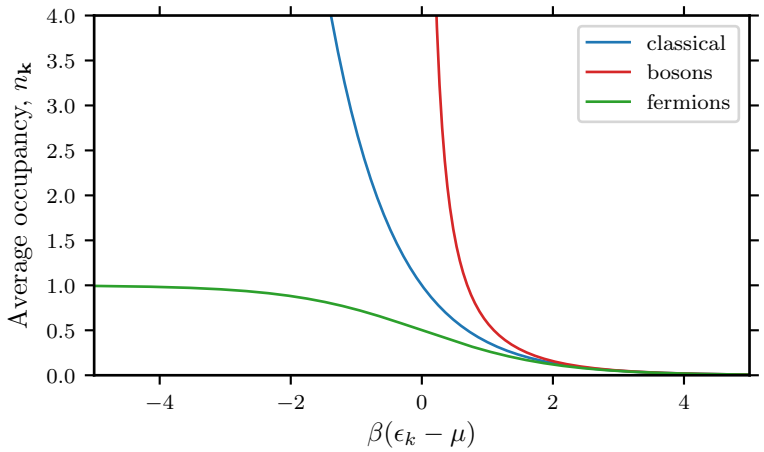

Figure 2.1: Average occupancy of the state $\mathbf{k}$ as a function of $\beta(\epsilon_{\mathbf{k}} - \mu)$. Note that the average occupancy of a quantum state in the system of fermions is never greater than 1, which is evident from the initial formulation of the grand partition function in Eq. (2.1).

states:

$$\sum_{\mathbf{k}} f(\epsilon_{\mathbf{k}}) \rightarrow \int_0^{\infty} g(\epsilon) f(\epsilon) \mathrm{d}\epsilon \tag{2.4}$$

The density of states, $g(\epsilon)$, can be derived for a given trapping potential and number of dimensions by counting the number of states that occupy a fixed volume in $\mathbf{k}$ space. In this thesis we restrict our discussion to harmonic trapping potentials in three dimensions as this is most relevant to the experiments discussed. It can be shown for a three-dimensional harmonic potential:

$$g_{3d_{\mathrm{ho}}}(\epsilon) = \frac{\epsilon^2}{2\left(\hbar\bar{\omega}\right)^3} \tag{2.5}$$

where $\bar{\omega}$ is the geometric mean of the trap frequencies of the harmonic potential. The method of Eq. (2.4) is valid when $k_{\mathrm{B}}T \gg \Delta E$, the energy separation between states, for all states that have a significant occupation. It will be shown later how this assumption breaks down when bosons at low temperatures are considered. With this density of states, one can derive the chemical potential, μ from the constraint of a fixed atom number:

$$N = \int_0^{\infty} g(\epsilon)\, n(\epsilon)\, \mathrm{d}\epsilon \tag{2.6}$$

By substituting the density of states (Eq. (2.5)) and the average occupation number (Eq. (2.3)) into Eq. (2.6), the chemical potential can be calculated. The chemical potential of an ideal classical gas, bosons and fermions are shown in Fig. 2.2. This shows that at

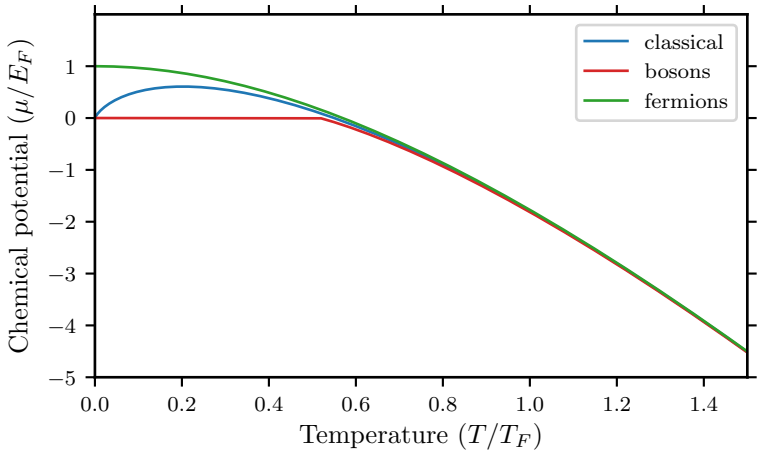

Figure 2.2: The chemical potential, μ in units of the Fermi energy E_F as a function of temperature, T, in units of Fermi temperature, T_F. The Fermi energy and temperature are defined in Eq. (2.12). The classical μ can be expressed analytically as $\frac{\mu}{E_F} = -\frac{T}{T_F}\ln\left(6\frac{T}{T_F}\right)$. μ for the fermionic and bosonic system cannot be expressed analytically and must be solved numerically from Eq. (2.6). Note that for the bosonic system, at sufficiently low T/T_F, it is not possible to find a (real) value for the chemical potential from Eq. (2.6). This temperature marks the transition to a Bose-Einstein condensate (see Eq. (2.8)).

high temperatures, the chemical potential of all the systems is large and negative and the classical limit discussed above is satisfied. For the classical system, Eq. (2.6) can be solved analytically for μ, whereas for the fermionic and bosonic system the integral in Eq. (2.6) can be written in terms of the polylogarithm function and solved numerically. Uniquely for the system of bosons, below some critical temperature, $T_c \approx 0.52T_F$ at which $\mu = 0$, Eq. (2.6) has no real solution for μ. Note that if μ is zero (or positive), then the occupation of a state with $\epsilon_{\mathbf{k}} = \mu$ becomes infinite which would violate the assumption in Eq. (2.6) that the atom number is a fixed constant. This non-physical divergence and lack of a solution for μ is due to the conversion of a sum to an integral described in Eq. (2.4). At sufficiently low temperatures, the assumption that $k_{\mathrm{B}}T \gg \Delta E$ is violated and the ground state of the system must be considered separately. Below this temperature T_c, it is not possible for the integral in Eq. (2.6) to have the same total atom number N as above T_c. Bose and Einstein [10] first showed that this effect could be explained if the missing atoms were in fact macroscopically[1] occupying the ground state of the system. Below T_c the chemical potential is zero and the integral in Eq. (2.6) equals the number of atoms in the excited states N_{ex} for which $\mathbf{k} \neq 0$. The number of condensed atoms, N_0,

[1]By macroscopic occupation it is meant that the occupation number of the ground state is proportional to the size of the system and hence cannot be neglected. Above T_c, $N_0/N \to 0$ as $N \to \infty$ for fixed $\frac{N}{V}$ meaning the occupation number in the ground state can be neglected.

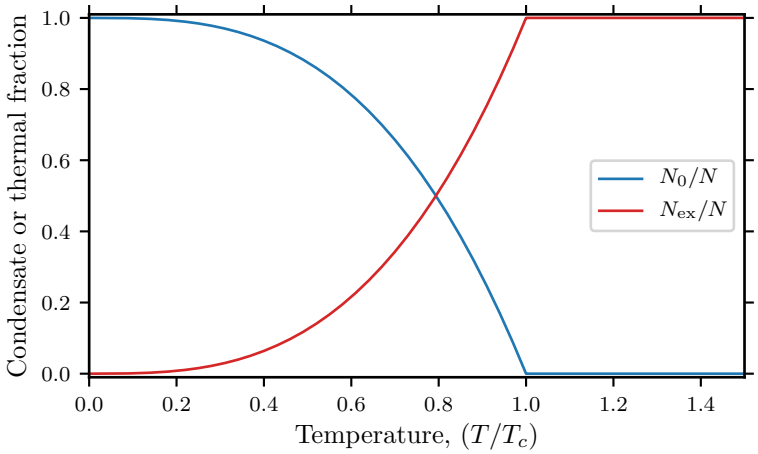

Figure 2.3: Change in condensate and thermal fraction as a function of temperature in units of the critical temperature, T_c. Below T_c macroscopic occupation of the ground state occurs and the fraction of condensed atoms increases according to Eq. (2.9). This form is only applicable for a three-dimensional harmonic trap. For other dimensions and trapping potentials, the exponent in Eq. (2.9) changes.

can then be derived as $N_0 = N - N_{\text{ex}}$.

$$T < T_c \Rightarrow \mu = 0 \Rightarrow N_{\text{ex}} = \frac{1}{2\left(\hbar\bar{\omega}\right)^3} \int_0^\infty \frac{\epsilon^2}{\mathrm{e}^{\frac{\epsilon}{\mathrm{k_B}T}} - 1} \mathrm{d}\epsilon = \left(\frac{\mathrm{k_B}T}{\hbar\bar{\omega}}\right)^3 \mathrm{Zeta}\left(3\right) \tag{2.7}$$

From the definition above, at T_c, $N = N_{\text{ex}}$, the T_c for Bose Einstein condensation in a 3-dimensional harmonic trap can be calculated as:

$$k_{\mathrm{B}}T_c = \left(\mathrm{Zeta}\left(3\right)\right)^{-\frac{1}{3}} N^{\frac{1}{3}} \hbar\bar{\omega} \approx 0.94 N^{\frac{1}{3}} \hbar\bar{\omega} \tag{2.8}$$

and hence the number of condensed atoms, N_0 obeys (as shown in Fig. 2.3):

$$N_0 = N - N_{\text{ex}} = N\left(1 - \left(\frac{T}{T_c}\right)^3\right) \tag{2.9}$$

The system of fermions does not have the same issues as the bosonic system when $\epsilon = \mu$ and $n_{\mathbf{k}}$ as defined in Eq. (2.3) remains finite. It can be seen in Fig. 2.2 that it is possible to have $\mu \geq 0$ and that due to Pauli's Exclusion Principle there will be no macroscopic occupation of the ground state at low temperatures. It is insightful to look at $n_{\mathbf{k}}$ at various temperatures, as shown in Fig. 2.4, and it can be seen that $n_{\mathbf{k}}$ tends to a step function as $T \to 0$:

$$n_{\mathbf{k}} = \begin{cases} 1 & (\epsilon_{\mathbf{k}} < \mu) \\ 0 & (\epsilon_{\mathbf{k}} > \mu) \end{cases} \tag{2.10}$$

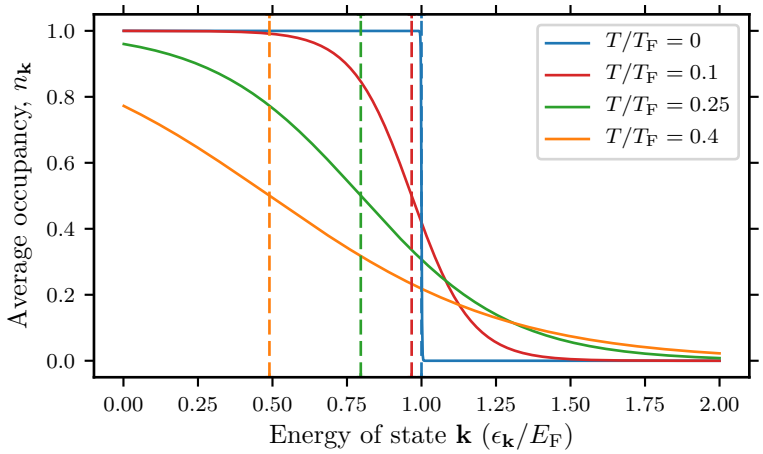

Figure 2.4: Average occupancy of a state $\mathbf{k}$ with energy $\epsilon_{\mathbf{k}}$ for various temperatures as denoted by the legend. The dashed vertical line represents the value of the chemical potential μ in units of E_F for the corresponding temperature and these values can be compared to Fig. 2.2. As $T \to 0$, the average occupancy approaches a step function. At higher temperatures the distribution gets broader around μ and μ shifts to values lower than E_F and eventually becomes negative as we reach the limit of a classical gas.

In the limit of $T \to 0$ the chemical potential approaches the Fermi energy, E_F. This quantity can be solved for analytically by using Eq. (2.6):

$$N = \int_0^{E_F} \overbrace{\frac{\epsilon^2}{2\left(\hbar\bar{\omega}\right)^3}}^{g(\epsilon)} \overbrace{1}^{n(\epsilon)} \mathrm{d}\epsilon = \frac{{E_F}^3}{6\left(\hbar\bar{\omega}\right)^3} \tag{2.11}$$

and hence:

$$\mu\left(T \to 0\right) = E_F = \left(6N\right)^{\frac{1}{3}} \hbar\bar{\omega} \tag{2.12}$$

In the zero temperature limit, all states up to an energy of E_F are occupied and the additional energy required to add a particle to the system will be E_F, which explains why $\mu\left(T \to 0\right) = E_F$. A Fermi temperature, T_F, can be defined such that $E_F = k_B T_F$.

In this section thermodynamics and quantum statistics have been used to compare ideal Bose and Fermi systems, with additional comparisons drawn to the ideal classical gas in the appropriate limits. The onset of Bose Einstein condensation has been derived for a three-dimensional harmonic trap and properties of a degenerate Fermi gas have been highlighted. In Section 2.2 basic scattering theory and Feshbach resonances are discussed and Section 2.3 covers the BEC-BCS crossover physics of fermions.

2.2 Scattering and Feshbach Resonances

Scattering and Elastic Collisions

In order to understand the collisional properties of ultracold quantum gases, this section covers the basic process of elastic scattering between atoms. The physics of scattering is a complex topic. To simplify the discussion it is assumed that the gas is at a low temperature such that:

$$r_0 \ll \lambda_{DB} = \sqrt{\frac{2\pi\hbar^2}{m\mathrm{k_B}T}} \tag{2.13}$$

where r_0 is the characteristic spatial range of the interatomic potential between the scattering atoms and λ_{DB} is the thermal De Broglie wavelength, and that the gas is dilute:

$$n{r_0}^3 \ll 1, \quad r_0 \ll {k_F}^{-1} \tag{2.14}$$

In the dilute limit, atoms interact pairwise as the probability of a three body collision is significantly lower than that of a two body. The discussion of quantum statistics in Section 2.1 indicated that the scattering properties will not only depend on the interatomic potential but also on whether the particles are distinguishable or indistinguishable bosons or fermions. At times long before[1] the collision event, both atoms are in momentum eigenstates, $\mathbf{k}$, and the wave function can be written as a plane wave. If we move to the center of mass frame with relative coordinates, the interatomic potential can be seen as a central potential $V(|\mathbf{r}_1 - \mathbf{r}_2|)$ that perturbs the wave function. It can be shown that for a central potential the radial and angular solutions of the Schrödinger equation can be separated, allowing the scattered wave function to be written as an outwards-propagating spherical wave [95, 97]:

$$\lim_{r\to\infty} \psi = \overbrace{\mathrm{e}^{ikz}}^{\text{incoming}} + \overbrace{f(\theta)\frac{\mathrm{e}^{ikr}}{r}}^{\text{scattered}} \tag{2.15}$$

Here we have chosen, for simplicity, the initial motion of the particles to be along the z axis. The term $f(\theta)$ is called the scattering amplitude with $|f(\theta)|^2$ giving the probability of scattering in a given direction. Here θ is the scattering angle and it is noted that the axial symmetry of the problem means that $f(\theta)$ does not depend on the azimuthal angle ϕ which defines the plane of scattering. Since the scattered wave function is a solution of the Schrödinger equation in a central potential, it can be expressed as the linear combination

[1] and hence at large distances from the collision event.

of radial and angular eigenfunctions:

$$\sum_{l=0}^{\infty}\sum_{m=-l}^{m=+l} c_{lm}R_l(k,r)Y_l^m(\theta,\phi) \tag{2.16}$$

By substitution it can then be shown [95,97] that the scattering amplitude can be written as a sum over the angular momentum quantum number, l:

$$f(\theta) = \frac{1}{2ik}\sum_{l=0}^{\infty}(2l+1)\left(\mathrm{e}^{2i\eta_l}-1\right)P_l(\cos\theta) \tag{2.17}$$

This is known as the partial wave decomposition where the constants[1] c_{lm} have been replaced with $\mathrm{e}^{i\eta_l}$ and P_l is the l^{th} order Legendre polynomial. This phase shift term allows for the correct asymptotic form of the wave function and is related to the interaction potential. Since the collision is elastic, $\hbar^2k^2/2m$, k and λ_{DB} are conserved and only the phase of the outgoing wave contains the information of the scattering event. In the limit $k \to 0$, which is relevant at the low energies and temperatures under consideration, it can be shown [95, 97] that for power-law potentials the $l = 0$ (s-wave scattering) term dominates Eq. (2.17). At this point we introduce an expression for the phase shift η_0, in terms of a length scale known as the scattering length, a. In the low energy approximation, the effective range expansion [97] can be performed that introduces an additional length scale, the effective range, r_e:

$$\lim_{k\to 0} k\cot(\eta_0) = -\frac{1}{a} + \frac{1}{2}k^2 r_e + \mathcal{O}(k^4) \tag{2.18}$$

The effective range length scale determines the range of k values over which a can be approximated as:

$$\lim_{k\to 0} a = -\frac{\tan(\eta_0)}{k} \tag{2.19}$$

In the limit where $|a| \gg r_0$, then $r_e \sim r_0$ and Eq. (2.19) is a good approximation. The scattering length is a measure of the interaction strength and is closely related to the phase shift of the scattered wave function. In many cases, the scattering length can be thought of as an effective radius of particles in the scattering process. The low energy (s-wave) scattering amplitude can, by substituting Eq. (2.18) in Eq. (2.17), be expressed as:

$$f_{l=0}(k) = \frac{1}{k\cot(\eta_0) - ik} \approx \frac{1}{-a^{-1} + \frac{k^2 r_e}{2} - ik} \tag{2.20}$$

[1] ψ is independent of ϕ, so $f(\theta)$ can be written independently of the magnetic quantum number, m.

where we see that for s-wave scattering the f no longer depends on θ. The total cross-section area, σ, describes the likelihood of a scattering event and can be defined as:

$$\sigma = \int_0^\pi 2\pi \sin(\theta)|f(\theta)|^2 \mathrm{d}\theta \tag{2.21}$$

One finds that generally [97]:

$$\sigma = \frac{4\pi}{k}\mathrm{Im}f(0) \tag{2.22}$$

This equation, known as the optical theorem, includes higher angular momentum scattering, however, using the form of the scattering amplitude in Eq. (2.20) gives an s-wave total cross-section of the form:

$$\sigma_{l=0} = \frac{4\pi a^2}{1 + k^2a^2\left(1 - \frac{r_e}{a}\right)} \tag{2.23}$$

neglecting terms $\mathcal{O}((a/r_e)^2)$ or smaller. It is interesting to note that the cross-section only depends on a^2 and hence that the collisional properties determined by the cross-section are independent of the sign of a, even though the thermodynamics depend noticeably on the sign of a. In typical cold atom experiments $r_e/a \ll 1$ meaning:

$$\sigma_{l=0} \approx \frac{4\pi a^2}{1 + k^2a^2} \tag{2.24}$$

In the limit of $k \to 0$ such that $ka \to 0$, as well, the s-wave scattering length simplifies to the form:

$$\lim_{k\to 0} \sigma_{l=0} = 4\pi a^2 \tag{2.25}$$

In the unitarity limit (which is discussed in more detail in Section 2.3) $a \to \infty$ and:

$$\lim_{a\to\infty} \sigma_{l=0} = \frac{4\pi}{k^2} \tag{2.26}$$

This regime is interesting as the scattering amplitude and hence the cross-section obey universal laws that are independent of any properties of the scattering interaction. We end the discussion of scattering by noting that the Eqs. (2.23) to (2.26) above are valid for distinguishable atoms in the scattering process. When the atoms are indistinguishable,

the quantum statistics play a role and affect the scattering amplitude [97]:

$$\text{scattering amplitude} = \begin{cases} f(\theta) \approx f_{l=0} \approx -a & \text{(distinguishable)} \\ f(\theta) + f(\pi - \theta) \approx 2f_{l=0} \approx -2a & \text{(bosons)} \\ f(\theta) - f(\pi - \theta) \approx 6f_{l=1}\cos(\theta) \propto k^2 & \text{(fermions)} \end{cases} \tag{2.27}$$

While the bosonic system has a factor of two larger scattering amplitude, fermions have an s-wave scattering amplitude that goes to zero, meaning the scattering amplitude is dominated by the much smaller $l = 1$ term. This term goes to zero in the limit $k \to 0$, which explains why degenerate Fermi gases do not thermalize.

Feshbach Resonances

We now turn our attention to how the spin of the interacting particles can affect the scattering process. It will be shown that the presence of a bound-state resonance in the continuum of states allows an in-situ manipulation of the scattering length. This allows ultracold quantum gases to be tuned from strongly interacting to non-interacting both repulsively and attractively. These (Fano-)Feshbach resonances [32] are used in many quantum gas experiments but have been extremely important in Fermi gases where the lifetime of the gas across the Feshbach resonance is still long as three body losses are suppressed by Pauli blocking. A comprehensive review of Feshbach resonances in ultracold atom experiments is given in [93, 94, 97, 98].

The spin dependence of the interaction during the scattering process means there are both open and closed channels. Here the open channel is defined as the scattering channel of the incoming particles in their initial spin configuration and the closed channel is the scattering channel of the particles in a different spin configuration, which supports some bound state[1]. In ultracold atom experiments these two channels are coupled because different hyperfine states can interact.

It can be seen from Eq. (2.20) that a resonance in the scattering amplitude occurs when:

$$k \cot \eta_0 = 0 \tag{2.28}$$

from which the scattering length around the resonance can be characterized. It can be shown that the resonance will occur whenever the bound state energy in the closed state

[1]The channel is referred to as closed as it is energetically inaccessible in the s-wave limit.

equals the incoming energy in the open channel [94,98]. Generally, the magnetic moment of the open and closed channels will be different and hence the difference between the bound state energy and the energy of the open channel can be tuned with a magnetic field due to the different Zeeman shifts. The scattering length, $a(B)$, across the Feshbach resonance can then be characterized in the simple form as function of magnetic field, B [94]:

$$a(B) = a_{\mathrm{bg}}\left(1 - \frac{\Delta_B}{B - B_0}\right) \tag{2.29}$$

where a_{bg} is background scattering length far from the resonance and B_0 and Δ_B characterize the position and width of the resonance in the magnetic field. To better understand the mechanism, consider the specific example [99] of the hyperfine states in the $2^2\mathrm{S}_{\frac{1}{2}}$ manifold of ^{6}Li used in the experiment. At sufficiently large magnetic fields ($> 200\,\mathrm{G}$), the electron spin is fully polarized and the colliding atoms have their spins aligned (triplet configuration in the open channel). The hyperfine interaction allows the exchange of electron and nuclear spin, meaning the open channel is coupled to the closed channel where the spins are oppositely aligned (singlet configuration in the closed channel). The coupling strength is defined by some off-diagonal potential with a characteristic range $\sim r_e$. The magnetic moment of the singlet channel is zero and different to the magnetic moment in the open channel of $\sim 2\mu_{\mathrm{B}}$, which means the asymptotic energies of the channels and the presence of the bound state can be tuned with the magnetic field. Notably, it is possible to tune the field such that the bound state in the closed channel is slightly below the threshold of the continuum in the open channel, to a situation where it is just above, which defines the Feshbach resonance field.

The parameters B_0 and Δ_B are often determined experimentally [100, 101] as theoretical models are limited by a lack of knowledge of short range microscopic potentials. In the limit that $k_F|r_e| \ll 1$, r_e does not affect the many-body physics which is determined only by $k_F a$ and the Feshbach resonance is described as broad. This is equivalent to saying that the energy width of the resonance is large compared to $\hbar^2k^2/2m$. In this case, all atoms in the gas have the same scattering length, which can be compared to the case of a narrow resonance where the scattering length depends on k. The three lowest hyperfine states of ^{6}Li ($|1\rangle, |2\rangle, |3\rangle$) have exceptionally broad Feshbach resonances between 600 G to 800 G (see Table 2.1). The $|12\rangle$ Feshbach resonance, characterized by equation Eq. (2.29), is shown in Fig. 2.5 and compared to the precisely characterized values determined in [101].

Close to the Feshbach resonance, at positive scattering length, shallow s-wave dimers (weakly bound molecules) exist and the wave function has a finite admixture of the closed

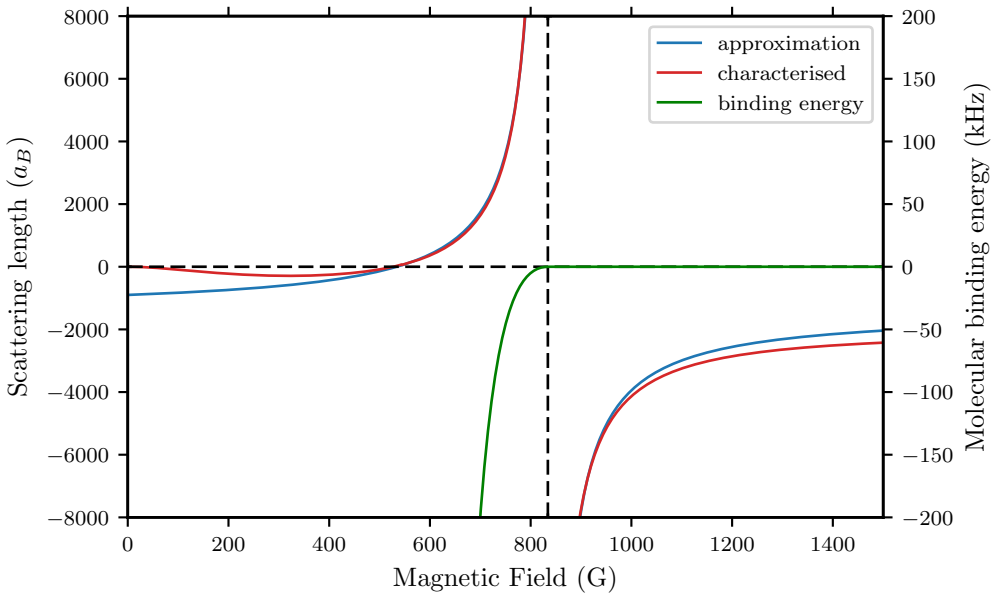

Figure 2.5: Feshbach resonance of the two lowest hyperfine states of ^{6}Li. The blue curve shows the approximation of the scattering length in units of a_B (left axis) in the form of Eq. (2.29), using the values for a_{bg}, B_0 and Δ_B from [100], which are also tabulated in Table 2.1. The red curve shows the accurately determined scattering length as a function of B, determined using radio-frequency dissociation spectroscopy of weakly bound molecules [101] (data for red curve taken from supplementary material of [101]). The comparison shows that the approximation works very well in the vicinity of the Feshbach resonance. The green curve shows the binding energy (right axis) of the weakly bound molecules that exist for positive a near the Feshbach resonance.

Table 2.1: Parameters to characterize the Feshbach resonances in the three lowest hyperfine states of ^{6}Li. Parameters are as defined in Eq. (2.29) and the values are taken from [100].

states	resonance field, B_0 (G)	resonance width, Δ_B (G)	background scattering length, a_{bg} (a_B)
$\|12\rangle$	834.15	-300	-1405
$\|13\rangle$	690.43	-122.3	-1727
$\|23\rangle$	811.22	-222.3	-1490

channel bound state. The molecules will have a characteristic size of a and a binding energy, ϵ_B, of [93, 94, 98]:

$$\epsilon_B = -\frac{\hbar^2}{2m_r a^2} \tag{2.30}$$

where m_r is the reduced mass of the two scattering particles. This binding energy is shown in kHz in Fig. 2.5 for ^{6}Li. These interacting dimers are composite bosonic molecules and lead to the BEC side of the BEC-BCS crossover (Section 2.3). Since these molecules are bosonic, they can scatter with indistinguishable molecules or distinguishable atoms, which plays a crucial role in the dramatic difference in lifetime of fermions and bosons at a Feshbach resonance. The weakly bound dimers are in the highest rotovibrational state, but can exchange energy in collisions and reach more deeply bound molecular states where the molecules have a size $\sim r_0$ [93]. This process releases a large energy $\sim \frac{\hbar^2}{mr_0^2}$, which can cause losses when converted to kinetic energy. A simple model of the relaxation process [93, 102–104] can be used to write:

$$\dot{n}_{\mathrm{a}} = -\alpha_{\mathrm{ad}} n_{\mathrm{a}} n_{\mathrm{d}} \tag{2.31}$$

$$\dot{n}_{\mathrm{d}} = -\alpha_{\mathrm{dd}} n_{\mathrm{d}}^2 \tag{2.32}$$

where n_a and n_d are the atom and dimer density respectively and α_{ad} and α_{dd} are loss coefficients. It can be shown [103] that for bosons, the α coefficients increase with increasing a but that for fermions, due to Pauli blocking, they decrease with increasing a. This ensures that degenerate Fermi gases are stable and have long lifetimes across the Feshbach resonance. It is also important to determine the parameters of how the dimers scatter with each other, which is relevant far on the BEC side of the Feshbach resonance where most atoms form molecules. By solving the three body Schrödinger equation[1] it was shown [102–104] that $a_{ad} = 1.2a$ and $a_{dd} = 0.6a$, where a_{ad} and a_{dd} are the atom-dimer and dimer-dimer scattering lengths, respectively.

Now that the fundamentals of the Feshbach resonance have been described and it has been shown that the interactions can be tuned in-situ over a large range, Section 2.3 will discuss how the physics of the interacting Fermi gas changes across the Feshbach resonance.

[1]Mean field theory gives [105] $a_{ad} = 8a/3$ and $a_{dd} = 2a$ which is significantly different to the corrected result given in the main text.

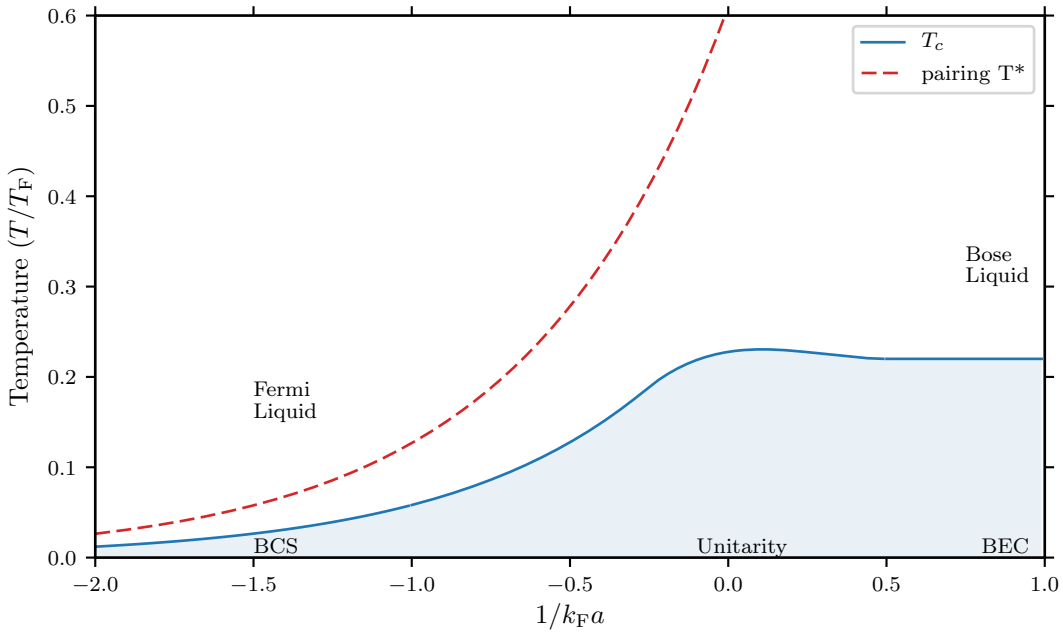

Figure 2.6: Phase diagram of the BEC-BCS crossover highlighting the critical temperature, T_c, and pairing temperature, T^*, as a function of the interaction paramter, $1/k_Fa$. The shaded blue region highlights the phase transition to the superfluid state. In the BEC regime this is approximately a constant as predicted by Eq. (2.8). In the BCS regime the critical temperature exponentially decays with $1/k_Fa$. The unitarity regime, where $1/k_Fa \to 0$, has the highest T_c/T_F of any known system. The form of T_c and T^* for this figure are derived using the method described in [106]. Whether there exist preformed pairs at a temperature above T_c in the unitarity/crossover regime is still a topic under much investigation [107].

2.3 The BEC-BCS Crossover

In Section 2.1 it was shown that for a non-interacting Fermi gas, as the temperature decreased, there was no phase transition. The chemical potential tended asymptotically to the Fermi energy and average occupation tended towards a step function (Figs. 2.1 and 2.2). If a spin-mixture of fermions is considered, the possibility of using the Feshbach resonances discussed in Section 2.2, makes clear how important interactions are in the physics of the system. For example, at large, positive scattering lengths, it was shown that the system will form repulsive bosonic dimers which can form a Bose-Einstein condensate. In this section the BEC, BCS and unitarity regimes of the BEC-BCS crossover will be discussed with a focus on highlighting the connection between the two regimes. Fig. 2.6 shows the phase diagram for the superfluid state across the BEC-BCS crossover, characterized by the dimensionless interaction parameter $1/k_Fa$.

The BEC Regime

In the BEC regime where $1/k_F a \gg 1$ the strongly attractive interaction potential is resolved by the formation of dimers, which interact repulsively and weakly ($a_{dd} = 0.6a$ see Section 2.2). Far in the BEC regime these dimers are tightly bound with the size of the pairs much smaller than ${k_F}^{-1}$ and they hence behave like the bosons discussed in Section 2.1.

The BCS Regime

In the regime where the s-wave scattering is negative, there is no bound state and hence molecule formation is not allowed. For $1/k_F a \ll -1$ there is a weak attractive interaction between fermions, however, at temperature $T/T_F \ll 1$ all states with momentum less than k_F are occupied, which dramatically changes the interacting many-body system. In solid state systems the effective weak attraction between electrons is mediated by the electron-phonon interaction. The Fröhlich Hamiltonian [108–110] which incorporates electron-phonon interactions has the form:

$$\mathcal{H} = \overbrace{\mathcal{H}_0}^{\text{non-interacting}} + \overbrace{\sum_{\mathbf{k},s,\mathbf{k}',s',\mathbf{q}} W_{\mathbf{k},\mathbf{k}',\mathbf{q}} c^\dagger_{\mathbf{k}'+\mathbf{q},s'} c^\dagger_{\mathbf{k}-\mathbf{q},s} c_{\mathbf{k},s} c_{\mathbf{k}',s'}}^{\text{electron-phonon}} \tag{2.33}$$

where $\mathcal{H}$ is the Hamiltonian of the non-interacting system, $c^\dagger$ and c are fermionic creation and annihilation operators and $W_{\mathbf{k},\mathbf{k}',\mathbf{q}}$ is the matrix element describing scattering between electrons of momentum $\mathbf{k}$ and $\mathbf{k}'$ mediated by a phonon quasiparticle of momentum $\mathbf{q}$. In 1957 Bardeen, Cooper and Schrieffer (BCS) first wrote down this Hamiltonian, with some simplifications, and used a variational approach to explore its properties [26]. To simplify Eq. (2.33) to the BCS Hamiltonian some assumptions must be introduced. It was postulated that the ground state of the system is a condensate of pairs with zero momentum. Hence, it is assumed that scattering events take place between pairs of particles of equal and opposite momentum[1] (Cooper pairs), which means in the summation in Eq. (2.33) only terms with $\mathbf{k} = -\mathbf{k}$ are considered. Additionally, Pauli blocking means that fermions of equal spin do not interact and hence, the pairs are made up of particles of different spin. Since the systems originally considered were electrons in a metal, the discussion was limited to spin 1/2 systems ($\uparrow, \downarrow$). This allows the BCS Hamiltonian to be

[1] If the center of mass momentum of a pair was non-zero, the density of states available for pairing would be dramatically reduced. This finite momentum pairing is the subject of FFLO superconductivity.

written as:

$$\mathcal{H}_{\text{BCS}} = \overbrace{\sum_{\mathbf{k},\mathbf{s}} (\epsilon_{\mathbf{k}} - \mu) c^{\dagger}_{\mathbf{k},\mathbf{s}} c_{\mathbf{k},\mathbf{s}}}^{\text{non-interacting}} + \overbrace{\sum_{\mathbf{k},\mathbf{k}'} V_{\mathbf{k},\mathbf{k}'} c^{\dagger}_{\mathbf{k},\uparrow} c^{\dagger}_{-\mathbf{k},\downarrow} c_{-\mathbf{k}',\downarrow} c_{\mathbf{k}',\uparrow}}^{\text{BCS interaction}} \tag{2.34}$$

The second term describes the destruction of a Cooper pair at momentum $|\mathbf{k}'|$ and the creation of another pair with momentum $|\mathbf{k}|$ with a coefficient of $V_{\mathbf{k},\mathbf{k}'}$. Hence, a negative $V_{\mathbf{k},\mathbf{k}'}$ corresponds to an overall attractive interaction between fermions. Given the form of the second term, a Bogoliubov-Valatin transformation [111] will be helpful in attempting to diagonalize $\mathcal{H}_{BCS}$, where new fermionic operators $\gamma_{\mathbf{k},\mathbf{s}}$ are introduced:

$$c_{\mathbf{k},\uparrow} = u^{*}_{\mathbf{k}} \gamma_{\mathbf{k},\uparrow} + v_{\mathbf{k}} \gamma^{\dagger}_{-\mathbf{k},\downarrow} \tag{2.35}$$

$$c^{\dagger}_{-\mathbf{k},\downarrow} = u_{\mathbf{k}} \gamma^{\dagger}_{-\mathbf{k},\downarrow} - v^{*}_{\mathbf{k}} \gamma_{\mathbf{k},\uparrow} \tag{2.36}$$

$$|u_{\mathbf{k}}|^2 + |v_{\mathbf{k}}|^2 = 1 \tag{2.37}$$

This transformation will not completely diagonalize $\mathcal{H}_{BCS}$, which involves terms with four creation/annihilation operators, however, a mean-field approach allows these terms to be approximated[1]. By substituting these equations into Eq. (2.34) and requiring that the overall Hamiltonian is diagonal in the $\gamma_{\mathbf{k},\mathbf{s}}$ basis, the following forms for the coefficients in the transformation can be found:

$$|u_{\mathbf{k}}|^2 = \frac{1}{2}\left(1 + \frac{\xi_{\mathbf{k}}}{\sqrt{\xi^2_{\mathbf{k}} + |\Delta_{\mathbf{k}}|^2}}\right) \tag{2.38}$$

$$|v_{\mathbf{k}}|^2 = \frac{1}{2}\left(1 - \frac{\xi_{\mathbf{k}}}{\sqrt{\xi^2_{\mathbf{k}} + |\Delta_{\mathbf{k}}|^2}}\right) \tag{2.39}$$

where $\xi_{\mathbf{k}} = \epsilon_{\mathbf{k}} - \mu$ and the gap function has been introduced as:

$$\Delta_{\mathbf{k}} = -\sum_{\mathbf{k}'} V_{\mathbf{k},\mathbf{k}'} \langle c_{-\mathbf{k}',\downarrow} c_{\mathbf{k}',\uparrow} \rangle \tag{2.40}$$

and hence the Hamiltonian can be written as:

$$\mathcal{H}_{BCS} = \sum_{\mathbf{k},\mathbf{s}} \overbrace{\sqrt{\xi_{\mathbf{k}} + |\Delta_{\mathbf{k}}|^2}}^{\text{excitation spectrum}} \gamma^{\dagger}_{\mathbf{k},\mathbf{s}} \gamma_{\mathbf{k},\mathbf{s}} + \overbrace{\sum_{\mathbf{k}} \left(\xi_{\mathbf{k}} - \sqrt{\xi_{\mathbf{k}} + |\Delta_{\mathbf{k}}|^2} + \Delta_{\mathbf{k}} \left\langle c^{\dagger}_{\mathbf{k}\uparrow} c^{\dagger}_{-\mathbf{k}\downarrow} \right\rangle\right)}^{\text{ground state energy}} \tag{2.41}$$

[1]The mean field decoupling is of the form [111]: $\left\langle c^{\dagger}_{\mathbf{k},\uparrow} c^{\dagger}_{-\mathbf{k},\downarrow} c_{-\mathbf{k}',\downarrow} c_{\mathbf{k}',\uparrow} \right\rangle \approx \left\langle c^{\dagger}_{\mathbf{k},\uparrow} c^{\dagger}_{-\mathbf{k},\downarrow} \right\rangle c_{-\mathbf{k}',\downarrow} c_{\mathbf{k}',\uparrow} + c^{\dagger}_{\mathbf{k},\uparrow} c^{\dagger}_{-\mathbf{k},\downarrow} \langle c_{-\mathbf{k}',\downarrow} c_{\mathbf{k}',\uparrow} \rangle - \left\langle c^{\dagger}_{\mathbf{k},\uparrow} c^{\dagger}_{-\mathbf{k},\downarrow} \right\rangle \langle c_{-\mathbf{k}',\downarrow} c_{\mathbf{k}',\uparrow} \rangle$.

The second term in Eq. (2.41) is some constant ground state energy and the first term shows the excitation spectrum, where $\gamma^{\dagger}_{\mathbf{k},\mathbf{s}}$ corresponds to the creation of a quasiparticle. Even at values of $k = k_F$ where $\xi_{\mathbf{k}} = 0$ (see Eq. (2.10)) the energy spectrum has a gap $|\Delta_{\mathbf{k}}|$ and hence an energy of at least $2|\Delta_{\mathbf{k}}|$ is required to excite quasiparticles. The gap can be determined self-consistently by substituting Eqs. (2.38) and (2.39) into Eq. (2.40). Following the discussion in Section 2.2, for Fermi gases around a Feshbach resonance, the interaction can be described by the s-wave scattering length which is independent of $\mathbf{k}$ and hence the gap is independent of $\mathbf{k}$ ($\Delta_{\mathbf{k}} = \Delta$). In the BCS limit it can be shown [112] that:

$$\Delta = \frac{8E_F}{\mathrm{e}^2}\mathrm{e}^{-\frac{\pi}{2k_F|a|}} \tag{2.42}$$

showing the exponential decay in Δ with $1/k_F a$.

The BCS wave function, $|\psi_{\mathrm{BCS}}\rangle$, can be written as an arbitrary combination of Cooper pairs [26, 112]:

$$|\psi_{\mathrm{BCS}}\rangle = \prod_k \left(u_{\mathbf{k}} + v_{\mathbf{k}} c^{\dagger}_{\mathbf{k},\uparrow} c^{\dagger}_{-\mathbf{k},\downarrow}\right)|0\rangle \tag{2.43}$$

This wave function is clearly not an eigenstate of the total number operator. From the wave function it is possible to see another interpretation for the parameters $u_{\mathbf{k}}$ and $v_{\mathbf{k}}$; they represent the probability densities that the Cooper pair at momentum $\mathbf{k}$ is occupied[1]. Since any perturbations to the system must be written with at least two creation or annihilation operators, it is clear that only pairs of quasiparticles can be excited. The amount the total energy is reduced by forming Cooper pairs is very small, as only a small number of atoms near the Fermi surface are affected by the attractive interaction. The formation of the gap corresponds to a second order phase transition to a superfluid state and off-diagonal long range order of Cooper pairs [26]. The superfluid transition temperature, T_c, is defined as the lowest temperature at which the $\Delta = 0$. By analyzing the pair amplitudes at finite temperature [112], the temperature dependence of the gap can be calculated. One can show that there is a relatively large many-body correction to T_c beyond mean field theory, known as the Gor'kov and Melik-Barkhudarov approximation[2] [112, 113], giving:

$$k_{\mathrm{B}} T_c \approx 0.277 E_{\mathrm{F}} \mathrm{e}^{-\frac{\pi}{2k_F|a|}} \tag{2.44}$$

[1] Bardeen, Cooper and Schrieffer originally started from a wave function like Eq. (2.43) and minimized the expectation value of $\mathcal{H}_{\mathrm{BCS}}$ to find the parameters $u_{\mathbf{k}}$ and $v_{\mathbf{k}}$.

[2] Mean field theory gives a prefactor of 0.613 compared to 0.277 in Eq. (2.44). This suppression of T_c by the many-body effect is due to higher order diagrams screening the bare interaction [112].

Unitarity and the Crossover

As $|1/k_F a| \to 0$ the unitarity regime is reached where the scattering length a diverges, becoming much larger than the inter particle distance, and hence all measurable quantities must obey universal laws. Universality means that these quantities are independent of microscopic details of the system[1]. The unitarity regime in the context of Fermi gases across a Feshbach resonance was first considered by Nikolic and Sachdev [33]. There is not yet any exact solution to the many-body problem for $|1/k_F a| \leq 1$ and approximate techniques must be used to investigate the unitarity regime (for example quantum Monte-Carlo techniques [75,114,115]). Further understanding of the unitarity regime was gained by a series of generalized relationships developed by Tan [35,36], which characterize many properties of the unitarity gas in terms of a contact parameter. These methods have predicted that the unitarity gas of fermions has the highest T_c/T_F for superfluidity of any known system [116]. In the unitarity regime, the characteristic size of pairs is similar to the interparticle distance and the picture of Cooper pairs of a size much greater than the interparticle distance (the BCS regime) is no longer valid. In fact at unitarity, the existence of pair formation does not imply superfluidity, whereas in the BCS regime the energy gap associated with the formation of Cooper pairs is equivalent to the order parameter [93].

The unitarity regime smoothly connects the repulsive BEC regime and the attractive BCS regime. This transition is a continuous crossover from bound molecules (BEC regime) to spatially separated Cooper pairs (BCS regime) as shown in Fig. 2.6. The mean field approach to the crossover was formulated by Leggett [117], using a variational BCS wave function through the entire crossover. The only difference between this formulation and the BCS theory presented above is that μ must now be solved self consistently with Δ, whereas in the BCS theory $\mu = E_F$. Following [117] and [118], the μ and Δ can be calculated in the crossover regime from the equations below:

$$\frac{1}{k_{\mathrm{F}} a} = -\frac{2}{\pi} I_1\left(\frac{\mu}{\Delta}\right)\left(\frac{2}{3 I_2\left(\frac{\mu}{\Delta}\right)}\right)^{1/3} \tag{2.45}$$

$$\frac{\Delta}{E_{\mathrm{F}}} = \left(\frac{2}{3 I_2\left(\frac{\mu}{\Delta}\right)}\right)^{2/3} \tag{2.46}$$

[1] up to corrections of the order $(k_F r^*)^2$.

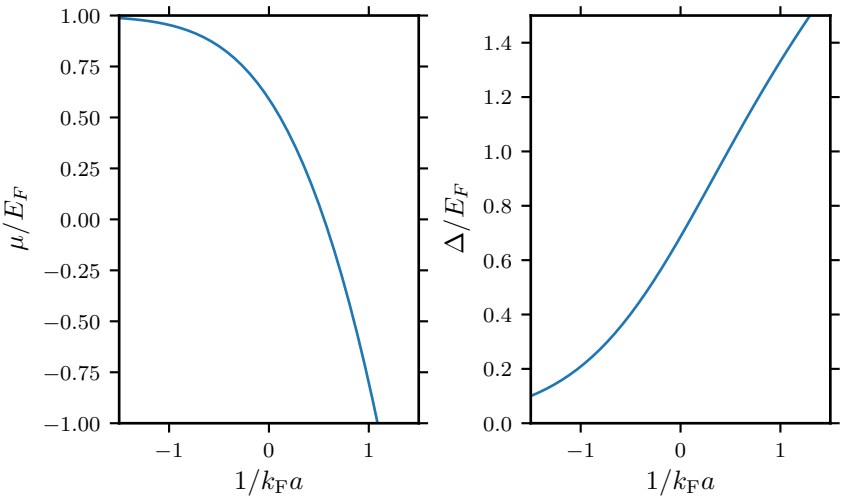

Figure 2.7: Chemical potential, μ, and gap, Δ, in the BEC-BCS crossover using the BCS variational approach (Eqs. (2.45) and (2.46)) as described in [117] and [118].

where:

$$I_1(z) = \int_0^\infty x^2 \left(\frac{1}{\sqrt{(x^2 - z)^2 + 1}} - \frac{1}{x^2} \right) \mathrm{d}x \tag{2.47}$$

$$I_2(z) = \int_0^\infty x^2 \left(1 - \frac{x^2 - z}{\sqrt{(x^2 - z)^2 + 1}} \right) \mathrm{d}x \tag{2.48}$$

Eq. (2.45) can be solved numerically to obtain μ/Δ for an arbitrary $1/k_\mathrm{F}a$. This μ/Δ can then be substituted into Eq. (2.46) to obtain Δ/E_F. These quantities are shown in Fig. 2.7 for $1/k_\mathrm{F}a$ varying from BCS to BEC. The mean field theory above overestimates Δ as a mean field theory is not appropriate in the regions of strong interactions where many-body and higher order diagrams play a significant role [112, 113].

Chapter 3

Experimental Setup

3.1 Introduction

This chapter details the construction and setup of the experimental apparatus, which was the first new experiment built after the research group relocated to the University of Bonn. How the system is then used to produce degenerate quantum gases is described in Chapters 4 and 5. In Section 3.2 the layout of the vacuum system is provided. Additional details of the vacuum bake-out and atomic oven can be found in Appendices B.1 and B.2. The many different laser systems used in the experiment are detailed in Section 3.3. An introduction to Helmholtz and anti-Helmholtz magnetic field coils is given in Section 3.4 followed by a detailed discussion of the magnetic coils used in the experiment. Section 3.4 also discusses the water cooling and the different electronics used for the high current coils. Details and schematics of the electronics can be found in Appendix B.3. Section 3.5 describes the radio frequency and microwave setup used in the experiment. Details of the experiment control software and how the experiment cycle is produced are given in Appendix B.5. Many elements of this chapter will also be in the thesis of Alexandra Behrle, which will specifically contain more detail on the vacuum system design and the ^{23}Na laser system.

3.2 Vacuum System

3.2.1 Construction and Layout

The experiment produces a quantum gas at temperatures $\sim 100\,\mathrm{nK}$ on a cycle every 15 to 20s. The cold atomic gas must be thermally isolated from the environment and protected from collisions with background gas. To achieve this, the atoms are prepared and cooled inside an ultra-high vacuum (UHV) chamber with a pressure less than $1 \times 10^{-11}\,\mathrm{mbar}$. The design of the vacuum system is shown in Fig. 3.1. Sources of ^{23}Na and ^{6}Li are heated in the oven chamber and produce a collimated beam of both species (Appendix B.2). The oven chamber is connected to the main vacuum system via a differential pumping tube that allows the heated oven chamber to be at significantly higher pressures ($8 \times 10^{-9}\,\mathrm{mbar}$) without affecting the UHV of the main chamber. The differential pumping tube connects to a long vacuum stage around which the decreasing field Zeeman slower coils are wound. The small Kimball chamber is at the zero-field crossing of the Zeeman slower and is a diagnosis point for the experiment and a pumping stage. The increasing field Zeeman slower inlet then connects to the main Kimball chamber, where the atoms are trapped. The main Kimball chamber was designed to have high optical access with large side viewports secured by crushing two thin copper knife edges [119]. The top and bottom of the Kimball chamber are attached to recessed buckets which hold the large magnetic coils used for magnetic trapping and the Feshbach fields. Viewports within these buckets (the UKEA viewports) provide optical axis along the vertical direction and may in the future allow for high resolution imaging. A drawing of the main Kimball chamber is shown in Fig. 3.2 which defines the axes used in the description of the experiment. Additionally, magnetic coils are wound around the side viewports to provide compensation or gradient fields. Beyond the main Kimball chamber is the main pumping tower which connects to the window through which the Zeeman slower light enters. The UHV is maintained by four ion pumps distributed across the experiment system and three titanium sublimation pumps. A gate valve is capable of sealing the oven chamber from the remaining system for when the atomic species need to be refilled and another valve can be used to replace the Zeeman slower window if it is coated with ^{6}Li. An additional valve attached to the main Kimball chamber could be used in the future for extensions. Bellows are between several stages of the experiment allowing the vacuum components to be aligned with respect to each other.

For UHV, standard CF vacuum connections must be used [120, 121]. Additionally, all

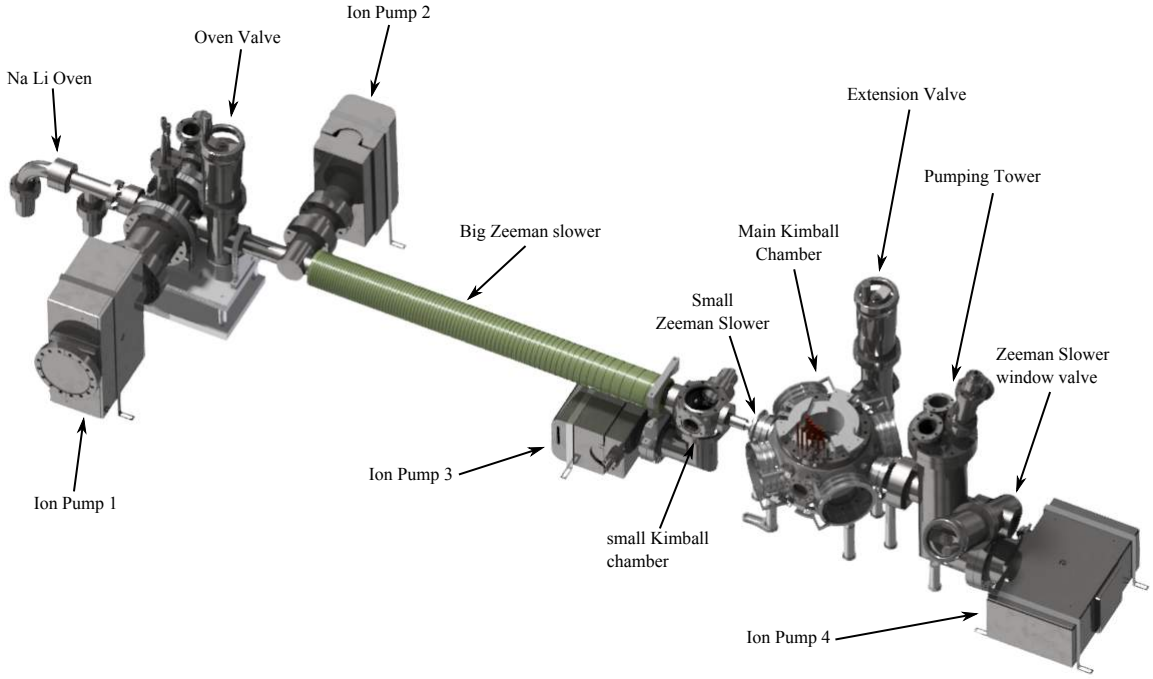

Figure 3.1: The design of the vacuum system highlighting the layout of the experiment. Principle components of the experiment are labeled in the image and will be referred to throughout this thesis. From left to right the atoms effuse from the heated oven, are slowed by the decreasing field (big) and increasing field (small) Zeeman slower, being trapped in the main science chamber.

components within the vacuum must be clean[1] and handled while wearing appropriate gloves. Complete details of the design and construction of the vacuum system will be in the thesis of Alexandra Behrle. Details of the vacuum bake-out and the atomic oven are given in Appendix B.1.

[1] All components were cleaned in an ultrasonic bath with acetone and isopropanol.

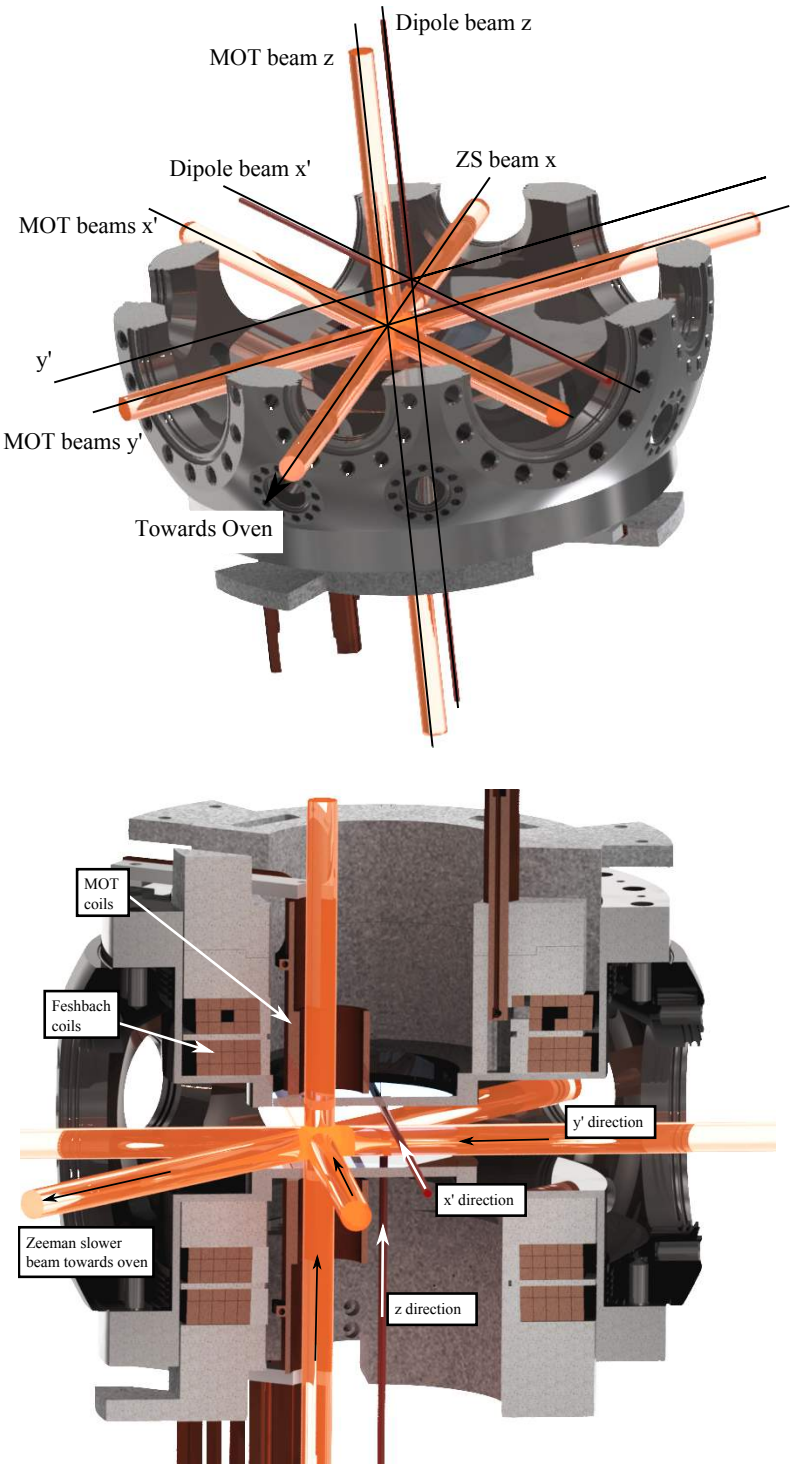

Figure 3.2: The inside of the main Kimball chamber from two different angles. Inside the main Kimball chamber atoms are initially collected in the MOT after reduction in speed from the Zeeman slower. The atoms are then magnetically transported to the final location, which corresponds to the Feshbach coils' symmetry point. This image annotates the definitions of the different directions in the experiment and from which directions the beams arrive. The x axis is defined along the Zeeman slower. The horizontal plane MOT beams are rotated 45° in the plane from the x axis and are called x', y' axes, respectively. The vertical direction along gravity is defined as the z axis. Two different origins are used depending on which stage of trapping is being referred to. The MOT origin is centered in the science chamber along the z-axis, but is displaced from the center in the x' and y' axis such that the MOT origin is as close as possible to the exit of the Zeeman slower. The final position origin is centered on the Feshbach coils. However, it is displaced along the z axis in the main science chamber upwards by 8 mm from the center, such that the atoms are only 3 mm beneath the viewport.

3.3 Laser Systems

The trapping potentials in the experiment are created by either magnetic fields or laser light. This section describes the different lasers used in the experiment and the setups used to produced the required power and frequency stability.

Table 3.1: Summary of the different laser systems used in the experiment and their specifications.

System	Manufacturer, Model	Wavelength (nm)	Max Power (W)
^{23}Na Laser	Toptica, DL Pro	1178 → 589	0.02
	MPB, Raman Fiber Amplifier		8
^{6}Li Laser	Eagleyard Photonics, EYP-RWE-670 GaAs Laser Diode	670	0.02 (per diode)
	Eagleyard Photonics, EYP-TPA-670-00500 Amplifier		0.5 (per TA)
Plug Laser	Lighthouse Photonics, Sprout G	532	15
Dipole Laser	IPG, Ytterbium Fiber Laser LP, YLR-50-LP	1070	50
Lattice Laser	Coherent, Mephisto MOPA	1064	55

3.3.1 ^{23}Na Laser System

The ^{23}Na Laser system provides the optics for slowing, cooling and trapping ^{23}Na atoms using the D_2 ($3^2S_{1/2} \rightarrow 3^2P_{3/2}$) transition. A 1178 nm Toptica DL Pro provides 20 mW seed light for the MPB Raman Fiber Amplifier[1] (RFA) which is capable of operating at up to 8 W. The RFA is operated[2] at 2.7 W and a *bow tie* frequency doubling [122, 123] cavity is used to produce 1.1 W of 589 nm. Frequency modulation spectroscopy is used to lock the laser to the $|F = 2\rangle \rightarrow |F' = 2\rangle\,|F' = 3\rangle$ crossover feature. The light is then split into several paths and the frequencies shifted by AOMs and EOMs to provide the necessary beams as shown in Fig. 3.3. All beams are fiber coupled and brought to the experiment table[3]. The frequency shifts and powers of the beams are tabulated in Tables 3.2 and 3.3. The details of the ^{23}Na laser system and spectroscopy will be discussed in the thesis of Alexandra Behrle. The purpose and optimization of these beams are described in Chapter 4.

[1] This laser had to be sent back to MPB after 6 months as a faulty connection on the internal photodiode meant it internally measured no output power, even though the laser was operating at full power. This caused the power regulation to fail.

[2] Currently the RFA cannot be operated at higher power as the damage threshold for the 1178 nm isolator would be exceeded.

[3] Both the Zeeman slower and the optical pumping lights are combined with the respective ^{6}Li laser light before the fiber that brings them to the experiment table together.

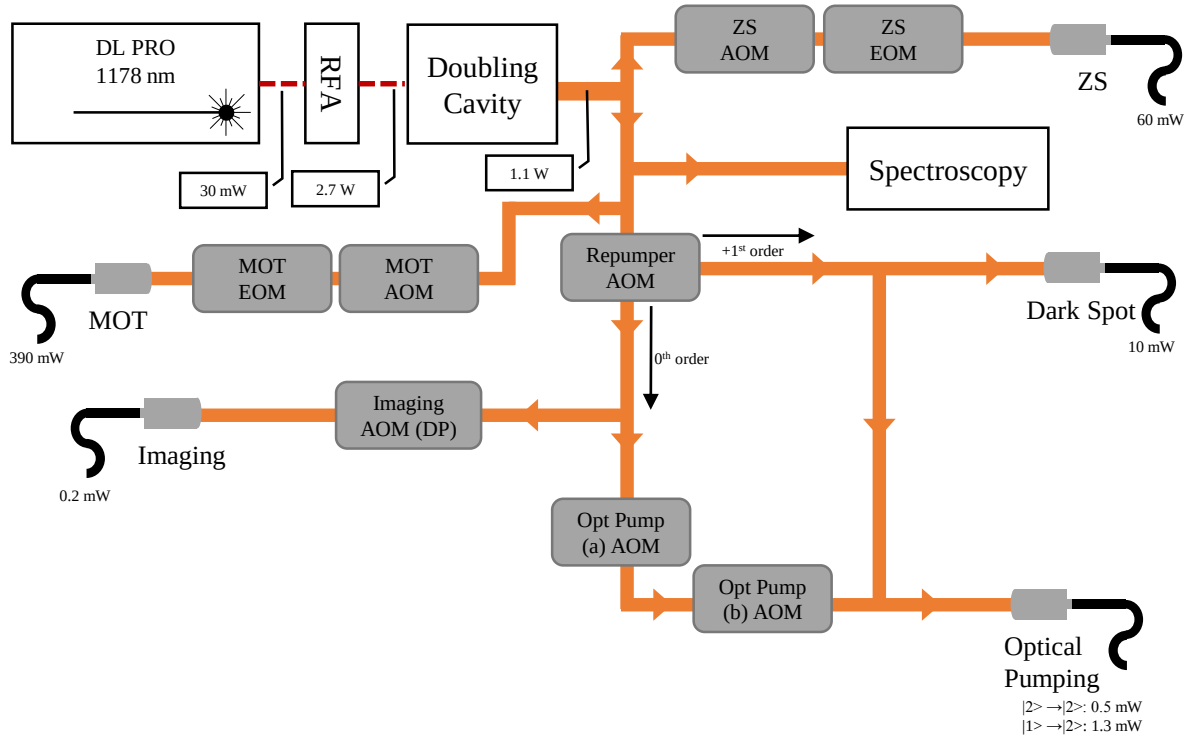

Figure 3.3: Schematic of the ^{23}Na laser system. Infrared light at 1178 nm is amplified and frequency doubled before being split into several paths for the ^{23}Na optics. The schematic shows how the beams are split and the frequencies shifted with AOMs and EOMs. The numbers under each fiber show the power after the fiber, on the experiment table. The repumper AOM has approximately 15 % diffraction efficiency in the first order and the zeroth order is also used for imaging and optical pumping light. AOMs that are in the double pass configuration are marked (DP). For the reference of future students, *Opt Pump (a) AOM* was often referred to as *Old Imaging AOM* and the *Opt Pump (b) AOM* was often referred to as *Optical Pumping 2-2 AOM* in older lab books.

Table 3.2: Tabulated values of the frequency shifts of the beams in the ^{23}Na laser system. All beams operate on the D_2 line and the frequency are given relative to a specific hyperfine transition: $3^2S_{1/2}\,|F\rangle \rightarrow 3^2P_{3/2}\,|F'\rangle$ as tabulated. The frequencies were calibrated by finding the imaging resonance of the ^{23}Na atoms, which is why the detuning of the imaging light is 0.0. A negative (positive) frequency corresponds to red (blue) detuning. All absolute frequencies were taken from [124]. The optimization of these frequencies is discussed later in Chapter 4.

Beam	Detuning (MHz)	Detuning (Γ)	Relative to ($\|F\rangle \rightarrow \|F'\rangle$)
MOT	-19	-1.9	$2 \rightarrow 3$
ZS	-502	-51.2	$2 \rightarrow 3$
Dark Spot	-21.5	-2.2	$1 \rightarrow 2$
Optical Pumping $\|F=1\rangle \rightarrow \|F'=2\rangle$	-21.5	-2.2	$1 \rightarrow 2$
Optical Pumping $\|F=2\rangle \rightarrow \|F'=2\rangle$	-12.5	-1.3	$2 \rightarrow 2$
Imaging	0	0	$2 \rightarrow 3$

Table 3.3: Tabulated values of the powers and peak intensities of the beams in the ^{23}Na laser system. All power values are after the fiber coupling to the experiment table. The collimated beam waist values allow a calculation of the intensity in units of the saturation intensity $I_{\mathrm{sat}} = 6.26\,\mathrm{mW\,cm^{-2}}$ [124]. Note that the Zeeman slower beam is focused towards the oven and the waist value at the exit of the Zeeman slower has been used. The intensity for the dark spot beam assumes there is no dark spot projection.

Beam	Beam Power (mW)	Beam waist radius (mm)	Intensity (peak) ($\mathrm{mW\,cm^{-2}}$)	I/I_{sat}
MOT (per beam)	45	20	7.2	1.1
ZS	60	16	14.9	2.4
Dark Spot	13	20	2.1	0.33
Optical Pumping $\lvert F=1\rangle \rightarrow \lvert F'=2\rangle$	1	11	0.5	0.08
Optical Pumping $\lvert F=2\rangle \rightarrow \lvert F'=2\rangle$	0.15	11	0.1	0.013
Imaging	0.23	4	0.9	0.15

3.3.2 ^{6}Li Laser System

The ^{6}Li laser system provides the light for slowing, cooling and trapping the ^{6}Li atoms. It is based on three multiple *Eagleyard Photonics, EYP-RWE-670 GaAs* laser diodes which are amplified with *Eagleyard Photonics, EYP-TPA-670-00500* 500 mW tapered amplifiers. The first laser is used for spectroscopy to provide a locking signal. The spectroscopy cell for ^{6}Li is very long to prevent contact of ^{6}Li with the windows and is evacuated under an argon environment. Details of the construction of the spectroscopy cell can be found in the Bachelor thesis of Christoph Linse [125]. The first laser, after two amplification stages and a 228 MHz EOM for repumping, provides approximately 300 mW of MOT light before the fiber. After the tapered amplifiers the beam shape is distorted and elliptical, which makes fiber coupling challenging. When optimized we have 45 to 55% coupling efficiency through fibers.

Light from the first laser is also coupled into a fiber EOM[1] which is beat with light from the second laser to provide a locking signal for the offset lock. The fiber EOM is driven with a Windfreak SynthNV (34 to 4400MHz) which can perform ramps in both frequency and amplitude allowing the frequency of the second laser to be changed during the sequence. This is implemented so that at the beginning of the sequence the Zeeman slower and optical pumping light can be derived from the second laser, however, later in the sequence the hyperfine states of ^{6}Li can be imaged at an arbitrary magnetic field. Since the experiment utilizes the Feshbach resonance at 835 G, high field imaging of

[1] Eospace, Lithium Niobate modulator PM-0S5-10-PFA-PFA-670.

any state in the hyperfine ground state manifold may be required at fields of up to 1200 G. By ramping the Windfreak frequency, the second laser can stay in lock and the frequency of the imaging can be shifted by over 2.2 GHz. The Windfreak is typically ramped over 0.5 s independent of the size of the ramp. The high field imaging and ramping of the offset lock is implemented in the experiment control software (see Appendix B.5.2). In this implementation the user selects the hyperfine state to image and polarization with which to image. The magnetic field at the time of imaging is then determined automatically from the sequence and the laser is ramped to the required frequency with some optional additional detuning. It was found experimentally that when ramping over 1 GHz the amplitude of the locking signal was reduced. It was found that increasing the RF amplitude at specific frequencies helped maintain a constant amplitude of the locking signal for sweeps of up to 2.5 GHz.

A third laser (laser 3) was later added to the laser system to implement gray molasses of ^{6}Li in the experiment. Since there was no way of combining or adding the gray molasses light on the experiment table, the light had to be produced and sent into the normal MOT fiber. To achieve this, laser 3 was beat with the first laser and had its frequency defined by an offset lock with approximately a 10 GHz shift. An additional AOM was used (GM Switch AOM in Fig. 3.4) and both the laser 1 and laser 3 were aligned through it. This AOM and the first tapered amplifier were aligned such that the zeroth (first) order of the first (third) laser was coupled into the first tapered amplifier. Although this alignment was difficult, it was achieved with only a 10 % reduction in efficiency of the first tapered amplifier. With this alignment, the light in the MOT fiber could be switched from laser 1 to laser 3 frequency very rapidly. An additional complication was that this switch caused the second laser, which was offset locked to the first laser, to fall out of lock. Hence, a sample and hold box was built that meant a TTL signal could be used to maintain all piezo voltages and current modulation signals for several milliseconds while the gray molasses was performed, before switching back to laser 1. The implementation of gray molasses is discussed in Section 4.3.1 and is not currently used in the experiment sequence. Laser 3 has also been used for high field imaging of the highest energy hyperfine state ($|6\rangle$) of the $2^2S_{1/2}$ manifold. At high fields this state is shifted by over 2.5 GHz from the lowest hyperfine state transition and this large ramp often caused the second laser to fall out of lock. The ^{23}Na laser imaging light is combined with the ^{6}Li laser imaging light and sent to an eight port fiber switch[1] which allows the imaging light to be sent along several different imaging axes. The 10 ms to 20 ms switching time means this is rarely done in a single experiment cycle, however, different cycles can easily have the

[1]Leoni model eol 1x8 FC/APC PM630.

Table 3.4: Tabulated values of the ^{6}Li laser system frequencies. Note that the small energy shifts between the hyperfine states in the excited state means that the exact value of F' is not important. The frequencies are calibrated by finding the imaging resonance of a specific hyperfine transition which is why the imaging detuning is fixed at zero. All absolute frequencies are taken from [126].

Beam	Detuning (MHz)	Detuning (Γ)	Relative to ($\|F\rangle \rightarrow \|F'\rangle$)
MOT	-25.9	-4.4	$3/2 \rightarrow 5/2$
cMOT	-16.7	-2.8	$3/2 \rightarrow 5/2$
Zeeman Slower	-512.5	-87.3	$3/2 \rightarrow 5/2$
Optical Pumping $\|3/2\rangle \rightarrow \|3/2\rangle$	-53	-9.0	$3/2 \rightarrow 5/2$
Optical Pumping $\|1/2\rangle \rightarrow \|3/2\rangle$	-53	-9.0	$1/2 \rightarrow 3/2$
Imaging	0	0.0	$3/2 \rightarrow 5/2$

imaging axis changed. The ^{23}Na and ^{6}Li Zeeman slower light are also combined into a single fiber, as are the ^{23}Na and ^{6}Li optical pumping beams. For the ^{6}Li MOT beams a 6 port polarization maintaining fiber splitter is used[1], and even with the 10 m input end we have found the polarization and power output to be adequately stable (power fluctuation of beams less than 5 %).

The frequency of the spectroscopy AOM and the current of the second tapered amplifier can be changed by separate analog control signals. This allows for fast and controlled changes in the detuning of the MOT beams' frequency and power to produce a compressed MOT (discussed in detail in Section 4.2.1). A basic schematic of ^{6}Li laser system is shown in Fig. 3.4 and the frequencies and powers of the beams are tabulated in Tables 3.4 and 3.5.

As expected, over time the power after the tapered amplifiers has degraded[2]. So far only the first tapered amplifier has ever been replaced, however, it is expected that the second and third tapered amplifiers will be replaced soon. Over two years of operation the power in the MOT beams has reduced from 20 mW per beam to 13.5 mW per beam.

3.3.3 Dipole Laser

To form the dipole trap, high intensity laser beams, red-detuned from the atomic transitions, are required to provide sufficient trap depth (see Section 5.5). For this purpose

[1] Evanescent Optics 1 by 6 PM Coupler Array.

[2] Over one and a half years the power after the first tapered amplifier and isolator reduced from 150 mW to 85 mW.

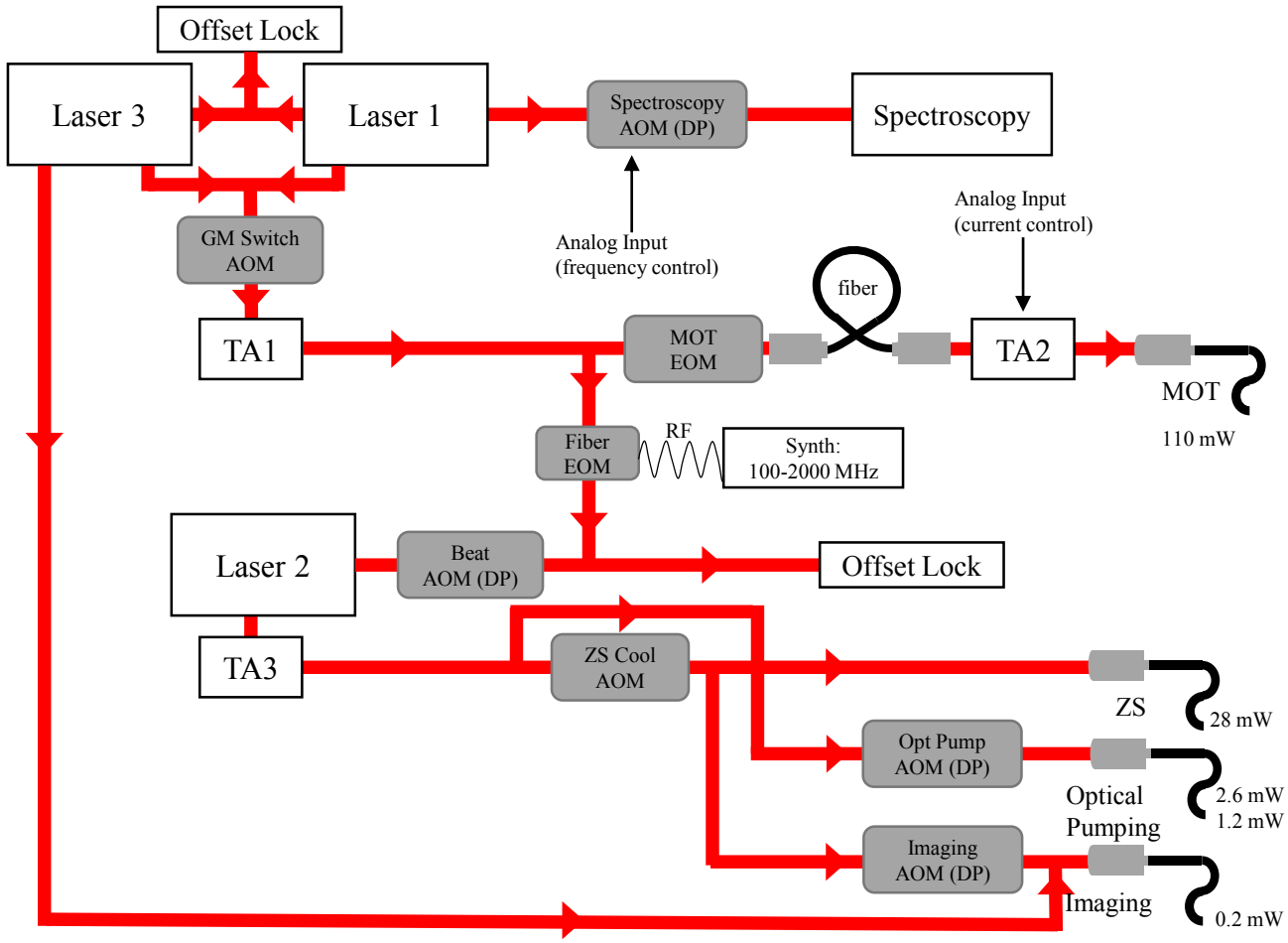

Figure 3.4: Schematic of the Li Laser System. Laser 1 provides the light for spectroscopy and after two stages of amplification for the MOT beams. Additional light is sent to the fiber EOM and is beat with laser 2 to provide a locking signal for the offset lock. Laser 2 provides the Zeeman slower and optical pumping light at the beginning of every sequence. By changing the frequency of the fiber EOM the frequency of laser 2 can be changed such that it can also be used for imaging many different hyperfine states of ^{6}Li at different magnetic fields. Laser 3 was initially used to implement gray molasses by providing D_1 laser light in the MOT fiber. Additionally it has been used for imaging of hyperfine states at high fields.

Table 3.5: Tabulated values of the ^{6}Li laser system powers. Given the approximate waist radii of the beam, the peak intensities are also calculated. $I_{\text{sat}} = 2.54\,\text{mW}\,\text{cm}^{-2}$ [126].

Beam	Beam Power (mW)	Beam waist radius (mm)	Intensity (peak) ($\text{mW}\,\text{cm}^{-2}$)	I/I_{sat}
MOT (per beam)	18	11	9.5	3.7
cMOT (per beam)	0.24	11	0.1	0.05
Zeeman Slower	28	16	7.0	2.7
Optical Pumping $\|3/2\rangle \rightarrow \|3/2\rangle$	2.6	11	1.4	0.54
Optical Pumping $\|1/2\rangle \rightarrow \|3/2\rangle$	1.2	11	0.6	0.25
Imaging	0.2	4	0.8	0.31

a 50 W IPG Ytterbium Fiber laser[1] with wavelength 1070 nm (red-detuned from both the ^{23}Na and ^{6}Li atomic transitions) is used. Despite the high power, this laser system was still built with fiber coupling between the laser box and the experiment table. The first version of the setup was then built as part of the Master thesis of Justas Andrijauskas [127]. The setup was changed to allow the laser to run at full power (50 W) and for the power after each fiber to be greater than 15 W.

When working with high power lasers it is crucial to operate the laser with maximum power up to the element being aligned. This is because the beam properties and shape can change dramatically depending on the total power output of the laser and because optical elements can behave differently when higher powers are used (e.g. thermal lensing). For example, in the dipole laser setup, the first stage of alignment was to shape the beam and pass the optical isolator. To shape the beam the laser was run at full power and the majority of the power dumped by a cube and waveplate into a water cooled copper block. The transmitted, low power beam can then be used for shaping. Similarly a waveplate, cube and beam-dump combination was installed permanently after the optical isolator such that all other optics could be aligned at low power before increasing the power in stages for the final alignment.

From our experience we have found that optical isolators and waveplates are relatively sensitive to high power, whereas (appropriate high power) cubes, mirrors and lenses are not as sensitive. AOMs do show some thermal lensing at high powers, however, we measured the affect of heating due to RF power on the AOM alignment to be much more significant.

The dipole laser light is split into three paths after the optical isolator (90% efficiency): two high power paths used for the horizontal and vertical dipole beam and one low power path used for debugging. AOMs are placed in each of the paths to allow for power regulation of the beams by varying the RF power to the AOM (maximum 87% efficiency). Before the fibers each high power path has approximately 20 W. Coupling such a high power into a fiber is non-trivial. NKT LMA-PM-15 polarization maintaining photonic crystal fibers (PCF) which have a large mode area allowing for high power densities were used. It was found that, when optimized and properly cooled, these fibers give better coupling efficiency and stability than standard single mode fibers at powers greater than 15 W, however, this improvement is much more significant at lower wavelengths (532 nm) (see Section 3.3.4).

[1] The laser was sent back to the manufacture after approximately 6 months because it was unable to turn on the device. It turned out this was due to a faulty SD card inside the controller.

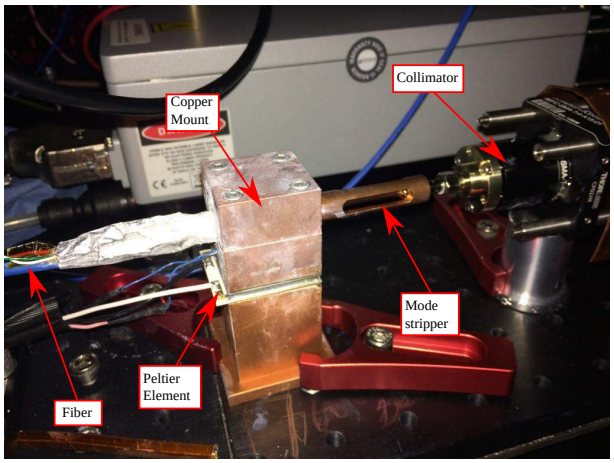

Figure 3.5: Image showing the copper mount structure that actively cools the PCF fibers allowing for high power fiber coupling (20 W before fiber, 15 W after fiber) without damaging the fiber.

After two fibers were destroyed during alignment/operation we spoke with NKT regarding the optimal procedure for fiber coupling[1]. Whilst the fiber core can tolerate very high powers and temperatures, the connection where the mode stripper joins the fiber is glued and coated. If the temperature of the glue or the coating gets too high, they burn and the discoloring and defects destroy the fiber in a runaway process [128]. This connection must be kept below 60 °C in order to prevent damage. A copper cooling structure was designed, which could have its temperature regulated by a Peltier element with the heat dumped into the optical table as shown in Fig. 3.5. By actively cooling the end mount of the fiber, much higher power and coupling efficiency was achieved with no damage to the fiber. Several thermal sensors are mounted on the fiber and an interlock system turns off the IPG laser if the temperature of the PCF fiber goes above 40 °C. With 20 W before the fiber, a temperature of 45 °C was reached during constant operation and 28 °C during the normal experiment sequence. In addition we have found these fibers are very sensitive to small bending radii, which can dramatically affect the polarization performance (a bending radius of at least 50 cm is now used). We have also obtained a small improvement in fiber coupling by using Schaefter-Kirchoff 60FC-SMA fiber couplers, which are specifically made for NKT PCF fibers. When fully optimized we have 15 W directly after the fiber (coupling efficiency 75 %).

During the experiment sequence the power of the dipole beams is changed by applying a

[1]While waiting for a replacement fiber a standard 1064 nm fiber purchased from Thorlabs was used and we were able to achieve approximately 70 % efficiency with 18 W before the fiber. However, we haven't been able to produce such good results with other similar fibers. This fiber has remained in place and runs at approximately 65 °C in continuous mode. It can now be replaced by a PCF fiber whenever required.

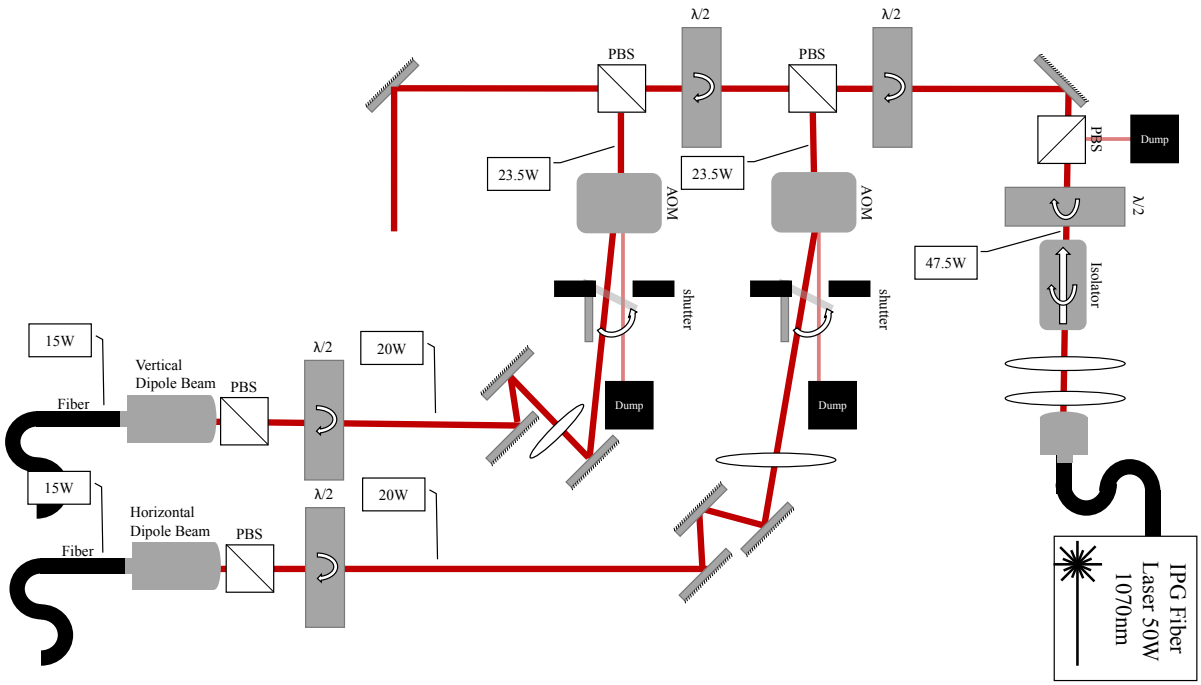

Figure 3.6: Schematic of the dipole laser box. The laser is run at full power through the isolator after which a waveplate, cube and beam dump combination allows the alignment of all optics to be performed with a low power beam while the laser operates at full power. The light is split into 3 paths: the vertical dipole beam, horizontal dipole beam and a path for debugging. Each path contains an AOM for power regulation. The shutter and beam dumps are water cooled so that the full power can be dumped continuously. In this setup: mirrors are Red Optronics MFH-2002 1064 nm; waveplates are Casix zeroth order 1064 nm; polarizing beam splitters (PBS) are Altechna high power 1064 nm; lenses are Thorlabs LA-YAG; isolator is Thorlabs IO-5-1064-VHP; AOMS are Gooch and Housego 23080-2-1.06-LTD, 1064 nm 80 MHz 2 W RF power. Fibers are NKT PCF LMA-PM-15; fiber couplers are Schäfter Kirchoff FC-SMA-T-4-A11-03.

variable RF power to the AOMs to control the diffraction efficiency. This means that there can be the full beam power in either the first order or the zeroth order. Additionally the first order must be blocked (at full power) by a shutter to ensure the AOM is running at full RF power and thermal equilibrium is reached before the dipole beam is first turned on. A commercial shutter (model GCI-7101M) was modified by replacing the thin stainless steel flags with slightly thicker aluminum flags[1]. A water cooled block of copper was placed between the shutters for the first and second beam paths and additional copper rods connected it thermally to the aluminum bodies of the shutters. The zeroth order is dumped into the body of the shutter. An 8 cm copper tube is placed in front of the shutter which diffuses light scattered from the shutter when it is closed.

[1]The 20 W beam burnt the original flags.

3.3.4 Plug Laser

To provide an optical barrier around the zero field region of the magnetic trap (see Section 5.4), a high intensity laser beam, blue-detuned from the atomic transitions, is required. For this a 15 W 532 nm Sprout-G-15 NET laser produced by Lighthouse Photonics is used[1]. Since it was unknown whether the high fiber coupling efficiency could be achieved for 532 nm at such high power, the plug laser system is the only laser system built directly on the experiment table. This meant that, if it was not possible to use fibers, the plug light could easily be sent directly into the main vacuum chamber. In addition, building the laser on the experiment table meant much shorter fibers could be used.

After beam shaping the full power laser light is coupled into an AOM for power regulation. After switching to a Gooche and Housego Model 3080-292 high power 532 nm AOM, a diffraction efficiency of 87 % (13 W) was achieved. Waveplate, cube and beam dump combinations are used directly after the laser head and directly after the AOM such that the laser is always operated at full power while initial alignment can be done at lower power. After the AOM, the beam is reshaped and coupled into a NKT Photonics crystal fiber (PCF), which is cooled by a Peltier element attached to a custom copper mounting body (see Fig. 3.5). Working with high power laser systems and high power fiber coupling was discussed in Section 3.3.3. It was noticeably harder to achieve high coupling efficiency and reasonable fiber temperatures while working at 532 nm compared to 1064 nm[2]. When fully optimized a coupling efficiency of 70 % through a 2 m NKT LMA-PM-15 PCF fiber was achieved (9 W after the fiber). However, it was observed that the polarization after the fiber was sensitive to the alignment and coupling efficiency. The reasons for this are still not understood but may be due to the thermal effects at the in coupling side. We have observed that the bending radius of the fiber must be kept very large (50 cm) to prevent losses, polarization issues and damage. The fiber is now mounted on a malleable copper tube to keep its shape fixed. Similarly to the dipole laser (Section 3.3.3) an interlock turns off the plug laser if the fiber goes above 40 °C. During the experiment cycle the fiber is at approximately 26° and an increase in the temperature is an early warning for misalignment.

[1] After approximately two years of operation the laser began to fail to reach maximum power. The operating power was reduced with the maximum achievable power decreasing over time. After approximately three years of operation the maximum power achievable was 9 W and the laser was sent back to Lighthouse Photonics for repair. The Nd:YVO4 gain crystal was damaged and was degrading over time. A replacement 10 W laser was loaned to us while the repair took place.

[2] This difference is even more noticeable given that we operate with 13 W before the fiber for the plug laser compared to 20 W before the fiber for the dipole laser.

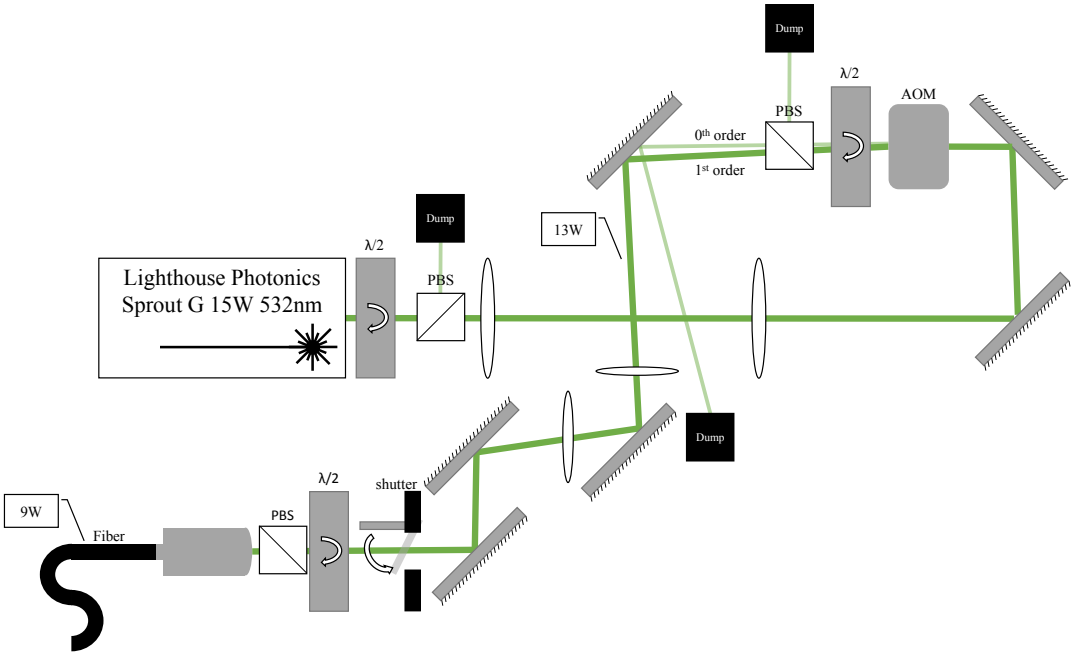

Figure 3.7: Schematic of the plug laser setup. The telescope changes the waist radius from 1.2 mm after the laser head to 0.5 mm for the AOM and fiber coupling. The zeroth order of the AOM is dumped and the first order is fiber coupled to allow power regulation of the beam. In this setup: mirrors are Altechna HR UVFS 532 nm; waveplates are Casix zeroth order 532 nm $\lambda/2$; polarizing beam splitters (PBS) are Altechna high power 532 nm; lenses are fused silica LA Thorlabs; AOM is a Gooch and Housego Model 3080-292 532 nm, 80 MHz, 5 W RF power; fiber is 2 m NKT PCF LMA-PM-15; fiber coupler is Schäfter Kirchoff 60FC-SMA-T-4-A15-01.

3.3.5 Lattice Laser

A Coherent Mephisto MOPA 55 W 1064 nm laser setup is being built for an optical lattice that may be implemented in the experiment in the future. The setup is very similar to that of the dipole laser. The beam will be split into three high power paths each with an AOM and shutter which reflects the high power beams into a water cooled dump. The Gaussian beam quality from the laser has been measured and the high power isolator installed. The beam has been split into three paths and is being aligned through the AOMs and PCF fibers. The completion of the lattice laser box will be described in the Master thesis of Andreas Kell.

3.4 Magnetic Field Coils

3.4.1 Introduction

A common technique for producing both uniform magnetic fields (B-fields) and gradient B-fields is to utilise a pair of coaxial coils in either a Helmholtz (uniform field) or anti-Helmholtz (gradient field) configuration. Whilst for the design of the most important coils the B-field is simulated numerically, much can be understood about the design procedure by looking at the equations of the ideal coil pair. Solutions of the field about the center of a coil pair can be calculated using elliptic integrals [129], however, for basic insight it will be sufficient to use the on axis equations, greatly simplifying the solution.

Consider a basic coaxial coil pair of N windings, carrying a current I, of radius R and separated by a distance, d. To find the field around the center of the coil pair, the result for the on axis B-field of a single coil of wire a distance z from the coil is used:

$$B_z(z) = \mu_0 I N \frac{R^2}{2(R^2+z^2)^{\frac{3}{2}}} \tag{3.1}$$

By combining Eq. (3.1) twice with an appropriately shifted origin, and accounting for the direction of the field in Helmholtz or anti-Helmholtz configuration we find:

$$B_{\substack{\text{Helmholtz}\\ \text{anti-Helmholtz}}}(z) = B_z\left(z-\frac{d}{2}\right) \pm B_z\left(z+\frac{d}{2}\right) \tag{3.2}$$

which simplifies to:

$$B_{\substack{\text{Helmholtz}\\ \text{anti-Helmholtz}}}(z) = \frac{\mu_0 I N}{2R}\left(\frac{1}{\left(1+\left(\frac{z}{R}-\frac{d}{2R}\right)^2\right)^{3/2}} \pm \frac{1}{\left(1+\left(\frac{z}{R}+\frac{d}{2R}\right)^2\right)^{3/2}}\right) \tag{3.3}$$

To show more clearly the difference between the Helmholtz and anti-Helmholtz configuration the Taylor expansion about z=0 to 2nd order in $\frac{z}{R}$ can be taken. This result will be valid for $\frac{z}{R} \ll 1$, which for the atoms in the experiment will always be satisfied.

$$B_{\text{Helmholtz}}(z) = \frac{\mu_0 I N}{2R}\left(\frac{2}{\left(1+\left(\frac{d}{2R}\right)^2\right)^{3/2}} + \frac{3\left(\left(\frac{d}{R}\right)^2-1\right)}{\left(1+\left(\frac{d}{2R}\right)^2\right)^{7/2}}\left(\frac{z}{R}\right)^2 + \mathcal{O}\left(\frac{z}{R}\right)^4\right) \tag{3.4}$$

$$B_{\text{anti-Helmholtz}}(z) = \frac{\mu_0 I N}{2R}\left(\frac{3\frac{d}{R}}{\left(1+\left(\frac{d}{2R}\right)^2\right)^{5/2}}\left(\frac{z}{R}\right)+\mathcal{O}\left(\frac{z}{R}\right)^3\right) \tag{3.5}$$

From the above equations it can be seen that the Helmholtz configuration produces a uniform field along the axis of the coil pair with a quadratic curvature that disappears when $d = R$. For the anti-Helmholtz configuration, a gradient field is produced along the axis of the coil and it can be shown that a gradient of half the magnitude and opposite sign is produced in the two orthogonal directions [129]. In general, the fields produced by the two configurations can be written as:

$$\mathbf{B}_{\text{Helmholtz}}(\mathbf{r}) = \begin{pmatrix}0\\0\\B_0\end{pmatrix} + B''\begin{pmatrix}0\\0\\-x^2-y^2+2z^2\end{pmatrix} + \mathcal{O}\left(\frac{\mathbf{r}}{R}\right)^4 \tag{3.6}$$

$$\mathbf{B}_{\text{anti-Helmholtz}}(\mathbf{r}) = B'\begin{pmatrix}-x\\-y\\2z\end{pmatrix} + \mathcal{O}\left(\frac{\mathbf{r}}{R}\right)^3 \tag{3.7}$$

where B_0, B'' and B' are coefficients which can be calculated from the Taylor expansions above. Note that in this thesis a reference to B-field gradient (curvature) always refers to B' (B'') which is half the value of the gradient (curvature) along the axis of the coils.

In the experiment the anti-Helmholtz configuration is used for the gradient fields required for the MOT, the magnetic transport and the magnetic quadrupole trap. The Helmholtz configuration is most crucially used for the Feshbach fields for ^{6}Li where a very uniform field over the atoms with minimal curvature field is required. Helmholtz coils are also used to provide a quantization axis for imaging and optically pumping the atoms and for compensating offset fields. The design and characterization of the Feshbach coils is discussed in Sections 3.4.2 to 3.4.4. The fast switching of the magnetic coils is described in Section 3.4.5, with specific attention on the Feshbach coils. Many of the coils in the experiment require large currents (up to 600 A) and require water cooling to operate at reasonable temperatures as explained in Section 3.4.6. A summary of all the different magnetic coils is given in Section 3.4.7.

3.4.2 Design of the Feshbach Coils

The Feshbach coils had to simultaneously satisfy many design criteria, whilst being restricted geometrically by the vacuum chamber. It was required that:

- The center position of the coils was at the final position of the atoms. This was necessary to ensure that the Feshbach fields would be uniform across that atomic cloud and also so that no additional optical transport from the magnetic trap to the final position was required. The final position of the atoms would be approximately 3 mm below the UKEA viewport, to permit high resolution imaging in the future.
- The coils needed to produce a uniform field of up to 1000 G and gradients of 120 G cm^{-1}. To create such a large field, whilst also approximately satisfying the Helmholtz condition ($R = d$), requires either large currents or a large number of windings.
- The magnetic fields need to be turned on and off very quickly (< 300 µs) to perform the rapid ramp technique (see Section 6.4) or imaging with short time-of-flight. This requires the coils to have a low inductance and hence a large current with a small number of windings was preferred.

The dimensions of the coils are shown in Fig. 3.8. Our coils consist of 6 layer pairs with the center point of the coils 3 mm below the UKEA viewport. The distance between the layers varies from 66.7 mm to 114 mm and the inner and outer radius are 51 mm and 72.5 mm, respectively. Using the central layer of the first three layers and the midpoint of the winding radius, we get $d = 75.3$ mm and $R = 64$ mm. The design of the coil was chosen to produce the most uniform Helmholtz field possible while satisfying the constraints described above.

In order to run high currents and still fit several windings, a hollow conductor wire[1] (square 4 mm by 4 mm with hollow circle of radius 1.25 mm) was chosen. This square wire allows for the most efficient packing of the coils and the circular hollow cross-section gives the most effective heat dissipation with water cooling. The resistance of the wire is 1.4 mΩ m^{-1}. In order to reduce the resistance of the coil and the required water pressure, a larger cross-section hollow conductor wire (square on square 7.7 mm outer and 4.4 mm inner), which slots over the coil wire, is used after the coils leave the winding body. The larger wires travel approximately 1 m each from the edge of the main Kimball chamber to connectors on the edge of the optical tables. The connectors are designed such that

[1] Purchased from Luvata. Due to the very large order quantity required our orders were part of end-runs from other customers orders.

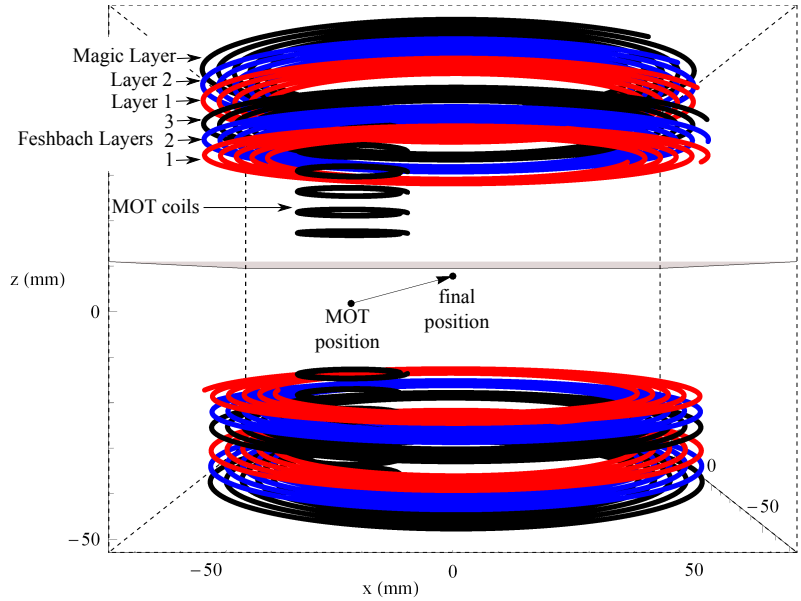

Figure 3.8: Three dimensional drawing of the ideal Feshbach coils. The top layers of the coil are labeled with the names referred to throughout this thesis. The MOT coils are also shown in black. Each labeled layer on top has a corresponding layer on the bottom which completes the pair. In the experiment Feshbach layers 1, 2 and 3 are run in series as are layers 1 and 2. The plane in the image represents the height of the top UKEA viewport. The position of the MOT and final position of the atoms are marked. The black line between them represents the path traveled during magnetic transport. The distance between Feshbach layer 1 is 66.7 mm. The inner (outer) radius of the coil winding is 51 mm (72.5 mm).

different layers can easily be connected together in series. In total 24 wires leave the vacuum chamber for these 6 coil pairs, and occupy the area underneath one of the first level breadboards (see Fig. 3.9).

Following discussions with the workshop, all layers of the coils were wound in parallel[1]. This meant the water could run in parallel, as well. The water distribution manifolds allow the flow rate for each layer to be controlled or blocked individually. In order to make the coils stable (both to slow thermal drifts and the inductive force from fast switching) the entire coils were mounted inside a Tekadur structure, which could be directly attached to the main Kimball chamber. The coils were wound directly onto the Tekadur body and were encased in non-magnetic epoxy. The top mount displaced the coils by 16.5 mm from the inverted viewport; for the bottom coil it is displaced by 0.5 mm to prevent heat dissipation. This asymmetry meant the center point is displaced to 3 mm below the UKEA viewport used for high resolution imaging. An image of the final coils is shown in Fig. 3.9. Note that the top and bottom coils are wound in opposite directions, which helps cancel the asymmetry from the spiral shape of the individual layers. The inductance

[1] An earlier attempt to make 3 layers from one individual length of wire was unsatisfactory as the centers of the different layers were displaced.

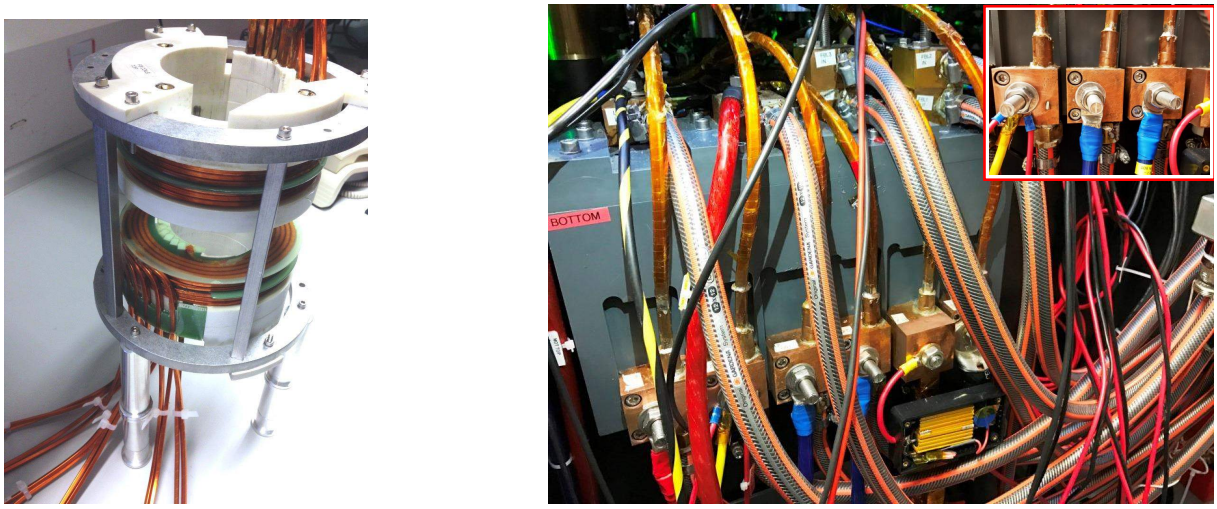

(a) Feshbach coils in testing rig.

(b) Connectors and water connections.

Figure 3.9: Image of the Feshbach coils mounted in the testing rig used for B-field measurements and image of the copper wire connectors and water cooling.

of the Feshbach coils is approximately 4 µH per layer.

The approximate distance of $d = 75.3\,\text{mm}$ and $R = 64\,\text{mm}$ is close to the Helmholtz condition but given the geometry of the coils and the fact that their dimension are on a similar order to both R and d, it is no longer valid to rely on the analytic equations derived in the previous section. To calculate the fields produced by the coils, a numerical simulation was made and will be described in Section 3.4.3. Recently, several groups have used a Bitter-type electromagnets, composed of several stacked sheets of copper, to produce uniform fields with efficient water cooling [130].

3.4.3 Simulations of the Magnetic Coils

To simulate the B-fields produced by the Feshbach and other coils, a numerical simulation was used that implements the Biot-Savart law for a conducting line element. By approximating the coils as a collection of short line elements, the B-field at an arbitrary position can be calculated. The numerical simulation accounts for the spiraling (not circular) nature of the coil with the spiraling rate determined by the thickness of the wire. The fact that each layer's winding begins at a slightly different angle in the plane of the coils and that the distance between the coils also depends on the wire thickness were also accounted for. Each layer was approximated by 1000 line elements[1]. By simulating the coils

[1]Increasing this to 10 000 line elements affected the result on the order $\mathcal{O}(1 \times 10^{-5})$.

Coil Pair	$\lvert B\rvert$ G A^{-1}	Curvature B'' (x,y,z)G cm^{-2} A^{-1}			Gradient B' (x,y,z)G cm^{-1} A^{-1}		
FBL1	0.691	-0.001955	-0.001940	0.001948	0.0717	0.0716	0.0715
FBL2	0.630	-0.003740	-0.003745	0.003750	0.0694	0.0689	0.069
FBL3	0.572	-0.004915	-0.004890	0.004900	0.0657	0.065	0.065
Layer 1	0.492	-0.005750	-0.005700	0.005700	0.059	0.0581	0.058
Layer 2	0.444	-0.005850	-0.005750	0.005800	0.0537	0.0532	0.0535
Magic Layer	0.400	-0.005700	-0.005650	0.005650	0.0487	0.0483	0.0485
2 Layer FB FBL1+FBL2	1.321	-0.005650	-0.005650	0.005675	0.141	0.14	0.141
3 Layer FB FBL1+FBL2+FBL3	1.893	-0.010600	-0.010550	0.010575	0.207	0.205	0.2065
2 Layer FB +Magic Layer	0.921	0.000026	-0.000058	0.000016	0.0923	0.0922	0.0923

Table 3.6: Tabulated values of the properties of the Feshbach coils. The field gradient, B', uses the anti-Helmholtz configuration as defined as in Eq. (3.7). The offset field, B_0, and curvature, B'', use the Helmholtz configuration as defined in Eq. (3.7). Each layer is defined as shown in Fig. 3.8. Additionally the properties of different combinations of layers are shown. Currently the 3 Layer FB combination is used for the Feshbach coils.

in Helmholtz (anti-Helmholtz) configuration and extracting the constant and quadratic (linear) coefficients, the offset and curvature (gradient) could be extracted. The simulated values for each layer are tabulated in Table 3.6. The final version of the top and bottom coils were wound with opposite symmetries as the initial simulations showed that winding with the same symmetry led to significant gradients in the Helmholtz configuration. Several other adjustments to the dimensions of the coil were made based on iterations of this simulation.

Table 3.6 shows that as we move outwards from the innermost pair, we deviate more from the Helmholtz condition, increasing the curvature. The geometry of the vacuum chamber prevented either bringing the coils any closer together (while maintaining the offset towards the UKEA viewport) or increasing the radius of the coils. If the innermost 3 layers are used for the Feshbach coils, we have a $B''/B_0 = 5.6 \times 10^{-3}\,\mathrm{cm}^{-2}$ and can reach $B_0 = 1140\,\mathrm{G}$ using the Delta 600 A 30 V power supply. If in future experiments the curvature is critical, the 2 layer Feshbach coils combination (with or without compensation from the magic layer) could be used to reduce the curvate (see Table 3.6). This could potentially reduce the curvature to $B''/B_0 = 1.7 \times 10^{-5}\,\mathrm{cm}^{-2}$, however, only a field of 550 G could be achieved without higher currents (and power dissipation). When quantifying the curvature of a Helmholtz field for a quantum gas experiment, it is useful to convert the curvature into a trapping frequency for the hyperfine state of interest

($g_J m_J \mu_B B'' x^2 = m\omega^2 x^2/2$). For the lowest hyperfine state of ^{6}Li this gives a trap frequency in the x', y' plane of $\omega = 2\pi \times 6.85\sqrt{B''\mathrm{G\,cm^{-2}}}$. Many groups [131, 132] use this confinement (typically $2\pi \times 15\,\mathrm{Hz}$) while evaporating ^{6}Li on the Feshbach resonance and this weak harmonic confinement from the Feshbach coils has also been used to perform matter wave Fourier optics [62, 133]. In anti-Helmholtz configuration the 3 layer Feshbach coils can produce $B' = 0.20\,\mathrm{G\,cm^{-1}\,A^{-1}}$ or $120\,\mathrm{G\,cm^{-1}}$ at full current. This is sufficiently high for magnetic trapping of ^{23}Na and ^{6}Li. Similar numerical simulations were also performed for the Zeeman slower, MOT coils and x', y' compensation coils. While the precise values of these coils were not so critical, it ensured that they were of the required magnitude.

3.4.4 Measurement of Magnetic Fields

For the many coils in the experiment it is necessary to accurately measure the magnetic fields before they are built in. This not only acts as a check for the assumptions of the simulations, but can also highlight manufacturing defects in the coils that may distort the fields. Eventually, the B-field of the Feshbach coils was measured with the atoms themselves as will be described in Section 6.3.

For the magnetic field measurements a miniature hall probe[1] was used, which is specified to an accuracy of 0.01 % on the scale of B fields measured. Initial checks were done to measure the field/probe stability without the coils by measuring the magnetic field overnight. This was found to be relatively stable with approximately 0.015 G fluctuations over 12 h. However, the measured B-field was found to drift dramatically on timescales $\sim 30\,\mathrm{min}$ when the coils were turned on. It was found this was due to the increase in temperature affecting the Hall probe (3 °C caused a noticeable drift). Even with the manufacturer's calibration, drift in the measured B-field with temperature was seen and performing the measurements at a constant temperature was critical. The measurement and recording of the B-field was automated, however, the movement of the probe was still manual.

Zeeman Slower

The Zeeman slower is split into two parts: the decreasing field component (big Zeeman slower) with length 0.9 m and increasing field component (small Zeeman slower) with

[1] Group3 DTM 151 with MPT.

length 80 mm separated by 0.2 m. A variable pitch helix is used for both components to create a field that precisely follows the ideal requirement [134]. The details of the design and parameter choice of the variable-pitch Zeeman slower will be given in the thesis of Alexandra Behrle and the principle of the Zeeman slower and its alignment are discussed in Section 4.1. The detuning of the ^{23}Na beam defines the required maximum field and hence the current required for operation of the coils. The big and small Zeeman slower are operated at 400 A and 34.3 A respectively after optimization. The high currents in the big Zeeman slower leads to high temperatures. Even with a 17 bar water pump dedicated to the big Zeeman slower, the experiment currently requires a 6 s wait time at the end of every cycle in order to operate the big Zeeman slower at reasonable temperatures[1].

In order to ensure the correct functioning of the Zeeman slower, it is necessary to measure the fields it produces. For the big (positive field) Zeeman slower the difficulty is measuring the field accurately in the center of the Zeeman slower over an 80 cm path. A circular mount was made that fit exactly inside the Zeeman slower, holding the probe in the center and in the correct orientation. This mount was attached to a 1 m M8 threaded rod which could be rotated to move the probe along in small increments. Due to the high heat dissipation around the big Zeeman slower when it is run at full current (400 A), the field measurements were made at 25 A where the temperature was stable. A similar mount and structure was made for the small (negative field) Zeeman slower. The measured B-field is shown in Fig. 3.10 and agrees very well with the simulated B-field.

Feshbach coils

Since the Feshbach coils were still under construction during the bake-out, it was not possible to test them mounted to the vacuum chamber. A simple aluminum ring structure was designed to hold the coils at the appropriate distance (see Fig. 3.9a) and allow access for the Hall probe mounted on a 3-axis 25 mm translation stage. Since there was no water cooling installed at this point, the coils were only run at 80 A and a fan[2] ensured the temperature was constant after a sufficient warm up time.

[1] Given that we are able to produce degenerate Fermi gases of over 5×10^6 atoms in 11 s, the 6 s wait time is significant. Two future improvements are possible. Firstly, one could operate the ^{6}Li oven hotter so that the MOT can be loaded faster, meaning the big Zeeman slower is on for a shorter time. Secondly, an additional copper block can be used to allow the water to be pumped across the two halves of the length of the Zeeman slower in parallel, thus doubling the flow rate. This will require cutting the Zeeman slower wire and re-soldering the connections on the experiment table and hence will not be attempted until a suitable time.

[2] The fan was positioned far away enough that it did not affect the B-field.

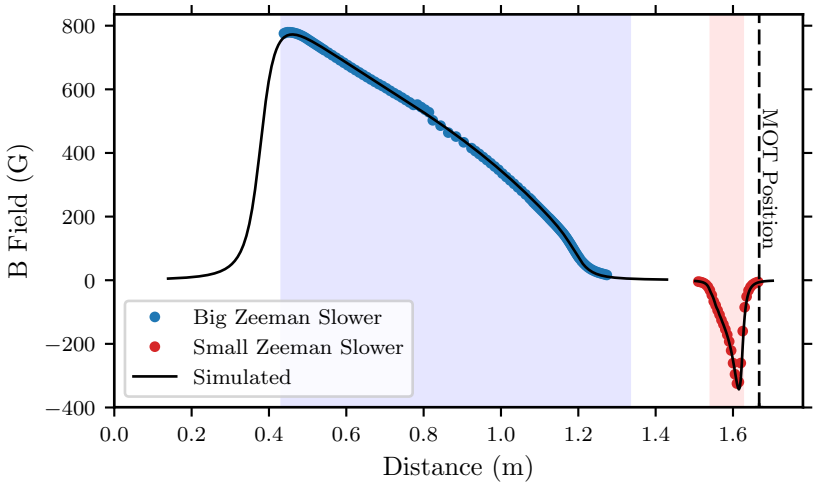

Figure 3.10: Measured B-fields of the big (blue) and small (red) Zeeman slower coils along their axis against distance from the oven exit nozzle (distance 0). The simulated values are also shown (black line). The fields were measured using the Group3 Hall Probe with a custom cylindrical mount that allowed the sensor to be centered in the Zeeman slower. A long M8 threaded rod passing through a fixed nut was then used to move the mount accurately over the length of the Zeeman slower by counting the number of revolutions. The Zeeman slowers were run at low currents (15 to 25A and the field values have been linearly multiplied to give the predicted fields when operated at full current. The variable pitch helix gives a smooth field profile compared to stages of wound solenoids. The background color represents the physical extent of the coils.

These coils needed to be measured in both Helmholtz and anti-Helmholtz configuration. Starting in anti-Helmholtz, the probe was centered in the x-y plane using a transparency. The probe was then moved in the z direction and the center z value, z_0, was found. Positioning the probe at $z = z_0$ and then switching the coils to Helmholtz, the field in the x, y plane was measured over a 25 mm grid with step size 0.5 mm. From this data the center value in the x, y plane could be found. Each layer was measured individually. The current was calibrated with an amp clamp. The field data was then compared to the simulation described in Section 3.4.3 and was found to be in very good agreement (0.1 to 0.5% error) as shown in Fig. 3.11. The z_0 value was also used to confirm that the center point would be the correct distance from the UKEA viewport.

MOT coils

The MOT coils were also mounted to the same structure and a similar method was used to measure the anti-Helmholtz gradient. The field gradient was measured as $0.654\,\mathrm{G\,cm^{-1}\,A^{-1}}$ compared to the expected $0.799\,\mathrm{G\,cm^{-1}\,A^{-1}}$. This is understandable given that the MOT coils spiral both outwards and upwards, whereas our simulations treat them as a series of planar spirals (see Fig. 3.8). This MOT stage does not require a large B-field gradient,

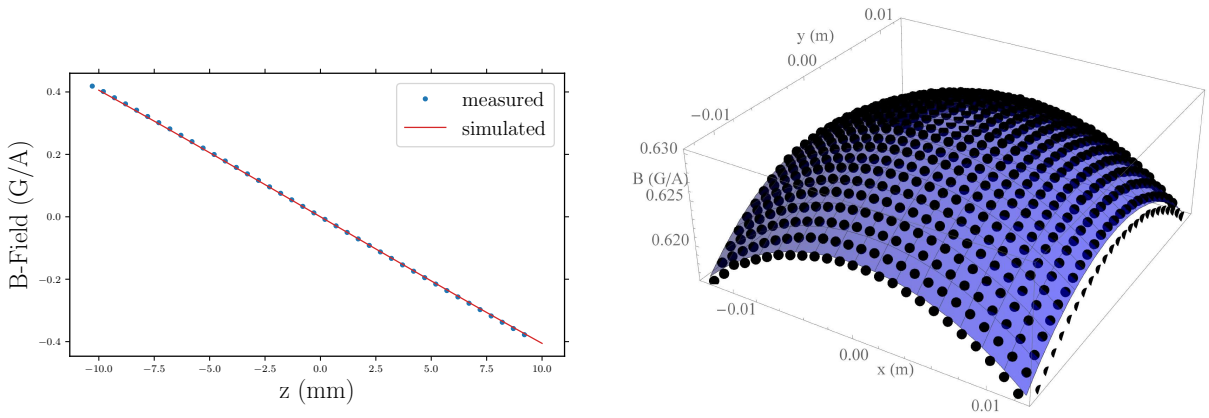

(a) Anti-Helmholtz **(b)** Helmholtz

Figure 3.11: B-field measurements of the Feshbach coils compared to the simulated B-field described in Section 3.4.3. The measured data has been renormalized to $\mathrm{G\,A^{-1}}$ by dividing by the current. The red curve and blue plane show the simulated field prediction for the anti-Helmholtz field (Fig. 3.11a) and Helmholtz field (Fig. 3.11b), respectively. For the 3 layer Feshbach coils, a gradient of $0.412\,\mathrm{G\,cm^{-1}\,A^{-1}}$ is measured compared to the simulated $0.413\,\mathrm{G\,cm^{-1}\,A^{-1}}$; an offset field of $1.895\,\mathrm{G\,A^{-1}}$ (compared to $1.893\,\mathrm{G\,A^{-1}}$) and a curvature of $0.0419\,\mathrm{G\,cm^{-2}\,A^{-1}}$ (compared to $0.0424\,\mathrm{G\,cm^{-2}\,A^{-1}}$).

however, these coils are used for the initial magnetic trap and transport, for which a high gradient is beneficial for trapping the hot atom cloud. For the MOT coils, the trap depth is limited by the radial distance at which the field is no longer linear and eventually begins to change gradient (see Fig. 3.12).

3.4.5 Fast Switching of Magnetic Coils

In the experiment, accurate control over the times at which the B-fields turn on and off is required. Whilst for the B-fields used in the laser cooling stages this might not be so critical, it can be very important for the Feshbach and imaging fields to be turned on and off rapidly.

Switching magnetic coils (essentially an inductor) induces a large voltage. This is a result of Faraday's law that states that a change in the magnetic environment creates an induced voltage, which opposes the change in the magnetic field. The law can be formulated as:

$$V_{\text{induced}} = -\frac{\mathrm{d}\Phi_B}{\mathrm{d}t} = -L\frac{\mathrm{d}I}{\mathrm{d}t} \tag{3.8}$$

where V_{induced} is the induced electromotive force, Φ_B is the magnetic flux, with $\frac{\mathrm{d}\Phi_B}{\mathrm{d}t}$ the rate of change of magnetic flux with respect to time, t. For a single inductor of inductance L with current I, this can be expressed as in Eq. (3.8) showing that the induced voltage is proportional to L and the rate of change of the current, $\frac{\mathrm{d}I}{\mathrm{d}t}$. For a Helmholtz pair with

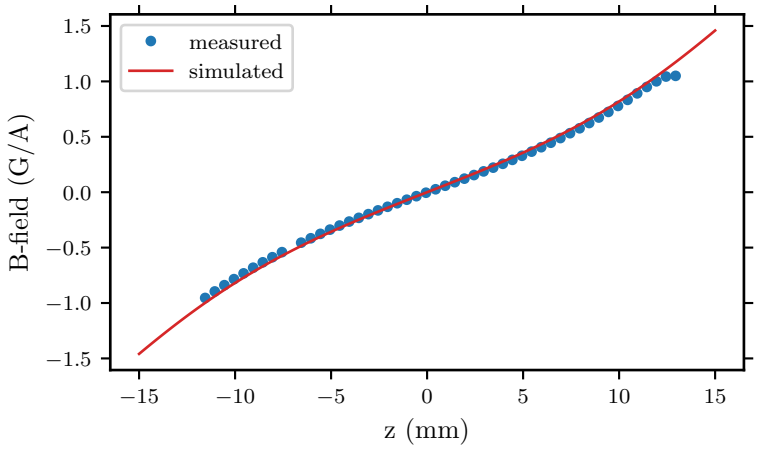

Figure 3.12: Measured and simulated field of the MOT coils in anti-Helmholtz configuration along the z direction. The measured gradient is slightly weaker than the predicted gradient, probably due to the fact that these coils spiral in the vertical plane, a feature that is not accounted for in the simulation.

$R \approx d$, it was derived in Eq. (3.4) that:

$$B_0 \propto \frac{IN}{R} \tag{3.9}$$

The inductance of an ideal coil is:

$$L \propto \frac{N^2 R^2}{l} \tag{3.10}$$

Where R^2 gives the cross-sectional area of the coil and l its length. For a fixed B_0, Eqs. (3.9) and (3.10) can be combined to show how V_{induced} scales:

$$V_{\text{induced}} \propto \frac{N R^3 B_0}{l} \tag{3.11}$$

Eq. (3.11) shows why it is desirable to use a magnetic coil with fewer windings running at higher currents to produce a B-field. Due to the quadratic scaling of the inductance with N, lower induced voltages are produced for the same field when fewer turns are used, meaning shorter switching times can be achieved for a given maximum induced voltage.

In the experiment, the maximum induced voltage permitted is defined by the insulation of the wires or maximum voltages tolerated by the IGBTs and MOSFETs. A typical limit for the Feshbach coil wire insulation[1] used in the experiment is 3600 kV. The high current (1600 A) IGBTs modules used are Fuji 1MBI600U4B-120 with a maximum collector emitter voltage specified as 1200 V. The high current MOSFETs (230 A) used in

[1] 180 µm of Kapton foil rated to 20 kV mm^{-1}.

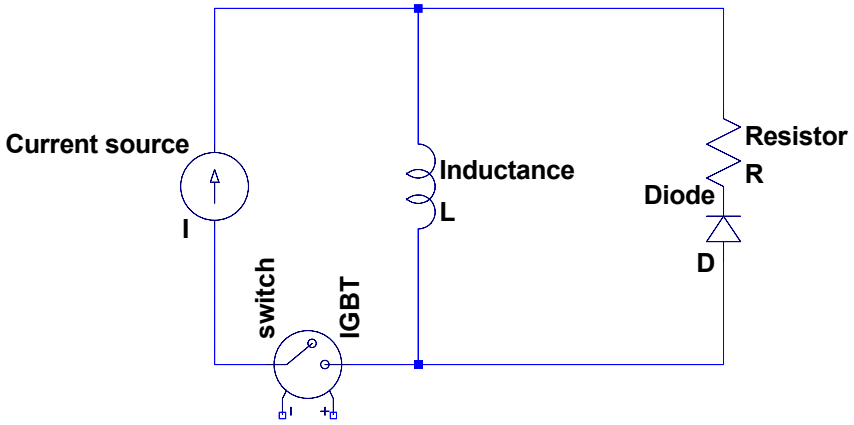

Figure 3.13: A standard snubber circuit uses a diode with a resistor. When the switch (IGBT or MOSFET) is opened, a large voltage is induced across the coils and a current can flow through the diode and resistor. This process dissipates the energy that was stored in the B-field into the resistor.

the experiment are IXFN230N10 (100 V max).

Anywhere where magnetic coils are to be switched, a ring-down (or snubber) circuit is required to allow the induced voltage from the field breakdown to flow as a current and for the energy that was in the B-field to be dissipated. The standard ring down circuit uses a diode, as shown in Fig. 3.13. When the switch (normally a MOSFET or IGBT in our experiment) is opened, the large induced voltage causes a current to flow in the opposite direction to normal operation, which can flow through the diode and series resistor. Increasing the resistor value will decrease the time required to turn off the fields, but with larger induced voltages across the coils.

The diode snubber circuit is reliable and easy to implement and is used for many of the coils where lower currents are used or fast switching times are not critical (e.g. Zeeman slower, MOT coils, compensation coils). For coils running at high currents where faster switching is critical, snubber circuits with a varistor are used. Additionally, the varistor snubber circuit is not directional and is used where current can flow in both directions through the coil.

A varistor is an electrical component that is composed of an array of metal oxide balls fused into a ceramic semiconductor. A varistor has a very high resistance below its clamping voltage V_c, and a very low resistance above V_c. The simulation of a diode and varistor snubber circuit shown in Fig. 3.14 shows why the varistor can lead to a faster switch time. During the ring down process, the induced voltage across the diode decays exponentially, meaning the rate at which energy is dissipated also decays exponentially. For the varistor circuit the voltage is kept at V_c or above and hence the rate of power

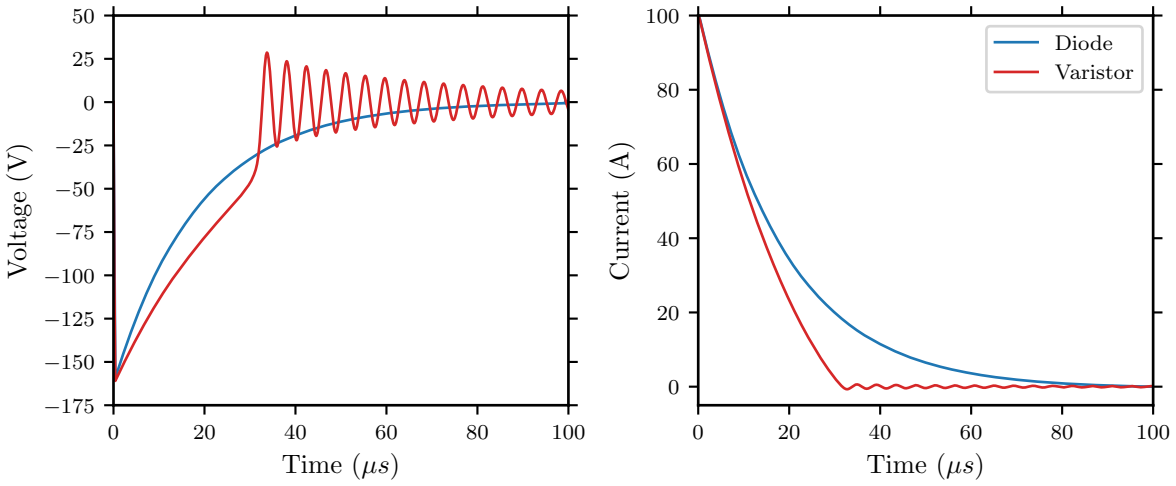

Figure 3.14: Comparison of the voltage and current response to a switch off when either a diode or varistor is used in the snubber circuit. The simulation, using LTSpice, assumes a 100 A initial current switched in 400 ns with a 1 Ω resistor in series with the diode or varistor. The simulated varistor is an EPCOS B72220S0170K101 (V_c = 50 V). The comparison shows that the varistor leads to a faster switch off. For the diode circuit both the voltage and current decay exponentially, whereas the varistor maintains a higher voltage for longer, leading to a faster reduction in current.

dissipation is faster. This can allow for much faster switching times when an appropriate V_c is chosen. Higher V_c values and higher resistor values both give faster switching times at the expense of a higher peak induced voltage.

The snubber circuits used across the Feshbach coils were designed to allow for fast switching times (600 A in less than 100 µs) and to keep the voltage across the coils less than 500 V to guarantee the protection of the coil insulation and IGBT modules. Many factors must be considered in the choice of the varistor. The clamping voltage should be chosen to be lower than the damage thresholds in the circuit (V_c can degrade and vary between varistor by 10 % or more). The maximum current surge for the varistor should be larger than the maximum currents in the coils and the maximum energy dissipation should be larger than the energy stored in your coil (estimated using $\frac{1}{2}LI^2$). Large energy dissipation usually requires a larger diameter of the varistor, which increases its capacitance. This capacitance can cause ringing and was included in the simulations. The snubber circuit uses EPCOS B72220S0170K101 varistors. These have a clamping voltage of 50 V. While this is substantially lower than our maximum, it was found that this provides suitably fast switch off and hence larger clamping voltages were not required. They can withstand a pulse current of 2000 A and a pulse of energy of 14 J compared to our maximum current of 600 A and energy stored in the coils of 5.5 J. Varistors can and do fail after many uses, however, the duty cycle in the experiment is very low (one voltage spike every 20 seconds)

and the chosen varistor is approximately 3 times larger than required. In addition, each varistor circuit is repeated in parallel twice around each coil. This redundancy provides additional protection in the case of failure[1]. The choice of resistor in the snubber circuit is also critical. Ideally, a low inductance resistor should be used. Attempts were made to use low inductance thick film resistors which should be able to withstand 200 W for 100 µs and 600 V. These resistors (CRM2512) were destroyed when switching at over 300 A with arcing audible and visible across them. Examination under a microscope showed that the thick film had been shattered and it is unknown whether this was caused by over-voltage or power dissipation. Attempts with standard wire wound power resistors were much more successful even though they would have a larger inductance. A standard aluminum housed 1 Ω, 50 W power resistor with a maximum voltage of 3000 V ($L \sim 100\,\mu H$) was used. Ringing of the current or voltage during the switch-off can occur due to the capacitance of the coils or varistor used. Putting a resistor in parallel with the coils damps this ringing with a lower parallel resistance giving more damping. However, this parallel resistor cannot be so small that it causes a substantial amount of the current through the coil to be diverted and it should be relatively precise and stable to ensure the current through each coil is the same and doesn't change with time.

The simulations performed used a Spice varistor model with parameters adapted manually to match the simulations provided by EPCOS for the varistor models used. It should be noted that a much simpler model using two Zener diodes created a reasonably good approximation to the final varistor circuit. To measure the large induced voltages on a fast time scale, an active differential high voltage probe[2] was used. The current was measured with the transducer used later for the field regulation (see Section 6.3.2). The measured voltages and currents are shown in Fig. 3.15 for a range of currents. Some oscillations are seen in the voltages after the voltage drops below V_c, similar to the simulations shown in Fig. 3.14. The measured current decays much faster than the voltage. Some very high frequency noise can be seen on the current soon after switching, however, it is hard to verify if this is real or an artifact from the transducer. The induced voltages for two different currents are directly compared to the LTSpice simulations in Fig. 3.16. The simulations reasonably match the measured voltages, meaning the simulations can be used for future redesigns or improvements to the snubber circuits. Whilst the decay time measured by the current transducer is very short (600 A in less than 20 µs), the field decay time will be limited by eddy currents. The stainless steel chamber, copper gaskets and

[1]Note that in the case of the failure of one varistor the magnitude of the voltage spike across the coil would double as the effective resistance of the snubber circuit would be doubled.

[2]Tektronix P5205A capable of measuring 1300 V, 100 MHz bandwidth and 590 V ns^{-1}.

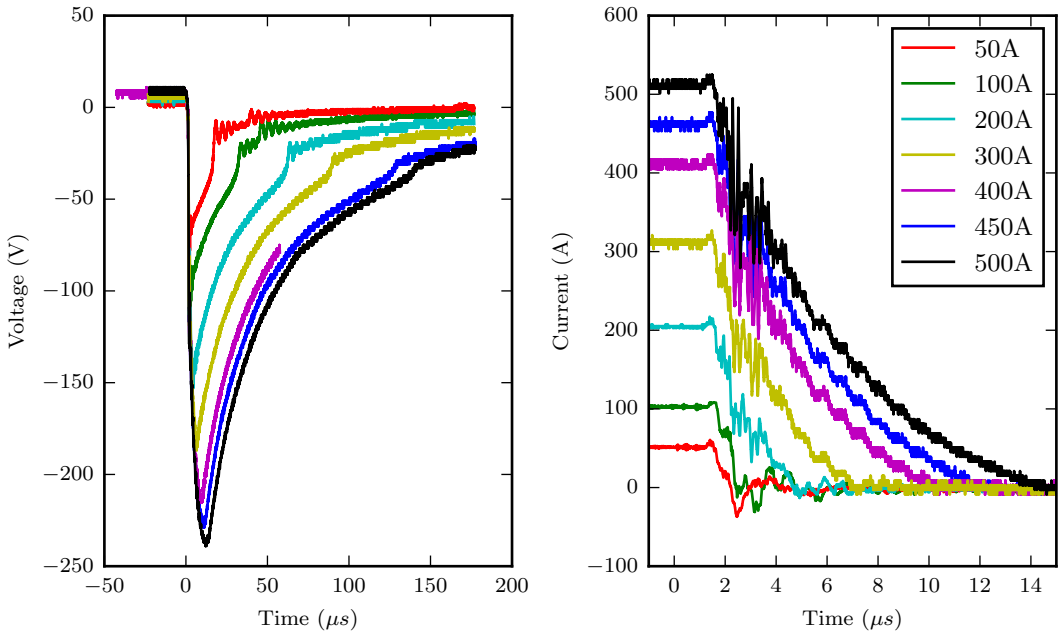

Figure 3.15: Induced voltage and current after switching of the Feshbach coils with the IGBT from various starting currents. The voltage decays much more slowly than the current.

other nearby coils[1] have a mutual inductance with the Feshbach coils, meaning that they experience an induced current when the Feshbach coils are switched. The eddy currents from switching the Feshbach coils were quantified using the atoms (see Section 6.4) and a discussion of their compensation in a cold atom experiment can be found in [135].

3.4.6 Power Dissipation and Water Cooling

Several coils in the experiment dissipate significant amounts of power and require water cooling to operate. In this section some useful methods and formulas that should be used when designing water cooling are provided. If we consider dissipating a power P, from the coils into a material with density ρ, and heat capacity C, which is flowing through the coils with a flow rate F, then an change in temperature of the material ΔT, can be calculated:

$$\Delta T = \frac{P}{\rho C F} \tag{3.12}$$

[1]To minimize this effect, all coils are connected to MOSFETs or IGBT and are open when the Feshbach coils switch.

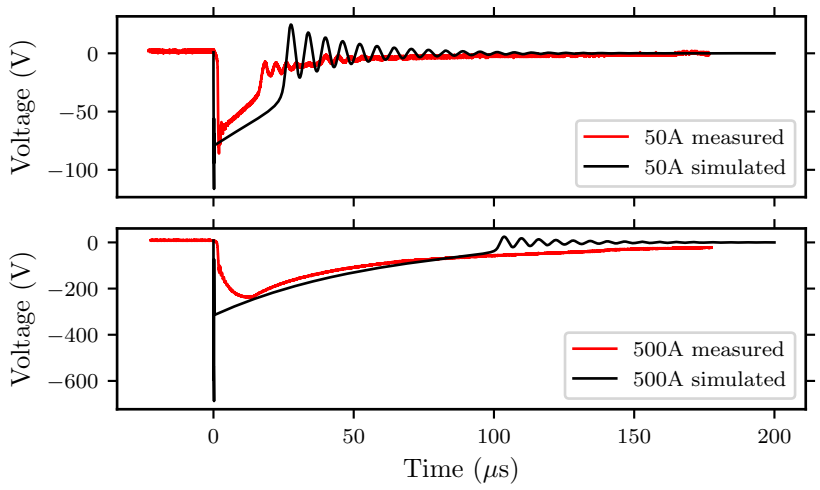

Figure 3.16: The induced voltage in the Feshbach coils is simulated and compared to the measured voltage for an initial current of 50 A (top) and 500 A (bottom). The simulations qualitatively match the measured voltages. The discrepancy could be due to inaccuracy in the inductance value, stray capacitance or mutual inductance effects.

This can be cast into a simpler form for water cooling and typical units used in the laboratory:

$$\Delta T\,(^{\circ}\mathrm{C}) = \frac{14.3P\,(\mathrm{kW})}{F(\mathrm{l/\,min})} \Rightarrow F(\mathrm{l/\,min}) = \frac{14.3P\,(\mathrm{kW})}{\Delta T\,(^{\circ}\mathrm{C})} \tag{3.13}$$

From Eq. (3.13), in order to dissipate a large power, a large ΔTF is required. To increase the flow rate, the resistance to flow must be decreased or the pumping pressure increased. The simplest way to reduce the resistance of water flow is to allow the water to flow in parallel across the system, however, this may require additional plumbing and water connections. In general, it is not desirable to have too large a ΔT, as this can cause temperature gradients across the table if the coils extend over a large region and also because this may cause larger periodic temperature changes during the experiment cycle. A large ΔT can also cause expansion of copper wires which may change the B-field slightly.

Once water cooling has been setup, F and ΔT should be measured. If ΔT is too large, then a higher pressure pump can be used or a change to the water cooling can be made, to increase the flow rate. If ΔT is small but the device still gets too hot, this implies you do not have good enough contact between the water and device. This often requires redesign or additional water cooling to solve.

The laboratory has a 6 °C and 17 °C water outlet. An additional 17 °C circuit is dedicated to the table air conditioning units. Another 17 °C circuit has been piped into the labora-

tory from the corridor to provide additional water flow. A closed circuit heat exchanger[1] is used for the critical water cooling applications on the experiment table. The heat exchanger is cooled by the 17 °C water and a valve can automatically open/close to regulate the temperature[2]. Less critical water cooling applications are run directly from the laboratory water. The 6 °C water is used for the air conditioning and cooling the tower which houses the high current power supplies. The water connections are split in parallel using TacoSys HighEnd manifolds with a variable number of outputs. These manifolds have a 0 to 5l min^{-1} flow meter and flow reducer built in and an additional rotary valve was placed on each output. The water connections and flow rates in the experiment are tabulated in Table 3.7 and the full schematic of water connections is drawn in Fig. 3.17.

Given the large number of water connections, leaks appeared over time, especially in the first few weeks of water flow. Commonly, these can be fixed by tightening jubilee clips or replacing the hose connector, however, sometimes a connection must be re-soldered. Some critical water leaks were successfully repaired using *J-B Water Weld Epoxy Putty*. The area was always drained and dried before the epoxy applied as curing the epoxy while wet never resolved the leak.

3.4.7 Summary of Experiment Coils

This section describes the different coils used in the experiment and the power supplies and switching boxes that control them. The MOSFET/IGBT boxes allow the current in the magnetic coils to be turned off (and if appropriately charged, on) rapidly. Additionally, they make the coils appear as open circuits when not in use, reducing eddy currents from other coils switching nearby. From a practical perspective, the MOSFET/IGBT boxes allow a single power supply to drive a current in multiple coils and for a single coil to be connected to different power supplies. A MOSFET/IGBT box can have several channels with each channel connected to a single power supply. Each channel can then have several sub-channels that can connect that power supply to different coils, which can be independently switched. Table 3.8 enumerates all the different coils used in the experiment and a brief description of what they are used for.

In the experiment there are five switching boxes used: Mini-Mosfet Box, MOSFET Box 1, MOSFET Box 2, IGBT Box 1 and the H-Bridge Box. Table 3.9 shows how each of the boxes are connected to the different coils and power supplies.

[1] NESLAB System 1 Liquid to Liquid, Thermo Electron Corporation.

[2] After the valve got stuck closed several times, the heat exchanger is now operated such that the

Table 3.7: Tabulated values of the water cooled devices in the experiment and what they are supplied from. An approximate flow rate is also given for each device. More detail can be seen in Fig. 3.17.

Water Outlet or Manifold	Connects to	Flow Rate ($l\,min^{-1}$)
6 °C	Air conditioning Power Supplies Tower	> 5
17 °C laboratory	Manifold x3 General	> 10
17 °C corridor	Manifold x5 Experiment Back	6.5
Manifold x5 Experiment Back	BZS Cooling Plate Bottom BZS Cooling Plate Top H Bridge Box IGBT Box Amplifier Tower Experiment	1.5 1.5 1 1 1.5
Manifold x10 Heat Exchanger	Short circuit BZS SZS Cold cup MOT Manifold x6 FB Top Manifold x6 FB Bottom Camera	0 0.5 1.5 0.5 1 > 5 > 5 0.5
Manifold x3 General	Heat Exchanger Manifold x5 Optics	> 5 2.5
Manifold x5 Optics	Amplifier Tower Na Lattice laser Heat Exchanger Amplifier Tower Li Dipole Box	1 0 1 0.5
Manifold x6 FB Top	All 6 layers of FB Top coils	1 (per layer)
Manifold x6 FB Bottom	All 6 layers of FB Bottom coils	1 (per layer)

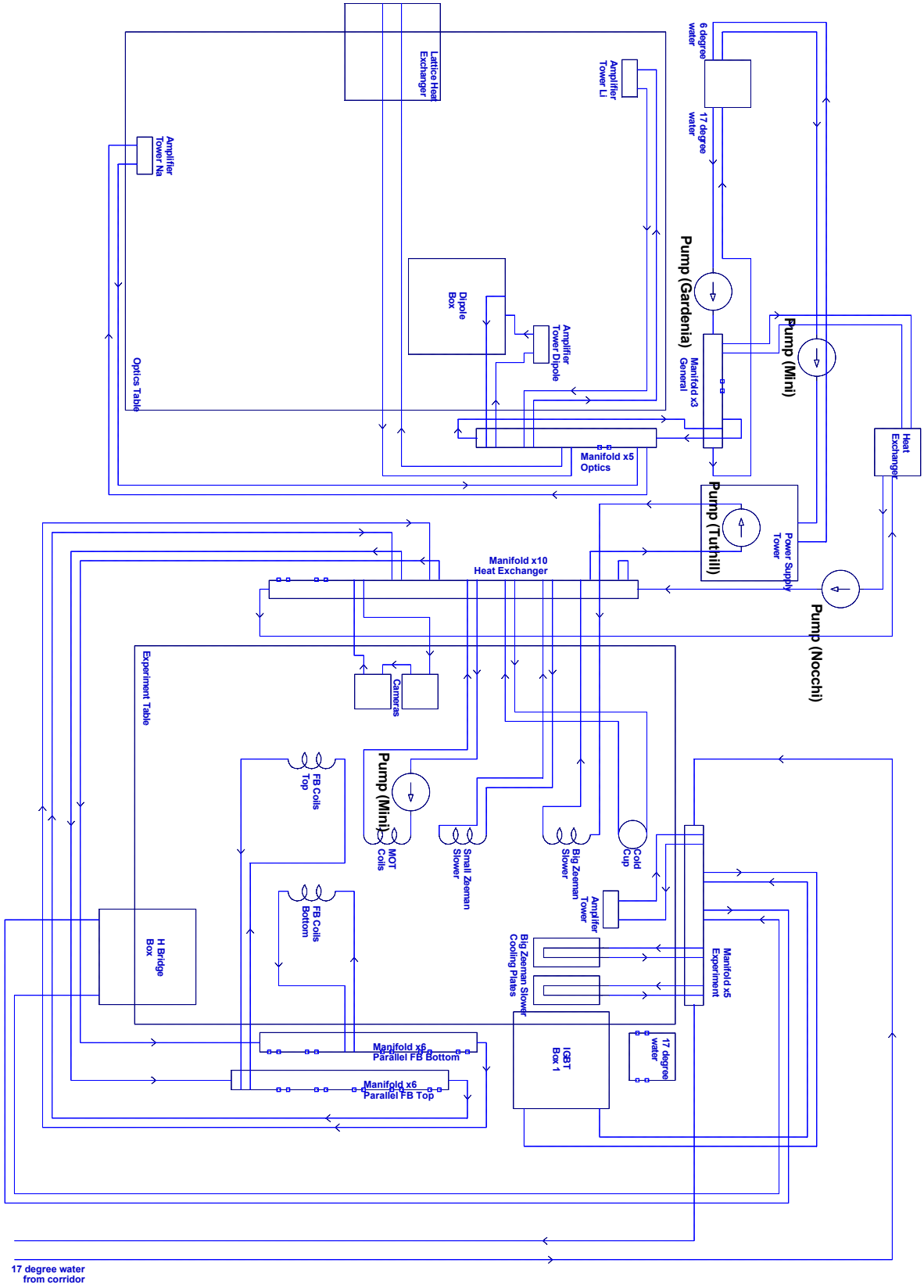

Figure 3.17: Schematic of the water cooling connections in the experiment. The layout of the room is approximated in this schematic. The lines do not necessarily follow the exact path of the real water pipes. Blue lines with directional arrows show water flow. The different connections are also tabulated in Table 3.7.

Table 3.8: Table of the magnetic coils used in the experiment. Where applicable, the Helmholtz field is given in $\mathrm{G\,A^{-1}}$ and the anti-Helmholtz gradient is given in $\mathrm{G\,cm^{-1}\,A^{-1}}$ (defined as in Eqs. (3.6) and (3.7)). The purpose column gives a brief description of what the coil is used for which is particularly important when a coil has multiple uses.

Coil	Helmholtz $\mathrm{G\,A^{-1}}$	Anti-Helmholtz $\mathrm{G\,cm^{-1}\,A^{-1}}$	Purpose
Big Zeeman slower	—	—	decreasing field Zeeman slower
Small Zeeman slower	—	—	increasing field Zeeman slower
Zeeman slower compensation $x2$	—	—	compensates turn off of Zeeman slower at MOT location
unused compensation $x1$	—	—	single unused compensation coil in x direction
x'A compensation coil	0.154	0.015	Helmholtz compensation in x' direction
x'B compensation coil	0.123	0.011	anti-Helmholtz compensation in x' direction
y'A compensation coil	0.154	0.015	Helmholtz compensation in y' direction
y'B compensation coil	0.123	0.011	anti-Helmholtz compensation in y' direction
MOT coils	0.69	0.325	MOT field initial magnetic trap magnetic transport
3 layer Feshbach	1.89	0.207	magnetic transport final magnetic trap Feshbach coils
L1 L2 combination	0.936	0.112	gradient and gravity compensation
magic layer	0.4	0.049	Helmholtz compensation z direction optical pumping bias field
gradient lines x' y'	—	—	create z field gradient in $x' - y'$ plane
600A discharge coil	—	—	allows rapid discharge of 600A power supply

Table 3.9: Table showing which boxes connect to which power supplies and coils. The information in this table is identical to that in Table B.1 but collected by the different boxes used in the experiment.

Box	Power Supply	Coils
Mini MOSFET	Delta 10 A 15 V (1) Delta 10 A 15 V (2) Delta 10 A 15 V (3) Delta 10 A 15 V (4)	x'A compensation coil x'B compensation coil y'A compensation coil y'B compensation coil
MOSFET Box 1	Delta 100 A 60 V	MOT coils y'A compensation coil L1 L2 combination
MOSFET Box 2	Delta 40 A 6 V(2) Delta 10 A 15 V (5)	Zeeman slower compensation $x2$ magic layer x'A compensation coil
IGBT Box 1	Lambda 400 A 25 V Delta 600 A 30 V	Big Zeeman slower MOT Coils 600 A discharge
H Bridge Box	Delta 600 A 30 V	3 layer Feshbach
Direct	Delta 40 A 6 V(1)	Small Zeeman slower

3.5 Radio Frequency and Microwave Setup

Whilst the initial cooling and trapping stages of the experiment drive atomic transitions with laser light (see Chapter 4), later in the experiment transitions between different hyperfine states are required, which typically occur at radio (RF) or microwave (MW) frequency (see Sections 5.4.2 and 5.6.1). Several RF and MW antennas were mounted inside the main Kimball chamber (Fig. 3.18a), which should have allowed for very good coupling between different hyperfine states due to the close proximity to the atom cloud. Unfortunately, during the operation of the experiment it was found that these coils provided very poor coupling. Since they were all designed to have a 50 Ω impedance at their required frequency, it is unlikely that the geometry of the coil is the problem. Instead, it is likely that the presence of the stainless steel vacuum chamber acts as a ground plate, which significantly changes the radiated power of the antennas [136]. Eventually, similar coils were placed outside the main Kimball chamber directly on top of the UKEA viewport that will later be used for high resolution imaging (Fig. 3.18b). These new coils were all secured together using cable ties and wrapped in Teflon tape so they could be

cooling valve is always open.

Table 3.10: Description and properties of the different MW and RF coils used in the experiment. The MW coils were wound with 6 mm by 2 mm wire and the RF coils were wound with 1 mm diameter circular wire.

Coil	Usage Freq (MHz)	Amplifier Power (W) (Model)	Purpose	Dimensions
MW 1	1700 to 1900	12.6 (A11381.7-2.1)	Evaporation of ^{23}Na in magnetic trap	C-shape radius 11 mm
MW 2	2000 to 2700	80 (KU PA BB 070270-80A)	RF flip ^{6}Li $\|1\rangle \rightarrow \|6\rangle$ at high B-field	C-shape radius 8 mm
RF 1	60 to 240	8 (ZHL-035WF)	Landau Zener sweeps ^{6}Li	rectangle 50 by 20 mm
RF 2	75 to 85	30 (LZY-22+)	Fast ^{6}Li RF flips $\|2\rangle \rightarrow \|3\rangle$	2 winding square 10 by 10 mm

placed on the UKEA viewport without scratching it. These coils are physically closer to the atoms and the improvement was immediately noticeable in the reduction in the ^{23}Na temperature after a fixed evaporation time. Each coil was soldered to a non-magnetic SMA connector and the SMA cable leaves the main Kimball chamber to a nearby set of amplifiers mounted on a cooling block on the top breadboard. The vertical imaging beam passes through the center of the coils. The original RF cables used were found to be magnetic and were magnetizing during the sequence, shifting the position of the atoms. A new non magnetic cable[1] is now used. The different RF coils that are currently used in the experiment are described in Table 3.10.

Several different sources are used to control the MW and RF in the experiment. For the Landau Zener sweeps that require fast ramps of the frequency (< 5 ms) a DDS (DLIC) box[2], which was made by a previous student in the group [137], is used. For RF pulses or slower ramps, commercial DDS boards[3] or commercial synthesizers are used. All these devices are programmed by the Experiment Snake control software (see Appendix B.5.2).

[1] Huber and Suhner Multiflex 86 1 dB m^{-1} at 1.75 GHz.

[2] Due to frequent software crashes these boxes are not used in the experiment except for the fast Landau Zener sweeps and for the ^{23}Na evaporation.

[3] Windfreak SynthNV or Windfreak SytnhHD.

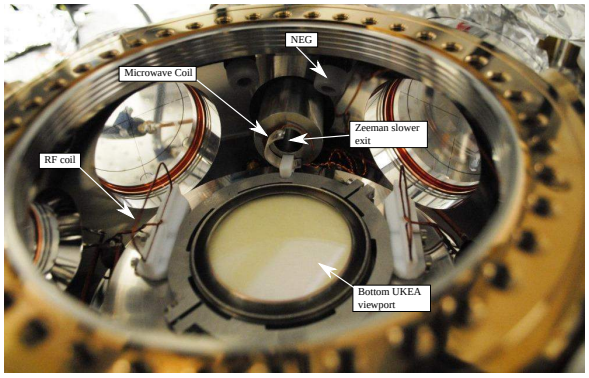

(a) Inside the main Kimball chamber.

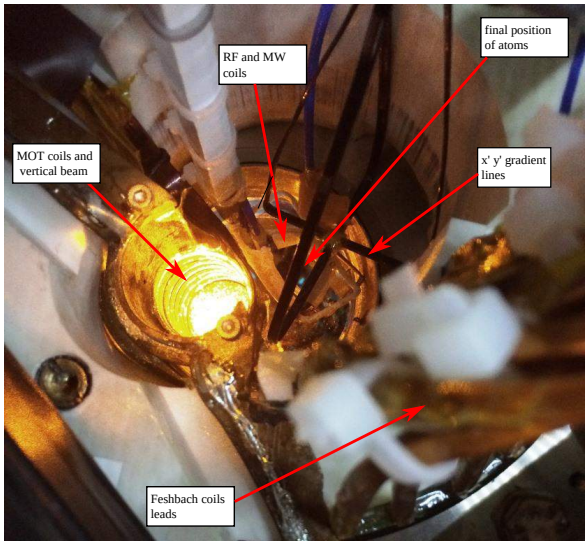

(b) RF coils mounted outside the main Kimball chamber.

Figure 3.18: Several RF and MW coils were mounted inside the main Kimball chamber (**Fig. 3.18a**) with the hope that this would give very high RF and MW coupling for hyperfine transitions. These coils were found to be very ineffective, probably due to the chamber acting as a ground plate. Additional coils mounted directly on the top UKEA viewport (**Fig. 3.18b**) were far more effective. The gradient x',y' lines are also visible in Fig. 3.18b, which are used to displace the cloud to measure the trap frequencies (Section 6.2).

Chapter 4

Laser Cooling: From the Oven to Optical Pumping

This section details the first slowing and trapping stages of the experiment and how the atoms are optically prepared for the magnetic trap. In a simple two-level atom picture, absorption of photons (with a momentum and energy) leads to a momentum change that can be equated to a force. This scattering force is utilized firstly to slow the atoms from the oven using a Zeeman slower (Section 4.1) and then to trap them in a Magneto-Optical trap (MOT) (Section 4.2). Later in the experiment, however, the scattering force leads to unwanted effects such as heating during optical pumping or broadening of the imaging resonance and steps will be taken to reduce its effect. A full discussion of the scattering force can be found in [138].

For a simple two-level atom picture, the scattering force, F_{scatt}, from incident photons of intensity I, momentum $\hbar\mathbf{k}$, and detuning from the atomic resonance δ, can be written as:

$$m\frac{\mathrm{d}\mathbf{v}}{\mathrm{d}t} = \mathbf{F}_{\text{scatt}} = \hbar\mathbf{k}\frac{\Gamma}{2}\frac{\frac{I}{I_{\text{sat}}}}{1+\frac{I}{I_{\text{sat}}}+4\frac{\delta^2}{\Gamma^2}} \tag{4.1}$$

where Γ is the linewidth of the atomic transition and I_{sat} is the saturation intensity. In the limit of $I/I_{\text{sat}} \gg 1$ and $I/I_{\text{sat}} \gg 4\delta^2/\Gamma^2$ the force tends to a maximum value of $\hbar\mathbf{k}\Gamma/2$, which is the case of a saturated transition where the scattering rate tends to $\Gamma/2$ and the population in the excited and ground states are equal. Note that the force is a vector quantity whose direction depends on the direction of incident photons.

4.1 Dual Species Spin Flip Zeeman Slower

Atoms effusing from the oven have a Maxwellian-like[1] distribution of speed, v:

$$P(v) = 2\frac{v^3}{u^4}\mathrm{e}^{-\left(\frac{v}{u}\right)^2} \tag{4.2}$$

where $u = \sqrt{\frac{2\mathrm{k_B}T}{m}}$ is a characteristic thermal velocity, giving a mean velocity from the oven of $\frac{3\sqrt{\pi}u}{4}$. For the typical oven temperatures used in the experiment this gives mean initial speeds of $880\,\mathrm{m\,s^{-1}}$ and $1800\,\mathrm{m\,s^{-1}}$ for ^{23}Na and ^{6}Li, respectively. These speeds need to be reduced to a few $\mathrm{m\,s^{-1}}$ in order to be captured by a typical MOT. Resonant laser radiation, propagating in the opposite direction of the effusive atomic beam can be used to decelerate the atoms, however, at such high speeds the Doppler shift of the light is significant and after some deceleration the light is no longer resonant in the frame of reference of the atom. The principle of a Zeeman slower is to use a spatially varying magnetic field to produce a spatially varying Zeeman shift that cancels the Doppler shift of the laser radiation such that the laser is always on resonance in the atomic frame. The detuning in the atomic frame, $\delta_{\mathrm{atom}}(v, z)$, where z is the direction of propagation, is then given by:

$$\delta_{\mathrm{atom}}(v, z) = \delta_{\mathrm{lab}} + kv(z) - \frac{\mu_{\mathrm{eff}}B(z)}{\hbar} \tag{4.3}$$

where δ_{lab} gives the detuning of the light from the zero-field atomic transition in the lab frame, μ_{eff} is the magnetic moment and $B(z)$ is the spatially dependent magnetic field leading to the Zeeman shift. Eq. (4.3) can be solved to always maintain resonance ($\delta_{\mathrm{atom}}(v, z) = 0$), giving a constant deceleration, a:

$$a = \frac{I/I_{\mathrm{sat}}}{1 + I/I_{\mathrm{sat}}}\frac{\hbar k\Gamma}{2m} \tag{4.4}$$

and a velocity profile:

$$v(z) = v_{\mathrm{initial}}\sqrt{1 - z/L} \tag{4.5}$$

where L is the distance required for an atom with initial velocity v_{initial} to be decelerated to rest:

$$L = \frac{1 + I/I_{\mathrm{sat}}}{I/I_{\mathrm{sat}}}\frac{mv_{\mathrm{initial}}^2}{\hbar k\Gamma} \tag{4.6}$$

[1] This distribution contains an additional factor of v as atoms with a higher velocity are more likely to be incident on the exit aperture.

and the required $B(z)$:

$$B(z) = B_1\sqrt{1 - \frac{z}{L}} + B_0 \tag{4.7}$$

with constants $B_0 = \hbar\delta_{\text{lab}}/\mu_{\text{eff}}$ and $B_1 = \hbar k v_{\text{c}}/\mu_{\text{eff}}$, the relevance of which will be discussed shortly. Eq. (4.6) shows that if the Zeeman slower is some wound coil of total length, L, then there is a maximum capture velocity, v_c, for which atoms with $v_{\text{initial}} > v_c$ will never be on resonance with the laser and hence are not slowed. Atoms with a velocity $v_{\text{initial}} < v_c$ will initially not be slowed, however, will come into resonance at some point and then converge to the velocity given by Eq. (4.5). The parameter B_1 defines the critical velocity that can be achieved for the Zeeman slower. The parameter δ_{lab} (which defines B_0) is a free parameter in the design of the Zeeman slower, which is usually much larger than zero such that the Zeeman slowing light is far detuned from the MOT light and does not interfere with the MOT [139]. Additionally, in this experiment, B_0 is chosen such that the Zeeman slower field crosses zero, which allows for a larger v_c without requiring excessively large absolute B-fields. The field profile and measurement of the Zeeman slower were discussed in Section 3.4.4.

The parameters of the Zeeman slower in the experiment are optimized for ^{23}Na, however, it is longer than required to provide adequate slowing of the much lighter ^{6}Li. Assuming $I/I_{\text{sat}} \gg 1$, the predicted critical velocities are $1250\,\text{m}\,\text{s}^{-1}$ and $1800\,\text{m}\,\text{s}^{-1}$ for ^{23}Na and ^{6}Li, respectively. The detuning and power of the beams can be found in Tables 3.4 to 3.3. The ^{6}Li Zeeman slower light runs on the $2^2S_{1/2}\,|F = 3/2, m_F = 3/2\rangle \rightarrow 2^2P_{3/2}\,|F = 5/2, m_F = 5/2\rangle$ transition and the ^{23}Na Zeeman slower light runs on the $3^2S_{1/2}\,|F = 2, m_F = 2\rangle \rightarrow 3^2P_{3/2}\,|F = 3, m_F = 3\rangle$. Whilst both these transitions are closed, a small amount of repumper (power and frequency optimized experimentally) is used for atoms that leave the cycling transition[1]. The Zeeman slower beam is focused down on the position of the oven exit nozzle (diameter 4 mm), whereas the diameter at the exit of the Zeeman slower matches the inlet size (diameter 16 mm). This focusing has two advantages. Firstly, the shape of the beam can approximately match the divergence of the atom cloud which expands transversely as the propagation speed is reduced. This maximizes the I/I_{sat} over the length of the Zeeman slower while covering the largest possible region of the atom beam. Secondly, having a lower I/I_{sat} near the exit of the Zeeman slower can reduce the number of atoms that are reversed back towards the oven [139].

The Zeeman slower coils create a small B-field at the location of the MOT. When the Zeeman slower coils are turned off, this change in B-field would cause a shift in the position

[1]The efficiency of the repumper is limited because the Zeeman shift for the repumper transition will not be identical to the cooling transition for all fields.

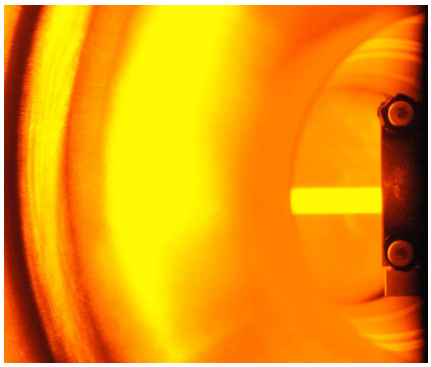

(a) ^{23}Na

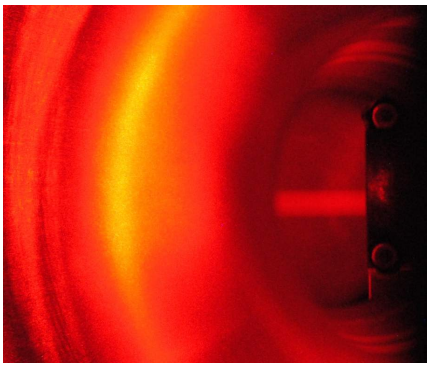

(b) ^{6}Li

Figure 4.1: Fluorescence of the collimated atomic beam from the incident Zeeman slower beam for ^{23}Na (Fig. 4.1a) and ^{6}Li (Fig. 4.1b). The pictures are taken from the sapphire window in the oven chamber. The exposure time for ^{6}Li is approximately 10 times larger than that of ^{23}Na.

of the MOT. This B-field shift is compensated for by the x Zeeman slower compensation coil in the x direction and the optimization of this field is discussed with the alignment of the MOT (Section 4.2). The smaller shifts in the y and z directions are not compensated for.

The alignment of the Zeeman slower was a multistage process that began before sealing the vacuum chamber. The Zeeman slower optics were installed around the chamber and a 1 mm waist radius beam was approximately aligned to the ZS exit and oven nozzle over the 2 m experiment. To accurately align the beam to the center of different vacuum components the CF plastic plugs that ship with vacuum components were used. The plugs have a dot that marks their center, which was drilled through, providing a small aperture for the alignment beam. The oven and vacuum components were adjusted such that the alignment beam passed centered through the entire system. The system was then aligned with the real Zeeman slower beam and the final lens position was adjusted to give a suitable waist at the exit of the Zeeman slower and oven exit nozzle. After the vacuum bake-out, the oven was heated and the Zeeman slower beam incident on the oven could be used as a diagnostic and for alignment. The fluorescence from the Zeeman slower beam was visible both in the small Kimball chamber and the main Kimball chamber. The atomic beam seemed to be at a small angle to the axis of the cooling beam as the brightest region was off-center. Two factors may have caused this misalignment in the experiment. Firstly, during the initial evacuation, the bellows near the oven had not been fixed properly and the evacuation caused them to move significantly, which may have slightly altered the position of the oven. Secondly, it was noted that the cold cup in the oven did not fit as designed and was mounted with a significant angle ($\approx$15°). Although this was ignored, it was later realized this would cause atoms with a $\approx$15° off-axis velocity

to see a slightly larger effective aperture and hence may have explained the observed misalignment. The oven was mounted such that it could be translated and tilted relative to the Zeeman slower such that this could be compensated for. Two additional diagnosis beams, resonant to the zero field transition, were installed to pass through the center of the small and main Kimball chamber, as shown in Fig. 4.2. These beams were extremely helpful in aligning the Zeeman slower. These alignment beams gave a fluorescence signal when crossing the slowed atomic beam that was visible by eye. By taking images of the fluorescence signal and processing them, the clipping of the atomic beam at the exit of the chamber was measurable. The oven was then moved in 1 mm steps to make the atomic profile symmetric and centered on the exit nozzle as shown in Fig. 4.3. By looking from the top of the vacuum chamber, it was also possible to ensure the atomic beam was centered on the position of the MOT. This method led us to the final alignment of the Zeeman slower. Walking and adjusting the beam to maximize the MOT fluorescence signal was later attempted, but was found to already be very close to the maximum value.

The Zeeman slower parameters (current, beam detunings and beam powers) were initially set to the predicted optimal values. Changes were then made to see if there was an increase in the slowed atomic flux and again the alignment beam provided a useful signal. Once the MOT had been set up and the atom number could be counted using the fluorescence signal, these parameters were optimized more accurately. Some of the optimization graphs are shown in Fig. 4.4. By measuring the absorption of the alignment beam and its angle relative to the propagation axis of the atoms, the slowed atomic flux of ^{23}Na was estimated [140] to be $1 \times 10^{12}\,\mathrm{s}^{-1}$. Additionally, by measuring the transverse size of the atomic beam at the exit of the Zeeman slower, one can calculate an approximate speed of $15\,\mathrm{m\,s}^{-1}$ for the ^{23}Na atoms at the exit.

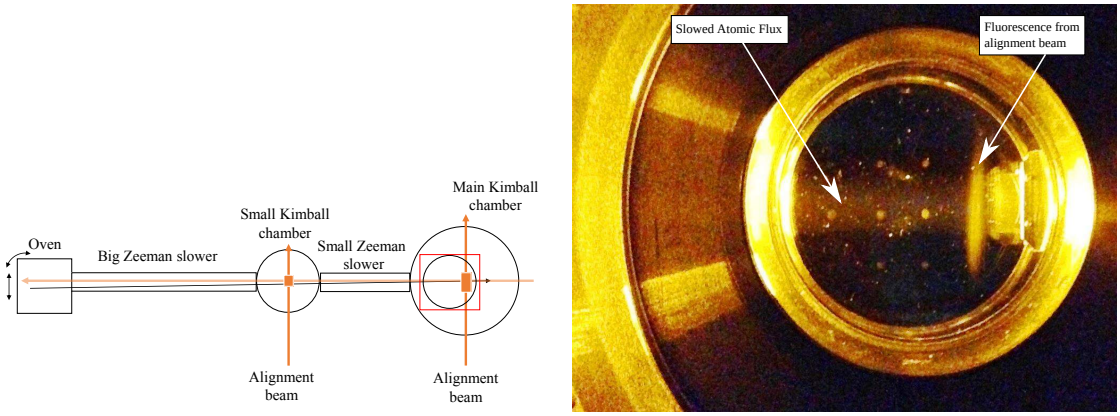

(a) Schematic **(b)** Image in main Kimball chamber

Figure 4.2: Alignment beams on resonance with the zero field cycling transitions were used to examine and align the atomic flux and Zeeman slower. It was found that the oven was misaligned with respect to the Zeeman slower and these beams allowed us to move the oven and optimize the system. **Fig. 4.2a**: Schematic showing how the alignment beams were used. The black arrow represents the misaligned atomic flux and the long orange arrow is the counter propagating Zeeman slower beam. The alignment beam was used in the small Kimball chamber and main Kimball chamber (thin orange arrows) and the visible fluorescence (orange rectangles) was used to align the oven, which could be translated and tilted. **Fig. 4.2b**: An image looking down on the main Kimball chamber (corresponds to red rectangle in Fig. 4.2a) to see the slowed atomic flux (large horizontal beam) and the fluorescence from the alignment beam (brighter and vertical). By imaging the bright region of the alignment beam, it was possible to get a clear signal to optimize the position and angle of the oven (see Fig. 4.3).

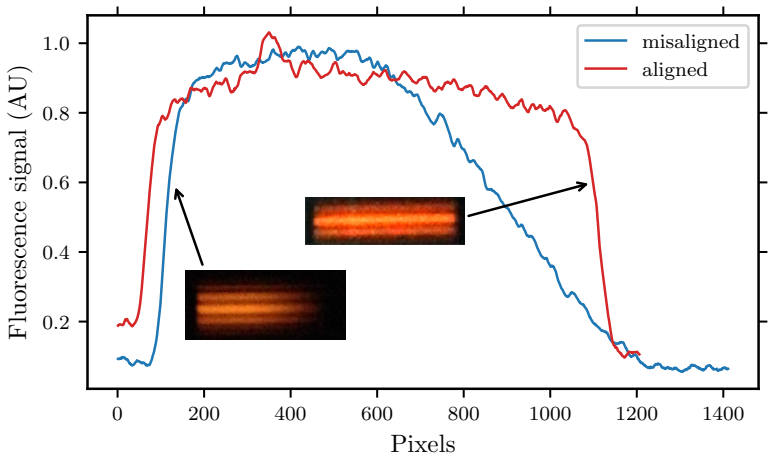

Figure 4.3: Integrated signal from the alignment beam for images before and after the alignment of the oven. The initial misaligned image (blue) shows clearly that the atomic beam is clipped on the left side. After tilting and translating the oven, it was possible to get a symmetric and uniform signal (red). The inset images show the real images the data is created from.

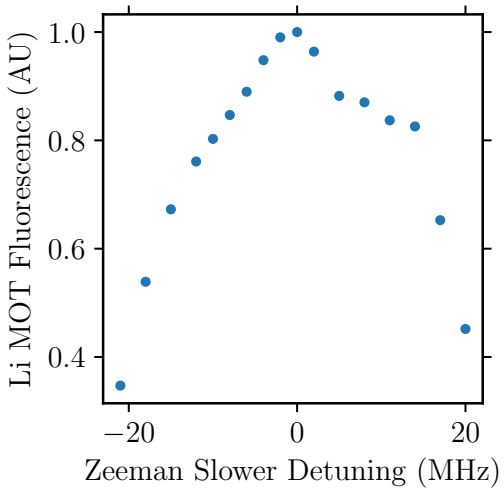

(a)

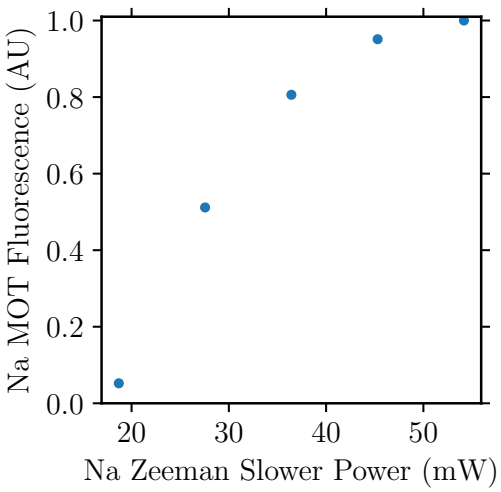

(b)

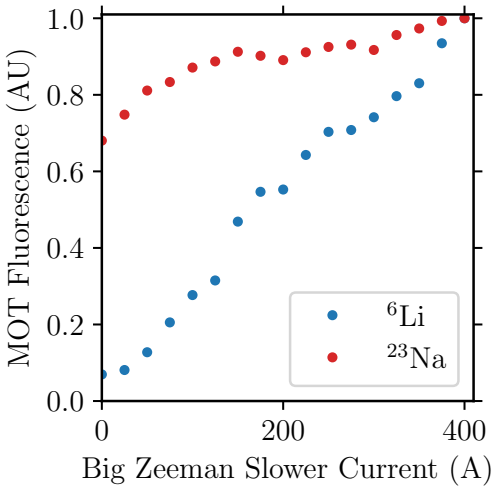

(c)

Figure 4.4: Examples of optimizations for the Zeeman slower parameters. **Fig. 4.4a**: Variation of the ^{6}Li MOT number with detuning of the Zeeman slower light. The repumper is always kept at a fixed frequency from the cooling light. As the light is detuned from the optimal value, the capture velocity of the Zeeman slower is effectively reduced leading to a lower MOT number. The MOT number is measured using a fluorescence image and is normalized to a maximum of 1. **Fig. 4.4b**: Variation of the ^{23}Na MOT number with the power of the Zeeman slower cooling light. As the power is reduced, the intensity is reduced proportionally and the reduction in I/I_{sat} leads to a reduction in the capture velocity. The saturation intensity for the cooling transition of ^{23}Na is $6.26\,\text{mW}\,\text{cm}^{-1}$ [124]. **Fig. 4.4c**: Variation of the ^{23}Na and ^{6}Li MOT numbers with the current in the Big Zeeman slower. Reducing this current affects the ^{6}Li MOT significantly more than the ^{23}Na MOT. This is because the capture velocity for ^{23}Na is considerably larger than the mean thermal velocity leaving the oven, whereas for ^{6}Li they are approximately equal, meaning a reduction in the field causes atoms with the mean thermal velocity to not be slowed.

4.2 Magneto Optical Trap

To create a dual species Magneto Optical trap (MOT) for ^{23}Na and ^{6}Li requires 6 beams of co-propagating 589 nm and 671 nm light, in the standard MOT configuration (Fig. 4.5 and [138]). Due to the high absorption in a large ^{23}Na MOT, retro reflected beams were not appropriate and so six MOT towers were designed[1]. The four towers that produce the four beams in the x-y plane are identical and simply combine the ^{23}Na and ^{6}Li MOT light. The two towers that provide the vertical MOT beams each play an additional role. The tower on the bottom breadboard provides the upwards vertical MOT beam and also combines the optical pumping light (Section 4.4). This requires that the optical pumping light for both ^{23}Na and ^{6}Li is coupled into an optical fiber with the same polarization. The optical pumping light will have opposite polarization ($\sigma^{\pm}$) compared to the upwards vertical MOT beam. The tower on the top breadboard that provides the vertical downwards MOT beam also provides the ^{23}Na MOT repumper. A dark-spot MOT [141] for ^{23}Na is used, meaning that the central region of the MOT has no repumper. This means atoms in the center occupy a dark state, allowing for much higher densities and atom number. The optics and characterization of the dark-SPOT MOT will be described in the thesis of Alexandra Behrle. The different MOT towers are drawn in Fig. 4.6 and the properties of the ^{23}Na and ^{6}Li MOT beams are shown in Table 4.1. The large diameter MOT beams were collimated using a shear plate. All light comes into the towers from optical fibers, with the six MOT beam fibers being produced by Evanescent optics fiber splitters, which convert a single input fiber to six equal power output fibers.

The initial alignment of the MOT beams was done using transparencies made from the CAD drawing of the experiment. This provided a coarse alignment of the 4 beams in the plane of the optical table. The vertical beams were aligned to propagate centrally through the MOT coils. The more precise alignment could then be done by checking that each MOT beam entered the opposite fiber collimator. Final precise alignment was done using

[1] manufactured by Radiant Dyes. The stability and alignment knobs of the MOT towers have been less than satisfactory. Most of these stability issues have eventually been overcome by gluing the mounts once they were aligned.

Table 4.1: Parameters of the MOT beams for ^{23}Na and ^{6}Li.

Species	Waist radius (mm)	Power per beam (mW)	Peak intensity (mW cm^{-2})	Peak intensity (I_{sat})	Approximate atom number
^{23}Na	19.8	45	7.3	1.2	>1E10
^{6}Li	11.1	18	9.3	3.7	1E8

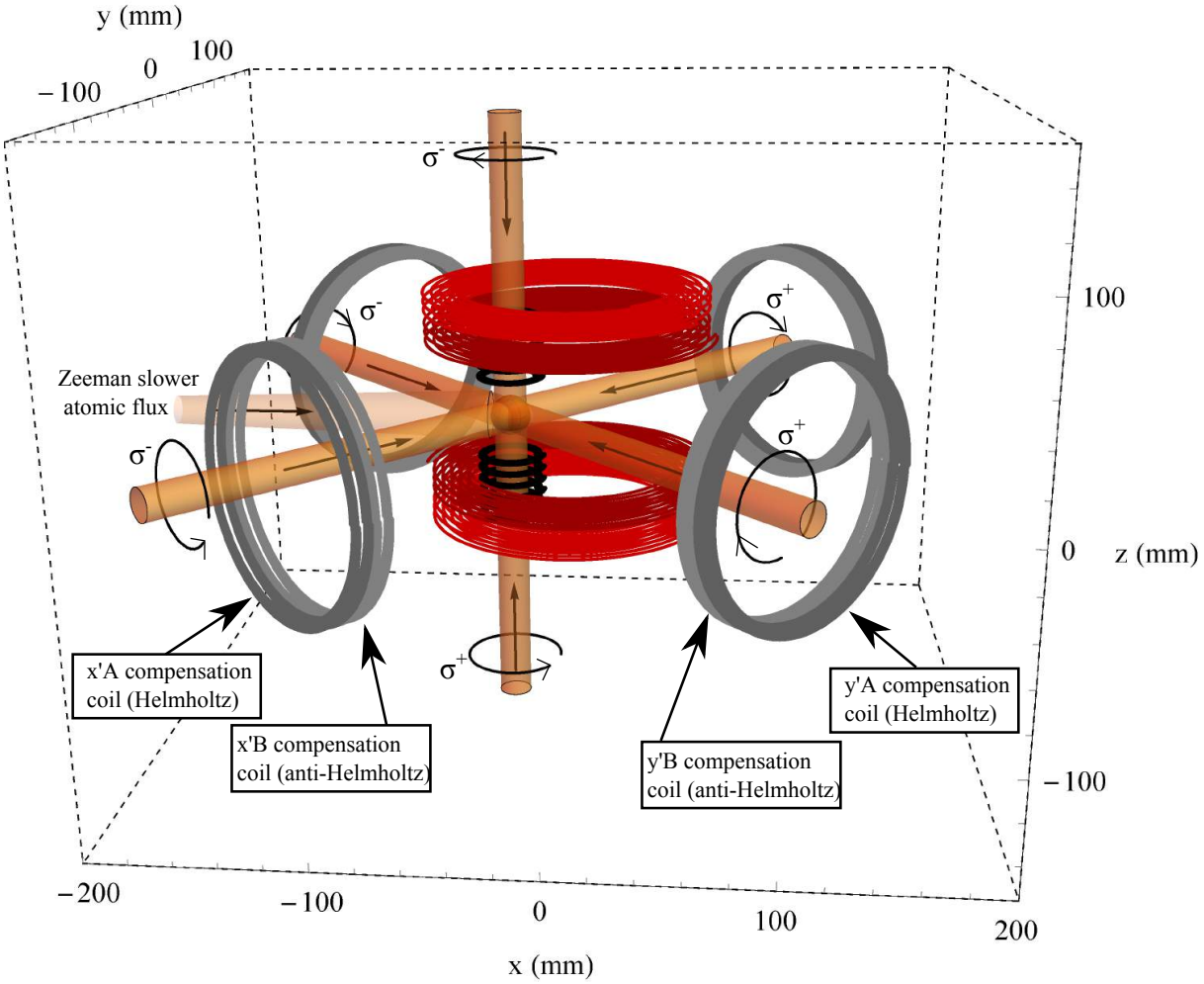

Figure 4.5: Sketch of the MOT beams and coils configuration. The red coils are the Feshbach coils that produce the final magnetic trap and Feshbach fields. The smaller black coils are the MOT coils that are in anti-Helmholtz configuration, producing an upwards field above the MOT and a downwards field below the MOT. The labeled grey coils are the compensation coils wrapped around the side viewports that can cancel stray magnetic fields during different stages of the MOT. The different MOT beams are shown in orange with their polarization labeled. The Zeeman slower is along the x direction and the slowed atomic flux beam is also shown.

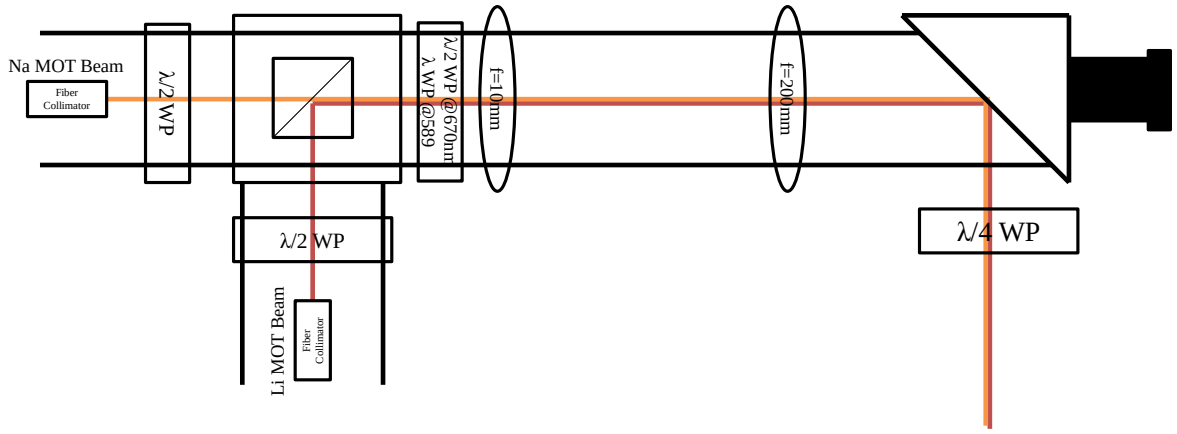

(a) MOT towers for side beams.

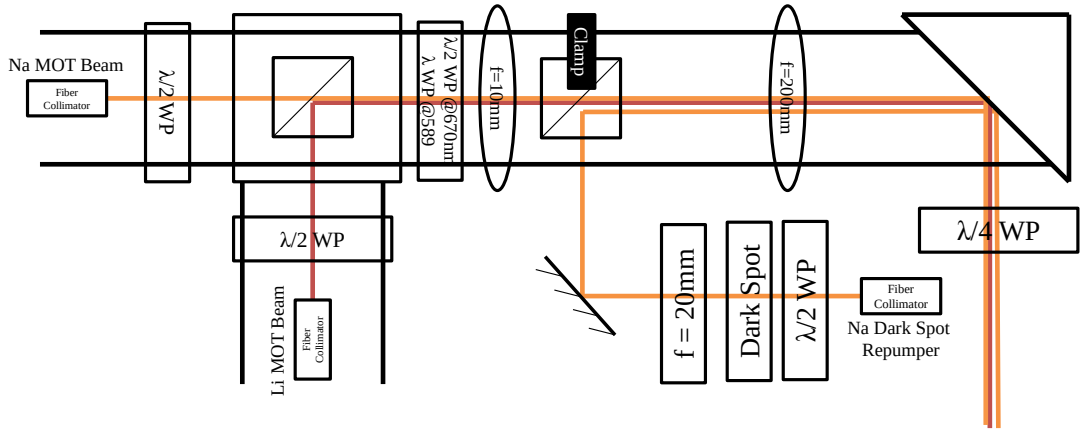

(b) MOT tower for downwards beam with ^{23}Na dark spot repumper.

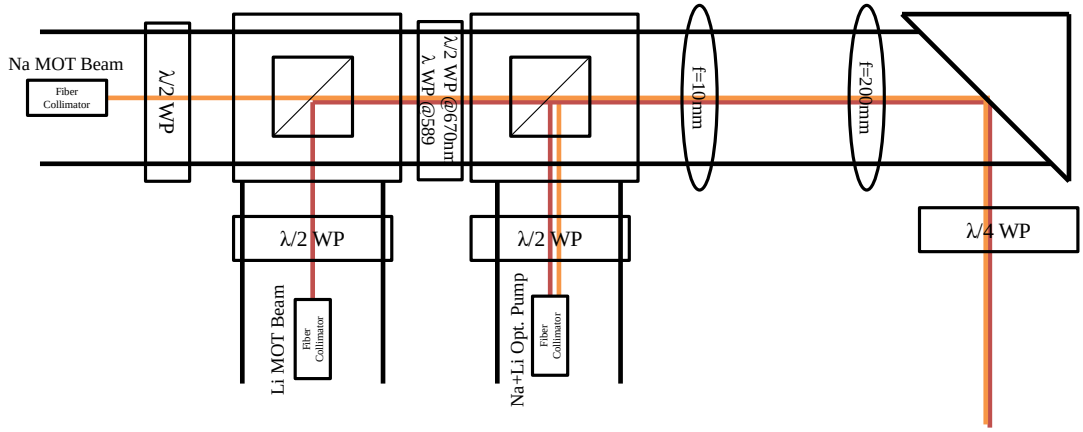

(c) MOT tower for upwards beam with optical pumping.

Figure 4.6: Diagrams of the 3 variations of MOT towers used in the experiment. These towers were custom made by Radiant Dyes using their cage system mounts. **Fig. 4.6a** shows the standard MOT tower that provides the 4 side beams for the MOT. It combines ^{23}Na and ^{6}Li MOT light on a PBS, rotates the polarization of the ^{6}Li light (without affecting the ^{23}Na light) using a dichroic waveplate, expands the beam and then rotates to the correct circular polarization for the MOT. The tower is mounted vertically to maximize available space on the breadboards. **Fig. 4.6b** is identical to the standard tower design but with an additional PBS for combining the ^{23}Na dark spot repumper beam. **Fig. 4.6c** is identical to the standard tower design but with an additional PBS to combine the ^{23}Na and ^{6}Li optical pumping beams, which are used before loading into the magnetic trap (see Section 4.4). The collimators used are Schaefter Kirchoff 60FC-F-4 (A11-02 for ^{23}Na MOT and dark spot repumper beams and A6.2-02 for ^{6}Li MOT beams and optical pumping). The $\frac{\lambda}{2}$ waveplates are CASIX zeroth order 633 nm. The dichroic waveplates are CASIX zeroth order $\frac{\lambda}{2}$ 670 nm, λ 589 nm. PBSs are Altechna 589 nm+670 nm optically contacted.

the fluorescence signal of the MOT and the expansion of the cloud during molasses. The powers of the beams were balanced using a 1 cm square photodiode with several different sized apertures.

100 ms before the end of the MOT phase, the atomic shutter and the Zeeman slower beam shutter are closed. Then the Zeeman slower coils and the necessary compensation coil are linearly ramped to 0 A. In order to perform molasses of ^{23}Na, and later the gray molasses of ^{6}Li, it was important to ensure the background fields were accurately zeroed with the compensation coils (see Fig. 4.5). An additional compensation coil is used to prevent a sudden movement of the atoms as the magnetic field of the Zeeman slower was turned off. Initially two Raspberry Pi cameras provided a live-stream video of the MOT. This was very helpful in the initial alignment and coarse canceling of the magnetic fields. Eventually, to accurately calculate the temperature during molasses, two Basler CMOS acA1300-60gm cameras were set up, which could be triggered during the sequence. The method below describes the routine for canceling the magnetic fields in the position of the MOT very accurately. The fluorescence from the ^{23}Na and ^{6}Li MOTs were focused onto photodiodes to provide a continuous signal of the MOT loading from which an estimate of the MOT numbers and loading times could be made (see Fig. 4.7). The final adjustment of the alignment and compensation fields can be made by seeing the effect of small changes in the B-field to the temperature after molasses. The detuning and power of the MOT beams were finally optimized to maximize the atom number in the magnetic trap. A picture of the ^{23}Na ^{6}Li MOT is shown in Fig. 4.8.

MOT B-field zeroing routine:

- Balance/align all MOT beams as well as possible.
- Take a fluorescence image at high MOT current to find the true zero field point of MOT coils (Image_0). Alternatively, take a fluorescence image in the initial magnetic trap that uses the MOT coils at high current.
- Take fluorescence image at the end of the power supply ramp downs just before molasses begins. This should give an accurate position for MOT field zero + compensation fields (Image_1).
- Use the compensation fields in x', y' and z directions to move the atoms after ramping down the Zeeman slower to the MOT field zero position from Image_0.
- Look at the image before the Zeeman slower ramp down (Image_2). If the position is different from Image_1 use the Zeeman slower x compensation coil to move the

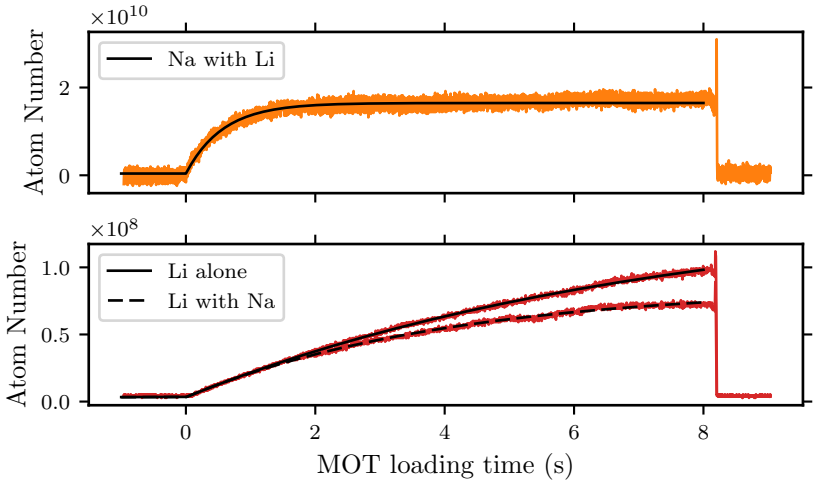

Figure 4.7: MOT loading times for ^{23}Na and ^{6}Li. The fluorescence from the ^{23}Na and ^{6}Li MOTs are collected by a 5 cm diameter lens. A dichroic mirror is used to separate the ^{23}Na and ^{6}Li fluorescence onto different photodiodes, which are each also covered with an appropriate bandpass filter to minimize the signal from stray light. Given the collection angle of light and the known conversions for the photodiode, this fluorescence voltage can be converted into an atom number and monitored to show the loading rate of the respective MOTs. By fitting an exponential function, $B + A(1 - e^{-t/\tau})$, a loading time τ can be quantified. The loading time for ^{23}Na is $\tau = 570$ ms. The ^{23}Na MOT is barely affected by the presence of the ^{6}Li MOT, reducing the ^{23}Na MOT number by approximately 5 % in the long time limit. This is expected as there are far fewer ^{6}Li atoms than ^{23}Na atoms. The ^{6}Li MOT, however, is noticeably affected by the presence of the ^{23}Na MOT which increases the loading time from 4.05 s to 7.30 s and reduces the final MOT number by 45 %. Note that the signal for ^{23}Na is really the dark-spot MOT fluorescence signal and hence may not be an accurate measure of the real atom number. The atom number axis for ^{23}Na is calibrated by using fluorescence imaging during the bright-molasses stage.

position of Image_2 to $\text{Image}_1 = \text{Image}_0$. Note that this does not correct the smaller shift in the z direction.

- Iterate as required.

4.2.1 Compressed MOT of ^{6}Li

Since both the ^{23}Na and ^{6}Li atoms in the MOT need to be loaded into the same magnetic trap directly, the clouds should have a similar size and temperature to maximize the transfer. However, these quantities are quite different for ^{23}Na and ^{6}Li. The temperature of the ^{23}Na atoms after molasses is 200 µK, slightly lower than the Doppler limit of 240 µK. The ^{6}Li atoms after the MOT have a temperature of around 700 µK to 800 µK, which is much higher than the Doppler limit. Additionally, the lower mass of ^{6}Li means the atoms will expand further in the same time, causing the size of the clouds to differ further for the transfer to the magnetic trap.

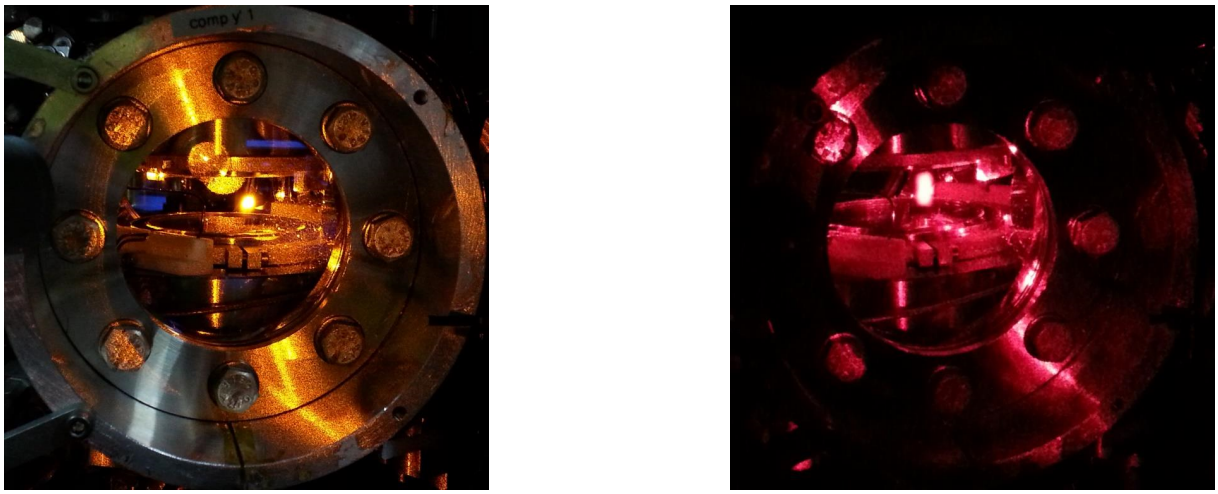

(a) ^{23}Na **(b)** ^{6}Li

Figure 4.8: Images of the dual species ^{23}Na ^{6}Li MOT.

Several research groups have used a *compressed*-MOT (cMOT) technique to improve the ^{6}Li temperature and size-matching for transfer to the magnetic trap [142–144]. A cMOT involves ramping the B-field gradient, and the detuning and power of the MOT beams in order to increase the phase space density. The cMOT was added to the experiment after magnetic transport/trapping had already been implemented, meaning the ^{6}Li atom number in the final magnetic trap could be used as an ideal parameter for optimization. The cMOT is implemented at the end of the MOT phase when the atomic shutter is closed and the Zeeman slower coils are ramping down. Over some cMOT ramp time the MOT gradient, detuning and power of the MOT beams are change simultaneously and then held constant for some cMOT hold time. The initial parameters used were taken from [143]. The change of the beam power was implemented by using the analog control of current to the tapered amplifier and the detuning by using the analog input of the VCO for the spectroscopy AOM (see Section 3.3.2). The cMOT led to a factor three gain in the ^{6}Li atom number in the magnetic trap after transport. The tabulated optimal parameters are shown in Table 4.2.

Table 4.2: Optimized parameters for the ^{6}Li cMOT.

Parameter	value MOT	value cMOT	Unit
cMOT ramp time	—	25	ms
cMOT hold time	—	1	ms
MOT beam power	18 3.7	0.24 0.05	mW I/I_{sat}
MOT beam detuning	25.9 4.4	16.7 2.8	MHz Γ
B-field gradient cMOT	13	13	$\mathrm{G\,cm^{-1}}$

4.3 Optical Molasses

At the end of the MOT stage, the Zeeman slower and compensation coils are ramped to 0 A over 100 ms whilst the MOT coils and beams remain on. At this point the MOT coils are rapidly switched off by a MOSFET (Section 3.4.7), while the MOT beams can remain on for several milliseconds. This technique known as optical molasses allows the clouds to be cooled to the Doppler temperature or, in certain cases where the MOT beams interfere to give a spatially varying polarization, considerably below the Doppler limit [145, 146]. The experiment currently implements a 2 ms optical molasses phase only for ^{23}Na, with the ^{6}Li MOT beams kept off. It was found that the ^{6}Li temperature after the cMOT was not improved by molasses and using too high a power actually heated the cloud. Increasing the length of molasses beyond 2 ms did decrease the temperature of the ^{23}Na cloud further, however, the rapid expansion of the ^{6}Li cloud meant this was kept short in order to maximize ^{6}Li transfer to the magnetic trap. After 10 ms of molasses, a temperature of 180 µK for ^{23}Na was achieved[1], below the Doppler temperature of 240 µK but higher than some other groups have reported (e.g. 100 µK [147]). This is attributed to the fact that the MOT beams are not detuned during the molasses phase in our experiment. Although a dark-spot MOT is used, during the molasses phase the repumper in the MOT beams is suddenly switched on in order to help optically pump the ^{23}Na atoms to the correct states for the magnetic trap. How sub-Doppler cooling functions when transitioning from a dark-spot MOT is not obvious and may explain the higher temperature observed.

As mentioned in Section 4.2, the images of the expanding cloud during and after molasses

[1] compared to 450 µK with no molasses.

provides an excellent diagnostic tool for the alignment of the MOT beams and precise zeroing of the bias fields. If the cloud is pushed in one direction, the beam power or bias field can be corrected depending on which is thought to be more accurately balanced. By looking for small shifts in the cloud after long expansion times, very symmetric expansions can be made. One can also minimize the temperature after a fixed expansion time, while varying the bias fields, in order to find the optimal values. A twisted or distorted cloud during the molasses can often be caused by beam misalignment or a non-uniform intensity profile.

4.3.1 Gray Molasses of ^{6}Li without Changing Optics

The ^{6}Li cloud is not significantly cooled by optical molasses and the larger ^{23}Na atom number means the ^{6}Li cloud thermalizes to the lower temperature of the ^{23}Na bath. For experiments that work solely with ^{6}Li, this high temperature after the MOT makes it difficult to load large clouds into magnetic or dipole traps. Several groups used ultraviolet MOTs for ^{6}Li where lower Doppler limits led to cooler temperatures after the MOT [148, 149]. More recently, the technique of D_1 gray molasses[1] has been applied to ^{6}Li [150–153], achieving temperatures of $< 50\,\mu$K. This has allowed groups to perform all optical preparation of degenerate ^{6}Li clouds [154,155], where the cloud after gray molasses is immediately loaded into a deep dipole trap. With such low temperatures reported, we decided to implement gray molasses in the experiment with the challenging constraint that we did not have space to mount additional optics on the experiment table. A third ^{6}Li laser was added with a 10 GHz offset lock relative to the first laser to bring the frequency to the D_1 line. By coupling the normal MOT and gray molasses light through the same AOM it was possible to rapidly switch between them (see Section 3.3.2 for details). Once the laser was setup, the D_1 transitions were identified by scanning the frequency of the offset lock and measuring the atom loss during a 2 ms pulse of the gray molasses light. After identifying the transitions, the gray molasses light could be detuned to the values optimized in [152] and the expansion of the cloud with and without gray molasses could be measured (without ^{23}Na present) as shown in Fig. 4.9. While the reduction in temperature from 390 µK with no molasses to 45 µK with gray molasses is significant, there is a noticeable loss in atom number (approximately a factor of three) during the gray molasses. The gray molasses cools the ^{6}Li cloud to temperatures lower than the ^{23}Na cloud, however, the ^{23}Na atom number is approximately a factor 100 larger

[1] Gray molasses is based on velocity-selective coherent population trapping in a three-level system. See [150–153] for details.

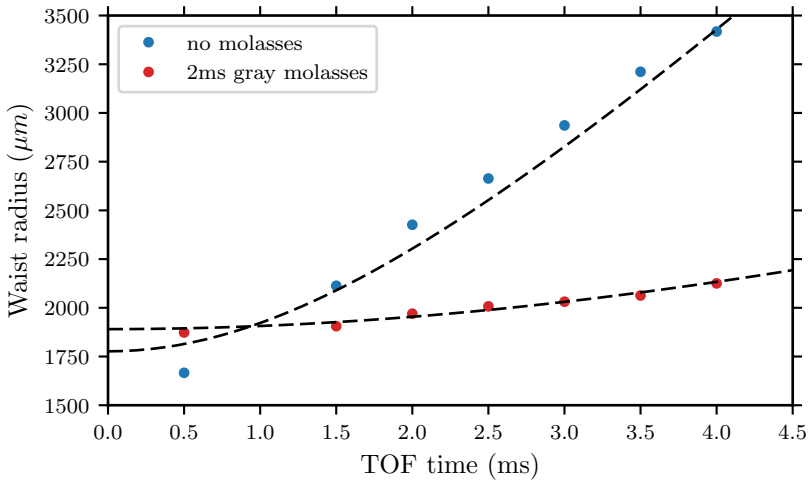

Figure 4.9: Expansion of the ^{6}Li cloud after gray molasses (red) compared to the expansion of the cloud with no molasses (blue). The y-axis shows the waist radius of the fitted 2 dimensional Gaussian (σ) and the x-axis is the expansion time, t. Assuming the cloud expands as $\sigma = \sqrt{{\sigma_0}^2 + (k_B T/m)t^2}$ (where σ_0 is the initial waist radius, T is temperature and m is the ^{6}Li atomic mass), a fit can be performed to determine the σ_0 and T. These fits, shown by the black dashed lines, give temperatures of 45 µK and 390 µK with and without gray molasses, respectively.

than the ^{6}Li number in the MOT. This means that once the atoms are in the initial magnetic trap, the ^{6}Li cloud rapidly thermalizes to the temperature of the much larger ^{23}Na bath, whilst the ^{6}Li temperature has a negligible effect on the ^{23}Na. Hence, it was observed that once ^{23}Na was re-introduced, the temperature of the ^{6}Li atoms in the magnetic trap was the same with and without gray molasses, but with a smaller atom number. As a result, the gray molasses phase is no longer implemented in the experiment sequence.

Even though the gray molasses is no longer used in the experiment sequence, it should be noted that this implementation requires no modification to the MOT optics and hence may be relevant for other experiments that wish to implement gray molasses but did not plan for it in the initial design. Furthermore, if in the future the experiment is operated with ^{6}Li only, the gray molasses can be used to reach a suitable temperature for direct loading into a high power dipole trap such as in [155]. Gray molasses of ^{23}Na has recently been achieved in [156], which is relevant for future improvements to the experiment.

4.4 Optical Pumping

After the MOT and additional molasses cooling stage, the atoms need to be loaded into a magnetic trap. Since only low field seeking states (see Section 5.1) can be magnetically trapped, the hyperfine state of the atoms must be correctly chosen. One of the first BECs was created in the $|F = 1, m_F = -1\rangle$ state of ^{23}Na [157] and the current largest BEC produced, with over 1×10^8 atoms[1], was also created in this state [159]. The first attempts using the $|F = 1, m_F = -1\rangle$ state of ^{23}Na with ^{6}Li in the $|F = 3/2, m_F = 3/2\rangle$ state showed that, while it was possible to cool the mixture, there were strong losses associated with spin-exchange collisions. Spin-exchange collisions preserve the total angular momentum but result in a change of the hyperfine state of the atoms, which can lead to the production of untrappable states or excess kinetic energy[2]. However, if one works in the maximally stretched states of $|F = 2, m_F = 2\rangle$ for ^{23}Na and $|F = 3/2, m_F = 3/2\rangle$ for ^{6}Li, spin-exchange collisions between ^{23}Na and ^{6}Li are forbidden[3]. Hence, after the molasses stage, both species must be simultaneously optically pumped to the stretched hyperfine states.

To perform this a repumper beam ($|F = 1\rangle \rightarrow |F' = 2\rangle$ for ^{23}Na and $|F = 1/2\rangle \rightarrow |F' = 3/2\rangle$ for ^{6}Li) and pumping beam ($|F = 2\rangle \rightarrow |F' = 2\rangle$ for ^{23}Na and $|F = 3/2\rangle \rightarrow |F' = 3/2\rangle$ for ^{6}Li) are prepared in the laser systems. The ^{23}Na and ^{6}Li repumper and pumping beams are coupled into the same fiber and brought to the experiment chamber where the bottom MOT tower sends the beam vertically through the chamber with σ^+ polarization. The polarization is critical for pumping the correct m_F states. To distinguish the different m_F levels, a bias field is applied across the cloud in the z-direction (using ML coil and MOSFET Box 2, see Section 3.4.7). Using a MOSFET allows the B-field to be ramped to 2.6 G in 250 µs and remain approximately uniform over the 1 ms duration of the optical pumping pulse. Whilst the field is turned on rapidly, it is allowed to turn off slowly, decaying over approximately 5 ms. This decay means there is always a well defined quantization axis for the different m_F states.

After a quick and unoptimized implementation of the optical pumping, the magnetic transport was implemented, giving a signal of the $|F = 2, m_F = 2\rangle$ ^{23}Na atoms in the final

[1] A larger BEC has been created with hydrogen using cryogenic techniques where they achieve 1×10^9 atoms [158].

[2] It should also be noted that the spin-exchange loss rate for ^{6}Li is much higher than for ^{23}Na and hence additional spin states of ^{6}Li are more detrimental [160].

[3] spin exchange collisions are also forbidden in the $|F = 1, m_F = -1\rangle$ and $|F = 1/2, m_F = -1/2\rangle$ states but the $|F = 1/2, mF = -1/2\rangle$ is only low field seeking at very low fields, making it unsuitable for magnetic trapping.

Table 4.3: Table of the optical pumping parameters used in the optimized experiment.

	repumper detuning (Γ)	pumping detuning (Γ)	repumper intensity (I/I_{sat})	pumping intensity (I/I_{sat})	pulse length (ms)	B-field G
^{23}Na	-2.2	-1.3	0.1	0.02	1	2.6
^{6}Li	-9	-9	0.54	0.25		

magnetic trap. This signal was then used for the optimization of the optical pumping parameters, which are tabulated in Table 4.3. While it was easy to distinguish between the different F states, distinguishing the different m_F (e.g. $|F = 2, m_F = 1\rangle$) was not implemented. It was found that increasing the length of the optical pumping pulse beyond 1 ms gave no significant increase in the final atom number. The pumping beam for ^{23}Na gives a 30 % enhancement to the final ^{23}Na number in the magnetic trap, which implies that the majority of the optical pumping is performed by the repumper beam. Whilst the intensity of the pumping ($2 \rightarrow 2$) beam is reduced from its maximum, the atom number continues to increase with increasing repumper ($1 \rightarrow 2$) and increasing this power could lead to further improvement.

During the optical pumping stage it is critical that the MOT and Zeeman slower light is completely blocked from the atoms. The ^{23}Na MOT light can be turned off with an AOM and beam shutter, however, the ^{6}Li MOT light only has a beam shutter. If the MOT light is present concurrently with the optical pumping bias field, the cloud will be cooled into a moving frame, leading to heating. Similarly, resonant light in the magnetic trap can lead to heating that becomes very significant at low temperatures. It should be stressed how important it is to use shutters and regularly check their timings. Additionally, photodiodes should be setup on back-reflections or transmissions from important beams to give a signal of the power in the experiment chamber. These photodiodes were crucial in resolving shutter timing issues in the experiment[1].

[1]For several weeks we had a factor of 10 reduction in the atom number of the ^{6}Li which was caused by the MOT shutter closing too late, leading to MOT light during the optical pumping phase.

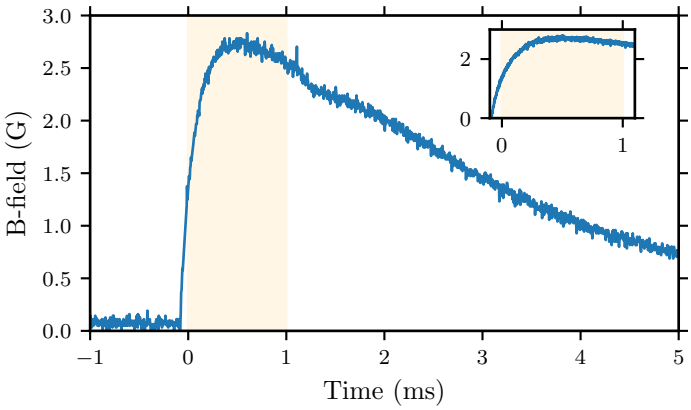

Figure 4.10: B-Field during the optical pumping phase. The B-field is created by the ML coil and is turned on rapidly (250 ms) by using MOSFET Box 2. The orange shaded region represents the time period over which we do optical pumping. The field is relatively uniform over this time and then decays exponentially to zero over several milliseconds. The inset plot shows the same data but zoomed on the region where optical pumping is performed. The field is measured with an amp clamp and using the current to Gauss conversion. The residual field that persists after the optical pumping is required to ensure that the different m_F are not degenerate.

4.5 Summary of the Experimental Sequence

This section has described how the ^{23}Na and ^{6}Li atoms leaving from the hot oven are slowed by the Zeeman slower to a speed where they can be capture by a MOT. The ^{23}Na atoms are loaded into a dark-spot MOT to allow for much higher densities of ^{23}Na atoms. As the atomic shutter is closed and the Zeeman slower ramped down, a cMOT stage for ^{6}Li is performed and, immediately after, we perform optical molasses for 2 ms on ^{23}Na while leaving ^{6}Li to expand. A bias field is rapidly applied to provide a quantization axis for different $|m_F\rangle$ states and then optical pumping is performed to bring the ^{23}Na and ^{6}Li atoms to the magnetically trappable stretched states $|F = 2, m_F = 2\rangle$ and $|F = 3/2, m_F = 3/2\rangle$, respectively. How the atoms are transferred into the magnetic trap, transported and then cooled to degeneracy will be the subject of Chapter 5. The laser experiment sequence up to optical molasses is shown below in Fig. 4.11.

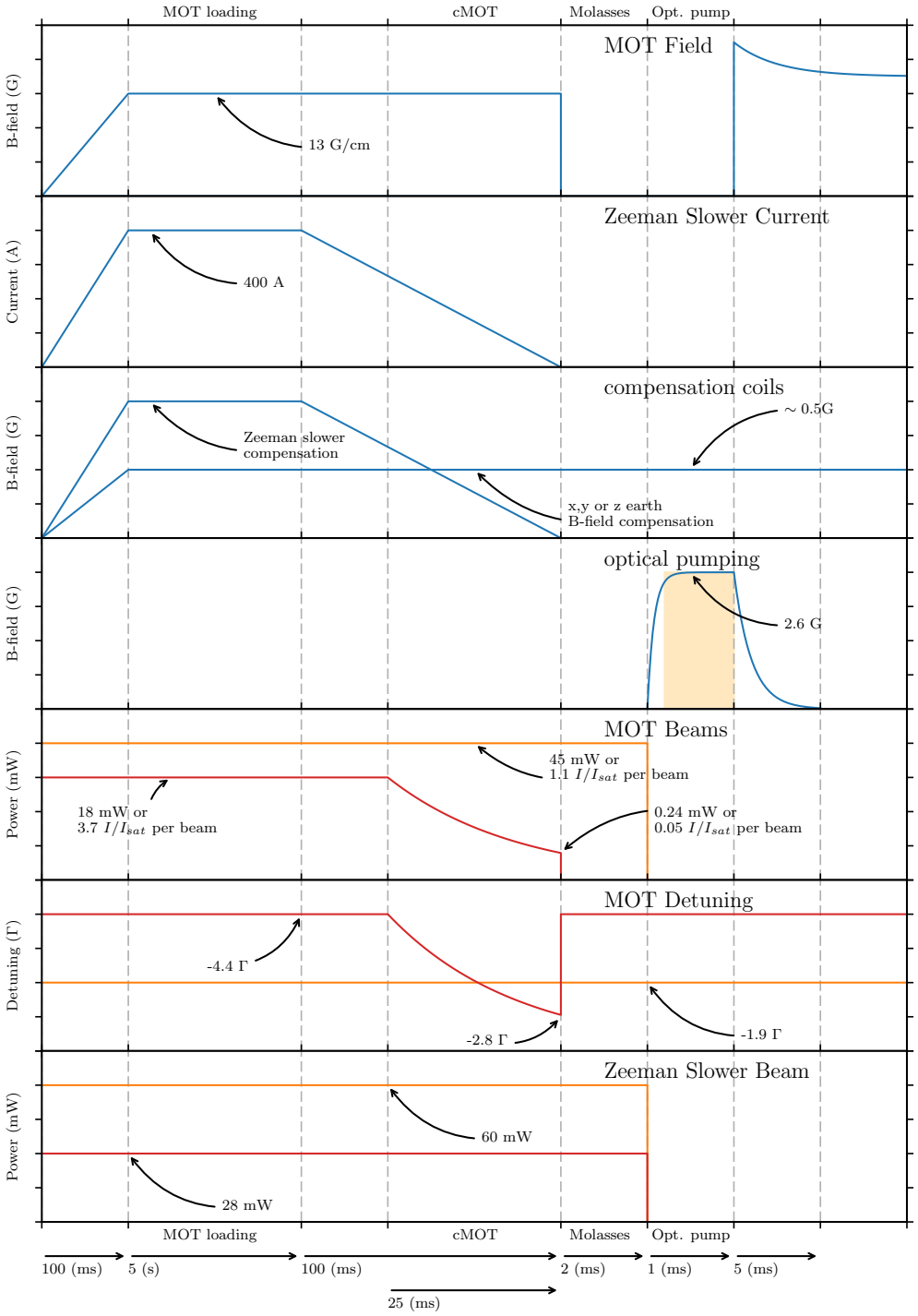

Figure 4.11: Summary of the experiment sequence from the start until optical pumping. Blue lines show the current or B-field in various coils. Orange and red lines show properties of the ^{23}Na and ^{6}Li beams, respectively. The time axis is non-linear to highlight all the events clearly and the time lengths are annotated on the bottom x-axis. The shaded region in the optical pumping graph shows the optical pumping light pulse.

Chapter 5

From Magnetic Transport to a Degenerate Gas

5.1 Magnetic Traps

5.1.1 Introduction

Magnetic traps take advantage of the finite magnetic moment of certain atomic hyperfine states. In the weak field limit the energy shift of an atom in the state $|F, m_F>$ due to the Zeeman effect is: $V = g_F m_F \mu_B |B|$. The energy thus only depends on the magnitude of the magnetic field $|B|$ and the quantum numbers which define g_F and m_F. By creating a spatially dependent B-field, a spatially dependent confining potential can be made. Such a B-field can be produced by coils in the anti-Helmholtz configuration. This produces a quadrupole B-field, as discussed in Section 3.4.1, which in the central region between the two coils can be approximated as:

$$\mathbf{B}_{\text{anti-Helmholtz}} = B' \begin{pmatrix} -x \\ -y \\ 2z \end{pmatrix} + \mathcal{O}(\mathbf{r}^3) \tag{5.1}$$

It is possible to create a confining or anti-confining potential depending on the sign of $m_F g_F$. A hyperfine state is called low field seeking if $m_F g_F > 0$ and high field seeking if $m_F g_F < 0$. Whilst this is valid in the low field limit, at higher fields F, m_F are no longer good quantum numbers and one must, more generally, look at the Breit-Rabi diagram (Appendix A) to see if a state is high or low field seeking by looking at the gradient of

the energy shift at a specific field. Even with the large gradient quadrupole coils used ($115\,\mathrm{G\,cm^{-1}}$) in this experiment, the small size of the cloud in the magnetic trap means the low field limit is always applicable. When designing or choosing the parameters of a quadrupole magnetic trap, there are three main properties to consider: the trap gradient B', the trap size and the trap depth.

5.1.2 Trap Gradient B'

The trap gradient, B', defines several thermodynamic properties of the trapped cloud and when it is changed sufficiently slowly, this adiabatic (de)compression changes these thermodynamic properties of the cloud. How the temperature T, density n, and collision rate $f_{\mathrm{collision}}$, scale with adiabatic changes to the trapping potential can be derived and the results are given below (Equations (5.2) to (5.10)) for a d dimensional potential of the form $U(r) \propto r^{\frac{d}{\delta}}$. The derivations and a detailed discussion can be found in [161,162].

$$T \propto \left(\frac{B'_{final}}{B'_{initial}}\right)^{\frac{2\delta}{2\delta+3}} \tag{5.2}$$

$$n \propto \left(\frac{B'_{final}}{B'_{initial}}\right)^{\frac{3\delta}{2\delta+3}} \tag{5.3}$$

$$f_{\mathrm{collision}} \propto \left(\frac{B'_{final}}{B'_{initial}}\right)^{\frac{4\delta}{2\delta+3}} \tag{5.4}$$

For the 3 dimensional quadrupole traps used in this experiment this simplifies to ($\delta = d = 3$):

$$T \propto \left(\frac{B'_{final}}{B'_{initial}}\right)^{\frac{2}{3}} \tag{5.5}$$

$$n \propto \left(\frac{B'_{final}}{B'_{initial}}\right) \tag{5.6}$$

$$f_{\mathrm{collision}} \propto \left(\frac{B'_{final}}{B'_{initial}}\right)^{\frac{4}{3}} \tag{5.7}$$

And for 3 dimensional harmonic traps (which are created by other magnetic trap configurations such as the Ioffe-Pritchard trap and dipole traps) ($\delta = 3/2, d = 3$):

$$T \propto \left(\frac{B'_{final}}{B'_{initial}}\right)^{\frac{1}{2}} \tag{5.8}$$

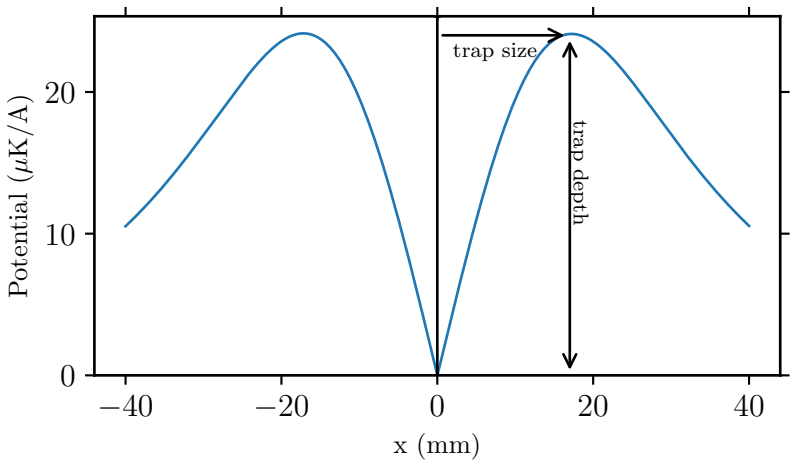

Figure 5.1: Potential of the magnetic trap formed by the MOT coils. This diagram shows the trap size and trap depth defined by the magnetic trap.

$$n \propto \left(\frac{B'_{final}}{B'_{initial}}\right)^{\frac{3}{4}} \tag{5.9}$$

$$f_{\text{collision}} \propto \left(\frac{B'_{final}}{B'_{initial}}\right) \tag{5.10}$$

5.1.3 Trap Size and Trap Depth

From Eq. (5.1) one might predict that the magnetic trap confines particles at any radius from the trap center, assuming that the quantum state remains low field seeking. However, at distances comparable to the coil radius, the $O(\mathbf{r}^3)$ term becomes significant and the field gradient changes sign ($\mathrm{d}B/\mathrm{d}x = 0$). At distance larger than the trap size the magnetic trap is no longer confining. For typical traps with coils with a large radius the trap size is much larger than the typical size of the atomic cloud. However, when catching the atomic cloud after optical pumping in the small radius MOT coils, the trap size must be taken into account for the transfer and also during transport. For a magnetic trap, the trap depth can be defined as the potential value (usually expressed in µK) at the position of the trap size.

5.2 Transfer from the MOT to the Magnetic Trap

After optically pumping the ^{23}Na and ^{6}Li atoms to the stretched $|2, 2\rangle$ and $|3/2, 3/2\rangle$ states respectively, the MOT coils are turned back on and used for the initial magnetic trap. The Lambda 400 A 25 V power supply, earlier used for the big Zeeman slower, can create a maximum B' of 125 G cm^{-1} with the MOT coils. Initially, however, the coils are turned on at a much lower current such that the characteristic size of the trapped cloud matches the size after the molasses and optical pumping. This should maximize the transfer and minimize heating. The matching is optimized for ^{23}Na and cannot be optimized for the size of ^{6}Li simultaneously. This is still satisfactory as the much large ^{23}Na number means the ^{6}Li cloud will rapidly thermalize with the ^{23}Na. The characteristic turn-on time of the power supply is of the order of 10 ms, much slower than the time scales seen by the atoms in the magnetic trap. By briefly setting the power supply to a fixed voltage with the IGBT still open, the capacitors in the power supply are charged. When the IGBT is closed they are discharged, meaning the trap can be turned on in less than 100 µs.

After molasses and optical pumping, the Gaussian waist radius of the ^{23}Na atom cloud is approximately 1.5 mm. By calculating the $1/r$ characteristic size of a gas in a linear quadrupole trap, the approximate initial B' can be chosen for a known temperature. Using this method, as shown in Fig. 5.2, a value of approximately 25 G cm^{-1} was calculated, slightly lower than the 35 G cm^{-1} value optimized by later maximizing the number of atoms in the final magnetic trap after transport.

After catching the initial atom cloud B' is adiabatically compressed to 125 G cm^{-1} in 150 ms to maximize the trap depth and confinement for magnetic transport. The trap size of the initial magnetic trap is defined by the radius of the MOT coils and the B-field simulations give a trap size of 17 mm, corresponding to a trap depth of 7.5 mK.

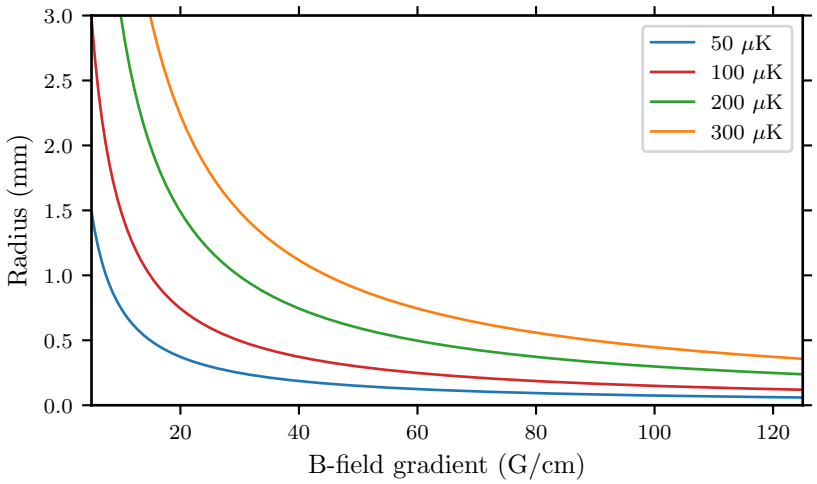

Figure 5.2: A classical non-interacting atom cloud in a linear magnetic trap has a density distribution $n(r) \propto \exp(-V(r)/k_B T) = A\exp(-r/r_0)$ where r_0 is the $1/r$ in trap radius of the cloud. This figure shows how this characteristic length scale depends on the magnetic trap gradient and the temperature of the cloud. The initial gradient is optimized to match the cloud size and temperature after optical molasses and optical pumping. The radius after molasses is around 1.5 mm, which for the 200 µK temperature corresponds to a gradient of around $25\,\mathrm{G\,cm^{-1}}$.

5.3 Magnetic Transport

5.3.1 Requirements

The position of the MOT is 2 cm away from the exit of the small Zeeman slower. This short distance allows for a large flux of slow ^{23}Na and ^{6}Li atoms at the position of the MOT. There are several reasons why this is not a desirable final position for the atoms:

- The final position of the atoms should not be in direct line of sight of the oven.
- The final position needs to be centered on the Feshbach coils which only have a highly uniform field about center position.
- The final position of the atoms should be displaced towards the top UKEA viewport so that high resolution imaging is possible.
- The MOT coils are not suitable for continuously creating a large enough gradient for efficient microwave evaporation of ^{23}Na.

For these reasons, after loading a large dual species MOT of ^{23}Na and ^{6}Li, both species are magnetically transported over 30 mm to the final position, which is 3 mm below the UKEA viewport in the center of the main Kimball chamber.

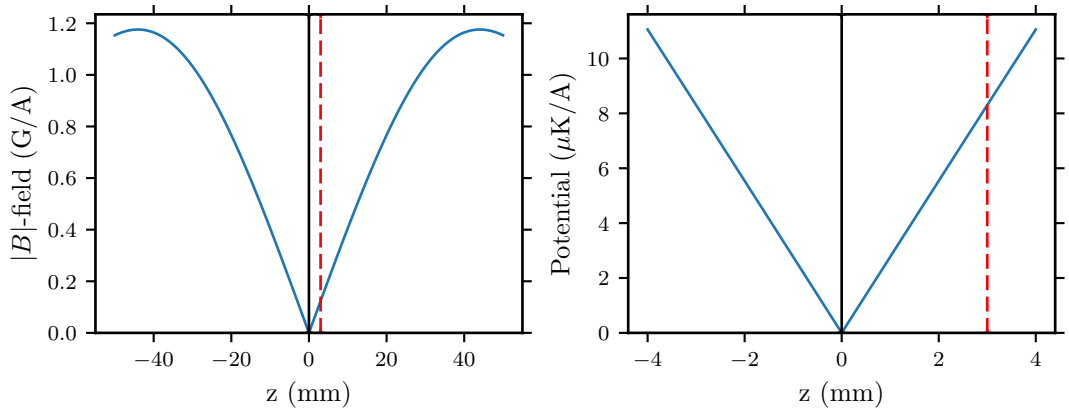

Figure 5.3: This figure shows the potential produced by the final magnetic trap in which ^{23}Na evaporation is performed. The left plot shows that the trap depth defined by the trap size is very large due to the large radius of the coils. The dashed red line shows the position of the vacuum chamber window which defines the trap depth and size experienced by the atoms. The vacuum window is 3 mm from the center of the magnetic trap. These coils produce a gradient of $0.205\,\mathrm{G\,cm^{-1}\,A^{-1}}$ in the x, y plane. During the magnetic transport and evaporation we apply a gradient of $110\,\mathrm{G\,cm^{-1}}$ (531 A) which produces a trap with a depth of 4.4 mK.

The final magnetic trap is created from the same coils used to create the Feshbach fields. They are switched from anti-Helmholtz to Helmholtz configuration using an H-bridge. These coils are capable of creating gradients of $125\,\mathrm{G\,cm^{-1}}$ (running at 600 A). These coils have a large radius and trap the atoms 3 mm below the UKEA window. Hence, for the final magnetic trap, the trap size is defined by the position of the vacuum window at 3 mm (once the atoms touch the window they do not re-enter the trap). This corresponds to a trap depth of 4.4 mK as shown in Fig. 5.3.

5.3.2 Magnetic Transport

The purpose of the magnetic transport is to displace the atomic cloud by 30 mm in the x direction and 8.5 mm in the z direction whilst minimizing heating and atom loss (see Fig. 3.8). To prevent heating, B' must be maintained throughout the transport procedure and to minimize losses the trap depth must remain sufficiently high. In a transport procedure with many coils, many currents can be changed in order to achieve these requirements. In this setup the transport between two locations is defined by two anti-Helmholtz coils, which greatly simplifies the analysis. Using the equations for two displaced ideal quadrupole coils, a simple characterization of the magnetic transport is derived. Later the results from the numerical simulations are shown which include the true potential created by the non-ideal coils. Consider two ideal anti-Helmholtz coils,

coil 1 and coil 2, with current $I_{1,2}$, B-field gradient per unit current $B'_{1,2}$, centered on $\begin{pmatrix} x_{c_{1,2}} & y_{c_{1,2}} & z_{c_{1,2}} \end{pmatrix}$ which produce a field:

$$\mathbf{B}_{1,2} = I_{1,2}B'_{1,2}\begin{pmatrix} -(x - x_{c_{1,2}}) \\ -(y - y_{c_{1,2}}) \\ 2(z - z_{c_{1,2}}) \end{pmatrix} \tag{5.11}$$

together they produced a field:

$$\mathbf{B} = I_1 B'_1 \begin{pmatrix} -(x - x_{c_1}) \\ -(y - y_{c_1}) \\ 2(z - z_{c_1}) \end{pmatrix} + I_2 B'_2 \begin{pmatrix} -(x - x_{c_2}) \\ -(y - y_{c_2}) \\ 2(z - z_{c_2}) \end{pmatrix} \tag{5.12}$$

which, due to the linear nature of the field, can also be written in the form:

$$\mathbf{B} = (I_1 B'_1 + I_2 B'_2) \begin{pmatrix} -(x - \frac{(I_1 B'_1 x_{c_1} + I_2 B'_2 x_{c_2})}{(I_1 B'_1 + I_2 B'_2)}) \\ -(y - \frac{(I_1 B'_1 y_{c_1} + I_2 B'_2 y_{c_2})}{(I_1 B'_1 + I_2 B'_2)}) \\ 2(z - \frac{(I_1 B'_1 z_{c_1} + I_2 B'_2 z_{c_2})}{(I_1 B'_1 + I_2 B'_2)}) \end{pmatrix} \tag{5.13}$$

From Eq. (5.13) one sees that the resultant potential is identical to that of an anti-Helmhotlz coil with gradient $(I_1 B'_1 + I_2 B'_2)$ and a center position which is a current weighted value between the centers of coil 1 and coil 2. Since $B'_{1,2}$ are fixed properties of the coils, the variable parameters for transport are the currents.

For the consideration of the transport $I_{1,2}$ become time dependent. Starting from an initial trap in coil 1 with $I_2(t = 0) = 0$, the ratio $\frac{I_1(t)}{I_2(t)}$ goes from $\frac{I_1(t=0)}{I_2(t=0)} = \infty$ to $\frac{I_1(t=T)}{I_2(t=T)} = 0$ where T is the total transport time. When transporting from coil 1 to coil 2, the initial current in coil 1, I_1^0, is chosen, defining the gradient at which transport occurs. This is usually chosen as the largest current (gradient) that is safe to use with the coil. For the initial attempts of magnetic transport a sine-squared and cosine-square ramp of the currents were used to transport the atoms while attempting to keep the gradient constant as shown in Fig. 5.5.

For the simulations of the real potential minimum and gradient during the transport, the B-field simulations described in Section 3.4.3 were used and the results are shown in Fig. 5.6. The movement is only along the x and z directions as expected with no significant deviation in the y direction. This is in agreement with the ideal behavior predicted in Eq. (5.13). The simulated gradient, however, shows a deviation from the ideal behavior in the region where $I_1 \approx I_2$. At this time, the cloud has been transported

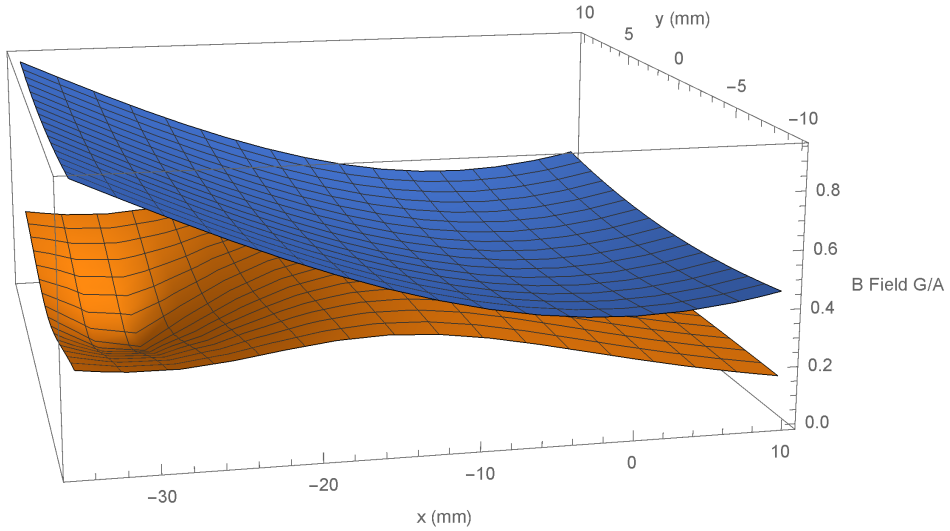

Figure 5.4: These surface plots show the non-ideal simulated anti-Helmholtz field of the MOT coils (initial magnetic trap) in orange and Feshbach coils (final magnetic trap) in blue. In this plot $z = 0$ (i.e. we are in the plane of the initial magnetic trap and MOT). This is why the anti-Helmholtz zero of the final magnetic trap is not visible as it is displaced 8 mm upwards from that of the MOT coils. As the current ratio is changed from the MOT coils to the Feshbach coils, the atoms can follow the potential minimum and are transported. One can clearly see that during the transport we will leave the ideal linear anti-Helmholtz region of the MOT coils where Eq. (5.13) still holds.

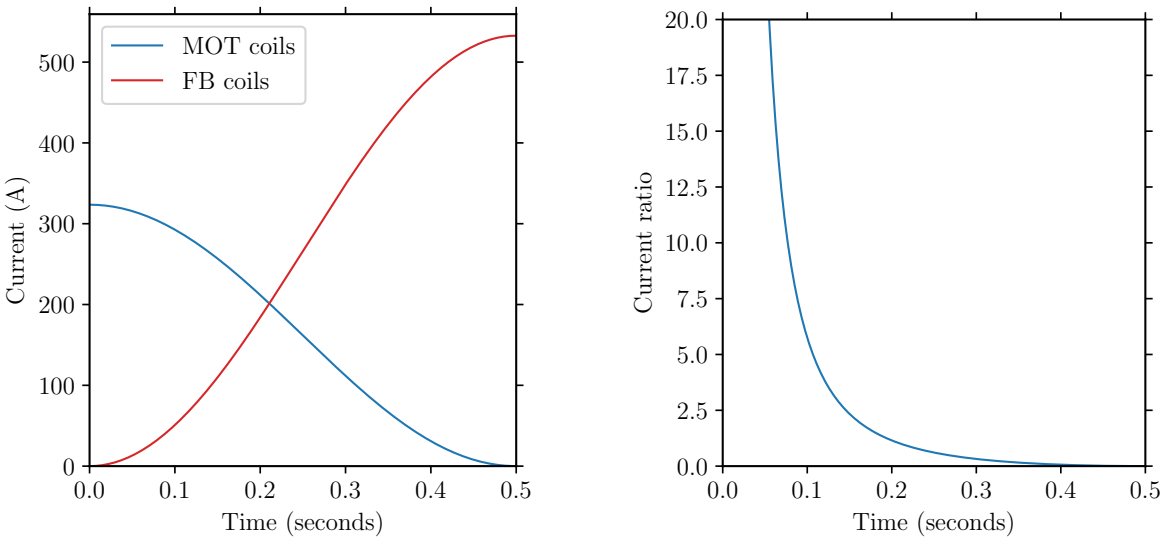

(a) Current against time

(b) Ratio of currents

Figure 5.5: The current ramps used in the experiment for magnetic transport as a function of time. Initially the cloud is in a magnetic trap defined by the MOT coils. During the transport a sine-squared ramp of the current transfers them to a magnetic trap defined by the Feshbach coils. During this ramp the position of the cloud is defined by the current ratio (see Eq. (5.13)) which varies from ∞ to 0.

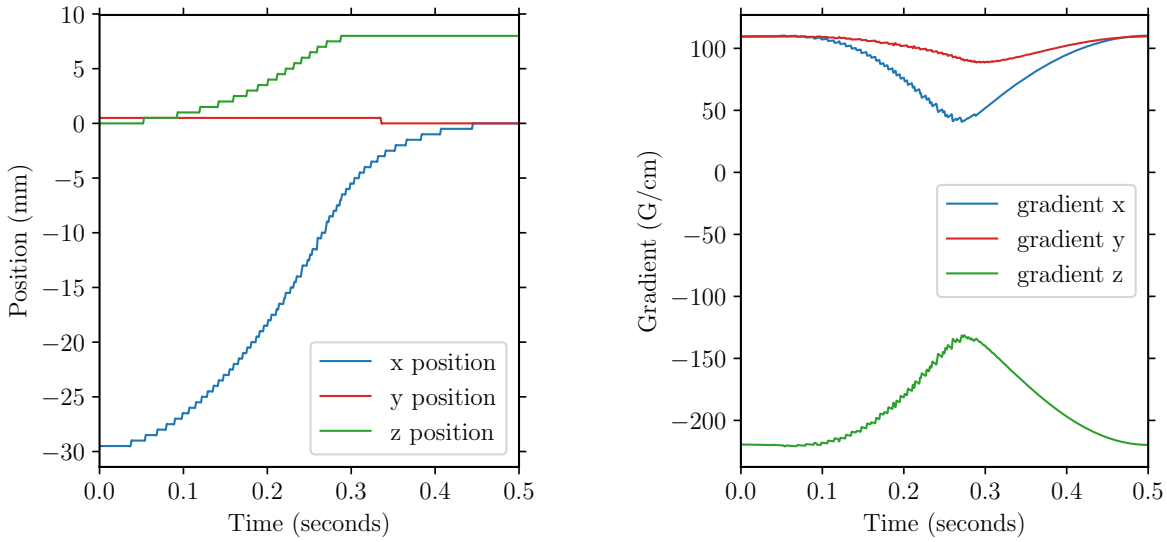

(a) Simulated positions

(b) Simulated gradients

Figure 5.6: The simulated potential minima positions and trap gradients in the x, y and z direction as a function of time. In Fig. 5.6a the positions of the trapped cloud is shown. The cloud moves primarily in the x direction (i.e. in the direction of the Zeeman slower) from the MOT coils to the Feshbach coils. There is additionally a smaller transport in the z direction as the atoms are brought upwards vertically to a position 3 mm below the UKEA viewport. In Fig. 5.6b the simulated values of the real gradients (beyond the linear anti-Helmholtz approximation) are shown. It is clear that the gradient in all directions drops in amplitude approximately at the halfway point of the transport. This is dominated by the MOT coils magnetic field. At a time of $t \approx 0.25$ s the distance traveled is similar or greater than the radius of the coils. This means the approximation used in Eq. (5.13) no longer holds and the deviation from a constant gradient is observed.

by approximately 15 mm, which is larger than the radius of the MOT coils and hence the ideal anti-Helmholtz equation (Eq. (5.1)) no longer holds. The simulated B-field is shown in Fig. 5.4 and the deviation from the ideal anti-Helmholtz behavior causes the gradient during the transport not to remain constant. At longer times, the current in the MOT coils is small and the field is dominated by the Feshbach coils, which have a much larger radius, meaning the gradient returns to the ideal (constant) value. While these changes in gradient and distortion of the trapping potential are not desired, this ramp was implemented and tested in the experiment. It may be beneficial that the cloud is moving fastest through the region where the non-ideal behavior occurs. This implementation transports more than 80 % of the ^{23}Na atoms in the MOT to the final magnetic trap position.

An additional simulation was performed that attempted to keep the x gradient more constant during transport. From Eq. (5.13), the ratio I_1/I_2 defines the trapping position and previously we kept $(I_1 B_1' + I_2 B_2')$ constant to maintain the ideal gradient of the trap. Instead it is possible to vary I_1, I_2 for a fixed ratio, such that the real non-ideal gradient is maximized. The results of the simulation for this transport are shown in Fig. 5.7. This ramp was not implemented in the experiment as the sine-squared was simpler and produced a good transfer efficiency for ^{23}Na, however, it may be useful to see if there is any gain from this improved transport, especially for ^{6}Li, where the transfer efficiency was not so well quantified.

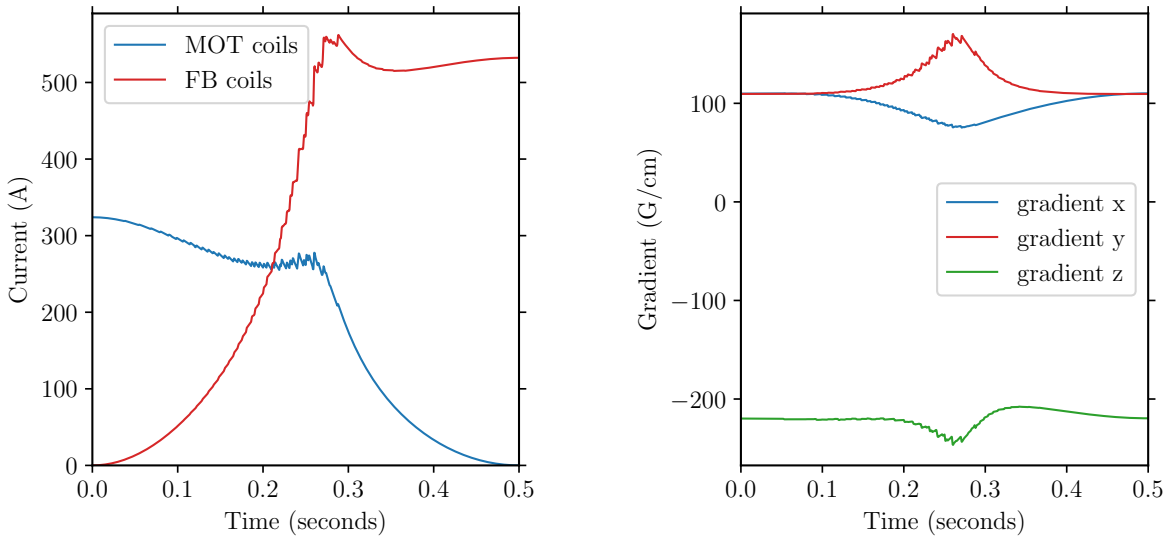

(a) Optimized currents

(b) Simulated gradients

Figure 5.7: The simulated current and trap gradients in the x, y and z direction as a function of time when the currents are scaled to minimize deviations in gradient. Here the currents are scaled numerically so as to minimize the deviations in trap gradient. Note that the current ratio will still vary identically from ∞ to 0 and hence the transport will still follow the same route in space at the same speed (see Fig. 5.6).

5.4 Forced Evaporation in an Optically Plugged Magnetic Trap

After the magnetic transport phase, a mixture of ^{23}Na atoms in the $|2,2\rangle$ state and ^{6}Li atoms in the $|3/2,3/2\rangle$ state are in the final magnetic trap at a gradient of $110\,\mathrm{G\,cm^{-1}}$. It is in this magnetic trap that the ^{23}Na atoms are evaporatively cooled, sympathetically cooling the ^{6}Li atoms. To prevent Majorana losses at the center of the linear magnetic trap, a blue-detuned laser is used as a plug. The theory of this loss mechanism and the implementation of the plug beam is described in Section 5.4.1 and the details of the ^{23}Na evaporation (both with and without ^{6}Li) is described in Section 5.4.2.

5.4.1 Optically Plugged Magnetic Traps

Quadrupole (linear) magnetic traps are advantageous as they provide a large trapping volume and tight confinement (see Eq. (5.7)) compared to harmonic confinement. In addition, they are simply produced with a pair of coils in anti-Helmholtz configuration allowing for greater optical access. The disadvantage of linear traps is that there exists

a region of the trap where the magnetic field is zero which leads to Majorana spin-flip loss [163] and heating. Near this central zero-field region, non-adiabatic spin flips to untrapped states can occur [164, 165]. From a qualitative description one can think of this as a single particle loss rate, as there is a finite probability of these spin flips occuring when an atom crosses the central region of the trap. The lower energy atoms spend a proportionally higher fraction of time near the central region and hence are more likely to be lost. Since lower energy atoms are preferentially lost, Majorana losses have an effective heating rate. In a simple model [164, 166, 167] the loss rate, Γ_{Majorana}, can be derived as:

$$\Gamma_{\text{Majorana}} = \frac{\sqrt[3]{24}\hbar}{32m}\left(\frac{g_F m_F \mu_B B'}{k_B T}\right)^2 \tag{5.14}$$

This loss and heating rate scales as $\Gamma_{\text{Majorana}} \propto (B'/T)^2$. From the scaling laws derived in Eq. (5.5) we know that adiabatic decompression of the trap affects the cloud's temperature and inserting this scaling into Eq. (5.14) shows that a change in B' by a factor $(B'_{\text{final}}/B'_{\text{initial}})$ will change the $\Gamma_{\text{Majorana}} \propto (B'_{\text{final}}/B'_{\text{initial}})^{\frac{2}{3}}$. Hence, decompressing the quadrupole trap reduces the Majorana losses (despite the decrease in temperature) at the expense of a reduced collision rate (Eq. (5.7)), which reduces the evaporation efficiency.

A blue-detuned laser beam focused to the small zero field central region of the quadrupole trap is used to reduce Majorana losses. The AC stark shift from laser light that is blue-detuned with respect to the atomic transitions provides a repulsive potential often called an *optical plug* (this effect will be described in more detail in Section 5.5). An appropriate laser wavelength that is blue-detuned from both ^{23}Na (589 nm) and ^{6}Li (671 nm) is a 532 nm laser. High powers are required to create a sufficiently strong repulsion to prevent atoms from entering the Majorana loss region and the 15 W Sprout-G laser described in Section 3.3.4 is used. From Eq. (5.14) one can see that the small mass of ^{6}Li will increase Γ_{Majorana} and the larger detuning (compared to ^{23}Na) will also make the repulsive potential weaker. Hence, in the experiment, it should be much harder to prevent the Majorana losses of the ^{6}Li. This is seen experimentally in the higher sensitivity to plug alignment and higher loss rates for ^{6}Li compared to ^{23}Na. The plug beam is brought to a focus at the atoms with a waist of 23 µm and maximum power of 9 W before the atoms. This beam has a Rayleigh range of 3 mm and hence the change in intensity along the direction of the plug can be neglected as the atomic cloud's size is much smaller than this, especially at temperatures where Majorana losses are significant. The simulated potential of the optically plugged magnetic trap is shown in Fig. 5.8 for both ^{23}Na and ^{6}Li. The heating rate from the plug beam can also be calculated (see Section 5.5.1). At the position of the

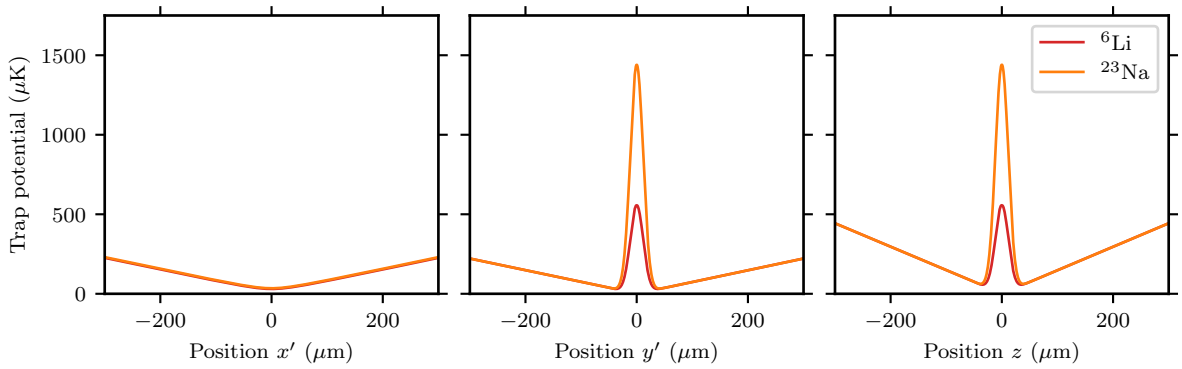

Figure 5.8: Simulated potential of the optically plugged magnetic trap. Position zero is at the center of the quadrupole trap where the B-field is zero. The y' and z plots are shown with the other coordinates set to zero. The x plot is shown with the other coordinates chosen to minimize the potential. The potential for both species is simulated and the plug is approximately 3 times stronger for ^{23}Na than for ^{6}Li. Both species have a similar magnetic trapping potential far from the plug as both the $|2,2\rangle$ state of ^{23}Na and $|3/2,3/2\rangle$ state of ^{6}Li have the same $g_F m_F = 1$. In this simulation the plug power is 7.5 W with a focused waist of 23 µm and B' 110 G cm^{-1}.

potential minimum (approximately 35 µm from the focus) a heating rate of 250 nK s^{-1} and 150 nK s^{-1} was calculated for ^{23}Na and ^{6}Li, respectively. This is negligible for the evaporation in the magnetic trap.

Choosing the waist of the plug beam requires the consideration of several factors. The waist should be large enough to cover the region around zero field where the losses can occur [164, 165, 167]. Additionally, it should be small enough that with the given power it provides a sufficient potential barrier. A simple model can be attained by using the formulation that the density $n(\mathbf{r})$ at a position $\mathbf{r}$, can be written as $n(\mathbf{r}) = n_0 e^{-\frac{V(\mathbf{r})}{k_B T}}$, where $V(\mathbf{r})$ is the potential of the magnetic trap and plug combined, T is the temperature of the cloud and n_0 is a normalization factor. Then by computing this integral over the region where the Majorana losses occur, one can estimate the number of particles that will occupy the loss region of the trap. For practical reasons the plug focused waist should not be too small as it becomes harder to align, and harder to keep the position stable on the field zero. Additionally, the variation of the potential across the cloud will become significant as the Rayleigh range gets smaller.

The alignment of the plug is a multi-stage process. A 2 m PCF fiber brings the plug beam to the vacuum chamber where it is reshaped and combined on the x' axis with the dipole beam using a 1064 nm 532 nm dichroic mirror. The reshaping and focusing of the plug is done by using Gaussian beam propagation (ABCD matrices) to calculate ideal focal lengths and positions of lenses and then measuring real beam waists with a camera in place, which will be discussed in more detail in Section 5.5.2 in relation to the

dipole beams. Assuming the plug beam is approximately aligned ($< 2\,\mathrm{mm}$) and focused with the appropriate waist to the atomic cloud, the next stage is to accurately move the plug to the B-field zero. To allow for accurate small movements in tightly focused beams, picomotor mirrors[1] were used. These mirrors have an angular range of $\pm 5^\circ$ and an angular resolution of $0.7\,\mu\mathrm{rad}$. They are controlled over Ethernet and are connected to the experiment control software (Appendix B.5). To align the plug, the atomic cloud should be evaporated a small amount ($T \approx 200\,\mu\mathrm{K}$) and some time-of-flight should be performed (typically 10 ms), such that the atoms occupy a large region of space, but there is still a reasonable optical density signal. The plug beam can be left on during the time-of-flight and a clear hole in the cloud should be seen as shown in Fig. 5.9a. The picomotor mirror can be used to bring the visible hole to the center of the atomic cloud. A reasonable first estimate of the zero position can be obtained by performing an in-trap or short time-of-flight image of the cloud and fitting a Gaussian to obtain the center position. The process can then be repeated with iteratively shorter time-of-flights. Depending on how cold the cloud was, there may be a visible difference in the atom number when the plug is aligned to the center. At this point one can then evaporate the cloud further to colder temperatures and repeat the procedure with smaller steps as shown in Fig. 5.9b. Once the improvement in atom number due to the plug is clear, the evaporation can be continued even further. On this much colder sample, one can image the atoms without the plug on during time-of-flight and maximize the atom number with plug position. From experience we have found that aligning each axis individually finds something very close to the global maximum and that it is not necessary to map out an entire grid, which can be difficult due to the hysteresis of the picomotors. With the above method the plug was aligned sufficiently well to observe Bose-Einstein condensation of ^{23}Na and to sympathetically cool ^{6}Li such that it could be loaded into the dipole trap. Once we had the degenerate Fermi gas signal (see Section 5.6) the plug position was re-optimized to maximize the phase space density of ^{6}Li. Given that ^{6}Li is more sensitive to plug misalignment than ^{23}Na, this provided a more sensitive signal. For this alignment the plug position (picomotors) remained fixed and we changed the y' and z compensation fields to align the magnetic field zero to the plug's position. When the atoms are in the optically plugged magnetic trap, the atom numbers in the optimized system are approximately 5×10^9 to 1×10^{10} ^{23}Na atoms and 1×10^8 to 3×10^8 ^{6}Li atoms. The error on these atom numbers are large as the clouds are optically dense (OD> 5) but are still hot and hence longer time-of-flight cannot be performed.

Since $\Gamma_{\mathrm{Majorana}}$ are highest at low temperatures, the losses become most significant at the

[1] Newport Picomotor Piezo Mirror Mounts 2-axis Model 8821.

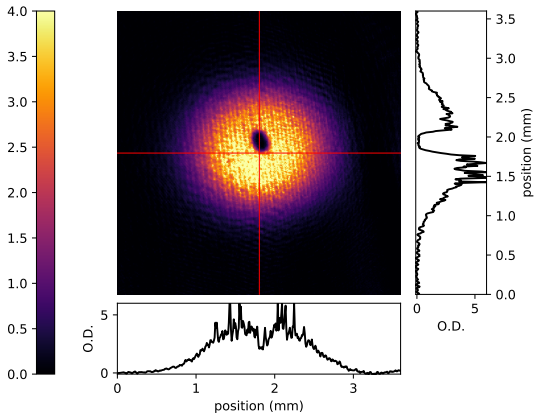

(a) plug alignment (thermal)

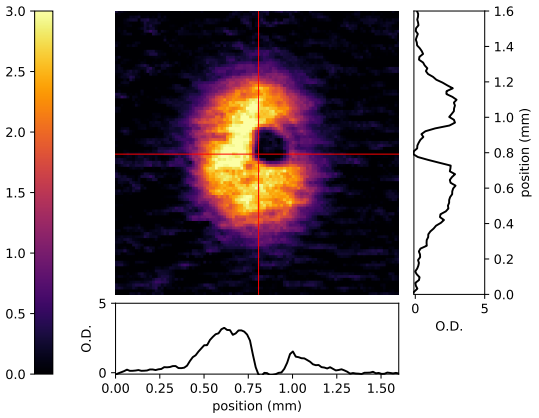

(b) misaligned plug

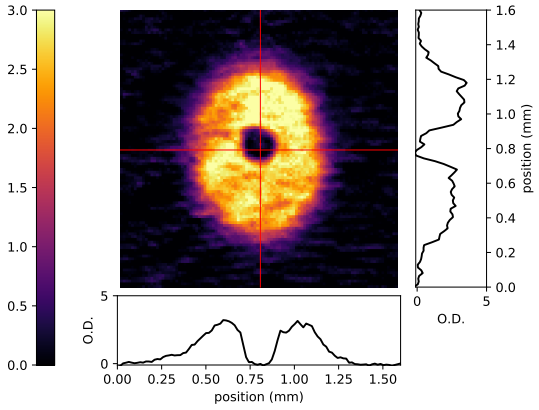

(c) aligned plug

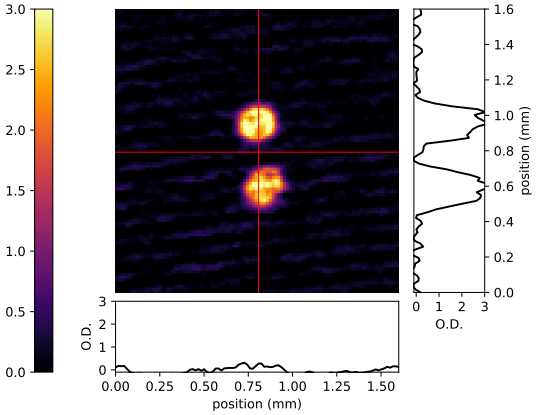

(d) After evaporation

Figure 5.9: Alignment of the optical plug. **Fig. 5.9a**: Initial alignment of the plug on a thermal cloud of ^{23}Na. A small amount of evaporation is performed to bring the temperature to around 150 µK and time-of-flight is performed for around 8 ms. The plug is left on during the time-of-flight expansion and creates a clear hole in the atomic cloud. The hole is much larger than the plug waist as the atoms expand into it. Note the different distance and OD scale for this figure. **Fig. 5.9b** and **Fig. 5.9c**: Alignment of the plug on a colder sample of ^{23}Na. As the plug is aligned closer to the zero field center, the atom number can be seen to enhance. For the final optimization of the plug position, the plug is turned off during time-of-flight and the increase in atom number with plug position is used. **Fig. 5.9d**: In trap image of the ^{23}Na cloud after MW evaporation in the optically plugged magnetic trap. A double well potential is created and at low temperatures, the cloud separates into the potential wells.

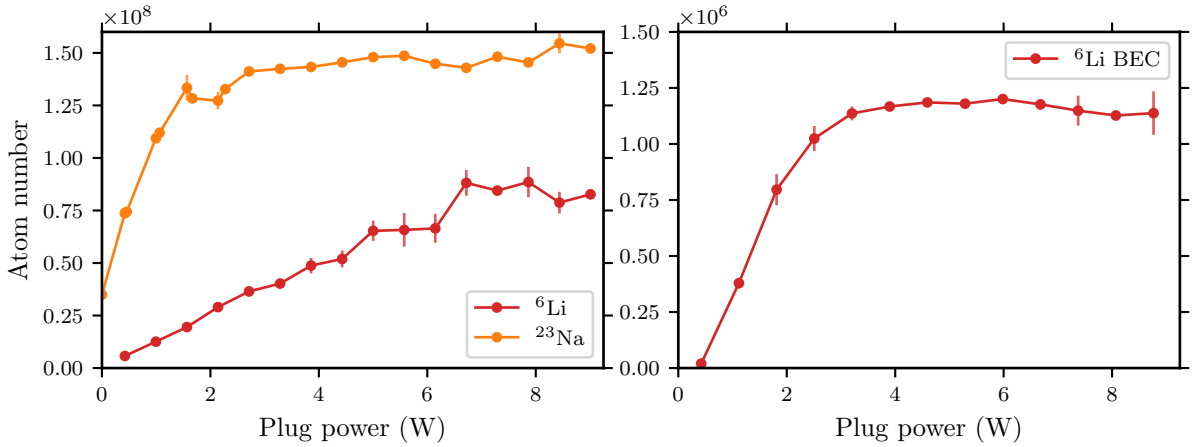

Figure 5.10: Atom number after forced evaporation for varying plug power. The left plot shows the atom number after five seconds evaporation in the magnetic trap. The ^{23}Na (orange) data is taken without any ^{6}Li present. The right plot shows the ^{6}Li BEC number in the dipole trap after evaporation on the Feshbach resonance. The ^{23}Na atom number saturates at approximately 2 to 3W plug power compared to 7 to 8W for the ^{6}Li atom number. This qualitatively agrees with Eq. (5.14), which requires a higher plug power to prevent Majorana losses. The right plot shows that the final number in the BEC for ^{6}Li saturates much earlier than in the magnetic trap. The exact reason for this is unknown but it is most likely that the dipole trap volume is completely filled and hence additional atoms in the magnetic trap cannot be transferred.

end of evaporation. In Fig. 5.10 the final atom number for ^{23}Na and ^{6}Li after evaporation is shown as a function of plug power. This clearly shows that a much higher plug power[1] is required to fully prevent Majorana losses of ^{6}Li than of ^{23}Na.

5.4.2 Microwave Evaporation of ^{23}Na and Sympathetic Cooling of ^{6}Li

The ^{23}Na atoms are evaporatively cooled by microwave (MW) transitions to an untrapped state, selectively removing the highest energy atoms, reducing the atom number and leaving the remaining atoms to thermalize to a lower temperature, increasing the phase space density. A detailed discussion of the mechanism, thermodynamics and efficiency of evaporative cooling can be found in [97, 161]. The ^{6}Li atoms thermalize with the ^{23}Na atoms and hence this evaporation process of ^{23}Na sympathetically cools the ^{6}Li, with ideally no loss of ^{6}Li atoms. Since Pauli blocking prevents the thermalization of spin-polarized fermions, sympathetic cooling provides an efficient mechanism to cool fermions. Since only the ^{23}Na atoms are removed, sympathetic cooling should result in a larger

[1] Interesting the final number in the ^{6}Li molecular BEC saturates earlier with plug power than it does in the magnetic trap see Fig. 5.10.

number of fermions at a lower temperature, increasing the phase space density.

From the Breit-Rabi diagram shown in Fig. A.1 it is clear that the states $|F, m_F\rangle = |2,2\rangle, |2,1\rangle, |2,0\rangle$ and $|1,-1\rangle$ are trappable states (low field seeking) and the $|F, m_F\rangle = |2,-1\rangle, |2,-2\rangle$, $|1,1\rangle$ and $|1,0\rangle$ are untrappable states (high field seeking). As discussed earlier, the ^{23}Na atoms in the magnetic trap are in the $|2,2\rangle$ state. Atoms in the $|2,2\rangle$ state can be flipped to the untrapped $|1,1\rangle$ state with the allowed electric dipole transition at a frequency of $1771.6\,\mathrm{MHz} + 1.4\,\mathrm{MHz\,G^{-1}} \times B$, where B is the absolute magnetic field in Gauss. Since B varies in space across the magnetic trap, MW can address specific spatial positions in the cloud and flip atoms to the untrapped state. By changing the frequency (position) of this microwave knife edge, the depth of the magnetic trap can be controlled, allowing the system to be evaporatively cooled. The peak phases space density, D, for a total atom number, N, is the figure of merit for evaporative cooling:

$$D = n\lambda_{\mathrm{dB}}^3 = n\left(\frac{h}{\sqrt{2\pi m \mathrm{k_B} T}}\right)^3 \tag{5.15}$$

where n is the peak density, which for a quadrupole trap has the form: $n = \frac{N}{4\pi\left(\frac{\mathrm{k_B}T}{g_F m_F \mu_\mathrm{B} B'}\right)^3}$. At the end of evaporation the harmonic confinement from the plug potential changes n. The evaporation efficiency[1] γ can be defined as $(D/D_0) = (N/N_0)^{-\gamma}$ and can be extracted as a straight line in a $\log - \log$ plot. The evaporation process for the ^{23}Na and ^{6}Li atoms is shown in Fig. 5.11 for several different configurations with fitted lines showing the efficiency. Fig. 5.11 shows that large pure BECs of ^{23}Na can be produced when the magnetic trap is decompressed to $50\,\mathrm{G\,cm^{-1}}$ towards the end of evaporation to mitigate Majorana and three body losses. When loading the maximum ^{6}Li number in the magnetic trap, there is not enough ^{23}Na to sympathetically cool the ^{6}Li below $D = 5 \times 10^{-3}$. Reducing the initial ^{6}Li number means they can be cooled further, however, strong losses were observed when the ^{6}Li cloud was cooled to approximately $D = 1 \times 10^{-1}$ to 1×10^{-2}. The cause of these losses was never confirmed[2], however, transferring a large number of ^{6}Li atoms to the dipole trap and continuing evaporation proved very effective. The final optimized evaporation of ^{23}Na (with ^{6}Li) in the $110\,\mathrm{G\,cm^{-1}}$ was a linear sweep of the MW from 1900 MHz to 1777 MHz in 5 s.

[1] In general the efficiency will be a function of N and sometimes the overall efficiency is defined between the initial and final evaporation points.

[2] It is possible that some unwanted spin states remained leading to spin exchange collisions or that the plug was not sufficient to prevent Majorana at lower temperatures.

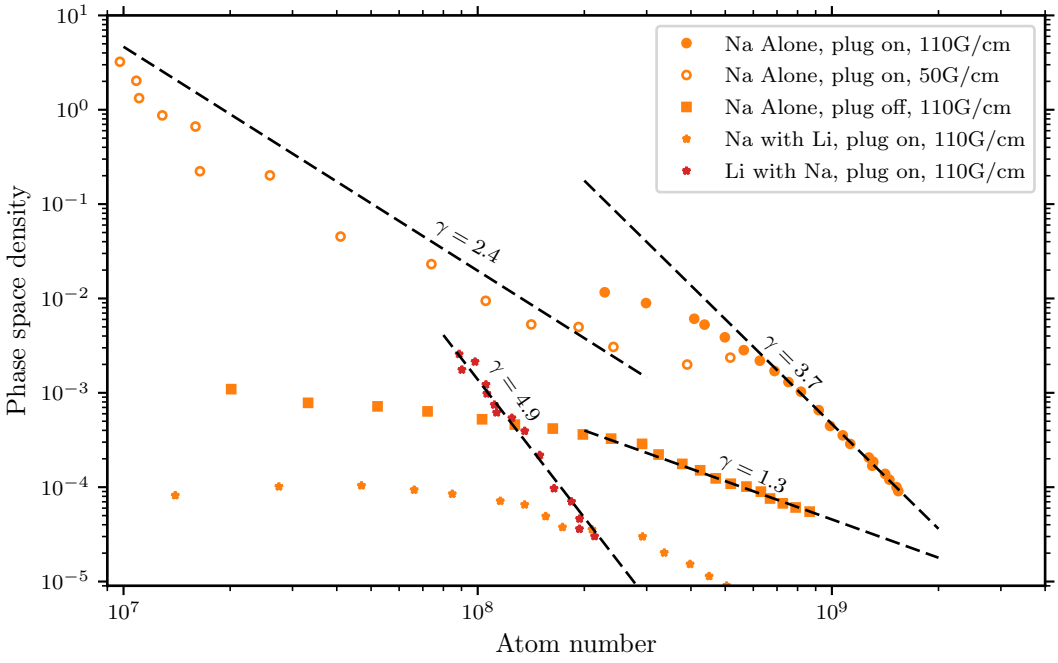

Figure 5.11: Phase space density, D, is plotted against the atom number, N, for various configurations (see legend) in the magnetic trap forced evaporation. Note that to achieve the ^{23}Na BEC it was necessary to decompress the magnetic trap from $110\,\mathrm{G\,cm^{-1}}$ to $50\,\mathrm{G\,cm^{-1}}$ as shown by the hollow orange circles. The black dashed lines are fits of the form $(D/D_0) = (N/N_0)^{-\gamma}$ from which the evaporation efficiency γ can be extracted.

5.5 Dipole Traps

Magnetic traps provide a reliable and effective method of creating large trap depths and allow an easy to implement RF/MW driven evaporation mechanism that does not affect the trapping geometry. However, they suffer from being selective in the states they can trap (i.e. they can only trap low field seeking states) and are distorted by additional magnetic fields. Dipole traps provide an optical method of trapping all atomic hyperfine states and are unaffected by additional magnetic fields used, for example, in Feshbach resonances. Dipole traps make use of the AC-stark shift such that a red-detuned laser can create a conservative potential proportional to intensity. The Gaussian propagation of laser beams then defines this potential and the parabolic approximation in the region of the atomic cloud means these traps are approximately harmonic.

5.5.1 Theory of Dipole Traps

This section will summarize the theory of optical dipole traps with a focus on the steps required to calculate the potential for the ^{23}Na and ^{6}Li atoms in our experiment. The basic theory follows the path and notation of [168]. There are fundamentally two different types of radiative forces [169]. Dissipative forces are associated with the transfer of momentum from photons and were discussed in Sections 4.1 and 4.2. These dissipative forces are always proportional to the momentum transfer $\hbar\mathbf{k}$ and the scattering rate, Γ_{sc}. Dipole forces, however, arise from spatially dependent light shifts of the ground state due to spatially dependent light intensity. Assuming the laser is far-detuned from resonance, the atoms remain in the ground state and this shift creates a spatially dependent potential.

In a semi-classical picture, the oscillating electric field, $\mathbf{E}$, of the laser light induces an oscillating dipole moment, $\mathbf{p}$, across an atom. The induced dipole moment interacts with the driving field, creating an interaction potential. This conservative potential arises from the in-phase oscillations of $\mathbf{p}$ and $\mathbf{E}$. The out of phase oscillations can be interpreted as absorption or in a photon picture as scattering events of absorption followed by spontaneous emission. It is common to calculate the pre-factors for the potential and scattering rate using Lorentz's model of the classical oscillator. These quantities can also be derived using second order perturbation theory [168–170], which makes the extension to

multi-level atoms and different polarization clearer:

$$\Delta E_i = \sum_{j \neq i} \Delta E_{ij} = \sum_{j \neq i} \frac{\left| \langle j \left| \mathcal{H} \right| i \rangle \right|^2}{\mathcal{E}_i - \mathcal{E}_j} \tag{5.16}$$

This gives the energy shift of a state $|i\rangle$ as a result of the presence of several other hyperfine states $|j\rangle$. $\mathcal{H} = e\mathbf{r} \cdot \mathbf{E}$ is the interaction Hamiltonian, $\mathcal{E}_i$ and $\mathcal{E}_j$ are the energies of the dressed states $|i\rangle$ and $|j\rangle$, respectively. This can be evaluated [169, 170] to give:

$$\Delta E_{ij} = C_{ij} \frac{3\pi c^2}{2\omega_{ij}^3} \Gamma \left(\frac{(\omega_{ij} - \omega_{laser})}{(\omega_{ij} - \omega_{laser})^2 + \frac{\Gamma^2}{4}} + \frac{(\omega_{ij} + \omega_{laser})}{(\omega_{ij} + \omega_{laser})^2 + \frac{\Gamma^2}{4}} \right) I(\mathbf{r}) \tag{5.17}$$

for a laser frequency ω_{laser}, and transition frequency ω_{ij}. C_{ij} is a transition coefficient accounting for the polarization, allowed transitions and angular momentum quantum numbers of the states [168]. Generally it is assumed that $(\omega_{ij} - \omega_{laser}) \gg \Gamma$, which is valid for typical dipole traps used in this experiment where $(\omega_{ij} - \omega_{laser}) \sim 100\,\mathrm{THz}$ and $\Gamma \sim 10\,\mathrm{MHz}$. This means several terms in the expansion of Eq. (5.17) can be neglected[1] allowing for the relatively simple form:

$$\Delta E_{ij} = C_{ij} \frac{3\pi c^2}{2\omega_{ij}^3} \Gamma \left(\frac{1}{(\omega_{ij} - \omega_{laser})} + \frac{1}{(\omega_{ij} + \omega_{laser})} \right) I(\mathbf{r}) \tag{5.18}$$

The intensity, $I(\mathbf{r})$, is usually factored out such that the potential can be expressed with a constant pre-factor, U_0:

$$V(\mathbf{r}) = U_0 I(\mathbf{r}) \tag{5.19}$$

For the simulations in this thesis, U_0 was calculated by numerically evaluating Eq. (5.17) including the effects of polarization and the different transition lines. However, a good approximation for U_0 can be made from considering a single (e.g. D2) line with σ^+ polarization, which allows equation Eq. (5.17) to be written in the simple form:

$$U_0 = \frac{a\lambda_{\mathrm{laser}}^2 - b\lambda_{\mathrm{laser}}^4}{(\lambda_{\mathrm{D2}} + \lambda_{\mathrm{laser}})^2 (\lambda_{\mathrm{laser}} - \lambda_{\mathrm{D2}})^2} \tag{5.20}$$

Eq. (5.20) provides a very good approximation to the required pre-factor, U_0(SI units), for both ^{23}Na and ^{6}Li for typical dipole laser wavelengths. For ^{6}Li, $a = 2.265\,44 \times 10^{-49}\,\mathrm{sm}^4$ and $b = 5.031\,96 \times 10^{-37}\,\mathrm{s\,m}^2$ and for ^{23}Na, $a = 1.731\,69 \times 10^{-49}\,\mathrm{sm}^4$ and $b = 4.988\,90 \times 10^{-37}\,\mathrm{s\,m}^2$. For both ^{23}Na and ^{6}Li, for $\lambda_{\mathrm{laser}} = 1064\,\mathrm{nm}$, the effect of changing polarization is

[1] The corrections from including these terms in the dipole traps used in our experiment are $\sim \mathcal{O}\left(10^{-14}\right)$.

$\Delta U_0 \approx \mathcal{O}\left(10^{-4}\right)$ and from including additional lines is $\Delta U_0 \approx \mathcal{O}\left(10^{-3}\right)$. It is often assumed that the laser is tuned relatively close to resonance, $|\omega - \omega_0| \ll \omega_0$, which is commonly known as the rotating wave approximation. This means one can neglect the second term in Eq. (5.18) and write the dipole potential term in the simple form $\Delta E_{ij} = C_{ij} \frac{3\pi c^2}{2\hbar\omega_{ij}^3} \frac{\Gamma}{\Delta} I\left(\mathbf{r}\right)$. However, for a 1064 nm laser on ^{23}Na or ^{6}Li, the counter rotating term contributes approximately 20 % of the total value and should not be neglected.

The $I\left(\mathbf{r}\right)$ term in Eq. (5.19) is most commonly the intensity profile of a Gaussian beam. The electric field of a Gaussian beam is a solution to the paraxial Helmholtz equation and the intensity of a beam propagating in the z direction and focused at position $\mathbf{0}$ can be defined as:

$$I(\mathbf{r}) = \frac{2P}{\pi w(w_{x0}, z, \lambda) w(w_{y0}, z, \lambda)} \mathrm{e}^{-2\left(\frac{x^2}{w^2(w_{x0}, z, \lambda)} + \frac{y^2}{w^2(w_{y0}, z, \lambda)}\right)} \tag{5.21}$$

where

$$w(w_0, z, \lambda) = w_0 \sqrt{1 + \left(\frac{z}{z_R(w_0, \lambda)}\right)^2} \tag{5.22}$$

$$z_R(w_0, \lambda) = \frac{\pi w_0^2}{\lambda} \tag{5.23}$$

and P is the beam power, $w_{x0,y0}$ are the focused beam waists in the x and y directions respectively, λ is the wavelength, w is the beam waist at a position z and z_R is the Rayleigh length.

Note that in Eq. (5.21) the intensity does not depend on the phase of the electric field and, assuming that there is no phase relation between them, the intensity of several beams can be found by adding each intensity linearly. For the dipole laser used in the experiment the coherence length is $< 200\,\mu$m meaning the different dipole beams do not interfere. The phase terms in the electric field become very important when calculating lattice potentials. The beam waist in equation Eq. (5.22) is the radius[1] at which the intensity falls to $1/\mathrm{e}^2$. From Eq. (5.21) it is clear that the dipole potential from each beam will be Gaussian, with a standard deviation defined by the beam waist, $w(z)$ at the position of the atoms and depth defined by the beam power, P, and the value of U_0. Since a cold atomic cloud will often only occupy the central region of the trapping potential, it is useful to expand the potential to second order and approximate the Gaussian trap as harmonic. Expanding to

[1] All beam waists in this thesis (and in the experiment) refer to waist radius as defined by Eq. (5.22).

second-order in the x direction[1] about the focus gives:

$$V(x) = \frac{2PU_0}{\pi w_{x0} w_{y0}} - \frac{4PU_0 x^2}{\pi w_{x0}^3 w_{y0}} + \mathcal{O}(x^3) \tag{5.24}$$

which is valid for $|x| \ll w_{x0}, w_{y0}$. The first term in Eq. (5.24) gives the potential depth and the second term, by equating it to the harmonic trap potential $\frac{1}{2}m\omega_x^2 x^2$, defines the trap frequency ω_x:

$$\text{Potential Depth} = U_0 \frac{2P}{\pi w_{x0} w_{y0}} \tag{5.25}$$

and

$$\omega_x = 2\sqrt{\frac{2U_0 P}{m\pi w_{x0}^3 w_{y0}}} \tag{5.26}$$

The trap frequency in the z direction is different as the change in waist along the propagation axis is defined by the Rayleigh range. Using the same method as above it can be shown that:

$$\omega_z = \lambda\sqrt{\frac{2U_0 P\left(w_{x0}^4 + w_{y0}^4\right)}{m\pi^3 w_{x0}^5 w_{y0}^5}} \tag{5.27}$$

For a given dipole beam, the trap frequency scales like $\omega \propto \sqrt{P}$ and the depth is defined by the peak intensity. When multiple perpendicular beams are used, the trap frequencies add in quadrature $\omega = \sqrt{\sum_{beam} \omega_{beam}^2}$ and the depths add linearly. Eqs. (5.24) to (5.27) provide useful physical insight into how the trap frequency and depth scale, however, in the experiment the dipole potential was simulated numerically and the depth and frequencies were extracted by fitting. The advantage of the numerical simulation is that many additional factors can easily be incorporated such as: gravity, additional magnetic field gradients, the curvature of the Feshbach fields, interference terms and non-orthogonal beams. This also allowed the transfer between different traps to be simulated.

The scattering rate discussed earlier was also calculated in these simulations. This scattering rate scales as $I(\mathbf{r})/\left(\omega_{ij} - \omega_{laser}\right)^2$, which shows that for a far-detuned dipole laser, the effects of scattering will be small. A value of approximately $75\,\mathrm{nK\,s^{-1}}$ and $15\,\mathrm{nK\,s^{-1}}$ was calculated for the full power dipole trap for ^{6}Li and ^{23}Na, respectively. The real heating rate in the dipole trap will be limited by technical noise on the beam powers.

[1] similar equations are found for the y direction by exchanging x and y.

5.5.2 Implementation of Dipole Traps

In the experiment a crossed two beam dipole trap is used. The horizontal dipole beam comes from the x' direction combined with the plug beam via a 1064 nm 532 nm dichroic mirror. The vertical beam comes from below and is retro-reflected of the upper UKEA viewport, which is HR for 1064 nm. The dipole beams are created from the 50 W IPG 1070 nm laser (see Section 3.3.3) and both beams are brought to the table via optical fibers with a maximum power of 13 W per beam in the chamber. The final chosen dipole waist radii were chosen to be 120 µm by 120 µm for the vertical beam and 110 µm by 53 µm for the horizontal beam in the y' and z directions, respectively. At maximum power this dipole trap should provide a depth of approximately 65 µK capable of trapping the ^{6}Li cloud after sympathetic cooling in the magnetic trap.

To prepare the beams to have the correct waists in the vacuum chamber the ABCD matrix formalism [171] was used to calculate the optimal lens positions. A beam profiling camera was then used to measure the beam waist during propagation and the results of one such measurement are shown in Fig. 5.12. Additionally, a small mirror was inserted directly before the vacuum window, and the waist of the reflected dipole beam measured at the correct distance to give the waist at the position of the atoms. These measurements were important in ensuring that the dipole beams had the correct aberration-free profiles.

The initial alignment of the dipole beams was performed by leaving them on at full power during the time-of-flight of a thermal ^{23}Na cloud, after a small amount of evaporation. The thermal atoms expand to cover a large region of space and an enhancement of the optical density is seen in the region of the dipole beams, as shown in Fig. 5.13.

5.5.3 Transfer from Magnetic Trap to Dipole Trap

After the forced evaporation of ^{23}Na in the optically plugged magnetic trap, the sympathetically cooled ^{6}Li needs to be transferred to the optical dipole trap. Performing this transfer with a high transfer efficiency and without heating or exciting oscillations in the dipole trap can be challenging. One must consider:

- Where precisely to align the dipole beams.
- When (and how) to turn on the dipole trap beams.
- How to turn off the optically plugged magnetic trap.

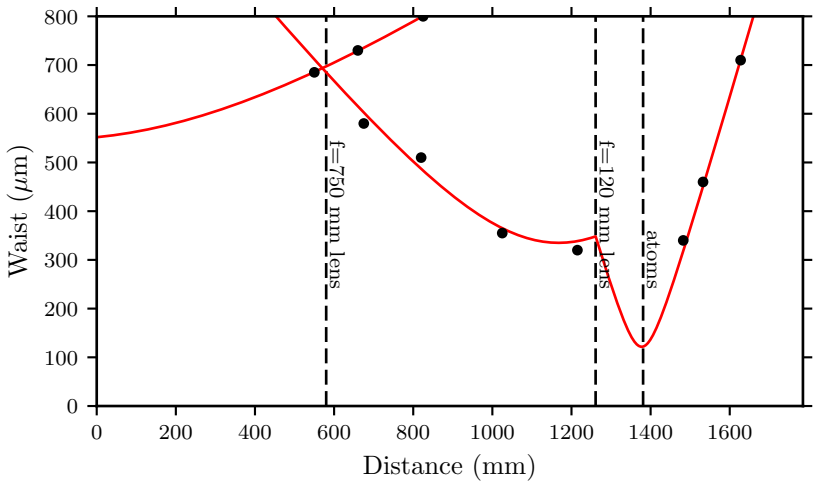

Figure 5.12: Simulated waist of the propagation of the vertical dipole beam through the system. The beam is collimated and leaves the fiber coupler at distance 0 and then propagates through free space before reaching an f=750 mm lens. It then reaches the final f=120 mm lens where it is focused onto the atoms. The black points are positions where the waist was measured. In some cases a mirror was inserted to measure the waist before the focusing of a lens. These plots were made for all the precise alignment beams in the experiment to ensure the beam waists were as expected and that simulated potentials would be accurate.

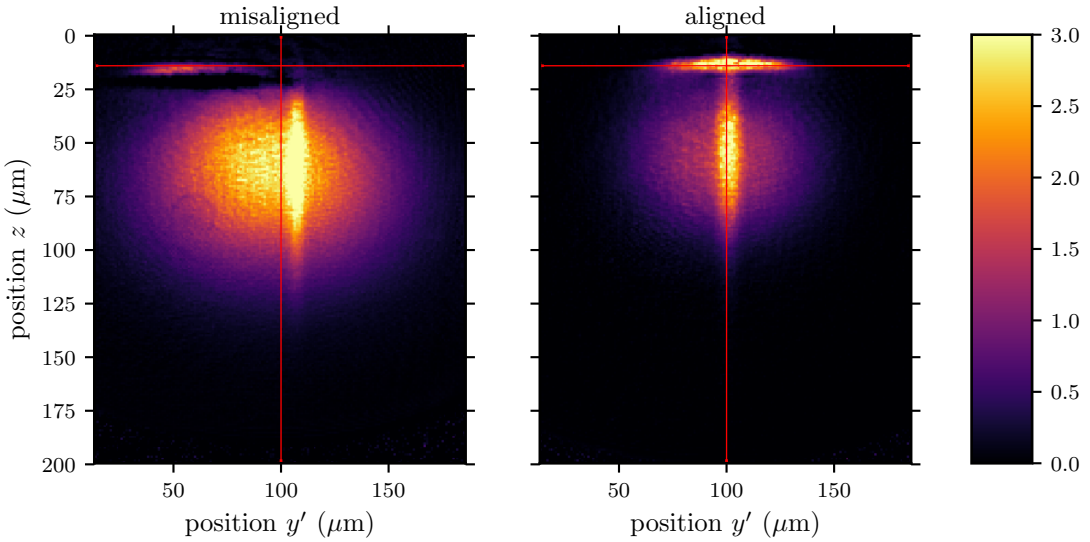

Figure 5.13: The dipole trap is initially aligned by leaving the dipole beam on during time-of-flight of a thermal ^{23}Na cloud. The presence of the dipole beams leads to an enhancement of the optical densities. The intersection of the red lines shows the center of the magnetic trap. During time-of-flight the cloud expands and falls under gravity (z). The dipole beams are aligned using the picomotor mirrors such that they cross at approximately the region of the center of the magnetic trap.

Towards the end of evaporation in the optically plugged magnetic trap, the repulsive plug potential is significant and forms the double well potential as was shown in Fig. 5.8. Aligning the dipole beams to the center of the magnetic trap would mean they simply reduce the repulsive potential at the trap center and the transfer process would go from a double well to a single well harmonic potential. It was found to be far more effective to align the dipole beams to one of the wells in the potential. This was done by evaporating a pure ^{23}Na cloud to very low temperatures where the individuals wells could clearly be distinguished (see Fig. 5.9d). By aligning the dipole trap to this position, the hybrid potential of the magnetic trap, plug beam and dipole beams could be made asymmetric meaning the atoms would occupy the single lower potential well, which was highly beneficial in the transfer procedure.

Ideally the dipole trap should be turned on adiabatically such that the atoms are transferred without heating. Experimentally, it was found to be suitable to ramp the dipole beams on, over 50 ms, 200 ms before the transfer. When the full MW evaporation was performed on the pure ^{23}Na cloud with the dipole beams on, losses at the end of the evaporation were observed. This was attributed to the increase in density from the effective trap compression when the dipole beams are present.

Turning off the optically plugged magnetic trap proved to be the most challenging factor in the transfer. It was observed that turning off the plug beam rapidly caused oscillations and losses in the dipole trap. The transfer was significantly improved by ramping the plug power and the magnetic trap gradient linearly and in proportion to each other over 150 ms. The reduction of plug power does not lead to significant Majorana losses as the decompression of the cloud simultaneously reduces the loss rate (Eq. (5.14)). Additionally, it was noted that as the magnetic trap was ramped down from $110\,\mathrm{G\,cm^{-1}}$ to $0\,\mathrm{G\,cm^{-1}}$, the position of the magnetic trap zero moved significantly. This was caused by background B-fields (in all directions) which, at low enough gradients, are able to significantly shift the quadrupole trap zero position. At the lowest gradients where ^{23}Na could still be trapped against gravity ($4\,\mathrm{G\,cm^{-1}}$ in the z-direction), the cloud moved by several cloud diameters. This was surprising as it was thought that the bias fields had been canceled at the position of the MOT and then at the position of the final magnetic trap. There were two causes for the shift. Firstly, the zero position of the quadrupole trap is much more sensitive to bias fields at low gradients[1]. Secondly, and more critically, it was found that the background bias field at the position of the atoms was changing slightly during the course of the experiment cycle. It was eventually found that this was caused by

[1] $\delta x = \frac{B_0}{B'}$ where δx is the shift in the zero position in a given direction, B_0 is the bias field in the same direction and B' is the magnetic trap gradient.

magnetization of the experiment apparatus during the magnetic trapping stage (and later due to the Feshbach fields) where large B-fields are used[1]. This was confirmed by using different field gradients for the magnetic trapping and watching the position of the shifted quadrupole trap drift over time. Whilst this was undesirable, it was found that the effect was highly reproducible when the field gradients used in the sequence remained the same for a few hours. Hence, the shift in the zero-position of the quadrupole during the ramp down of the magnetic trap could be compensated by changing the bias compensation fields that were used for the initial MOT stage and for the high gradient magnetic trap. The final values of these bias fields were optimized to make the position of the cloud not shift during the ramp down of the magnetic trap, with the dipole beams off. Towards the end of the transfer when the potential is dominated by the dipole beams, a small bias field $\sim 1\,\mathrm{G}$ is ramped on in the z-direction to provide a quantization field for the $|m_F\rangle$ states. The optimized turn-off of the magnetic trap involved ramping the B-field gradient and plug beam down, while simultaneously ramping the bias fields to maintain a constant position of the cloud. A 100 ms hold at 1000 G (Helmholtz) followed by a 100 ms hold at $110\,\mathrm{G\,cm^{-1}}$ is now performed at the end of every experiment cycle to demagnetize (or repeatably magnetize) the system.

Even after ramping down the plug power from 9 W to 0 W and turning off the AOM, there was still a weak beam coupled through the fiber to the experiment table of a few tens of mW. Whilst this didn't initially cause any problems it was found to cause significant heating and distortion of the dipole trap when evaporating to lower temperatures. This was resolved by installing a beam shutter that blocked the plug after the transfer. With these steps implemented it was possible to get relatively high transfer efficiency into the optical trap ($> 50\,\%$) with approximately 5×10^7 ^{6}Li atoms at a temperature of 13 µK. The simulated hybrid potential is shown in Fig. 5.14 at various stages in the transfer.

[1]It has never been confirmed exactly which part of the experiment magnetizes. The problem was first discovered when the SMA connector being used for the MW evaporation coils were found to be magnetic. Since their removal the magnetization effects were greatly reduced but were still measurable and are most likely caused by the weld from the main Kimball chamber to the UKEA window, or simply the residual magnetic permeability of the stainless steel chamber even though it is *316L non-magnetic stainless steel*.

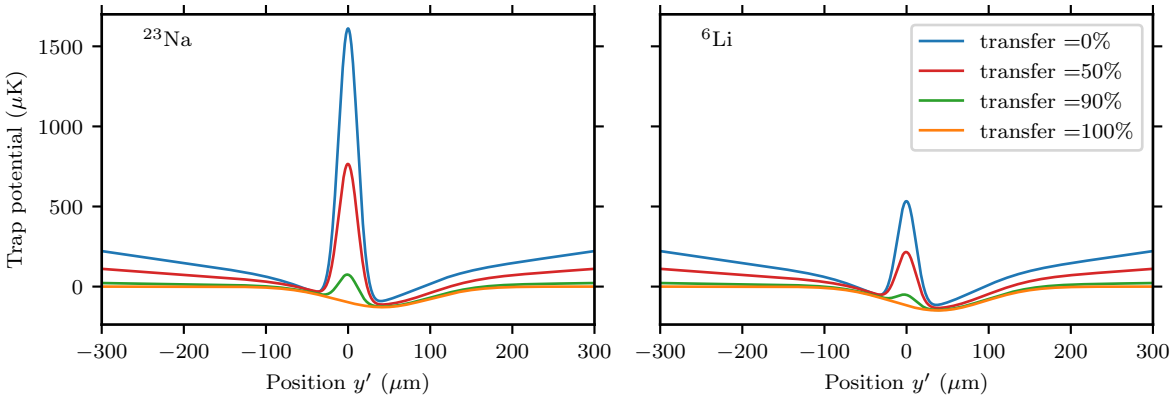

Figure 5.14: Form of the combined trapping potential in µK from the magnetic trap, plug beam and dipole beams during the transfer from the optically plugged magnetic trap to the dipole trap. The left and right figures show the potential for ^{23}Na and ^{6}Li, respectively. The different curves (see legend) show different fractions into the transfer process: with 0% with the plug beam at full power and magnetic trap gradient maximum and 100% with the plug beam off and the gradient zero with only the dipole potential remaining. Note that the presence of the dipole trap initially causes an asymmetry in the trap potential already visible before the transfer (0%). This asymmetry becomes much clearer as the plug is ramped down with the magnetic field gradient.

5.6 Forced Evaporation of ^{6}Li on the Feshbach Resonance

5.6.1 State Preparation

Once the atoms have been transferred to the dipole trap, they are still in the $|6\rangle$ hyperfine state used for magnetic trapping. This spin polarized cloud of ^{6}Li cannot thermalize alone (see Eq. (2.27)) and it was found that leaving a small admixture of ^{23}Na in the magnetic trap ($\sim 10\,\%$ of the ^{6}Li number) increased the transfer efficiency and reduced the temperature in the initial dipole trap compared with evaporating all the ^{23}Na. Once in the dipole trap, there is no longer the constraint of using low-field seeking hyperfine states and a mixture of the $|1\rangle + |2\rangle$ state should be produced, such that the broad Feshbach resonance discussed in Section 2.2 can be used.

The spin mixture of ^{6}Li is created by two successive RF Landau-Zener [172] sweeps: $|6\rangle \rightarrow |1\rangle$ followed by a $|1\rangle \rightarrow 50\%\,|1\rangle + 50\%\,|2\rangle$. For a Landau-Zener sweep the probability of transfer between a state $|a\rangle$ and $|b\rangle$ is given by:

$$P_{|a\rangle\rightarrow|b\rangle} = 1 - \mathrm{e}^{\frac{-2\pi\Omega_0^2}{\dot{\omega}}} \tag{5.28}$$

where Ω_0 is the Rabi frequency and $\dot{\omega}$ is the rate of change of the driving field frequency. This shows that to maximize the transfer efficiency, RF power which controls the Ω_0, should be high and the sweep should be slow. It was found to be beneficial to perform these sweeps as soon as possible after transferring to the dipole trap to ensure the ^{6}Li atoms thermalize quickly and evaporation can begin. The H-bridge box is used to let the Feshbach coils, which were previously used for the quadrupole magnetic trap, run in Helmholtz configuration and provide an offset field. It was found that in the transfer from the magnetic trap, some atoms were only trapped along the axial path of the horizontal dipole beam and not in the crossed dipole beam. This meant that as they traveled outwards in the horizontal beam in the $|6\rangle$ state, they experience a weak anti-confining potential from the residual curvature of the Feshbach field. After the RF flip to the $|1\rangle$ state, the atoms suddenly had the opposite magnetic moment and the residual curvature field provided a trapping potential, which sent the atoms back towards the trap center with a large potential energy. Performing the sweep quickly and at low B-field meant that the $|6\rangle$ atoms could not travel far from the center and that the anti-confining potential was very weak, reducing this issue. 15 ms after the magnetic trap is ramped off, the $|6\rangle \rightarrow |1\rangle$ sweep is performed. This is done by ramping the B-field from 5.6 G to 7.1 G over 10 ms while applying an RF frequency[1] of 240.3 MHz with an 8 W amplifier, achieving over 96 % transfer efficiency. The $|1\rangle \rightarrow 50\%\,|1\rangle + 50\%\,|2\rangle$ transfer is performed at 102.8 G by sweeping the RF frequency[2] from 60.375 MHz to 60.625 MHz linearly in 1 ms using the same 8 W amplifier and RF coil. By reducing the RF power, the fraction of transferred atoms can easily be reduced from more than 97 % to 50 %.

The Landau-Zener sweep produces a pure quantum state, such that the second RF sweep is really $|1\rangle \rightarrow \frac{1}{\sqrt{2}}(|1\rangle + |2\rangle)$. When all the atoms are in this superposition state the cloud is still *spin-polarized* in the sense that all the particles are identical and hence scattering is suppressed. In order for the cloud to thermalize, decoherence is required such that a statistically mixed state is produced. In some experiments this decoherence is implemented by doing many high efficiency Landau-Zener sweeps, back and forth from the $|1\rangle \rightarrow |2\rangle$, until a 50:50 mixture is achieved. It was found to be adequate to simply hold the superposition state for approximately 100 ms as the field is ramped to just below the Feshbach resonances. Once a basic version of the evaporation in the dipole trap had been implemented, the decoherence time was varied and the effect on the final atom number after evaporation was measured. Fig. 5.15 clearly shows that after 100 ms the cloud has fully decohered. However, if much shorter decoherence times are used (< 50 ms), then

[1] using Windfreak Synth NV 34 to 4400MHz.
[2] using a DLIC box.

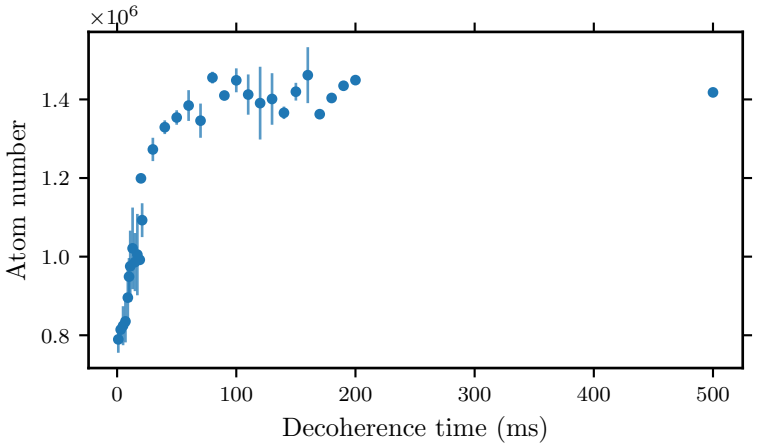

Figure 5.15: Variation of the final atom number after evaporation in the dipole trap against the time allowed for the $|1\rangle + |2\rangle$ to decohere. The decoherence is required for efficient thermalization and evaporation of the cloud of fermionic ^{6}Li. After approximately 100 ms the cloud has fully decohered increasing the time further has no effect. If the time is much less than the decoherence time, then the evaporation is very inefficient leading to a smaller atom number.

the evaporation becomes inefficient as the cloud is essentially non-interacting, reducing the final atom number. The ratio of the $|1\rangle$ $|2\rangle$ mixture can be controlled with RF power to produce spin imbalanced mixtures as shown in Fig. 5.16.

For some recent experiments the atoms have also been prepared in a $|1\rangle$, $|3\rangle$. When required this sweep is done at the same field (102.8 G) 10 ms after the $|1\rangle \rightarrow |2\rangle$ sweep. The sweep is from 120.65 MHz to 121.15 MHz over 1 ms and uses maximum RF power (8 W) with a transfer efficiency of over 95 %. After this sweep the atoms are in a coherent state $\frac{1}{\sqrt{2}}(|1\rangle+|3\rangle)$ and the same decoherence wait time as described above is required.

5.6.2 Evaporation in the Dipole Trap

At this point the spin mixture of the $|1\rangle$ and $|2\rangle$ state has been produced and the B-field is ramped to 795 G, slightly below the Feshbach resonance at 834 G. In this strongly interacting regime the scattering length is approximately $10^4 a_B$ (Section 2.2) and the short collision time means thermalization and hence evaporation can be very efficient.

During the MW evaporation in the magnetic trap, discussed in Section 5.4, the trap depth was defined by the applied MW frequency and could be controlled independently of the trap shape. In the dipole trap the depth is determined by the energy of the potential above which atoms are no longer confined to the crossed region of the dipole beams. This depth can be lowered by decreasing the beam powers, which simultaneously changes the

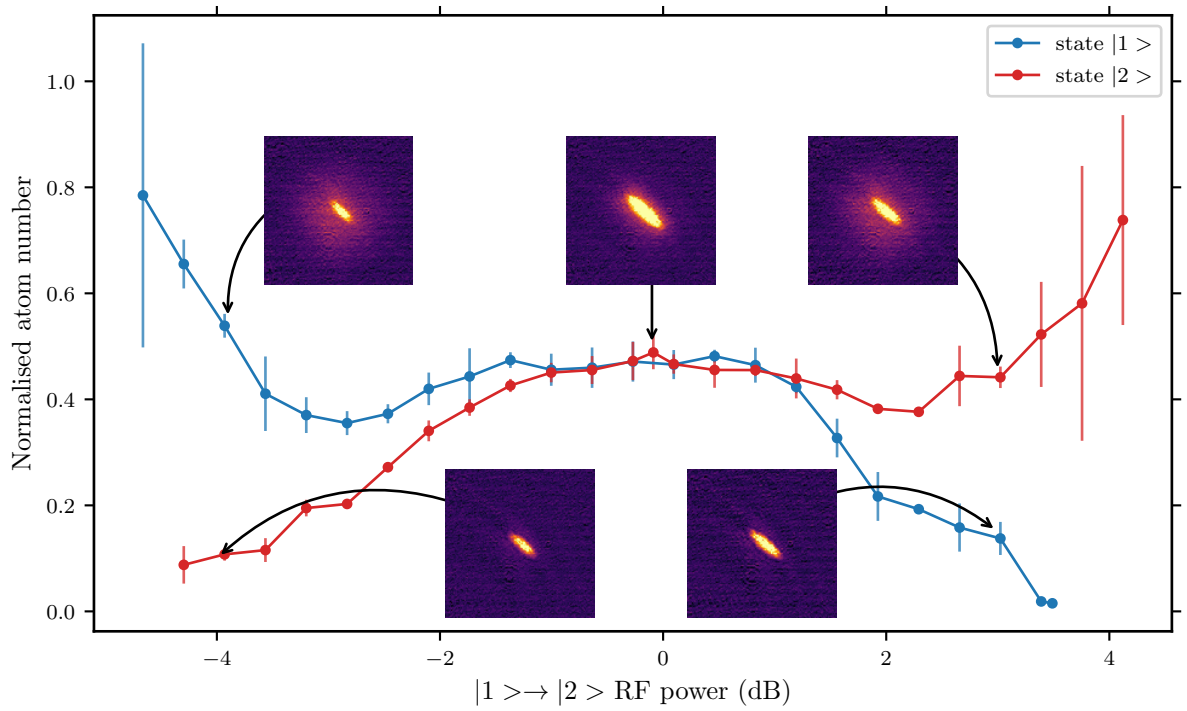

Figure 5.16: Atom number after evaporation in the $|1\rangle$ and $|2\rangle$ state of ^{6}Li as the RF power driving the $|1\rangle \rightarrow |2\rangle$ is varied. A measurement like this is used to optimize the spin balance of the mixture and adjust the RF power to an optimal value. When the power is too low (left of graph), not enough $|1\rangle$ atoms are converted to $|2\rangle$ and a large thermal background can be seen in the $|1\rangle$ state surrounding the denser molecular signal. A similar signature is seen for the $|2\rangle$ state when too much RF power is used. A broad region of RF power provides a spin-balanced mixture with an equal number of $|1\rangle$ and $|2\rangle$ state atoms after evaporation. This is because the molecules experience a deeper trapping potential and hence the unpaired atoms are preferentially evaporated. This leads to a spin balanced mixture, even if the initial mixture was slightly imbalanced. Note the relative dB scale with our optimal position set as the 0 dB reference.

trap geometry (see Eqs. (5.25) to (5.27)). The central trapping region of the dipole traps is harmonic, which means properties such as the temperature and density scale differently with trap geometry compared to the linear magnetic quadrupole trap, as was discussed in Section 5.1.2. Despite these differences the evaporation process in the dipole trap can still be optimized in a similar way to the evaporation in the magnetic trap.

The dipole beams are ramped exponentially over 0.9 s from 13 W to 0.13 W and 2×12 W to 0 W for the horizontal and vertical beams, respectively. This corresponds to changing the trap depth from 63 µK to 800 nK. Additionally, the decay constants for the evaporation can be optimized independently. It is interesting that the highest phase space densities achieved have been with evaporation that brings the vertical beam to zero confinement. In this configuration the axial trapping along the dipole beam is provided by the curvature of the Feshbach fields and is approximately 15 Hz. At the beginning of the evaporation routine the weakest confining direction is the x' direction, however, approximately half way into the evaporation the z direction becomes the weakest confining direction defining the trap depth. The z direction has the added advantage that the Feshbach field provides an anti-confining potential in this direction and hence atoms that leave along the z axis can never return to the trap. Whilst ramping down the vertical beam to zero was effective in the evaporation, it was often desirable for some investigations to have a more symmetric trap potential. It was found that the evaporation could also be optimized with the vertical beam remaining at a finite power leading to a much more symmetric trap. The two different evaporation schemes are tabulated in Table 5.1. It was found that the optimal initial vertical beam power is lower than the maximum, the reasons for this are not fully understood but are most likely caused by density related losses. In the future this additional power can be sent through the horizontal beam.

The strong interaction of ^{6}Li during time-of-flight means that it is difficult to obtain an accurate temperature. Furthermore, when the dipole trap is turned off, the cloud is expanding in a very weak harmonic potential provided by the curvature of the Feshbach fields. These problems are remedied by the rapid ramp technique (discussed in Section 6.4), which allows us to more accurately quantify the temperature and distinguish the normal and superfluid component. Nevertheless, it was possible to optimize the dipole trap evaporation by minizing the size of the expanded cloud after a fixed TOF time and to then maximize atom number at this temperature. Using the rapid ramp technique the evaporation routine in the dipole trap was characterized as shown in Fig. 5.17, which shows the appearance of the fermionic condensate. The condensate fraction was also quantified as a function of temperature and B-field in the BEC-BCS crossover (see

Table 5.1: Tabulated values of the parameters used for the forced evaporation of the dipole trap. The horizontal and vertical beam powers are exponentially ramped down according to the equation: $P_i + (P_i - P_f)\left(\frac{1-e^{-\frac{Rt}{T}}}{1-e^{-R}}\right)$ where P_i and P_f are the initial and final powers respectively, T is the total evaporation time and R is the exponential decay rate factor.

	Evaporation version 1		Evaporation version 2		Unit
Beam	Horizontal	Vertical	Horizontal	Vertical	
Initial power	13	2×4	13	2×4	W
Initial depth	65		65		µK
Final power	0.14	0	0.28	2×0.15	W
Final depth	0.8		1.1		µK
Final					
trap frequencies:	16		92		
x	69		151		2πHz
y	166		235		
z					
Atom number at T_c	1×10^7		6×10^6		

Fig. 5.18), which can be compared to the first observations in [42].

The evaporated ^{6}Li cloud is typically imaged at a high B-field. This is because as the field is ramped down, the BEC regime is entered with the formation of weakly bound and eventually tightly bound dimers. From Eq. (2.30), the binding energy of the molecule can be estimated for a given field. For sufficiently high binding energies the detuning of the molecular transition becomes significant compared to the atomic linewidth [173]. We have found that it is difficult to image the ^{6}Li molecules below 680 G. For the optimization of the evaporation, the field is simply left at the evaporation field of 795 G for the imaging process. The change in imaging frequency was automated for the experiment such that the ^{6}Li laser would automatically ramp to the correct imaging frequency by reading the field set point, ^{6}Li state and desired imaging polarization from the sequence. This was automated using part of the control software, Experiment Snake as discussed in Appendix B.5.2.

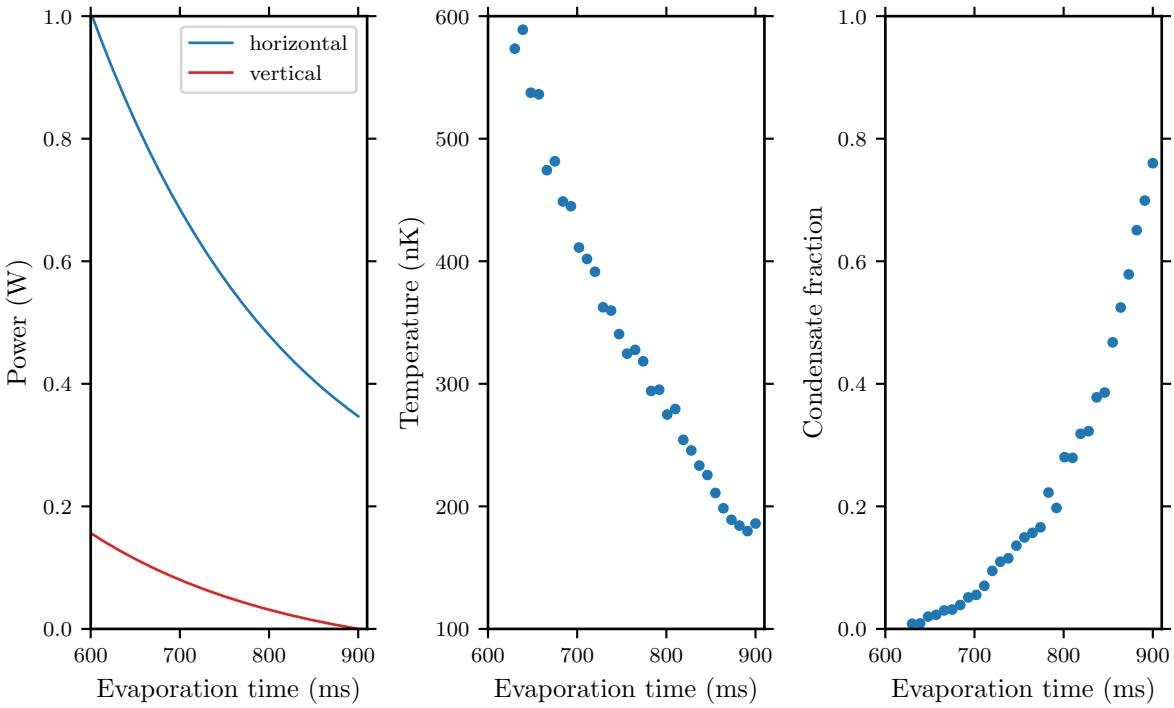

(a) Evaporation routine

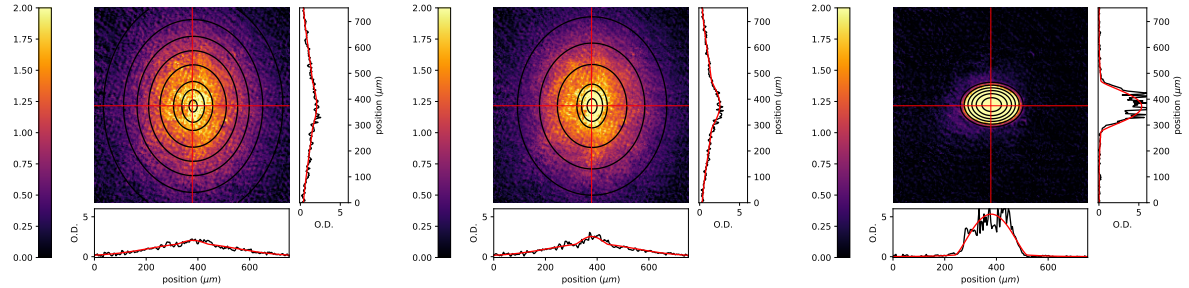

(b) 630 ms (above T_c) **(c)** 650 ms (at T_c) **(d)** 900 ms (below T_c)

Figure 5.17: Fig. 5.17a: Evaporation procedure of ^{6}Li at 795 G on the Feshbach resonance. The left plot shows the horizontal and vertical dipole beam ramps towards the end of the 0.9 s evaporation. The central plot shows the temperature fitted from the Gaussian background after rapid ramp. This underestimates the temperature due to the expansion into the harmonic confinement of the Feshbach field. **Figs. 5.17b to 5.17d**: The fitted condensate fraction at various points in the evaporation, showing the phase transition. The sliced plots are the optical densities of the single row or column shown by the red line in the image. The red line in the sliced plot is the bimodal fitted optical density shown by the contours on the image.

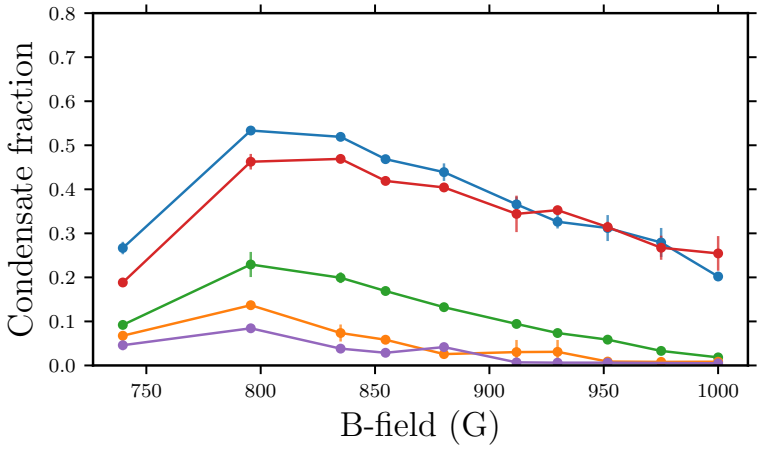

(a) With recompression

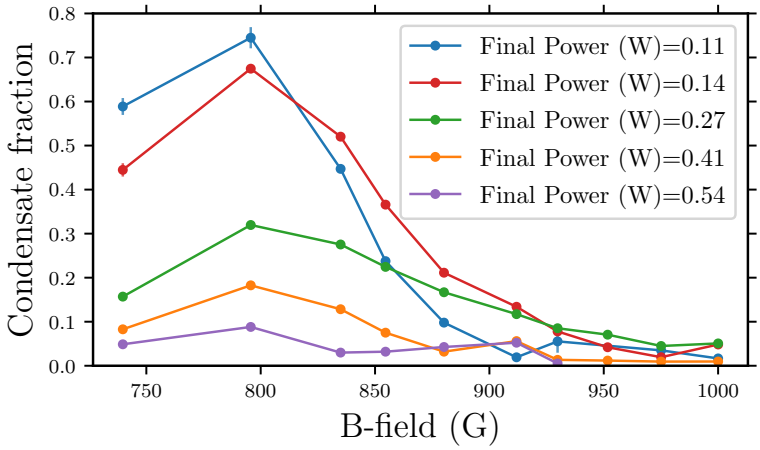

(b) Without recompression

Figure 5.18: Variation of the condensate fraction after ramping to various fields in the BEC-BCS crossover. The condensate fraction is measured with rapid ramp and the evaporation is always performed at 795 G before ramping the field. In Fig. 5.18a the trap was recompressed to the same value after the evaporation before ramping the field. This means the trap frequencies are always comparable and the trap is always large enough to hold the BCS superfluid. In Fig. 5.18b the depth was reduced without recompression and so has very low condensate fraction in the BCS regime, but the largest condensate fraction at unitarity.

5.6.3 Summary of the Experimental Sequence

This chapter has described how the ultracold Fermi gas is prepared from the MOT. With this system and experimental sequence, it is now possible to perform experiments in the BEC-BCS crossover. The sequence is summarized in Fig. 4.11 and can be studied in conjunction with Fig. 4.11, which describes the initial part of the experiment sequence. The investigations discussed towards the end of this thesis are all based on this initial sequence to produce an ultracold Fermi gas. In Chapter 6 some remaining measurements to characterize the experimental system and techniques for the investigations are discussed.

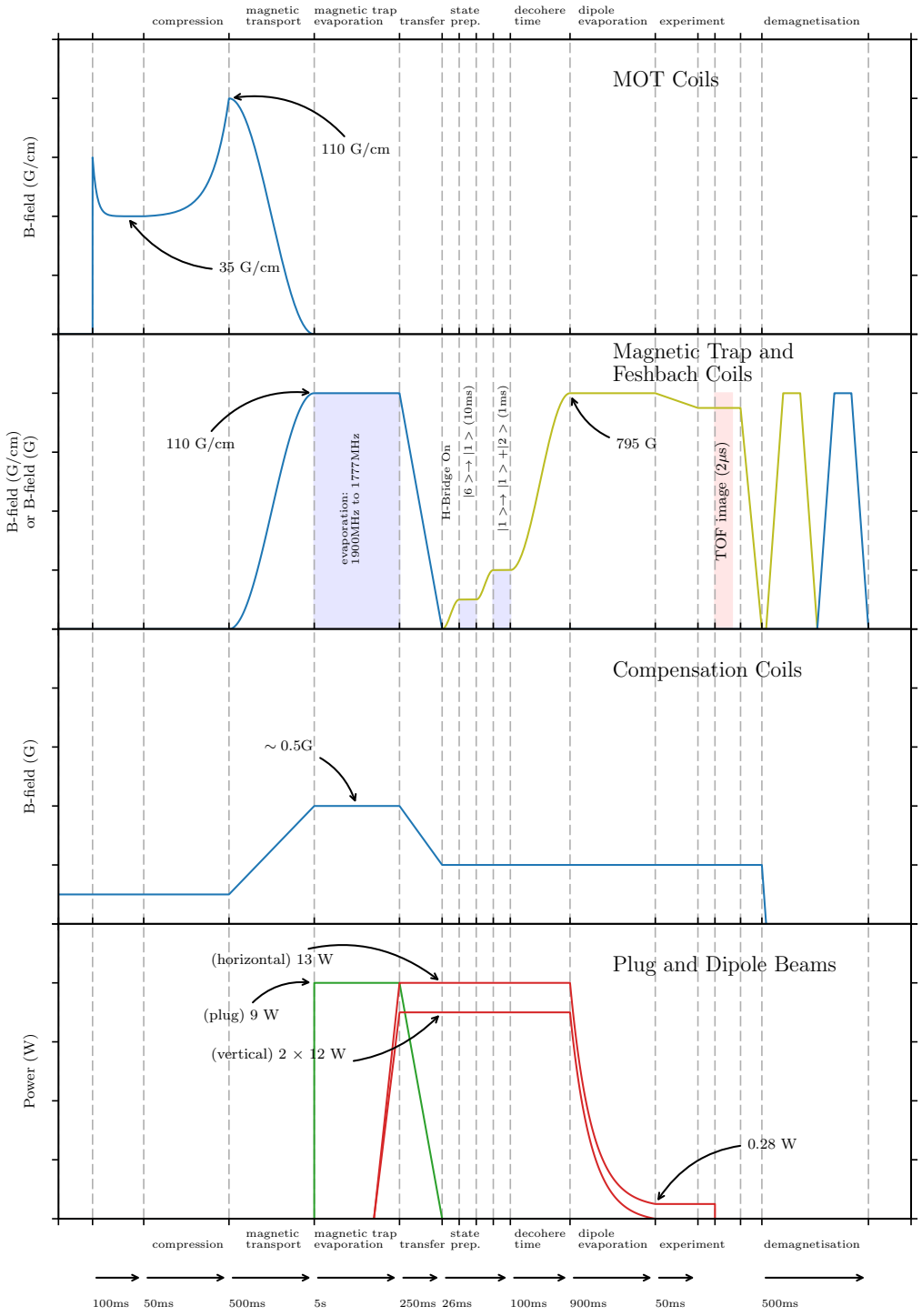

Figure 5.19: Summary of the experimental sequence from the capturing of atoms in the initial magnetic trap to the production of a BEC of ^{6}Li molecules. This plot follows on from Fig. 4.11 which shows the sequence from the Zeeman slower phase through to the optical pumping. Note that the time scale is non-linear to highlight all important steps equally. In the *Magnetic Trap and FB Coils*, the blue curve represents the field gradient when the coils are in anti-Helmholtz configuration and the yellow curve represent the field when the coils are in Helmholtz configuration. This change in coil configuration is performed by the H-Bridge. The time lengths and events are described on the x-axis. The rapid ramp technique is not shown here (see Section 6.4).

Chapter 6

Characterization of the System

6.1 Imaging

The primary measurement method in the experiment is (destructive) absorption imaging of the atoms once per cycle. This section begins by briefly introducing the basics of absorption imaging. Secondly, the manipulations performed to convert the raw CCD images into an optical density are described. Finally, the method used to calibrate the atom number more accurately, using high intensity imaging light, is explained.

Several different cameras are used in the experiment with the cheaper cameras being used for calibration and checks on the hot thermal clouds and the more expensive low noise CCD cameras being used for data taking on the degenerate clouds. Two 12-bit Basler cameras (model: acA1300-60gm) are used to take fluorescence images of the ^{23}Na and ^{6}Li MOT, respectively. A 12-bit Apogee U1 CCD camera is used along x' direction to image thermal clouds of ^{23}Na or ^{6}Li in the magnetic or dipole trap. Two 16-bit Andor iXon Ultra-897 CCD cameras are used along the x' and z axes respectively for higher quality imaging. The Andor camera has a 16 µm by 16 µm pixel size and 512 by 1024 active pixels. It is able to operate in *fast kinetics* mode where two pictures can be taken rapidly in succession (less than 10 ms apart)[1]. All the cameras discussed can be externally triggered via a TTL signal defined by the experiment control. The discussion below focuses on the analysis of the images taken with the Andor iXon cameras but is applicable to all the absorption images we take.

[1]This works by having a sub-region of the sensor illuminated. After the set exposure time the sensor is clocked vertically, shifting the image data to the area that is not illuminated. The illuminated part of the sensor can then immediately be used again and the final readout will contain several sub-images taken at different times.

6.1.1 Absorption Imaging

Absorption imaging is the most common technique for probing ultracold atoms due to its simplicity and high signal to noise ratio. This method uses the spontaneous absorption of photons in the imaging beam incident on the atomic cloud to infer a density distribution of the atoms at the time of the image[1]. A full discussion of the theory of absorption imaging (and other techniques) can be found in, for example [118, 162], with the most important results highlighted below.

The refractive index, n_{ref}, of a dilute atomic cloud is dependent on the density, $n(x, y, z)$. The imaging laser light electric field, $\vec{E}(x, y)$, traveling in the z direction, after passing through the atomic cloud, will have the form:

$$\vec{E}(x, y) = \vec{E_0} \mathrm{e}^{-\frac{2\pi i}{\lambda} \int (n_{\text{ref}}(x,y,z)-1) \mathrm{d}z} = t\vec{E_0} \mathrm{e}^{i\phi} \tag{6.1}$$

where $\vec{E_0}$ is the initial electric field vector and λ is the imaging light wavelength. This leads to a change in the amplitude, characterized by the transmission, t, and phase, ϕ, of $\vec{E_0}$. Since the CCD cameras measure the intensity, they are insensitive to the phase ϕ and measure $|\vec{E}(x, y)| \propto t^2$. Using a simple two-level atom picture for the imaging transition with the rotating wave approximation and assuming $I \ll I_{\text{sat}}$, gives a simple form for t^2:

$$t^2 = \mathrm{e}^{\left(-\frac{\tilde{n}(x,y)\sigma_0}{1+\left(\frac{2\delta}{\Gamma}\right)^2} \right)} \tag{6.2}$$

Here, $\tilde{n}(x, y) = \int n_{\text{ref}}(x, y, z)\mathrm{d}z$ is the integrated column density, δ is the detuning from resonance, Γ the transition linewidth and σ_0 the resonant cross-section (Eq. (2.25)). The term in the exponent is commonly identified as the optical density, $\tilde{D}(x, y)$, such that:

$$-\ln(t^2) = \tilde{D}(x, y) \implies \tilde{n}(x, y) = \frac{\tilde{D}(x, y)(1 + \left(\frac{2\delta}{\Gamma}\right)^2)}{\sigma_0} \tag{6.3}$$

To know t^2 one must have the intensity before and after the atomic cloud. Since this is not achievable in a single image, two images are taken in rapid succession. The first image with the atoms gives a distribution of counts on the camera, C_{atom}. Shortly after, the second image is taken with no atoms present giving a distribution, C_{light}. It is then possible to calculate $t^2 = I_{\text{atom}}/I_{\text{light}} = C_{\text{atom}}/C_{\text{light}}$, where it is assumed that both imaging pulses have the same initial intensity and pulse duration, τ. In general, the background signal from the camera is removed by taking an image with no light, giving a distribution,

[1] In comparison, fluorescence imaging uses the spontaneous emission of photons and dispersive imaging takes advantage of the change of phase of photons from the imaging beam

C_{dark}, with $C_{\text{atom}} \to C_{\text{atom}} - C_{\text{dark}}$ and $C_{\text{light}} \to C_{\text{light}} - C_{\text{dark}}$. Then $\tilde{D}(x, y)$ can be derived from the two images as:

$$\tilde{D}(x, y) = -\ln\left(\frac{C_{\text{atom}}}{C_{\text{light}}}\right) \tag{6.4}$$

Further details on how the image is processed is given in Section 6.1.2. In order to extract quantitative information about the density distribution, the magnification of the image, defined by the setup must be known. The different imaging axes in the experiment have different magnifications so that they can image different size (temperature) clouds. Fortunately, the x' imaging beam, which has the lowest magnification, also cuts a small metal feature used to house a cylindrical lens[1]. From the known dimensions of this feature, a relatively accurate magnification can be calculated. To confirm this method is not affected by distortions or diffraction of the image, a cross check was performed. A cold cloud was released from the dipole trap and its center position on the CCD was recorded as it fell under gravity with all magnetic fields off. By fitting a parabola[2] to the center position against TOF, the magnification could be extracted. The two magnifications agreed with each other to within 3 %, which could be explained by the presence of a background field gradient[3] of $0.05\,\text{G}\,\text{cm}^{-1}$. Once the magnification along one axis is known, it can be calculated for all axes by imaging an identical cloud and comparing the sizes on the different cameras. If an optical lattice is used in the experiment, a very accurate determination of the magnification is possible by looking at the density-density correlations in TOF, as described in [174, 175].

The focusing and alignment of the imaging path can be quite challenging. All imaging beams should travel through the center of the optical elements to minimize distortion. The large waist beams, sometimes needed for high magnification, should be checked to ensure they are not clipped. Once a signal is visible, the camera is moved in steps[4] to minimize the size of the imaged atom cloud as shown in Fig. 6.2. Using an in-trap BEC provides a very small feature, which can be used to focus the imaging system accurately. Dust and dirt on elements in the optical path lead to fringes and defects, and whilst they can sometimes be removed by cleaning, it is also beneficial to align the imaging system such that the beam is far from any defects.

[1] This lens may be used for ARPES in future investigations.

[2] fitting function $z = \frac{gM}{z_{\text{p}}}t^2 + z_0$, where z is the fitted center position in pixels, M is the magnification, z_{p} is the pixel size in metre, t is TOF duration, and z_0 is the initial center position on the CCD camera in pixels.

[3] The residual field gradient could be determined by using hyperfine states with different magnetic moment and comparing how they fall under gravity.

[4] step size will depend on the magnification.

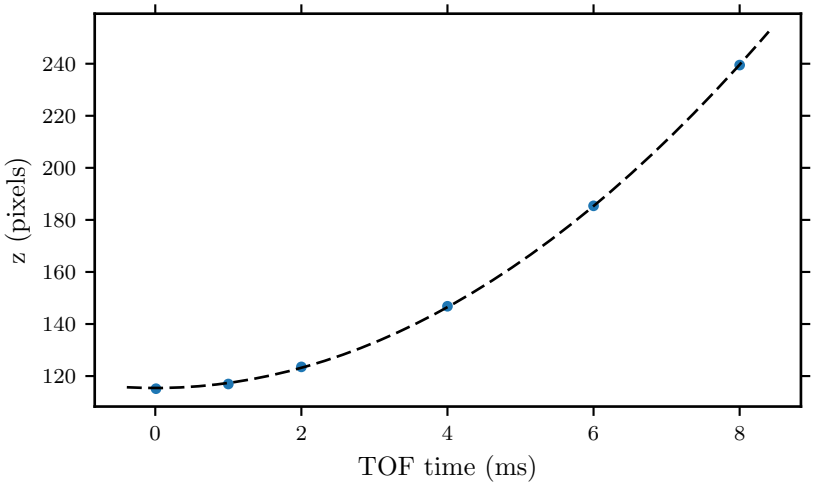

Figure 6.1: Center position of the cloud in pixels in the direction of gravity against TOF. By fitting a parabola to the center position, the magnification of the imaging system can be derived. This method assumes that there is not a large residual magnetic field gradient during the time-of-flight imaging.

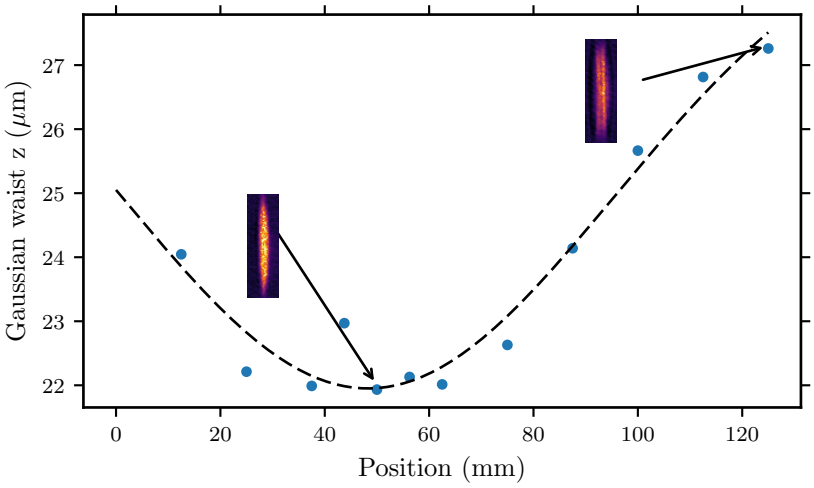

Figure 6.2: The position of the camera is varied to give the smallest focused image of the atom cloud. When the camera is far from the focused position, fringing can be seen.

Imaging should be performed with a bias field to provide a quantization axis for the different hyperfine states. When imaging the ^{6}Li atoms across the Feshbach resonance, this is often provided by the Feshbach coils. The imaging transition will also be polarization specific. A motorized waveplate mount holds a $\lambda/4$ waveplate along the z axis for imaging, meaning both σ^+ and σ^- light can be used. This is important as the strongest closed cycling imaging transition for the $|1\rangle$ and $|6\rangle$ state will be σ^- and σ^+, respectively. The automatic imaging frequency calculation implemented in the experiment control accounts for the polarization used. When imaging along the x' or y' direction in the presence of the Feshbach field, the imaging light is perpendicular to the field, meaning π polarization imaging light should be used.

6.1.2 Image Processing

Every experiment cycle, the Andor iXon camera produces one 512 by 1024 pixel image that contains both the atoms and the light image. This image can be thought of as a 2-dimensional array of integers. Following the definitions in Section 6.1.1 we first wish to remove as best as possible any dark counts from the raw image. The statistics of the dark counts are gathered by running the normal experiment cycle with the imaging optical shutters closed. It is important that one does not use a substantially different sequence for analyzing the dark images as timings and surrounding lights during the sequence can affect the average number of dark counts. By taking several hundred dark images, one can accurately determine the average and standard deviation of dark counts for a given pixel. Fig. 6.3 shows the small variation in dark counts across the image which is most likely due to the additional holding time of the second half of the CCD chip during fast kinetics imaging. The mean of the standard deviations on all pixels is 8.9 counts. This array of mean dark counts can directly be subtracted from the raw image. This average should be retaken every month to compensate for drifts or changes in the sequence timings.

After dark subtraction, there is an optional step of rescaling the images that is sometimes required for very short imaging pulses. Here a 100 by 100 region of pixels is selected far away from the atoms but also far from the CCD chip edges. The number of counts over this region is averaged for the light and atom pictures, respectively. The atom picture is then scaled by the ratio of these two averages. This can account for the imaging intensity being slightly different for the atom and light imaging pulse. It was observed that for the typical 2 µs image with around 500 counts this effect was typically less than 0.1% and hence is not included by default in the image processing.

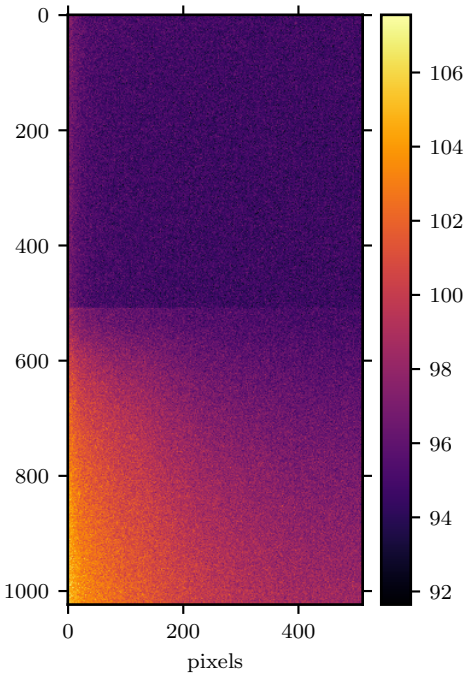

Figure 6.3: The average of several hundred dark counts images on the Andor camera. The mean dark count is 96.6 with the mean of the standard deviation across all pixels equal to 8.9. This image is subtracted from the raw atoms-light image before further processing. The counts increase slightly on one half of the image because due to the additional hold time of the second half of the CCD chip during fast kinetic imaging.

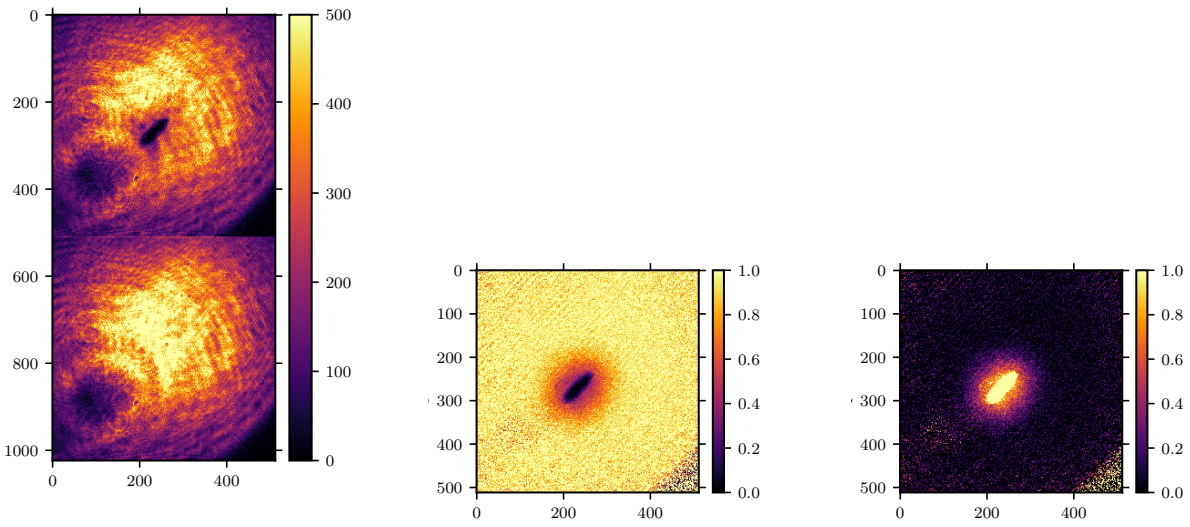

(a) raw-dark **(b)** atoms/light **(c)** optical density

Figure 6.4: Different stages of the image processing. The initial raw image (Fig. 6.4a) has the dark counts subtracted. Then the atoms and light images are cropped from the raw image and divided by one another (Fig. 6.4b). The optical density (Fig. 6.4c) is then derived by taking the negative of the natural logarithm of the image. This image shows a ^{6}Li molecular BEC after 15 ms TOF.

At this point, the atoms and light counts arrays are both corrected and the optical density is then derived using Eq. (6.4). The route from the raw image to the optical density is shown in Fig. 6.4. Note that for high optical densities, there is a non-negligible probability that C_f will be negative due to statistical fluctuations in the dark counts. This would cause obvious problems when taking the logarithm and hence the C_f array is clipped to a value of 1 count, which is the lowest valid number of counts that can be interpreted from the camera. For cases where accurate atom numbers are required, one must convert the naive optical density into a real optical density using the method described in Section 6.1.3. Finally the image is then rotated if necessary and the Experiment Eagle Software can perform fits or analysis on the image, as described in Appendix B.5.3. Additional details and measured properties of the Andor iXon camera used in the experiment can be found in the master thesis of Till Leuteritz [176].

6.1.3 High Intensity Imaging and Atom Number Calibration

Limits of Imaging ^{6}Li

In the previous section it was shown that the density distribution of the atoms can be obtained through the inversion of the optical density. In this section some important

constraints on the imaging parameters, specifically due to the low mass of ^{6}Li will be discussed. For the investigations discussed in Chapters 7 and 8 it was important to have an accurate atom number and the method of using high intensity imaging to calibrate the effective saturation intensity and calculate a more accurate atom number will be explained.

When imaging with near resonant light, the same scattering force(Eq. (4.1)) that was used in the laser cooling stages of the experiment is present. This means that the atoms will experience the scattering force during the imaging process. This causes them to accelerate and their finite velocity can lead to a Doppler shift bringing them out of resonance with the imaging light, and a finite displacement, bringing them out of the focus of the imaging system. The low mass of ^{6}Li means that the velocity change and displacement are larger than for other alkali atoms.

Assuming the light is initially on resonance ($\delta = 0$), the initial acceleration will be (Eq. (4.1)):

$$m\frac{\mathrm{d}\mathbf{v}}{\mathrm{d}t} = \hbar\mathbf{k}\frac{\Gamma}{2}\frac{\frac{I}{I_{\mathrm{sat}}}}{1+\frac{I}{I_{\mathrm{sat}}}} \tag{6.5}$$

For an imaging pulse of length, τ, and wave-vector, k, the Doppler shift will be negligible if the atoms do not acquire a velocity such that they are shifted by more than the intensity broadened linewidth. This is equivalent to:

$$\overbrace{\frac{\hbar k^2\Gamma}{2m}\frac{\frac{I}{I_{\mathrm{sat}}}}{1+\frac{I}{I_{\mathrm{sat}}}}\tau}^{\text{doppler shift}} \ll \overbrace{\Gamma\sqrt{1+\frac{I}{I_{\mathrm{sat}}}}}^{\text{linewidth}} \tag{6.6}$$

which can be simplified to give a limit on τ:

$$\tau \ll \frac{2m}{\hbar k^2}\frac{\left(1+\frac{I}{I_{\mathrm{sat}}}\right)^{3/2}}{\frac{I}{I_{\mathrm{sat}}}} \implies \tau_{^6\mathrm{Li}} \ll 2.16\,\mu\mathrm{s}\frac{\left(1+\frac{I}{I_{\mathrm{sat}}}\right)^{3/2}}{\frac{I}{I_{\mathrm{sat}}}} \tag{6.7}$$

where the properties of ^{6}Li have been used to give the numerical form. For a typical intensity of $\frac{I}{I_{\mathrm{sat}}} \approx 0.3$, this gives a limit of $\tau \ll 14.2\,\mu\mathrm{s}$. In Fig. 6.5, the imaged atom number is shown against the detuning for various pulse lengths at fixed $\frac{I}{I_{\mathrm{sat}}} \approx 0.3$. As the pulse length is increased the resonance frequency shifts and broadens and the peak amplitude is reduced. A pulse length of 2 µs is typically used in the experiment. To predict the Doppler broadened profiles in the limit of large τ or $\frac{I}{I_{\mathrm{sat}}}$ one must account for the changing Doppler shift during the imaging pulse as the atoms are accelerated [177].

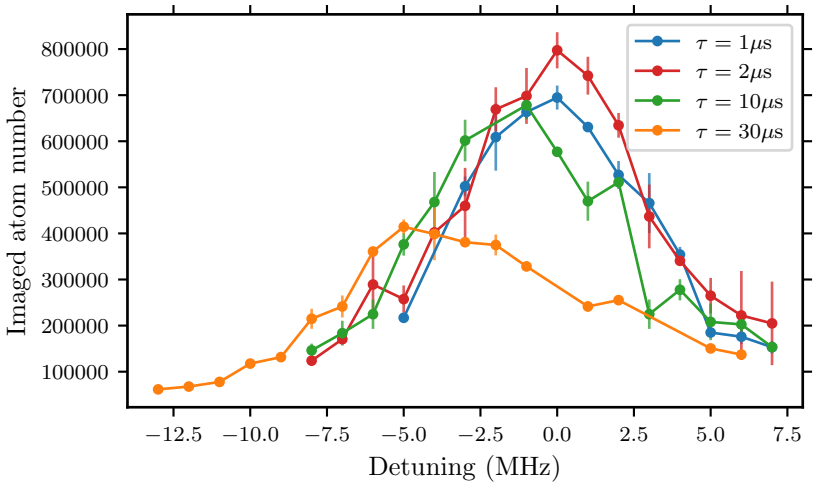

Figure 6.5: Number of atoms imaged as detuning is varied for various pulse lengths at fixed I/I_{sat}. As the pulse length becomes longer, the Doppler shift during the imaging pulse becomes significant and so the center frequency is shifted, the resonance broadened and reduced in amplitude. In the experiment a pulse length of 2 µs is typically used.

Secondly, the distance traveled by the atoms from the imaging pulse must be shorter than the depth of field, $d = \frac{\lambda}{\text{NA}^2}$, which, again using Eq. (6.5), gives a limit on τ:

$$\tau \ll 2\sqrt{\frac{md}{\hbar k\Gamma}\left(\frac{1}{I/I_{\text{sat}}}+1\right)} \implies \tau_{^6\text{Li}} \ll 1.04\times10^{-3}\,\text{sm}^{-1/2}\sqrt{d\left(\frac{1}{I/I_{\text{sat}}}+1\right)} \tag{6.8}$$

where again the properties of ^{6}Li have been used for the numerical form on the right hand side. For the z imaging axis, which has a depth of focus of approximately 110 µm, this gives a limit of $\tau_{^6\text{Li}} \ll 11\,\mu\text{s}\sqrt{\left(\frac{1}{I/I_{\text{sat}}}+1\right)}$, providing a similar bound to the Doppler shift limit for the typical I/I_{sat} used. For the absorption imaging to provide quantitative results, the conditions in Eqs. (6.7) and (6.8) must always be met, regardless of the I/I_{sat}. For ^{6}Li, the low mass means these limits are quite low and a pulse length of 2 µs is used by default. It is challenging to perform pulses of uniform power of less than 1 µs and pulses of less than 100 ns approach the limit of the AOMs used. The 2 µs pulse time means both the Doppler and depth of field limit are well met and the explicit check shown in Fig. 6.5 confirms this. The limits are shown in Fig. 6.6.

High Intensity Calibration of the Saturation Intensity

In Section 6.1.1 it was shown how the optical density could be inverted into an atomic density which can be used to calculate the atom number. However, this conversion de-

pended on the saturation intensity for the two level transition, I_{sat}. During the imaging process, the effective saturation intensity may be changed by optical pumping, polarization effects or the presence of magnetic fields, which can be captured by a heuristic scaling: $I_{\text{sat}} \to I_{\text{sat}}^{\text{eff}}/\alpha$. Characterizing and correcting this $I_{\text{sat}}^{\text{eff}}$ was first performed in [178] and is also shown in [174, 175, 179]. Following [178], Beer's law for the variation of the intensity of resonant light over the atomic cloud can then be written as:

$$\frac{\mathrm{d}I}{\mathrm{d}z} = -n\frac{\sigma_0}{\alpha}\frac{1}{1+I/I_{\text{sat}}^{\text{eff}}}I = -n\sigma(I)I \tag{6.9}$$

where σ_0 is the resonant cross-section, n, is the atomic density, and the right hand side shows that this can also be recast as a cross-section, σ, that depends on the intensity, I. In Section 6.1.1 it was assumed that $\sigma(I) \to \sigma_0$, leading to exponential decay of I. Eq. (6.9) can be solved to give:

$$n\sigma_0 = -\alpha\overbrace{\ln\left(\frac{I_{\text{atom}}}{I_{\text{light}}}\right)}^{\text{optical density}} + \overbrace{\frac{I_{\text{light}} - I_{\text{atom}}}{I_{\text{sat}}}}^{\text{high-intensity correction}} \tag{6.10}$$

which shows that in the low intensity limit ($I_i \ll I_{\text{sat}}$), the density only has the correction factor, α, meaning this parameter is required to extract accurate densities. Of course, in the experiment the counts on the CCD camera, rather than the real intensity are measured which means Eq. (6.10) should be recast as:

$$n\sigma_0 = -\alpha\overbrace{\ln\left(\frac{C_{\text{atom}}}{C_{\text{light}}}\right)}^{\text{optical density (x-axis)}} + \overbrace{\frac{C_{\text{light}} - C_{\text{atom}}}{C_{\text{sat}}\frac{\tau}{\tau_0}}}^{\text{high-intensity correction (y-axis)}} \tag{6.11}$$

where $I_{\text{light,atom}}$ have been replaced by $C_{\text{light,atom}}$, for a pulse of length τ. C_{sat} is the number of counts at I_{sat} with a pulse, of arbitrarily chosen length, τ_0. The *x-axis* and *y-axis* labels in Eq. (6.11) refer to those in Fig. 6.8. By preparing an identical cloud many times with same sequence it can be assumed that the real n is the same in each image taken. Hence, by binning the image of the atom into rings of approximately uniform density, and plotting the two terms in Eq. (6.11), α can be determined for each ring of uniform density. To do this the intensity or pulse length of the imaging must be varied from image to image to scan a sufficient range on the x and y axes. Simultaneously the two limits shown in Eqs. (6.7) and (6.8) must be satisfied as highlighted by the black points in Fig. 6.6. The average number of counts in the region of the atoms on the CCD was calibrated for various AOM RF powers (I/I_{sat}) and τ. C_{sat} is calculated by measuring the imaging beam power

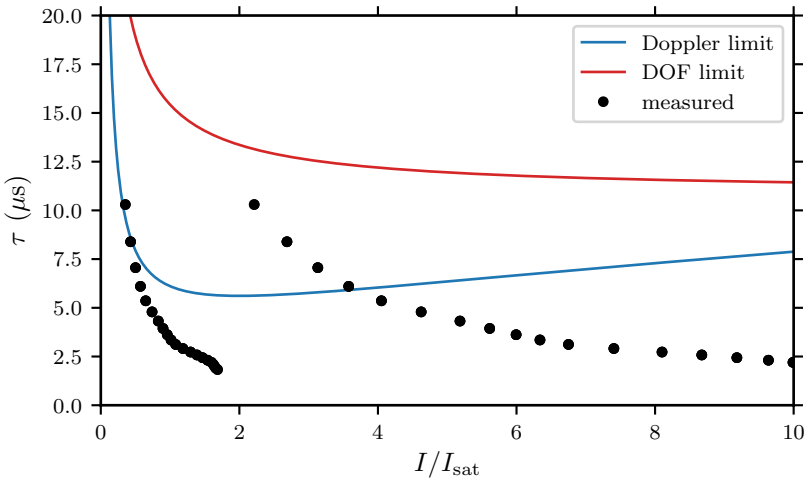

Figure 6.6: Imaging constraints caused by the Doppler limit (Eq. (6.6)) and the depth-of-field limit (Eq. (6.8)). The black points show the imaging pulses used for the measurements for the atom number calibration. Almost all of the points were below the required limits.

and counts on the camera. The beam waists of the imaging beam are measured with a profiling camera and ABCD matrices are used to extrapolate the waist of the imaging beam at the position of the atoms. A photodiode was used to ensure that the power when pulsing the AOM for the image was similar to that when using the power meter continuously. Given the $I_{\mathrm{sat}} = 2.54\,\mathrm{mW\,cm^{-2}}$ for ^{6}Li, a value of $C_{\mathrm{sat}} = 1650(100)$ was calculated, where the uncertainty is limited by the power measurement.

An example of an analyzed image is shown in Fig. 6.7. The image is fitted with a Gaussian, which gives a center position and aspect ratio of the cloud. Elliptical rings (shown by the thin red lines) are then drawn about the fitted center with a fixed ring width to match the aspect ratio of the cloud. These thin elliptical rings mark the regions that are assumed to have approximately constant density. For each ring, the x-axis and y-axis quantities defined in Eq. (6.11) are calculated by averaging these quantities over all pixels within the ring. The standard deviation of these quantities is also calculated to provide the error bars. The extracted data is shown in Fig. 6.8, where each individual colored point is the average over a single ring in a single TOF image. For various images, the same rings have the same colors. For each individual ring (a single set of colored points), assumed to have uniform density, a straight line can be fitted that allows α to be extracted. This α value can be associated with a particular average optical density and it is seen that α varies with optical density, particularly at optical densities greater than three. This whole procedure can be done for different TOFs which changes the density distribution. This acts as a useful check, that a similar α calibration is determined, independently of

the chosen TOF. It was noted that for very dense clouds, when the number of counts was low, the method does not work well and very steep gradients were fitted giving very high values of α. At these optical densities, almost no light reaches the CCD camera after the atoms, and the shot noise and variations in dark counts can dominate the image. To better characterize these high optical densities, the limits of Eqs. (6.7) and (6.8) were approached which may give a more accurate α at higher optical densities. The calibrated value of α can then be plotted as a function of optical density. Using an interpolation function, this calibration has been implemented in the experiment analysis software to allow for an optional correction of images, before fitting, where all optical densities are scaled by $\alpha(\mathrm{OD})$. This calibration curve is shown in Fig. 6.9, where the α error bars are derived from the standard error in the fitted gradient and the optical density error bars come from the standard deviation in optical density over a given ring. At very high optical densities above 3.5, the fitted gradients have a very large error. These values are ignored in the interpolation function. Ideally, to quantify an accurate atom number in the experiment, the TOF should be adjusted to keep the optical density below two over the image. However, when imaging the large ^{6}Li molecular BECs after the rapid ramp, at our coldest temperatures the condensate still has an optical density larger than four after 15 ms TOF. Detuning, the imaging light is often one solution for dealing with very large optical densities. However, detuning by large amounts introduces refraction effects and can distort the image. Furthermore, when detuning it can be impossible to find a regime where both the condensate and thermal fraction can both be seen with reasonable optical densities. These high densities in the condensate can still lead to underestimating the condensate fraction in the experiment. When the experiment is far on the BCS side of the Feshbach resonance, or when the system is quenched out of equilibrium, the condensate fraction is low, meaning this does not affect the numbers so greatly.

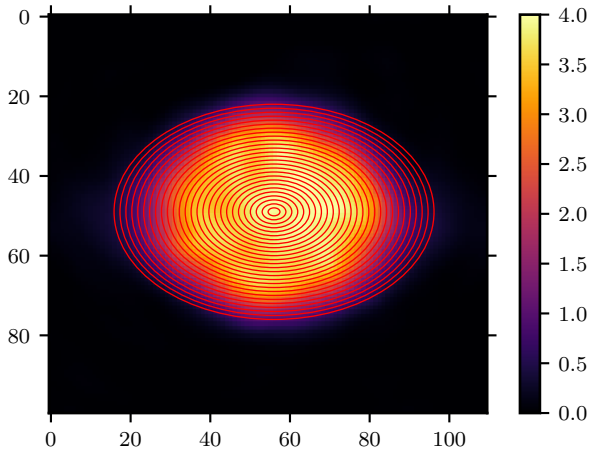

Figure 6.7: An example image of the ^{6}Li cloud after a fixed TOF time with a chosen intensity, I, and pulse length, τ. By repeating the same preparation sequence for the atoms, an identical cloud is repeatedly produced. The red lines highlight the elliptical rings that form the bins for the analysis. It is assumed that the same ring has the same constant density in every picture. The cloud is fitted by a Gaussian to determine the center and aspect ratio of the rings. Each ring in a single image produces a single point in Fig. 6.8. A single ring is given a particular color point in Fig. 6.8 and over many images provides many points which can be fitted with a straight line to extract α. The number of pixels in a ring will increase with the radius and hence the noise in the central rings may be larger due to fewer pixels.

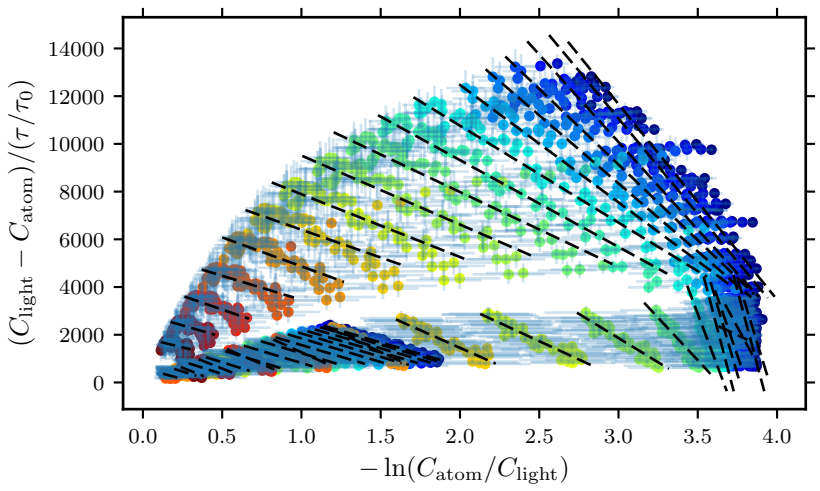

Figure 6.8: Scatter plot used to extract the values of α for varying optical density. Each group of colored points represents a single ring imaged with many different intensities or pulse lengths. Each group of colored points can then be fitted with a straight line to extract the value of α given the measured value of C_{sat}. The error bars on each point are given by the standard deviation of the x-axis and y-axis quantities over the ring. The whole procedure can be repeated for different TOF times, for which the rings are recalculated. This is why the figure can be seen to split into two parts, where the lower lines were from a different TOF time. It can be seen that at high optical densities, with low count numbers it is not possible to extract a gradient.

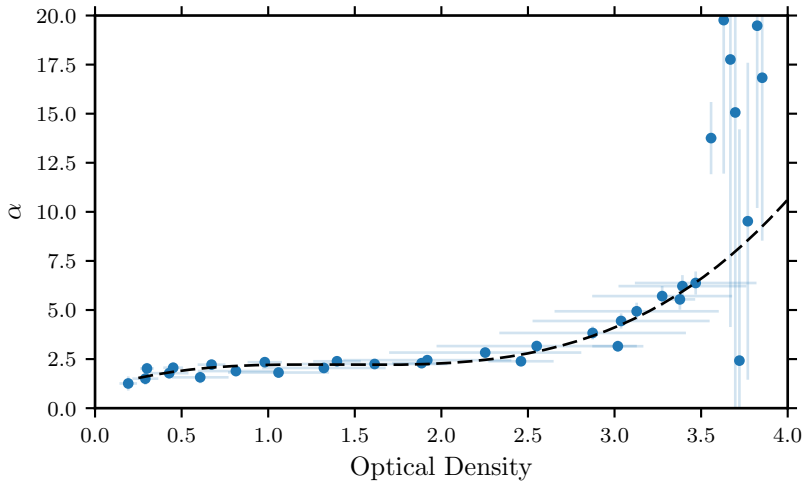

Figure 6.9: Calibration curve of α against optical density. From Fig. 6.8, a value of alpha can be calculated for a given OD for each fitted line. The average OD for a given line (corresponding to a single ring) gives the value on the x-axis, and the standard deviation of the optical densities in a ring provides the x error bar. The error in the α value is determined from the uncertainty in the fitted gradient. At high optical densities some of the low count images give unreliable fits with large error bars and are not included in the fitted curve shown by the dashed black line. The dashed black line is a cubic fit. This calibration can be used to scale the images from the experiment before fitting to extract an accurate atom number.

6.2 Measurement of the Trap Frequencies

The potential experienced by atoms in the dipole trap can be well approximated by a harmonic potential, as was discussed in Section 5.5. This harmonic potential can be completely characterized by the beam waists and powers, which together define the trap depth and frequencies. These trapping frequencies define the time scales for dynamics in the trap and the energy scale for degeneracy. Hence, an accurate measurement of these frequencies is often required to calibrate the Fermi energy and densities for the investigations performed. Whilst the numerical simulations discussed in Section 5.5.1 give a predicted value of the trap frequencies, it is important to actually measure the real frequencies. This firstly acts as a confirmation that the dipole beams are well aligned and have a good beam profile, as distortions or defects in the beam profile will often substantially change the potential and lead to anharmonicity. Secondly, by measuring the exact trapping frequencies with a known beam power, it is possible to extract an accurate measure of the beam waists and magnetic field gradients across the atoms.

Several methods have been used to measure the trap frequencies in the experiment. The first attempts to measure the trap frequencies were performed by exciting a breathing mode in the cloud by pulsing one of the dipole beams off for approximately a quarter pe-

riod. The breathing mode can be seen in the oscillation of the size of the Gaussian cloud in TOF expansion and for a classical gas should oscillate at twice the trap frequency in a given direction. This method has the advantage that it works well with clouds that are still quite hot and when the trap depth is still quite high. However, at low temperatures, interactions can affect the breathing mode frequency, meaning this method is not well suited for extracting the harmonic frequencies [180–183]. An alternative method is to oscillate one of the dipole beam powers at a frequency, ω_{drive}, and observe at which frequencies there is significant heating or atom loss. Whenever $\omega_{\text{drive}} = 2\omega_i$ there should be significant heating and by varying ω_{drive} it should be possible to extract the trap frequencies. This method is sensitive to anharmonicities in the trap and the peaks we observed were very broad for high temperatures, where it is likely some of the cloud occupies space outside the harmonic regime of the trap. Some groups use the parametetric heating's sensitivity to anharmonicity to extract a precise measurement of the trap frequencies [184]. Parametric heating provided a reproducible and controllable method to heat the cloud, which was used for some of the non-equilibrium experiments in Chapter 8.

The third method involves displacing the atom cloud by a small amount (typically 1/4 the $1/e$ in-trap radius in the given direction) and then releasing it and observing the subsequent oscillations in the harmonic potential. This method, which directly excites the dipole mode, has proven to be the most effective in our experiment. One disadvantage of this method is that when the cloud is very hot or the trap frequencies very high, it can be difficult to displace the cloud by enough that the oscillations can be easily observed.

To displace the cloud, the gradient x'-y' line wires were used (attached to MOSFET Box 2 see Section 3.4.7), which run along the x' and y' directions approximately 6 mm above the atoms in the z direction. These wires apply a gradient in the z direction B-field in the x'-y' plane and hence displace the cloud in both the x' and y' direction. How large the displacement is depends on the actual trap frequencies with a smaller frequency leading to a larger displacement. To excite the dipole mode, the current in the coil is ramped to 40 A in 15 ms, displacing the cloud by approximately 5 to 50 µm and then the current is suddenly turned off using a MOSFET. The displaced cloud then oscillates in the original harmonic potential and the trap frequencies can be extracted by recording the displacement of the fitted center of the cloud against time. The method is very similar for the z direction except with a different coil being used to provide the displacement. Gravity will slightly affect the trap frequency in the z direction.

An example of this measurement is shown in Fig. 6.10 at the end of the standard evaporation routine, giving fitted trap frequencies of $(\omega_x, \omega_y, \omega_z) = 2\pi \times (16.3, 69.4, 166.0)$Hz.

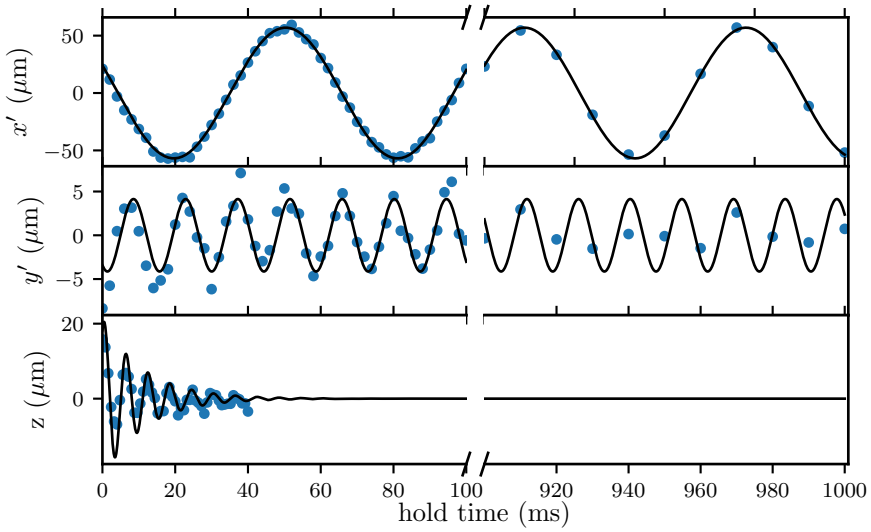

Figure 6.10: Measurement of the trap frequencies in all directions using the dipole mode. By ramping a B-field gradient in the z direction over 15 ms, the cloud is displaced by a few tens of µm before suddenly turning the field gradient off. The cloud then oscillates in the harmonic potential provided by the dipole beams. There is very little damping in the x' and y' directions and oscillations still persist after nearly 1 s. This gives an accurate determination of the trapping frequency. In the z direction the decay is much faster as atoms spill out of the trap during the oscillation. The black lines show the fitted curves to the data over the entire time range from which the frequencies $(\omega_x, \omega_y, \omega_z) = 2\pi \times (16.3, 69.4, 166.0)$Hz are extracted.

It is interesting to see that in the x' and y' directions there is very little damping in the oscillations even after 1 s. In the z direction much more significant damping is observed. Since the z direction has the lowest trap depth, it was found that during the dipole mode excitation many atoms would leave the trap along the z direction during the oscillation, taking energy from the system and leading to damping. To extract this frequency an exponentially decaying sine-squared was fitted to the data, which accounts for the slowing of the frequency from the decay. Note that with the vertical beam off, the confinement in the x' direction ($2\pi \times 16.3$ Hz) is provided by the residual curvature of the Feshbach fields.

By taking one set of measurements with the vertical dipole beam off and one with both beams on, the trapping frequencies as a function of beam power can be extracted for both beams. Furthermore, if the trap frequencies are measured for several different powers, one can fit the simulated trap frequencies using the framework described in Section 5.5.1 to extract a precise value for the different beam waists. This is shown in Fig. 6.11 and clearly shows the effect of gravity on the trapping potential as the intensity is reduced. From this measurement the extracted focused beam waist radii were found to be 59 µm by 155 µm (z by y') for the horizontal beam and 106 µm by 96 µm (x' by y') for the vertical beam.

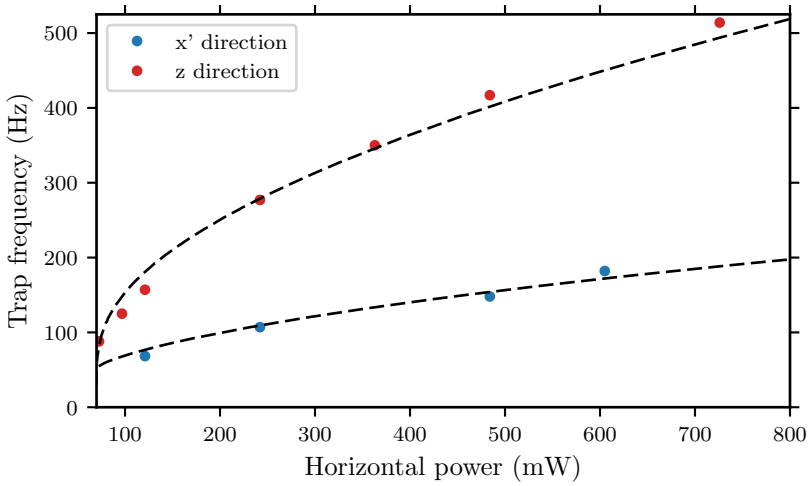

Figure 6.11: Measured trap frequency against the power in the horizontal beam. By fitting this data to the simulated curves for varying beam waist, estimations of the real beam waist at the position of the atoms can be made. This measurement was also done for the vertical beam waist and the black dashed lines represent the simulated values when using the fitted beam waists that minimize the residual error in all data sets. Note that for the z-direction it clearly deviates from the $\omega \propto \sqrt{P}$ due to the effect of gravity distorting the trapping potential at low powers.

This is in reasonable agreement with the chosen values measured with the beam-profiling cameras of 50 µm by 120 µm and 120 µm by 120 µm as described in Section 5.5.2.

6.3 Calibration of the Magnetic Field

For the investigations discussed in this thesis (Chapters 7 and 8), which take advantage of the broad Feshbach resonance of ^{6}Li, a precise control of the B-field at the position of the atoms is required. The B-field of the Feshbach coils was measured before the vacuum chamber was closed (see Section 3.4.4), however, for these values to be useful, an accurate value of the current is required. Furthermore, if the atoms are off-center from the symmetry point of the coils or if some part of the vacuum system is magnetized during the cycle, it may be difficult to predict the true B-field at the position of the atoms. Several techniques are used to measure and calibrate the B-field at the position of the atoms in the experiment with increasing levels of precision. Section 6.3.1 discussed how the imaging resonance of ^{6}Li was used to provide a coarse B-field calibration over a large range. Section 6.3.2 describes how the B-field is actively regulated at crucial time steps to provide a more stable and precise B-field than the internal regulation of the power supply. Finally, in Section 6.3.3 the physics of Rabi oscillations and how they were used to accurately measure the B-field and quantify the stability is explained.

6.3.1 Calibration with High Field Imaging of ^{6}Li

During the setup of state preparation and Feshbach evaporation stages, it was necessary to image the ^{6}Li atoms at various fields (0 to 800G). The resonance frequency of the (strongest) imaging transition depends on the hyperfine state, the polarization and, crucially, the B-field. The exact resonance frequency for a given B-field can be predicted from the Breit-Rabi diagrams and accurately known properties of ^{6}Li (see Fig. A.2). By measuring the location of the imaging resonance, the real magnetic field can then be extracted. The accuracy of this method is determined by the linewidth of the imaging transition (5.8724 MHz [126]) and the gradient of the imaging frequency with magnetic field ($\sim 1.4\,\mathrm{MHz\,G^{-1}}$ for the $|1\rangle$ state, polarization σ^-). Since the center frequency of the Lorentzian can be accurately determined (typical standard error of 150 kHz[1]) this method can determine the B-field value to approximately 200 mG. In Fig. 6.12a some example data from this method is shown. A given B-field set point is chosen by using the measured current to field conversion and assuming a perfect linear response of the power supply current with the control voltage used to set the current. This set point also gives an initial guess for the real B-field and imaging frequency. The B-field is determined by measuring the deviation of the imaging resonance frequency from the predicted frequency for the set point. This method was performed for 25 different field values and the real B-field as a function of set-point B-field was fitted with a third order polynomial as shown in Fig. 6.12b. This calibration meant the B-field was known to approximately 200 mG over the range 0 to 1150G. Additionally, using this field calibration gave the imaging frequency required (for any state or polarization) at a given B-field. This was used in the automatic frequency shift to image the ^{6}Li atoms at high field as described in Appendix B.5.2.

6.3.2 Field Regulation and Measurement with Current Transducer

The Feshbach coils are powered by the Delta 600 A 30 V hybrid power supply composed of two Delta 400 A 15 V and one Delta 200 A 30 V running in master-slave configuration. The specified current stability of this supply is 10×10^{-5} with an rms ripple plus noise of 2 mA [185]. The noise and stability of the power supply can cause issues when performing RF flips (as discussed in Section 6.3.3) and is crucial to some of the investigations performed. In Fig. 6.13, the variation of the average field during the Feshbach evaporation is plotted

[1]Standard error calculated from the estimated covariance matrix of the fitted parameters.

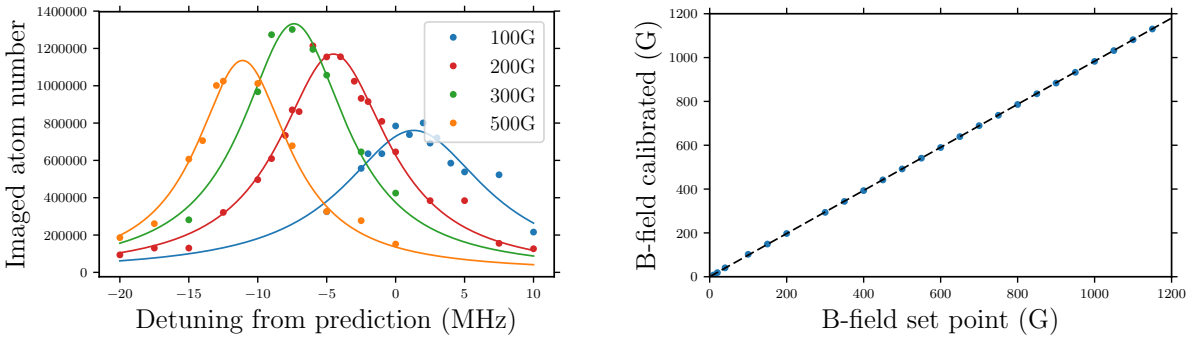

(a) Finding the imaging resonance at different B-fields.

(b) B-field set point against calibrated field.

Figure 6.12: Fig. 6.12a: Imaging resonance of ^{6}Li at various magnetic field set values. For a given field, the frequency of the imaging resonance can be accurately predicted from the known Breit-Rabi shifts of the ground and excited states. By comparing how much the imaging frequency needs to be detuned from the predicted value, the real B-field for a given set point B-field can be extracted. The x-axis shows the detuning in MHz from the predicted resonance frequency. The different color curves are for different B field set points (i.e. different coil currents) with the set points calculated using the $\mathrm{G\,A^{-1}}$ property of the coil. The solid curves are fitted Lorentzians with the center frequency giving the real field measurement. The linewidths are all fitted at approximately 6 MHz close to the known value for the linewidth of ^{6}Li. These curves were taken with the ^{6}Li atoms in the $|1\rangle$ state using σ^- polarization. The differences in peak imaged atom number can be due to the variation of the imaging transition strength with B-field. **Fig. 6.12b**: resulting calibration of the B-field using this method. Each fitted Lorentzian in Fig. 6.12a gives a single data point which are then fitted with a third order polynomial. This calibration is permanently used to determine the imaging frequency at arbitrary fields.

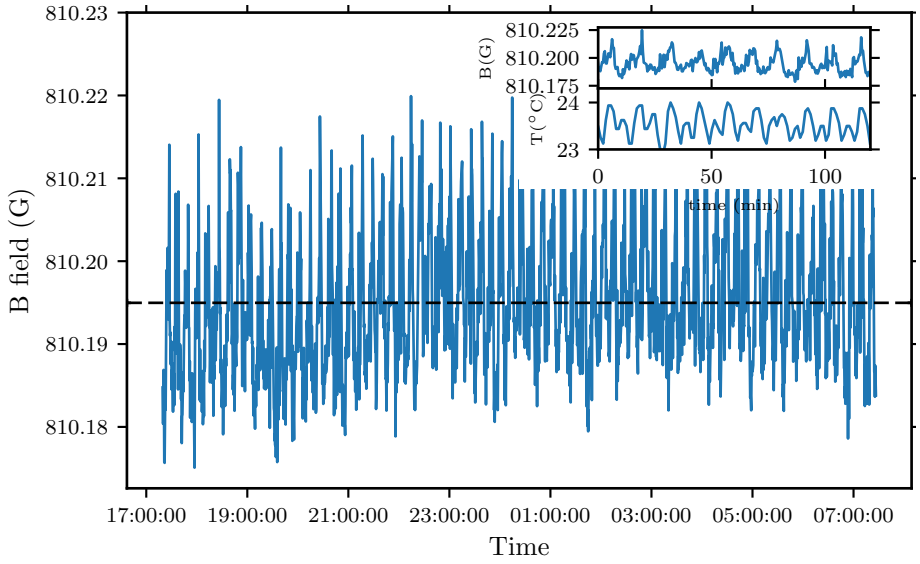

Figure 6.13: Average field value during the Feshbach evaporation without active PID regulation of the current. The field value is derived from the measured current in the coils using the current transducer. A slow drift is visible in addition to an oscillation of peak-to-peak amplitude 40 mG and period 11 min. The black dashed line shows the mean of the average fields. The inset plot shows the same field recording with the temperature inside the cooling tower where the power supplies are stored. From this plot it is clear the drift in current through the coils is correlated with the oscillating temperature (approximately 0.75 °C).

against time. The slow drift and oscillations were found to be correlated to the 0.75 °C oscillation[1] of temperature inside the cooling tower housing the power supplies. This section describes how the current of the Delta 600 A 30 V is actively regulated to reduce the noise and increase the reproducibility of the magnetic field. In Section 6.3.3 the atoms will be used to measure the field noise and reproducibility, confirming the results found from accurately measuring the current in this section.

Implementation

The magnetic field is regulated based on the measured current. The current is measured by an *ITN-600s Ultrastab* transducer capable of measuring currents with 1×10^{-6} accuracy with a bandwidth of 1 kHz. The output current of the transducer is converted to a voltage using a 5 Ω metal foil resistor[2] with an extremely low thermal coefficient of 0.2ppm°C^{-1}. Two identical current transducers are used in the setup. The signal from the first current

[1] This is much larger than the temperature oscillation on the experiment table, which is regulated by the FFU air conditioning to less than 0.1 °C.

[2] The resistor *Vishay Y1690-10A-ND* will actually be dominated by self heating $4 \times 10^{-6}\,\Omega\,\mathrm{W}^{-1}$ and at maximum current 0.8 W will be dissipated. Two 10 Ω resistors are used in parallel and are mounted to a copper block to provide thermal dissipation.

transducer, positioned inside the H-bridge box, is sent to a custom built digitally controlled PID circuit designed within the research group by Akos Hoffman and Daniel Pertot. A functional block diagram and some additional details of the PID circuit are provided in Fig. 6.14. The set point for the PID comes from an analog channel[1] (NI-PCI-6733) from the experiment control system (Appendix B.5). The second current transducer is used to independently monitor the current. It is positioned across the copper leads of the top Feshbach coils[2] and the signal is sent to a 5×10^{-7} accuracy digital multimeter (*Agilent 34411A*). This digital multimeter is controlled by the Experiment Snake software (see Appendix B.5.2) and can be triggered to record the current signal during the sequence[3]. Since the majority of the sequence had been programmed and optimized without the B-field regulation, it would not have been convenient to switch to a system where the B-field regulation was always used. Furthermore, the PID parameters required for the fast ramps and varying field values, used in the beginning of the sequence, would be very different to the PID parameters required to optimize the high constant fields needed for the precise RF flips. Hence, an analog switch was used such that in normal operation the power supply was directly controlled by an analog signal, and with a TTL trigger, could be controlled via the described PID circuit. A sketch of the described implementation is shown in Fig. 6.15.

Analyzing the field stability

Whilst the atoms will be used for the most accurate measure of the field stability, the current transducer also gives an accurate measure of the B-field. By taking many traces of the current with the transducer and digital multimeter, the drift in the average field, rms noise and noise spectrum can be calculated. By comparing these quantities with and without the active regulation, the improvement can be quantified. Before analyzing the PID circuit, the properties of the analog signal and the residual noise on the multimeter were analyzed. The analog signal was found to have a relative noise of $V_{\mathrm{rms}}/\bar{V} = 2.6 \times 10^{-6}$ at set voltage of 5 V, which provides a limit to the accuracy that can be achieved with the PID regulation. By measuring the voltage on the multimeter when it is short-circuited,

[1] The internal set-point multiplier of the PID box is used such that the 2 V corresponding to 600 A becomes 8 V making better use of the 0 to 10V range of the analog signal.

[2] It is positioned such that it does not measure the current through the 500 Ω parallel resistor (see Section 3.4.5) in the snubber circuit, but only the current through the Feshbach coils.

[3] The implementation with Experiment Snake means sequence variables control the precision of the multimeter and the measurement duration. The sample time of the measurement is automatically chosen as the minimum time to give the specified precision. The complete time-current trace is saved for every sequence for later comparisons and analysis. The data from theses traces is used to produce many of the figures in this section (Figs. 6.13, 6.16, 6.17 and 6.19).

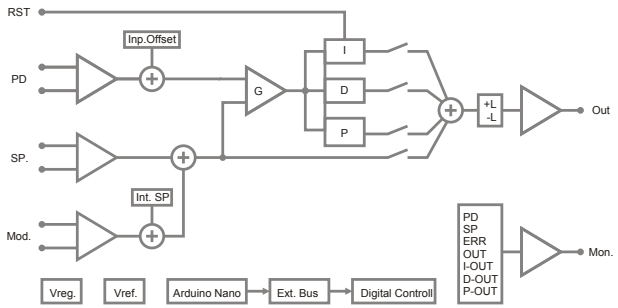

Figure 6.14: Functional block diagram of the PID circuit used for the regulation of the Feshbach coils current, designed within the research group by Akos Hoffman and Daniel Pertot. The digitally controlled analog PID was made to have very low noise specifications. The proportional, integrator, differential components utilize AD712 (Analog Instruments) precision op-amps with DAC8811 (Texas Instruments) 16-Bit digital-to-analog converters. The P, I and D gain values can be digitally controlled via the external bus which is typically controlled using the on-board micro-controller (Arduino-Nano) and user interface. The integrator can be reset internally via the bus or using a TTL trigger. The input gain and offset, as well as the set point gain and offset can be controlled internally. The output can be limited to any voltage less than $\pm 15\,\mathrm{V}$ using an additional 16-bit DAC control. The monitor signal can show several different signals using an internally controlled switch.

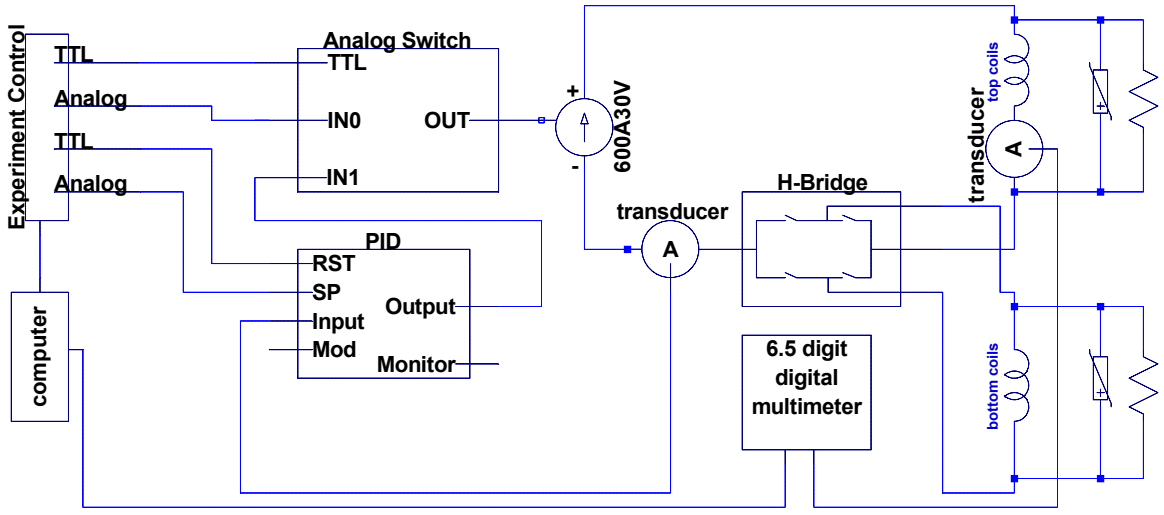

Figure 6.15: Sketch of the wiring for the regulation of the Feshbach current. The current is driven by the Delta 600 A 30 V connected to the H-bridge box to allow the coils to run in Helmholtz or anti Helmholtz configuration as described in Section 3.4.1. Two ITN-600s Ultrastab current transducers are used for measuring the current. One signal is sent to the PID box input for regulation. The other signal is sent to the digital multimeter for recording, analyzing and monitoring the current stability. An analog switch is used such that the Delta 600 A 30 V current can either be controlled directly by an analog signal from the experiment control, or from the output of the PID box.

the limits of the multimeter can be quantified. In Fig. 6.16 the average of the Fourier transform of many traces for the 5 V analog signal and for the short-circuit are compared. One can see the analog signal noise is dominated by low frequency drifts which can affect the sequence to sequence reproducibility. There are also notable 50 Hz and higher harmonics on both the analog signal and the short-circuited signal. The fact the 50 Hz noise is larger for the analog signal implies it is not just an artifact from the measurement with the multimeter.

Given these checks, the voltage signal from the current transducer can be analyzed similarly to provide noise spectra of the current with and without the PID regulation. This voltage can be converted to a current and then a magnetic field, giving the second B-field axis in the spectra shown in Fig. 6.17. The shot to shot variation of the average field in a trace was more than a factor of three larger without the PID, which shows the drift problem highlighted in Fig. 6.13 has been improved. With the PID regulation, the standard deviation of the average field is 3 mG. From the spectra in Fig. 6.17 it is clear the PID greatly improved the low frequency noise related to the slow drift in current from the internally regulated power supply. Interestingly it would seem that the 50 Hz noise increased with the addition of the PID. There may be two reasons for this. Firstly, the PID setup involves several additional cables which must travel from the transducers to the PID box to the power supplies. Approximately 10 m of additional cable length is used for the PID configuration, which may act as a pickup for additional 50 Hz noise, especially as this cable covers a much wider area of the laboratory. Secondly, the ±18 V power supply used to power the PID circuit has relatively large 50 Hz noise and this may be put directly onto the output signal. The origin of the smaller broad peak at approximately 350 Hz is not fully understood, but may be related to the overlap of the resonance frequency of the coils and the PID circuit. With the PID regulation, the total field noise is $B_{\mathrm{rms}} = 12\,\mathrm{mG}$ giving $B_{\mathrm{rms}}/\bar{B} = 1.3 \times 10^{-5}$. Whilst this is still larger than the 2.6×10^{-6} limit from the analog signal, this field accuracy was good enough to start the investigations that were planned. However, the large 50 Hz noise was problematic in that for short RF pulses ($< 1\,\mathrm{ms}$) it looked like a random shift in the B-field, depending on where in the 50 Hz line-cycle the pulse was started. The next section discusses how this issue was resolved.

Mains Frequency Synchronization

The 50 Hz noise originates from the mains frequency. This noise can be transmitted from many different devices in the lab, and although its amplitude may be further reduced,

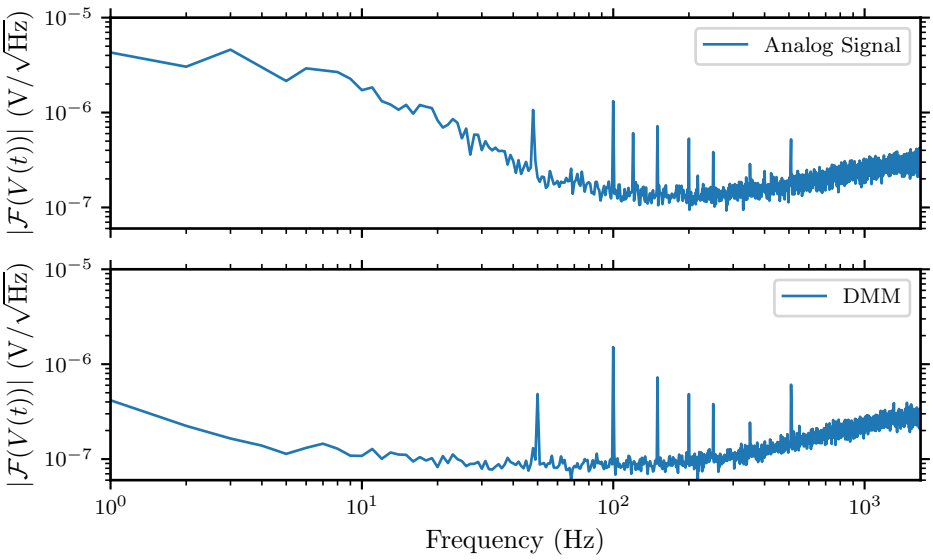

Figure 6.16: Amplitude spectra from the traces of the recorded voltage using the digital multimeter for the analog signal at 5 V set point and a short circuit. Several tens of traces are taken for each plot and the amplitude of the normalized discrete Fourier transforms are averaged. The higher plot shows the amplitude spectrum for the analog signal and has a total $V_{\text{rms}} = 15\,\mu\text{V}$. The lower plot shows the amplitude spectrum for the short-circuit and has a total $V_{\text{rms}} = 8.5\,\mu\text{V}$. Note the log-log scale on the figures. The axes limits of both figures are identical for comparison.

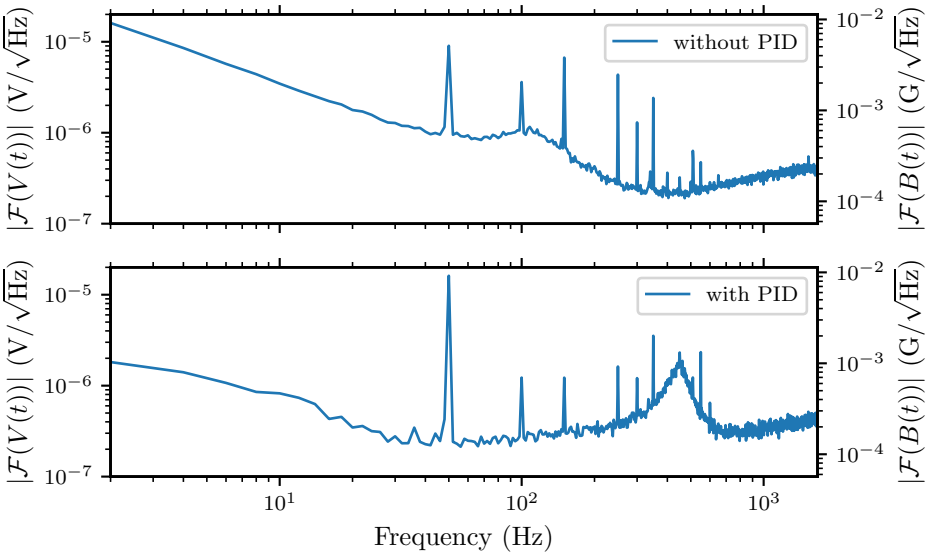

Figure 6.17: Amplitude spectra from the traces of the recorded voltage using the digital multimeter for the current without and with the PID regulation. Several tens of traces are taken for each plot and the amplitude of the normalized discrete Fourier transforms are averaged. The measured voltage can be converted to a current and then to a magnetic field, providing the second y-axis on the right. The PID substantially reduces the low frequency noise and drift, however, the 50 Hz noise increases slightly. Note the log-log scale on the figures. The axes limits of both figures are identical for comparison.

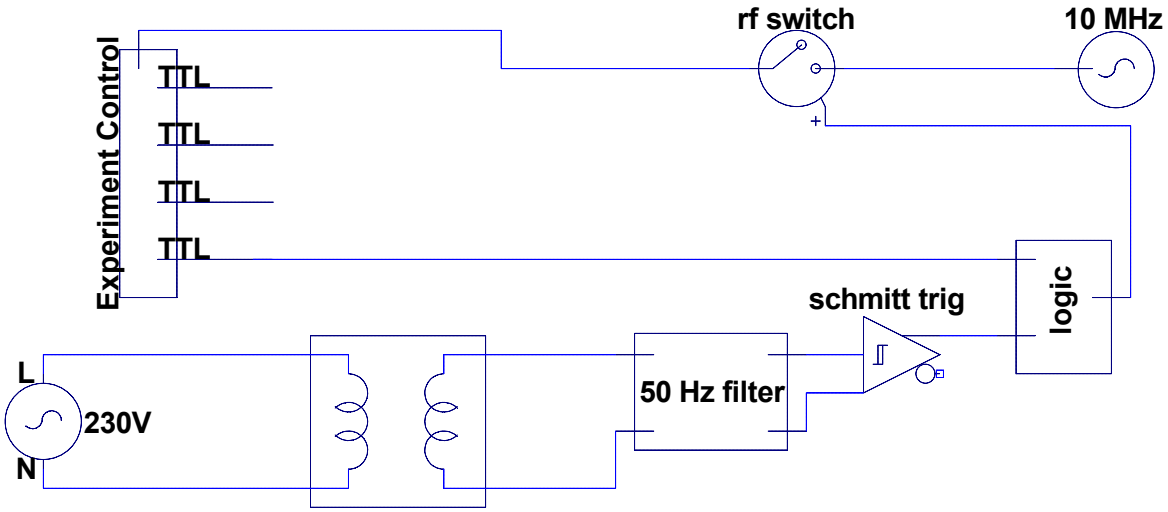

Figure 6.18: Sketch of how the AC phase synchronization is configured in the experiment. In typical operation the 10 MHz clock signal is sent to the experiment control hardware, through the RF switch. A rising edge of a TTL signal from the experiment control hardware causes the RF switch to open, meaning a 0 V signal is sent to the experiment control hardware clock input. The logic setup means the RF switch will not close again until it has received a rising edge from the second (AC-Line input). A transformer is connected to the mains line. A wire wrapped several times around the transformer acts as the 50 Hz pick up signal. It is filtered and then digitized by a Schmitt trigger, which provides the second input for the logic setup. Hence the RF switch will only be closed, and the clock signal returned to the experiment control hardware, at some fixed phase of the 50 Hz line cycle.

50 Hz and its harmonics are likely to always be the dominant noise on the B-field. The issue is made worse because the sequence will not always start at the same point in the phase-line-cycle. Furthermore, the local load can lead to phase shifts on short time scales. A solution to this issue was made by pausing the 10 MHz clock signal, used to synchronize the experiment during the sequence, and restarting it at a fixed point in the phase-line-cycle. When this feature is used, there will be a time step which can have a variable length (0 to 20ms) depending on the phase-line-cycle. The implementation details are described in Fig. 6.18. The AC synchronization works extremely well as shown in Fig. 6.19.

Future Improvements

Once the 50 Hz AC synchronization had been implemented, the field was reproducible enough to perform the investigations discussed in this thesis. However, the field stability is still worse than the 1×10^{-6} that has been achieved in other experiments in our research group and others [101, 174]. Itemized below are some steps that could be taken to improve the field stability. Some of these have simply not been implemented because the experiment is currently being used to take data and making these changes may lead to a

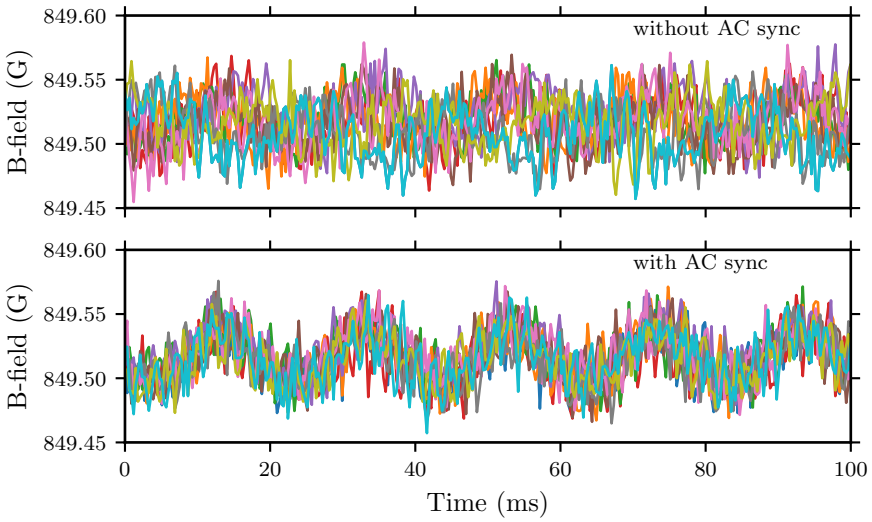

Figure 6.19: Traces of the magnetic field against time without (higher plot) and with (lower plot) 50 Hz phase line synchronization. Each figure shows the data for ten sequential experiment sequences. Without the AC synchronization, the 50 Hz noise relative phase is random and leads to the initial field at a fixed time varying substantially. When the synchronization is performed, the field is very reproducible at all times.

small change in the regulated field and require re-calibration.

- Replace PID power supply with ultra stable ±18 V supply.

- Put PID and analog switch inside grounded metal box with above power supply inside. Currently, the PID circuit is on a trolley exposed in the center of the laboratory.

- Move PID box to near the location of analog output cards and Delta 600 A 30 V. This will reduce several cable lengths and requires only one long cable to take the signal from the current transducer to the PID box.

- Use a high accuracy voltage reference plus a divided down analog signal to provide the set point for the PID. This should increase the resolution and stability of the set point.

- Clean all connections. Some groups reported that dirty or old connectors led to spurious voltages leading to higher field noise.

6.3.3 Calibration with RF Transitions

RF transitions between different hyperfine states ($|a\rangle$ and $|b\rangle$) are used in several stages of the experiment. The application of RF radiation can couple different hyperfine states and by applying the RF continuously, the oscillatory driving field leads to the population in the hyperfine states oscillating in a process known as Rabi oscillations. An oscillatory coupling term between $|a\rangle$ and $|b\rangle$ leads to a time dependent population probability in the state $|b\rangle$ of the form[1]:

$$P_{\mathrm{b}} = \frac{{\Omega_0}^2}{{\Omega_0}^2 + \delta^2} \sin^2\left(\frac{\sqrt{{\Omega_0}^2 + \delta^2}t}{2}\right) \tag{6.12}$$

where δ is the detuning of the driving frequency from the transition frequency between $|a\rangle$ and $|b\rangle$ and Ω_0 is known as the Rabi frequency, which is a measure of how strongly the states $|a\rangle$ and $|b\rangle$ are coupled by the driving field. When the continuous driving field is laser radiation and the electric dipole transition is allowed, then $\Omega_0 = \frac{\langle a \,|\, e\mathbf{r}\cdot\mathbf{E}_0 \,|\, b\rangle}{\hbar}$, where $e\mathbf{r}$ is the dipole moment and $\mathbf{E}_0$ is the peak electric field vector from the radiation field. However, for hyperfine transitions within the same fine structure manifold, which are typically at RF or MW frequencies, there is no electric dipole transition by symmetry and the transition is dominated by the magnetic dipole transition. In this case $\Omega_0 \propto |\mathbf{B}_0|$ where $\mathbf{B}_0$ is the peak magnetic field vector from the radiation field.

From Eq. (6.12) it can be seen that the maximum population transfer to state $|b\rangle$ is $\frac{{\Omega_0}^2}{{\Omega_0}^2+\delta^2}$, giving complete transfer only when $\delta = 0$. The frequency of the oscillations is not generally at Ω_0 but at some modified general Rabi frequency, $\sqrt{{\Omega_0}^2 + \delta^2}$. The population in state $|a\rangle$, is by number conservation always $P_{\mathrm{a}} = 1 - P_{\mathrm{b}}$.

Given the reasonable calibration of the B-field described in Section 6.3.1, for a given B-field set point it is possible to predict the RF transition frequency required for maximum transfer. By applying the RF for a variable time to an initially spin-imbalanced mixture of the $|1\rangle$ and $|2\rangle$ hyperfine states of ^{6}Li and monitoring the population in the $|2\rangle$ state, the Rabi oscillations can be observed as shown in Fig. 6.20. It can be seen that the amplitude of the oscillation decays over time. This decoherence can be caused by several effects, for example if the B-field is not perfectly uniform over the atom cloud.

Once an approximate resonance has been found and oscillations are visible in the time domain, these oscillations can be used to accurately measure the B-field value and stability.

[1] Assuming that all atoms are initially in state $|a\rangle$ and using the rotating wave approximation that $|\omega_0 - \omega| \ll \omega_0$.

Firstly, the measurement in the time domain can give a reasonable approximation for the time required to invert the population, often called the pi-pulse time, $\tau_\pi = \pi/\Omega_0$. If the duration of the pulse is held constant at approximately $t = \tau_\pi$ and δ is varied, the population in the $|2\rangle$ state will follow a sinc-squared function[1]. The center frequency of the sinc^2 curve then determines the B-field and the FWHM is given by $1.60\Omega_0$. Since $\Omega_0 \propto B$, then $\Omega_0 \propto \sqrt{P}$ with RF power, P. By reducing the RF power and therefore reducing Ω_0, τ_π increases and the FWHM decreases meaning the center frequency can be determined more accurately. At some point, however, the curve will no longer be Fourier limited by the pulse duration, but limited by the magnetic field stability itself. If we assume that there is some Gaussian field noise δB around the average field $\bar{B}_0$ across the atoms, then this can be converted into an uncertainty in the center frequency by using the known shifts in transition frequency with B-fields. In the high field limit, for hyperfine states with the same m_J quantum number this shift is often quite small ($1.4\,\mathrm{kHz\,G^{-1}}$ for $|1\rangle \rightarrow |2\rangle$). However, when the transition changes the m_J quantum number it can be quite large, meaning the transition frequency is very sensitive to the field value ($2.8\,\mathrm{MHz\,G^{-1}}$ for $|1\rangle \rightarrow |6\rangle$). By reaching a limit where the width of the spectrum is dominated by the field noise, rather than the pulse length, the field stability can be quantified.

Some example Fourier limited spectra are shown in Fig. 6.21, where the increasing pulse length gives narrower spectra, allowing the real field value to be more accurately extracted. By using the $|1\rangle \rightarrow |2\rangle$ transition, which is very insensitive to field fluctuations, very accurate values of $\bar{B}_0$ ($\sim 2\,\mathrm{mG}$) can be obtained[2]. To quantify the stability of the field, it is much easier to use the $|1\rangle \rightarrow |6\rangle$ transition, however, for technical reasons[3], we instead used much longer pulses of the $|1\rangle \rightarrow |2\rangle$ as shown in Fig. 6.21. At a pulse length of 80 ms the measured FWHM was 34(4) Hz, larger than the Fourier limit of $1.89/80\,\mathrm{ms} = 24\,\mathrm{Hz}$. Hence, the width of this spectrum can be associated with a $\delta B = 20\,\mathrm{mG}$ [4] or $\delta B/\bar{B}_0 \approx 2 \times 10^{-5}$, which is in good agreement with the value calculated from integrating the noise amplitude spectrum in Section 6.3.2.

Finally, RF transitions can also be used to see how reproducible the field is from sequence

[1]Note that if the pulse duration is not exactly $t = \tau_\pi$, then the width of the spectra may change slightly. It will still, however, have the form of a sinc^2 as long as the time is not closer to $t = 2\tau_\pi$. If this occurs, then the resonance frequency would give a maximum population rather than a minimum and would no longer look like a sinc^2. The resonance frequency will always be the symmetry point of the spectrum regardless of the chosen t.

[2]The estimate of this uncertainty in $\bar{B}_0$ is taken from the sinc-square fit estimate of the covariance matrix in Fig. 6.21a, which gives a standard error of 2 Hz. Using the $1.4\,\mathrm{kHz\,G^{-1}}$ conversion this gives an uncertainty in $\bar{B}_0$ of approximately 2 mG.

[3]at the time when the field stability was being measured and the PID regulation installed the high field imaging of the $|6\rangle$ state had not been implemented.

[4]defining δB as the standard deviation of a Gaussian noise and converting the FWHM.

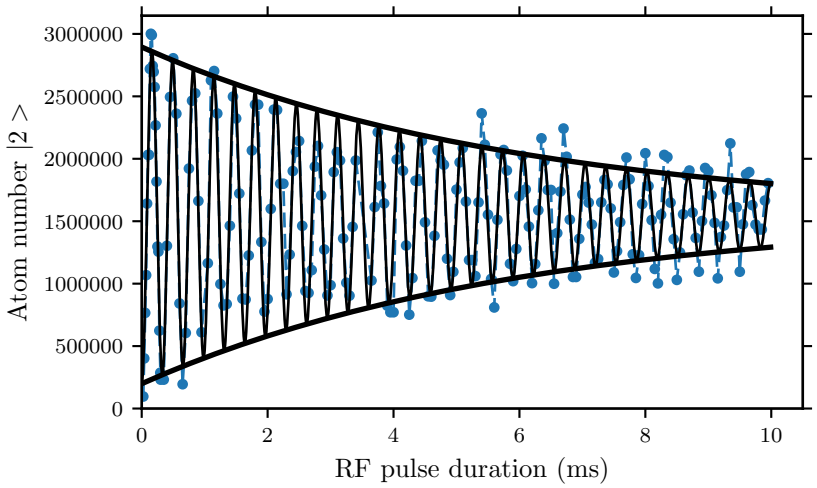

Figure 6.20: Population of the $|2\rangle$ state atoms during oscillations from an applied RF drive. The initial conditions are spin imbalanced mixture ($|1\rangle : |2\rangle = 90 : 10$). The RF drive frequency is then applied at approximately the resonance frequency for a variable time and the population in the $|2\rangle$ state is measured. The population clearly oscillates, with a frequency of approximately 3 kHz, and the amplitude of the oscillations decays with a time constant of approximately 6 ms. The dashed blue line connects the measured blue points and the solid black line is the fitted exponentially decaying sine-squared fit. The thick black lines show the envelope of the decay. This oscillation was taken at 746.2 G with a drive frequency of 76.135 365 MHz.

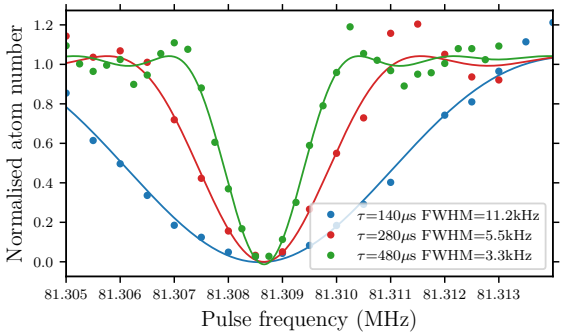

(a) Fourier limited by pulse length.

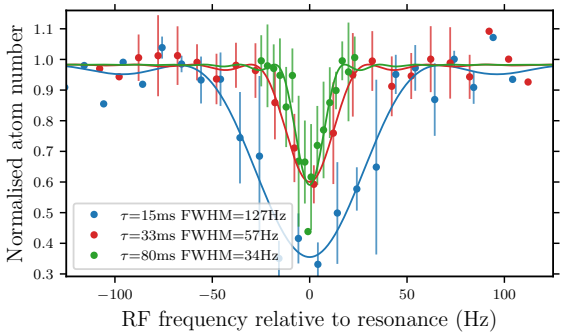

(b) Reaching the field stability limit.

Figure 6.21: Example spectra used to accurately measure the B field, $\bar{B}_0$ and stability, δB. An RF pulse with a fixed time length is applied to an initially spin imbalanced mixture of $|1\rangle$ and $|2\rangle$ atoms. As the frequency of the RF is varied the number of atoms remaining in the $|1\rangle$ state after the pulse is measured. The various pulse durations are shown by the different colors (see legends). The RF power is always reduced such that the pulse duration, τ, is approximately τ_π. By fitting a sinc^2 curve, an accurate measure of the $\bar{B}_0$ can be extracted. For short pulse lengths the widths of the sinc^2 spectra are Fourier limited (Fig. 6.21a), however, in Fig. 6.21b the pulse duration is increased substantially. Whilst the pulse of 33 ms is still Fourier limited (FWHM $= 1.89/t = 57$ Hz), the pulse of 80 ms has a measured FWHM of 34 Hz, larger than the Fourier limit of 23.5 Hz. Hence, the spectrum width of the 80 ms pulse is limited by the field noise, δB. The error bars in Fig. 6.21b show the standard deviation of several repetitions.

to sequence. Since the transition frequency at a magnetic field is a global property, by taking RF spectra as described above at various time intervals, any systematic drifts in the field with time can be checked. This is shown in Fig. 6.22 where the spectra are taken at 15 min intervals with and without the active regulation. It was found that the internal regulation of the power supply was quite sensitive to the internal temperature, which sometimes varied over the course of the day and could be an explanation for the difference seen in Fig. 6.22. This better reproducibility is another benefit of the field regulation, besides reducing the RMS noise.

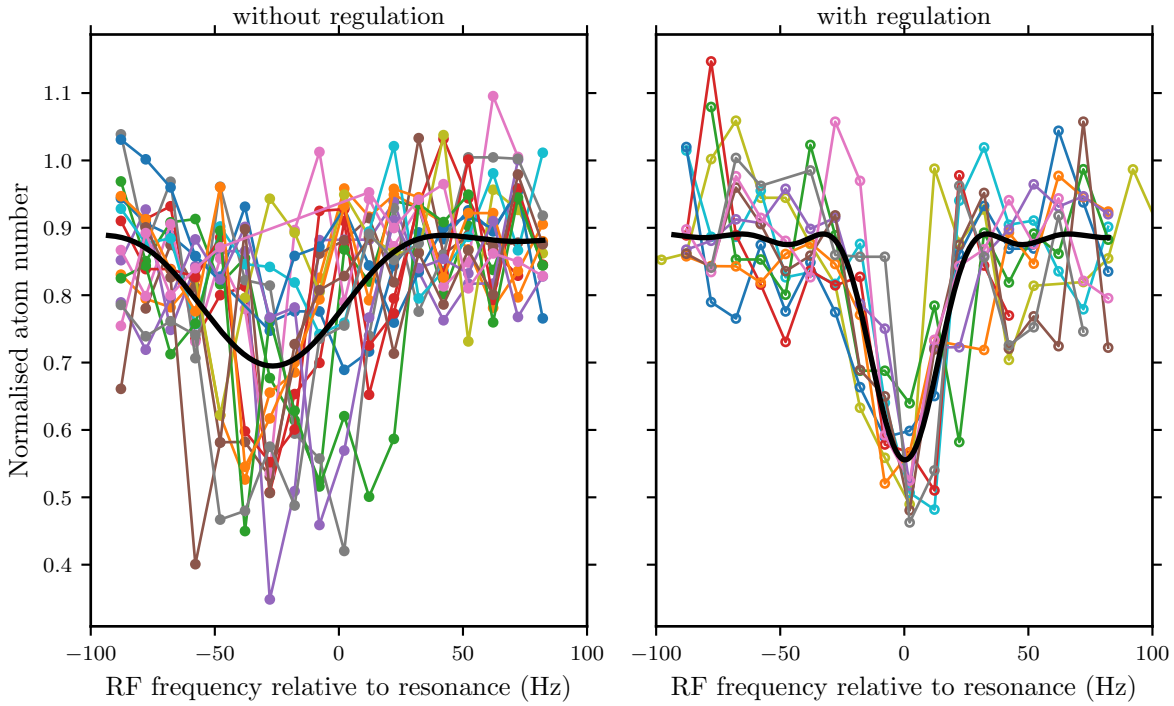

(a) RF spectra taken at regular intervals to measure the drift in the B field with and without regulation. The solid black line shows the sinc-squared fit to all data points.

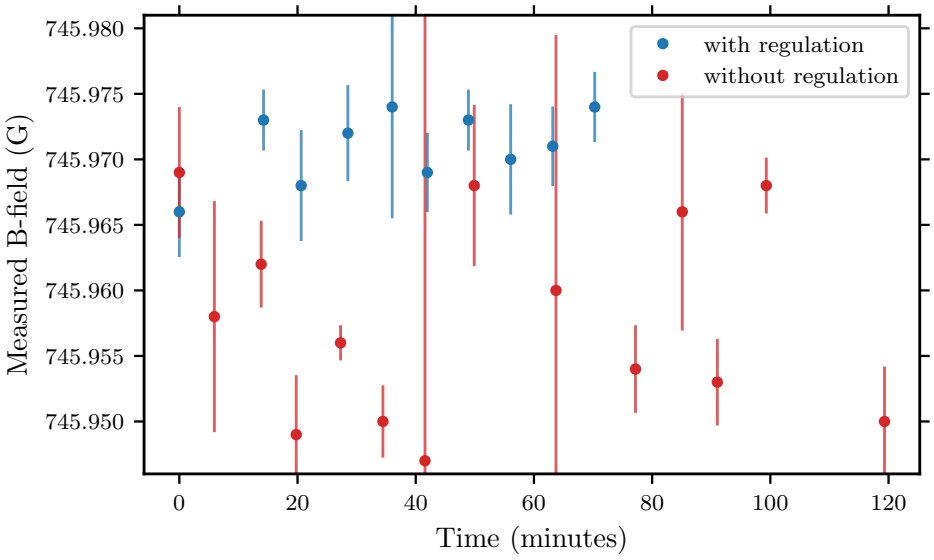

(b) Measured B-field values at regular intervals with and without regulation.

Figure 6.22: Measurement of the B-field reproducibility. In Fig. 6.22a the spectra described in this section are measured approximately every 15 min. By examining the shift in the center frequency of the spectrum, the drift of the magnetic field can be measured. The left and right plot in Fig. 6.22a show the spectra without and with the active B-field regulation, respectively, with the solid black line being a sinc^2 fit to all data points. In Fig. 6.22b the extracted center frequencies of each spectra are converted to B-field values and these are plotted against the time the measurements were taken. It is clear that the field without active regulation drifts significantly more than regulated magnetic field. The error bars are derived from the uncertainty in the center frequency fits.

6.4 The Rapid Ramp Technique

Measuring the pair momentum distribution in the BEC-BCS crossover of ^{6}Li using time-of-flight is challenging. Firstly, the fragile Cooper pairs break apart during standard time-of-flight imaging. Secondly, strong interactions during the time-of-flight affect the expansion of the cloud. The rapid ramp technique was developed firstly for ^{40}K [39] and later adapted to ^{6}Li [42] and allowed the probing of the pairing correlations. The rapid ramp technique uses a fast magnetic sweep to project the many-body atomic state to molecules. For a sufficiently fast sweep, the system is out of equilibrium and the final state momentum distribution of the molecules should reflect that of the pairing correlations in the initial state. In the opposite limit of a slow adiabatic field sweep, the final state would be a Bose-Einstein condensate of molecules depending only on the initial temperature, not the pairing in the initial state. The question of what is sufficiently fast has led to many studies on the validity of the rapid ramp technique and the different time scales involved. Primarily, the magnetic field sweep must be faster than the relaxation time [74, 118, 186]. The conversion efficiency of the projection has also been investigated theoretically [187, 188].

The rapid ramp technique is implemented by ramping the B-field down shortly after the dipole trap is turned off and time-of-flight begins. The field value is reduced to 550 G (for the $|12\rangle$ mixture), where the scattering length between the two spin states is zero. The field is held at this value for approximately 10 ms at which point the field is ramped to 760 G (for the $|12\rangle$ mixture), where the molecules on the BEC side can be imaged.

Reducing the field so rapidly and then allowing it to stably and reproducibly recover is technically challenging and the implementation steps are listed below. The fast switching of the Feshbach coils is performed using the H-bridge and varistor snubber circuit described in Section 3.4.5. In order to get more control of the recovery of the current an additional IGBT (1MBI600U4B-120 FUJI) with a short circuit is placed across the 600 A power supply that is used for the Fesbach coils, allowing the power supply to discharge more rapidly. The rapid ramp is performed in the several steps listed below:

1. Dipole trap is turned off.
2. After a short delay time of t_{delay} ≈0 µs to 2 µs the H-bridge IGBTs are turned off and the discharge IGBT is turned on.
3. The H-bridge IGBTs are then turned back on after a time t_{off} ≈20 µs to 70 µs.
4. The discharge IGBT is then turned off after a time $t_{\text{discharge}}$ ≈50 µs to 200 µs.

5. The B-field is then held approximately constant at 550 G for a time $t_{\text{hold}} \approx 10\,\text{ms}$.

6. The B-field is then ramped to a value where the molecules can be imaged in a time $t_{\text{ramp}} \approx 5\,\text{ms}$, such that the total time is equal to the desired TOF time.

The current transducer used to monitor the current for PID regulation is capable of measuring ramps of $100\,\text{A}\,\mu\text{s}^{-1}$ and can measure the current through the Feshbach coils during the rapid ramp. Whilst the current in the Feshbach coils is ramped very rapidly, the real B-field experienced by the atoms will decay slower due to eddy currents. A novel technique was developed by imaging the ^{6}Li atoms with a 2 µs pulse during the rapid ramp and measuring the absolute resonant imaging frequency. Near the Feshbach resonance, where the binding energy is small, this imaging frequency could be converted into a B-field, which meant the real B-field could be measured with 2 µs resolution during the rapid ramp. The form of the rapid ramp B-field, measured with the current transducer and with the atomic imaging frequency, are shown in Figs. 6.23 and 6.24.

From these measurements, the initial rate of change of the B-field during the rapid ramp was measured as $3.7\,\text{G}\,\mu\text{s}^{-1}$, taking us from the unitarity to molecular regime in approximately 25 µs. This is much slower than the initial rate of change in current in the coil which would be equivalent to $150\,\text{G}\,\mu\text{s}^{-1}$.

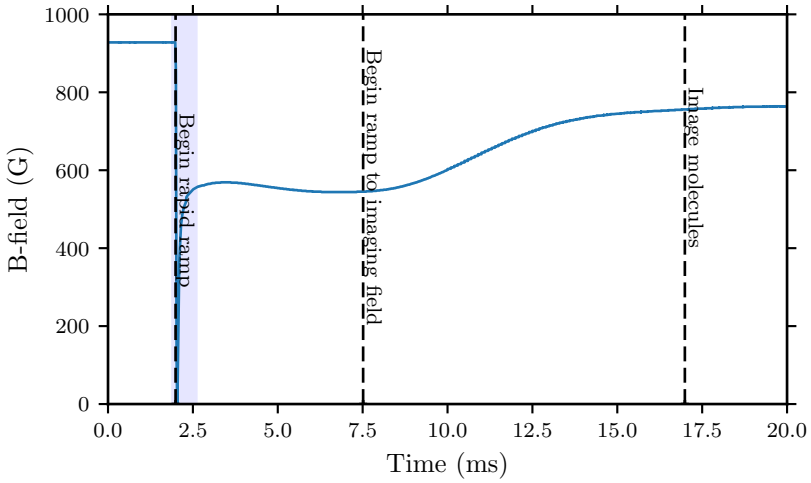

Figure 6.23: Variation of the magnetic field in the Feshbach coils during the rapid ramp procedure. The field is measured using the ITN-STAB current transducer capable of measuring ramps of speeds up to $100\,\mathrm{A\,\mu s^{-1}}$. The blue region is the area shown in Fig. 6.24 during which the fast switching of the IGBTs and discharge circuit occurs.

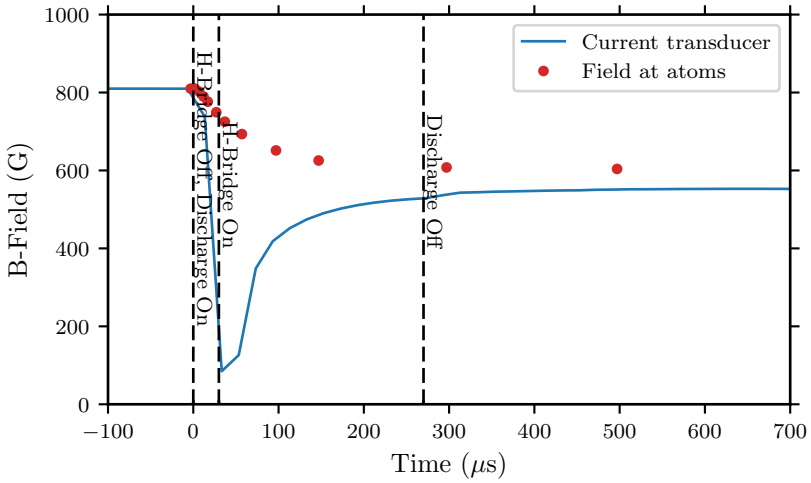

Figure 6.24: Variation of the B-field immediately after the rapid ramp begins. The blue line shows the current measured by the transducer and the red point show the B-field measured with the atoms. The B-field was measured using a 2 µs imaging pulse during the rapid ramp and searching for the imaging resonance. This provides a high time resolution measurement of the B-field during the rapid ramp and can be compared with the value measured by the current transducer.

Chapter 7

Measuring the Gap in the BEC-BCS Crossover

7.1 Introduction

This chapter describes the first main investigation that was performed with the new ^{23}Na ^{6}Li quantum gas machine. The results from this chapter are currently being prepared for publication and this chapter aims to provide additional details on the methods used as well as further examination of the results. The novel technique in this investigation was the manipulation of hyperfine states with RF frequency, typically used for state preparation or probing, to drive or perturb the superfluid in the BEC-BCS crossover.

The BCS superconductor has an order parameter, Δ, which is equivalent to the energy gap as was discussed in Section 2.3, Eq. (2.40) [189]. This quantity is, in general, complex and can be described by an amplitude, $|\Delta|$, and phase, ϕ, with $\Delta = |\Delta|e^{i\phi}$. The energy of the superconducting state as a function of the order parameter has the *Mexican Hat* potential as shown in Fig. 7.1. The minimum energy corresponds to a finite $|\Delta| = |\Delta_{eq}|$ and this equilibrium energy is independent of the phase[1], ϕ. The Goldstone theorem [190, 191] shows that the invariance of the energy with ϕ leads to the existence of a zero-energy (massless) mode known as the Nambu-Goldstone mode, which is shown by the blue line in Fig. 7.1. This mode requires a vanishingly small energy to excite at zero-momentum [192]. The perpendicular mode, corresponding to oscillations in the amplitude of the order parameter,$|\Delta|$, was first studied in the context of particle physics by Higgs[2] in 1964 [85].

[1]This is why the phase ϕ was arbitrarily set to zero in Section 2.3.

[2]Three independent groups published theories in 1964 (see [85, 193, 194]). The mechanism was origi-

It was not until much later that its analogous form in superconductivity was examined [67,84,196]. Due to the formal analogy between the amplitude mode in superconductivity and the Higgs mechanism [85] in particle physics, the amplitude mode is often referred to as the Higgs mode[1]. The Nambu-Goldstone modes have been observed (often referred to as the Bogoliubov-Anderson modes [65,199]) in superconductors, for example, by measuring the microwave resonant absorption [200]. Early evidence of the Higgs mode came from the observation of anomalous peaks in Raman scattering experiments of superconductors [87]. The Higgs mode has not yet been observed in Fermi gases, however, it has recently been observed in solid state superconductors [88, 89] by using a THz pulse to induce oscillations in the order parameter, and in bosonic lattice experiments near the Mott-insulator transition, which provides the necessary particle-hole symmetry [86, 197]. The Higgs mode is of vital importance in the standard model of particle physics and is a fundamental collective mode in quantum many-body systems. The existence of the Higgs and phase modes is deeply related to the concept of spontaneous symmetry breaking. However, the existence and damping of the Higgs mode in more exotic situations such as lower dimensions [201, 202], systems without Lorentz invariance [91] and systems with strong coupling [198] are still under intense study.

Following [198], the collective modes can be understood more quantitatively by writing down the action density for a system with a complex order parameter, Δ, using time-reversal invariant and gauge invariant operators:

$$\mathcal{L} = \overbrace{-r|\Delta(\mathbf{r},t)|^2 + \frac{U}{2}|\Delta(\mathbf{r},t)|^4 + \xi^2(\nabla\Delta^*(\mathbf{r},t))(\nabla\Delta(\mathbf{r},t))}^{\text{static}} + \overbrace{iK_1\Delta^*(\mathbf{r},t)\frac{\partial\Delta(\mathbf{r},t)}{\partial t} - K_2\left(\frac{\partial\Delta(\mathbf{r},t)}{\partial t}\right)\left(\frac{\partial\Delta^*(\mathbf{r},t)}{\partial t}\right)}^{\text{dynamic}} \quad (7.1)$$

where, r, U, ξ, K_1 and K_2 are constants dependent on the physical systems. The terms noted as static define the minimum of the *Mexican Hat* potential giving an equilibrium value for Δ dependent on r and U. The dynamic terms allow for the calculation of time-dependent fluctuations giving rise to the Goldstone and Higgs modes under specific conditions. It is important to note that only if $K_1 = 0$ and $K_2 \neq 0$ is the system

nally proposed by Anderson in 1962 [195].

[1]Technically the term Higgs mode is reserved for locally gauge-invariant systems [85], which include superconductors. However, sometimes condensed matter systems are only globally gauge invariant, for example the bosons in a lattice [86, 197] and these are defined as amplitude modes. The distinction between Higgs and amplitude modes is rarely upheld in the literature [198].

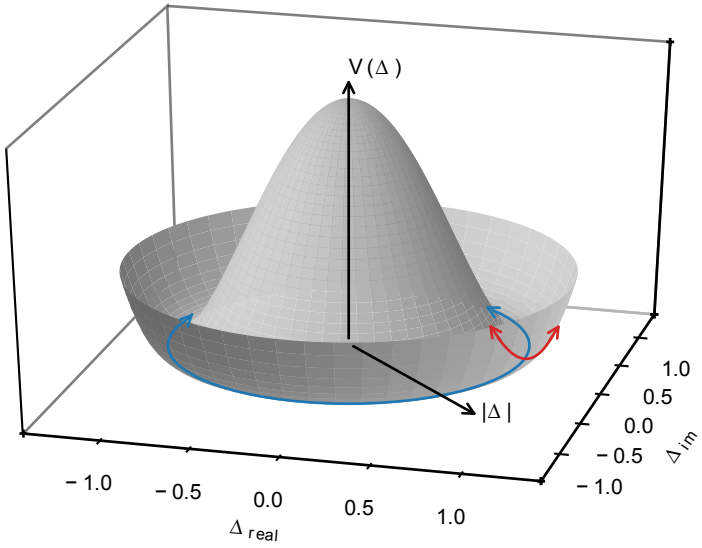

Figure 7.1: *Mexican Hat* potential showing the energy of a superfluid state as a function of the order parameter, $\Delta = |\Delta|e^{i\phi}$. There exists a minimum energy at a fixed $|\Delta|$, independent of the phase, ϕ. The invariance with ϕ leads to the existence of the Nambu-Goldstone mode (shown by the blue line), where there are oscillations in the phase of the order parameter. The perpendicular oscillations of the amplitude of the order parameter (shown by the red line) is known as the amplitude or Higgs mode. Note that $\Delta = 0$ is an unstable state for $T < T_c$, however, at $T > T_c$ where there is no gap, $\Delta = 0$ corresponds to the stable potential minimum.

Lorentz invariant, as was considered in the original Anderson-Higgs mechanism [85]. In the context of a BCS superfluid, it is the particle-hole symmetry that gives rise to the effective Lorentz invariance [198, 203]. By analyzing small fluctuations in ϕ and $|\Delta|$, one can study the collective excitations. In the case of maximal particle-hole asymmetry ($K_1 \neq 0$ and $K_2 = 0$), the phase and Higgs modes are completely coupled with a Bogoliubov dispersion of the form $\omega \propto k$ [198]. In the perfectly particle-hole symmetric case ($K_1 = 0$ and $K_2 \neq 0$), the modes are distinct and orthogonal. The phase mode still has a dispersion of the form $\omega \propto k$, however, the distinct Higgs mode now has an energy gap meaning the dispersion relation has a finite value at $k = 0$. In particle physics the relativistic energy momentum relationship is given by the dispersion, meaning a finite value at $k = 0$ corresponds to a finite rest mass. This is why the Higgs mode is called massive. Note that the presence of a *Mexican Hat* potential is not sufficient to have a distinct massive Higgs mode, which requires Lorentz invariance. A small amount of particle-hole asymmetry ($K_1 \neq 0$ and $K_2 \neq 0$), breaking the Lorentz invariance slightly, leads to the phase and

amplitude modes mixing [198, 204].

In [73] the idea of exciting the Higgs mode in a Fermi superfluid to measure the gap in the spectrum of fermionic excitations was proposed. In the time domain, the response of the system to certain quenches of the interaction parameter should lead to oscillations in $|\Delta|$ at a frequency of $2\Delta_{\text{gap}}/\hbar$, where $\Delta_{\text{gap}} = |\Delta|$ in the BCS regime and $\Delta_{\text{gap}} = \sqrt{\mu^2 + \Delta^2}$ in the BEC regime. Furthermore, they considered performing oscillations of the interaction parameter at frequencies around $2\Delta_{\text{gap}}/\hbar$. When the frequency of the oscillation is on resonance, the superfluid is more strongly excited, leading to the fastest decay in the gap. The gap in the BCS limit is well understood, originating from the order parameter and going to zero for $T \geq T_c$ and was discussed in detail in Section 2.3. The value and formation of the gap in strongly interacting systems, such as the unitary Fermi gas, is far more complex and has been challenging to study theoretically. However, the behavior of strongly interacting systems is of great importance in condensed matter physics with the observed properties of gapless phases [205] and high-temperature superconductors. Furthermore, the existence of a pseudo-gap phase [107], where there exist non-condensed pairs[1], is still under intense study. Despite its importance, it has been challenging to measure the gap in the BEC-BCS crossover. Early attempts [50,206] were strongly affected by final state interactions and trap effects. The best measurement so far, performed RF spectroscopy on a spin-imbalanced cloud [207] to extract the Hartree shift and the gap. However, this method required estimation of the final state interactions and the chemical potential calculated from mean-field theory or quantum Monte Carlo techniques. If the Higgs mode could be excited as proposed in [73], this would provide a new technique for measuring the gap, that could be compared to mean-field theory, quantum Monte Carlo simulations and previous measurements [207].

It has been proposed [72,73] that the quenches or modulation of the interaction parameter could be performed over the Feshbach resonance by rapidly changing the magnetic field. This, however, is a major difficulty for the experimentalist. These quenches need to be performed on time scales smaller than $\hbar/E_F$, which in the typical experiments can be $\sim$10 µs to 100 µs. The inductance of the magnetic coils mean that fast changes ($\sim$100 G in 20 µs) like these require large voltages and, in addition, eddy currents induced from the rapid switching can persist for several hundred microseconds. For the oscillating fields it is challenging to have uniform amplitude high frequency oscillations on the magnetic coils[2]. Early experiments at MIT [74] measured the response of the condensate fraction

[1] There are several different definitions of the pseudo-gap. See [107] for a detailed discussion in the context of Fermi gases.

[2] We attempted to perform $1/k_F a$ quenches by rapidly turning off the B-field, however, it was difficult

to an oscillation in the B-field, however, the oscillations were driven with a period of approximately 4 ms, much slower than the timescales required for the excitation of the Higgs mode. Early experiments at JILA [208], using ^{40}K, performed a faster modulation of the B-field to dissociate molecules and measure the binding energy.

^{6}Li is unique because there are several broad Feshbach resonances between the lowest hyperfine states at similar fields (Section 2.2). Starting with a $|12\rangle$ superfluid, if a RF π pulse could transfer the population of $|2\rangle \rightarrow |3\rangle$ at some magnetic field, B_0, the $1/k_F a$ would change by an amount dependent on B_0. Furthermore, by changing the RF power and detuning, the modulation frequency could be changed to see if the superfluid is excited at specific frequencies. Whether modulating the population of the $|2\rangle$ state would really couple to the Higgs mode in the same way as directly modulating $1/k_F a$ via B_0, was still an open question at the beginning of the investigation. A theoretical study in the reserach group of Corinna Kollath has helped this topic to be understood. Typically, studies use Bogoliubov-de Gennes equations [73] to formulate the time dynamics of Δ in response to a quench, however, this framework is not suitable with the introduction of the third state coupled via RF. Instead, the full Hamiltonian is used and the equations of motion of a set of correlator operators, including the order parameter, are formulated. In the canonical ensemble, the Hamiltonian can be written as:

$$\mathcal{H} = \mathcal{H}_{\mathrm{BCS}} + \sum_k (\epsilon_k - \delta)\, n_{k,3} + \frac{\Omega_0}{2} \sum_k \left(c^\dagger_{\mathbf{k},3} c_{\mathbf{k},2} + c^\dagger_{\mathbf{k},2} c_{\mathbf{k},3} \right) \tag{7.2}$$

where δ is the RF detuning, Ω_0 the Rabi frequency and $\mathcal{H}_{\mathrm{BCS}}$ was defined in Eq. (2.41). Here the rotating wave approximation has been used and for the numerical solutions it is assumed that the population in the $|3\rangle$ state always remains small ($\mu_3 = 0$). Preliminary results from the numerical solutions show that the RF coupling terms in Eq. (7.2) do indeed lead to the excitation of the Higgs mode. Further investigations are being performed to see if analytic solutions to the set of differential equations are possible, under certain assumptions, to better understand the mechanism by which the Higgs mode is excited. A related theoretical investigation into the time dynamics of the superfluid during an RF drive using a time-dependent Bogoliubov-de Gennes formalism can be found in [209, 210], which does not discuss the Higgs mode.

This chapter is organized as follows: firstly, how the RF flips were performed and confirmation that the Rabi frequency was large enough to perform fast quenches is discussed in

to disentangle the quench dynamics from the slow dynamics due to the drift and ringing of the field after the quench was performed.

Section 7.2; secondly, the calibration of the frequencies is explained in Section 7.3; thirdly, the dynamics is examined for varying population transfer amplitude in Section 7.4 and finally, the results of the spectra and measurement of the gap are summarized in Section 7.5.

7.2 Fast RF Inversions

While calibrating the B-field using the hyperfine transitions, as discussed in Section 6.3.3, some different RF coils were tested to try and improve the RF coupling. During this period a new 10 mm square coil was tested with two windings, which was simulated to have a 50 Ω impedance at 80 MHz. It was positioned directly on the UKEA viewport (surrounding the vertical imaging beam), sitting approximately 7 mm above the atoms. This new coil gave a significant reduction (factor 2.2) in τ_π and by using a new 30 W amplifier Rabi frequencies as high as 23.5 kHz ($\tau_\pi = 21\,\mu s$) were achieved. It was surprising that the coupling efficiency was so high with this coil as it is orientated parallel to the Feshbach field. It was expected that a coil perpendicular to the Feshbach field would give the optimal polarization and highest efficiency. This behavior was attributed to near field effects and the fact that the square coil may not be perfectly symmetric or centered on the atoms.

This new RF configuration opened up the possibility of rapidly changing or driving the superfluid over the BEC-BCS crossover. A full inversion of a single component could be performed faster than the Fermi time, $t_F = h/E_F$, and gap-time, $t_\Delta = h/\Delta$. By detuning the RF frequency, and thus not performing a full inversion, the system could be driven much faster. Since the different spin configurations have very different scattering lengths, a_{12} and a_{13}, over these fields (Table 2.1), these RF flips could be interpreted as a rapid change or driving of the interaction strength. Assuming a simple Rabi oscillations picture, from Eq. (6.12), it can be seen that the population of the atoms will be driven with a frequency, $\Omega_{\text{eff}} = \sqrt{{\Omega_0}^2 + \delta^2}$ and peak population transfer, $\alpha = \frac{{\Omega_0}^2}{{\Omega_0}^2+\delta^2}$. Let us look at these quantities in the low α ($\frac{\delta}{\Omega_0} \gg 1$) and high α ($\frac{\delta}{\Omega_0} \ll 1$) limit:

$$\Omega_{\text{eff}} = \begin{cases} \Omega_0 \left(1 + \frac{1}{2}\left(\frac{\delta}{\Omega_0}\right)^2 + \mathcal{O}\left(\frac{\delta}{\Omega_0}\right)^4\right) & \left(\frac{\delta}{\Omega_0} \ll 1, \alpha \approx 1\right) \\ \\ \delta \left(1 + \frac{1}{2}\left(\frac{\Omega_0}{\delta}\right)^2 + \mathcal{O}\left(\frac{\Omega_0}{\delta}\right)^4\right) & \left(\frac{\Omega_0}{\delta} \ll 1, \alpha \approx 0\right) \end{cases} \tag{7.3}$$

$$\alpha = \begin{cases} \left(1 - \left(\frac{\delta}{\Omega_0}\right)^2 + \mathcal{O}\left(\frac{\delta}{\Omega_0}\right)^4\right) \approx 1 & \left(\frac{\delta}{\Omega_0} \ll 1\right) \\ \\ \left(\left(\frac{\Omega_0}{\delta}\right)^2 + \mathcal{O}\left(\frac{\Omega_0}{\delta}\right)^4\right) \approx 0 & \left(\frac{\Omega_0}{\delta} \ll 1\right) \end{cases} \tag{7.4}$$

In the $\alpha \approx 1$ limit, the modulation frequency is dominated by, Ω_0, with $\alpha = 1$ only possible at detuning $\delta = 0$. In the low α limit, the modulation frequency is dominated by δ. The first attempts at driving the $|12\rangle$ condensate at $\alpha \approx 1$ are shown in Fig. 7.2. Here the rapid ramp is performed immediately after some variable RF pulse duration time which drives $|2\rangle \rightarrow |3\rangle$. The RF pulse frequency was chosen to give the minimum number of $|2\rangle$ at τ_π, (maximizing α). The rapid ramp technique means the normal and condensed components can be quantified and compared to the total atom number. This was performed at a field of 910 G corresponding to $1/k_F a_{12} \approx -0.5$. Many coherent oscillations of the total atom number are seen without significant damping. The condensed number, and hence the condensate fraction, oscillates with a similar frequency but the amplitude rapidly decays. The atoms are clearly not lost, as the total number at $t = 2n\tau_\pi$ stays constant, but can be seen in the slight increase in the thermal atoms. It is interesting that this $t = 2\tau_\pi$ oscillation causes the condensed number to be reduced so rapidly and significantly. By reducing the RF power, it was possible to change the resonant drive frequency and observe how the dynamics in the condensate fraction changed as shown in Fig. 7.3. Whilst the oscillations in the total atom number have a $\sin^2$ shape, as would be expected for Rabi oscillations, the oscillations in the condensed number show a sharper feature. This behavior is not understood, but is thought to be related to the strong interactions in the system.

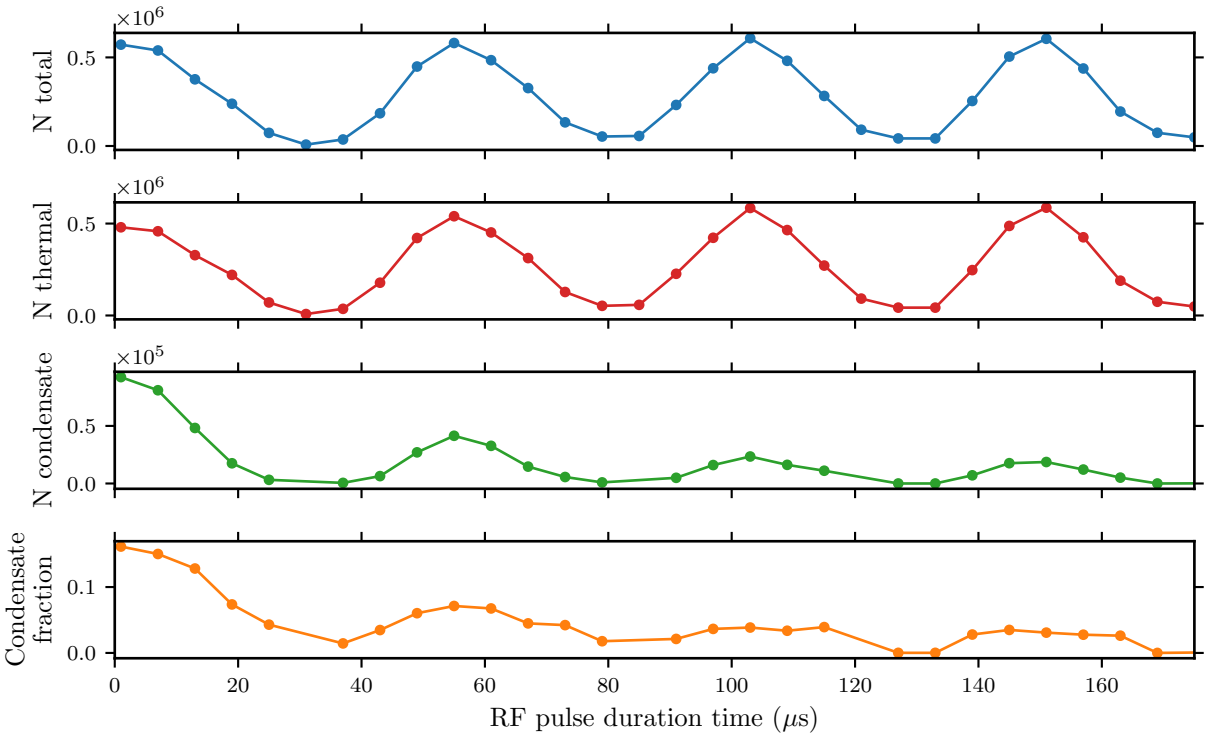

Figure 7.2: Driving fast Rabi oscillations on a fermionic condensate at $1/k_F a_{12} \approx -0.5$. The RF frequency was chosen to maximize the population transfer. There are many coherent oscillations of the total atom number. By performing rapid ramp the condensate and thermal fraction can be quantified using a bimodal fit. The number of condensed atoms rapidly decays, however, oscillations can still be observed. The atoms removed from the condensate are not lost but can be seen in the increased thermal fraction. Note that the fitted condensate fraction is not valid where the total atom number is near zero. The decay rate became slightly faster as $1/k_F a_{12} \to 0$ (not shown here).

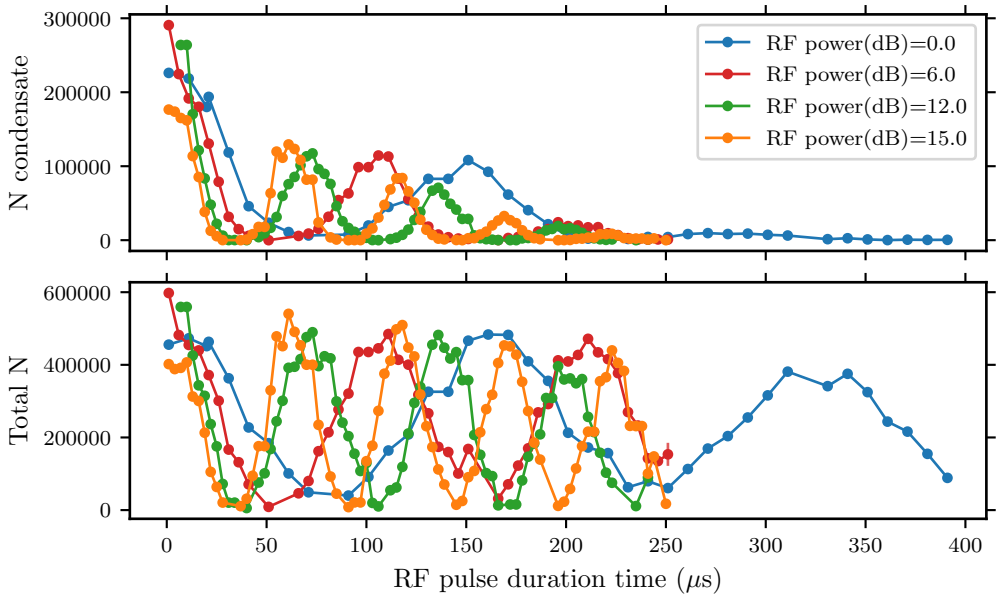

Figure 7.3: Evolution of the condensate and total atom number with varying Rabi frequencies controlled by the RF power ($1/k_F a_{12} \approx -0.5$). The RF frequency (detuning from atomic transition) was chosen to maximize the total population transfer. Again the total atom number shows several coherent oscillations without significant decay. The condensate number decays rapidly, however, the decay is approximately constant in units of τ_π, or equivalently, the reduction in the condensate is similar at $t = 2\tau_\pi$ for several different Rabi frequencies.

7.3 Calibration of the Modulation Frequency

For these studies, it was necessary to modulate the population of a single component of the two component Fermi gas with a known amplitude, α and modulation frequency, Ω_{eff}. For an ideal collection of non-interacting two-level atoms this could trivially be implemented with Rabi oscillations. By varying Ω_0 (RF power) and δ (RF frequency), constant α should be maintained while varying Ω_{eff} by satisfying:

$$\delta(\Omega_0) = \Omega_0 \sqrt{\frac{1-\alpha}{\alpha}} \tag{7.5}$$

For the superfluid system in the BEC-BCS crossover the system is far more complex than a gas of non-interacting two-level atoms. The response to RF in the BEC-BCS crossover has been measured in several RF spectroscopy experiments [41, 50, 211], showing features of both paired and unpaired atoms. Furthermore, for ^{6}Li the $|1\rangle$, $|2\rangle$ and $|3\rangle$ states are all strongly interacting and the effects of the final state interactions cannot be ignored. Additionally, the trapping geometry leads to a varying density profile, causing a varying interaction shift that further complicates the issue. These final state and trap effects

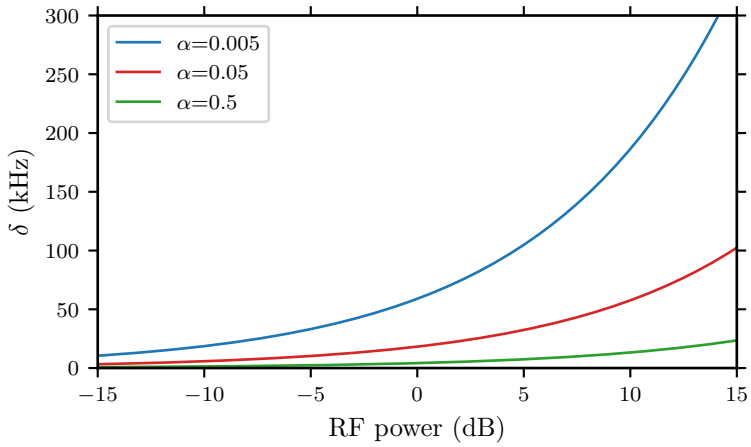

Figure 7.4: Detuning δ (kHz) against RF power (dB) for various curves of constant α (see legend). The RF power controls the bare Rabi frequency Ω_0. In the low α limit, $\Omega_{\text{eff}} \approx \delta$ and a large range of driving frequencies can be used. In the dB scale 15 dB corresponds to the maximum power of the amplifier. In the experiment the $\alpha = 0.005$ value is used and additional attenuators are added such that the lower frequencies can be reached.

have been analyzed theoretically for ^{6}Li in the context of RF spectroscopy, for example in [212–215]. Whilst the RF spectra have been thoroughly studied, the dynamics during an RF drive have, to our knowledge, only been considered theoretically in [209]. Hence, it was necessary to confirm if the population of the $|2\rangle$ state could be modulated as desired and how the necessary values for the RF power and frequency could be chosen. This section describes the methods used to calibrate and check the modulation frequency.

For the large amplitude oscillations, the modulation frequency could easily be checked by looking at the oscillations in the total atom number (Fig. 7.3). However, following the propsed scheme in [73] it was desirable to make a very small amplitude modulation. To achieve this, we assumed the Rabi oscillations picture was reasonable in the low α limit (i.e. that there was a Lorentzian lineshape with detuning) and different techniques were used to confirm that the modulation frequency in the system matched the predicted value. The main difficulty was deciding at which value $\delta = 0$ for the superfluid system in the BEC-BCS crossover. It is known that the frequency will be shifted from the atomic resonance frequency due to the binding energy of pairs and interaction shifts. These effects have been observed, for example in [41, 50, 207, 211], and also by performing molecular dissociation in the experiment ourselves. For this investigation, $\delta = 0$ is defined as the position where α is maximized. With this definition, the Ω_{eff} should be varied by changing the δ and RF power, such that α is constant (as shown in Fig. 7.4). We then attempted to verify that Ω_{eff} can be varied in a predictable way.

The initial calibration of the $\delta = 0$ frequency used a 90 µs RF pulse and varied the frequency to minimize the number of $|2\rangle$ state atoms. The pulse is Fourier limited with a FWHM of 17 kHz. In the low α limit, where the variation in total atom number cannot be resolved, two techniques were developed for measuring Ω_{eff}. The first method involved holding the cloud for some time, $T \approx 2$ ms without RF, after the pulse. After the RF pulse is stopped, the condensate fraction continues to decay and it was found that it decayed significantly more rapidly at odd half-integer period times. This led to relatively large oscillations in the condensate fraction, which could be seen even for very small $\alpha \approx 0.05$. The second method, found later, was simply to look at the atoms transferred to the $|3\rangle$ state with very short time of flight, which provided a reasonable signal even at $\alpha \approx 0.03$.

By varying the δ and RF power to maintain constant α, a predicted modulation frequency, $\Omega_{\text{eff}}^{\text{predicted}}$, could be compared to the measured frequency, $\Omega_{\text{eff}}^{\text{measured}}$, from the oscillations in the condensate fraction or the evolution of the $|3\rangle$ state. This could be performed both red and blue-detuned[1] and the ratio $\Omega_{\text{eff}}^{\text{measured}}/\Omega_{\text{eff}}^{\text{predicted}}$ is plotted against $\Omega_{\text{eff}}^{\text{predicted}}$ in Fig. 7.5. The blue points show the values after the initial calibration described above. We assume that there is some small error in the detuning, because of the error in finding the resonance frequency, such that $\delta \rightarrow \delta + \delta_{\text{err}}$. Propagating this error through the calculations used to generate the curves of constant α (Eq. (7.5) and Fig. 7.4) gives an expression for $\Omega_{\text{eff}}^{\text{measured}}/\Omega_{\text{eff}}^{\text{predicted}}$ in terms of δ_{err} and the chosen constant α:

$$\frac{\Omega_{\text{eff}}^{\text{measured}}}{\Omega_{\text{eff}}^{\text{predicted}}} = \left| 1 + \frac{\delta_{\text{err}}}{\Omega_{\text{eff}}^{\text{predicted}} \sqrt{1-\alpha}} \right| \tag{7.6}$$

This shows that the measured modulation frequency will diverge from the predicted value for predicted frequencies $\Omega_{\text{eff}}^{\text{predicted}} \sim \delta_{\text{err}}$. In Eq. (7.6) the α refers to the predicted constant value. However, this δ_{err} will also cause an error in the real α :

$$\alpha_{\text{real}} = \frac{\alpha}{1 + 2\sqrt{1-\alpha}\left(\frac{\delta_{\text{err}}}{\Omega_{\text{eff}}^{\text{predicted}}}\right) + \left(\frac{\delta_{\text{err}}}{\Omega_{\text{eff}}^{\text{predicted}}}\right)^2} \tag{7.7}$$

which means α_{real} will deviate from the predicted α for $\Omega_{\text{eff}}^{\text{predicted}} \sim \delta_{\text{err}}$. For each field, the quantity $\Omega_{\text{eff}}^{\text{measured}}/\Omega_{\text{eff}}^{\text{predicted}}$ can be measured for several $\Omega_{\text{eff}}^{\text{predicted}}$ and fitted to the form of Eq. (7.6). This gives a value of δ_{err} that can be used to provide an iterative correction. This routine is shown for a fixed field in Fig. 7.5. Here the blue points are

[1] The condensate fraction decayed much more rapidly when blue-detuned for reasons that are discussed later.

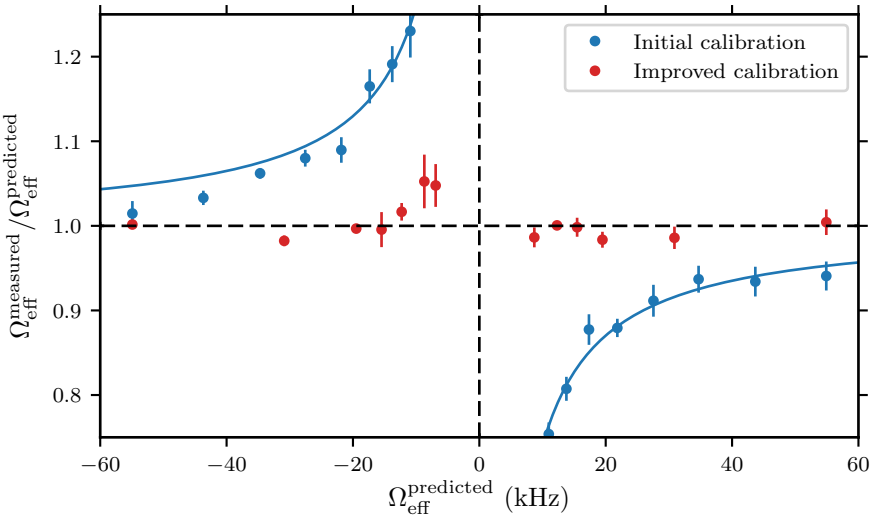

Figure 7.5: Calibration of the modulation frequency for small $\alpha = 0.04$. The modulation frequencies were measured by observing the change in the condensate fractions after a variable pulse length with a fixed hold time (2 ms) after the pulse. An accurate frequency $\Omega_{\text{eff}}^{\text{measured}}$ could be obtained and compared to the predicted frequency $\Omega_{\text{eff}}^{\text{predicted}}$. An error in the resonance frequency leads to a divergence, which can be fitted to extract an error in the detuning, δ_{err}. The blue points show $\Omega_{\text{eff}}^{\text{measured}}/\Omega_{\text{eff}}^{\text{predicted}}$ for the initial calibration and the solid blue line is the fit giving a correction of 2.54 kHz. After applying the correction and repeating the calibration, the red points were obtained, which were significantly closer to the ideal value of 1. Note importantly, that if $\Omega_{\text{eff}}^{\text{measured}}/\Omega_{\text{eff}}^{\text{predicted}}$ moves away from 1, α will not remain constant.

the initially measured $\Omega_{\text{eff}}^{\text{measured}}/\Omega_{\text{eff}}^{\text{predicted}}$, from which the fit (blue line) gives a correction of $\delta_{\text{err}} \approx 2.5$ kHz. Retaking the frequency calibration data with this correction showed a significant improvement (red points) where the measured and predicted frequencies matched even at small drive frequencies. A cross check of this measurement was then performed by looking at the $|3\rangle$ state atoms' population during the RF pulse. Using the newly calibrated $\delta = 0$ reference, a drive was attempted both at -6.9 kHz and 6.9 kHz (i.e. both red and blue-detuned). Fig. 7.6 shows how, with the new calibration, the real drive frequencies were very similar both red and blue-detuned and matched the predicted value.

Whilst this method of measuring the modulation frequency and then correcting the detuning with Eq. (7.6) was effective, it was time consuming, as every graph like Fig. 7.5 required many sequence cycles for each data point. Furthermore, it was noted that the correction (i.e the $\delta = 0$ frequency) depended on the trap geometry as this would affect the density and hence the value of $1/(k_F a)$. It would be much more efficient if the original method of using the RF spectrum had higher accuracy. Longer pulses would, of course, give better frequency resolution, however, it was observed that for pulses longer than 1 ms

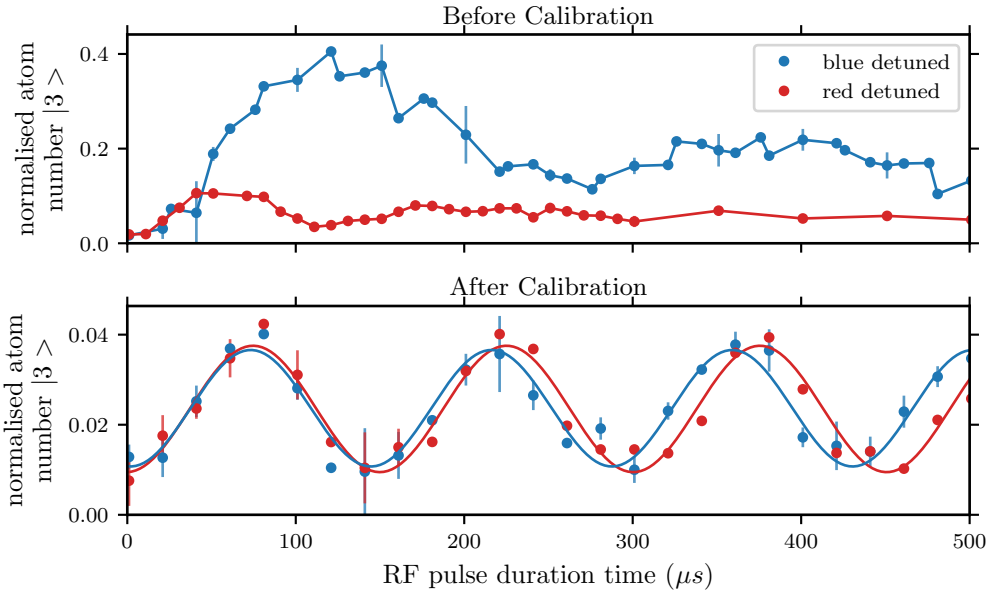

Figure 7.6: An additional method for measuring the drive frequencies was to look at the small population transferred to the $|3\rangle$ state. This figure shows the evolution of the $|3\rangle$ state population with RF power and detuning predicted to give $\alpha = 0.04$ and $\Omega_{\text{eff}} = 2\pi \times 6.9\,\text{kHz}$ for both red and blue-detuning. Before the calibration method shown in Fig. 7.5, at low frequencies, the modulation frequency and α were not as predicted. After the correction, red and blue-detuning give similar frequencies, suggesting the symmetry point is correct. Fitting the data (solid lines) after the calibration gives a frequency of 7.0 kHz and 6.65 kHz for blue and red-detuning, respectively.

there was very little revival of the total $|2\rangle$ state. It is likely that the strong interactions lead to rapid decoherence and then strong three-body losses. It was found, however, that if a much shorter time of flight was used, a reasonable signal could still be obtained by using a pulse of approximately τ_π and varying the frequency in much smaller steps. By fitting a parabola to the central region of the spectrum, a good approximation of the center frequency could be made. The frequencies derived from this method were compared to that from the more accurate calibration described above and were found to agree to within 0.5 kHz. Since from Eqs. (7.6) and (7.7) it can be seen that the errors scale with $\delta_{\text{err}}/\Omega_{\text{eff}}^{\text{predicted}}$, as long as $\Omega_{\text{eff}}^{\text{predicted}} \gg \delta_{\text{err}}$, the $\Omega_{\text{eff}}^{\text{predicted}}$ and constant α should match the predictions. In the spectra taken to measure the gap, the lowest modulation frequency ($\Omega_{\text{eff}}^{\text{predicted}}$) used is approximately $10\,\text{kHz} \gg 0.5\,\text{kHz}$.

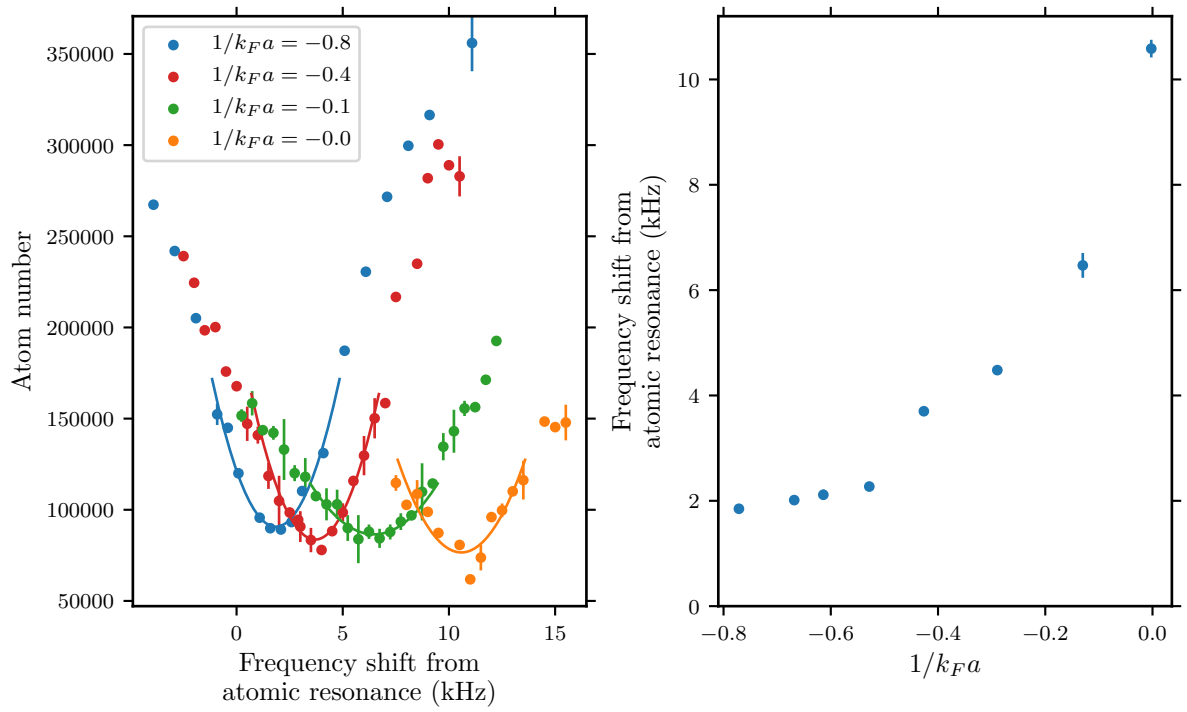

Figure 7.7: RF spectra with $\alpha \approx 1$ and a short time-of-flight, such that very small remaining populations of atoms in the $|2\rangle$ state can be detected. For every B-field ($1/k_Fa$) value, a spectrum was taken to calibrate the $\alpha = 1$, $\delta = 0$ position. Some example spectra are shown in the left plot, where the RF frequency is shown in kHz relative to the atomic transition calculated from the Breit-Rabi transition and calibrated B-field. The resonance is always blue shifted away from the atomic transition and the shift increases for increasing $1/k_Fa$. The solid lines show a parabolic fit to the central region of each data set. The error bars represent the standard deviation of approximately three repetitions. The right figure shows the fitted resonance frequency against $1/k_Fa$, extracted from the parabolic fits. The values on the BEC side cannot be shown on this scale as they are significantly larger due to the large binding energy. The value of the shift is affected by the binding energy, the gap value and interaction shifts. Note that when performing the spectra to measure the gap, a frequency red-detuned from both the atomic transition and the $\alpha = 1$, $\delta = 0$ resonance is used. Changing the trap frequencies (which affects the density and hence the $1/k_Fa$) also affects the position of the resonance and hence an identical trap geometry was used for all spectra measurements. The $\alpha = 1$, $\delta = 0$ found with this method agreed well ($\sim 0.5\,$kHz) with the method described in Figs. 7.5 and 7.6.

7.4 Small Amplitude Driving

With the ability to drive the system at a chosen frequency, it was of interest to see how the condensate fraction varied depending on α. Using the calibration method described in Section 7.3, it was possible to vary the RF power and detuning (relative to the $\delta = 0, \alpha = 1$ point) to have a fixed modulation frequency while varying α. In relation to the $1/k_F a$ modulation experiment proposed in [73], our α was analogous to the amplitude of the modulation. Our plan, following [73], was to modulate the system for a fixed time with a low α at various drive frequencies and see if the condensate fraction decreased substantially at some resonance frequency. This could be interpreted as an excitation of the Higgs mode, from which we could potentially measure the gap. By examining how the condensate fraction decayed in time for various α, as shown in Fig. 7.8, it was possible to determine valid parameter regimes that could be used. For each value of α, a decay rate for the condensate fraction was extracted by fitting a linear slope to the initial decay. In Fig. 7.8 the RF frequency is red-detuned (from both the atomic and $\alpha = 1$ resonance frequency). When a similar measurement was taken blue-detuned, the decay was approximately a factor of 10 to 20 times faster, which is attributed to the blue-detuned RF being able to break pairs and lead to single-particle excitations into the continuum of excited states[1]. Note that in all these measurements the total atom number is conserved, however, there are fast oscillations in the $|2\rangle$ state number, which are negligible for $\alpha \approx 0$. As expected in linear response theory, the decay gradient becomes steeper as α is increased. At this point, we began examining how the condensate fraction changed, for a fixed small α, when the system was driven red-detuned at various frequencies for a fixed time, much longer than the driving period. Here we first began to notice that the decay gradient in the time domain became steeper around some specific frequency, with a slower decay at high frequencies and also at lower frequencies $\ll 2\Delta$. Before we began to take the spectra, which will be described in Section 7.5, it was necessary to choose the value of α and total drive time, t_0.

For the modulation experiments proposed in [73], it is desirable to perform a small amplitude perturbation for long times in order to improve the spectral resolution. For the measurements shown in Section 7.5 a value of $\alpha = 0.005$ was used with $t_0 = 30\,\text{ms}$. These values were chosen by taking spectra and changing both the α and t_0 to produce the narrowest spectral signal possible. We found that reducing α further did not make the signal noticeably narrower. Since we finished taking the spectra data at $\alpha = 0.005$ and

[1] Initially we studied all these phenomena blue-detuned and the rapid decay made this very challenging and it was impossible to achieve spectra like those in Section 7.5.

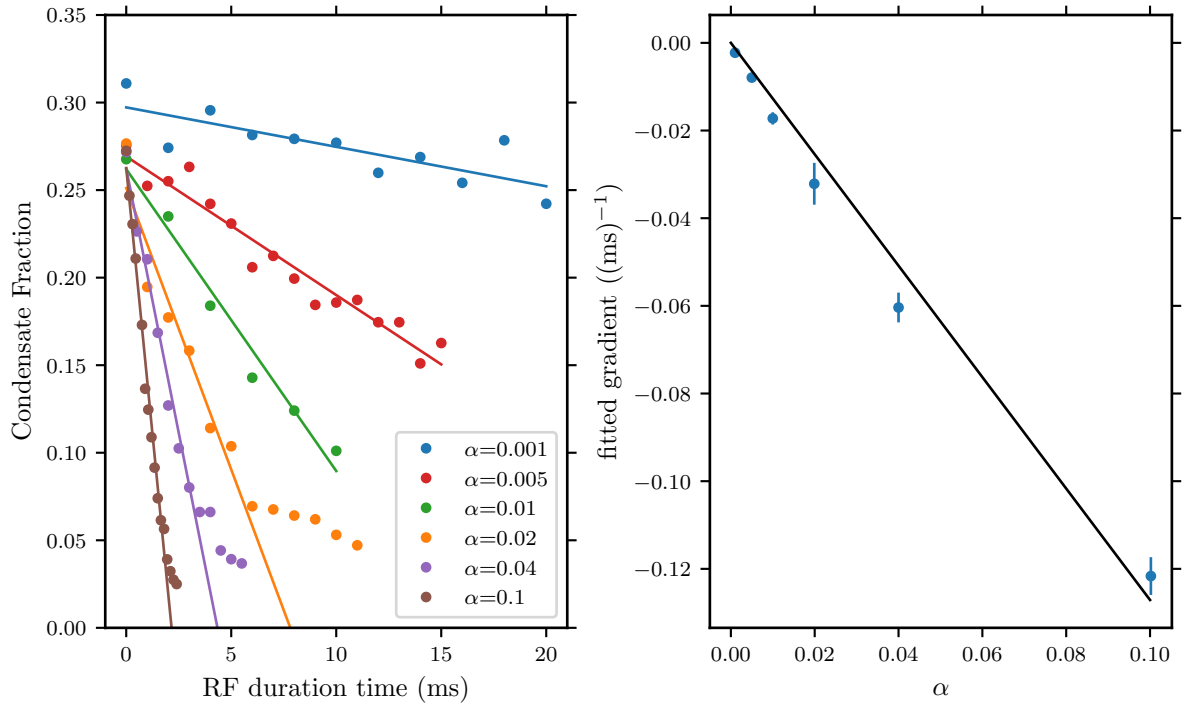

Figure 7.8: Variation of the condensate fraction at 910 G during an applied RF pulse with varying α (left figure). The RF power and frequency are changed such that α is varied from 0.001 to 0.1 while $\Omega_{\text{eff}} \approx 23\,\text{kHz}$ is kept constant. Each color (see legend) shows the decay in time for a different α with the solid lines being a linear fit to each data set. The kinks at low condensate fraction (for example the orange $\alpha = 0.02$ curve) may be caused by poor bimodal fits when the condensate fraction is very low, leading to an overestimation of the condensate fraction. The right figure shows the fitted gradients against α, where the gradient is in units of condensate fraction per millisecond. The gradient scales approximately linearly with α.

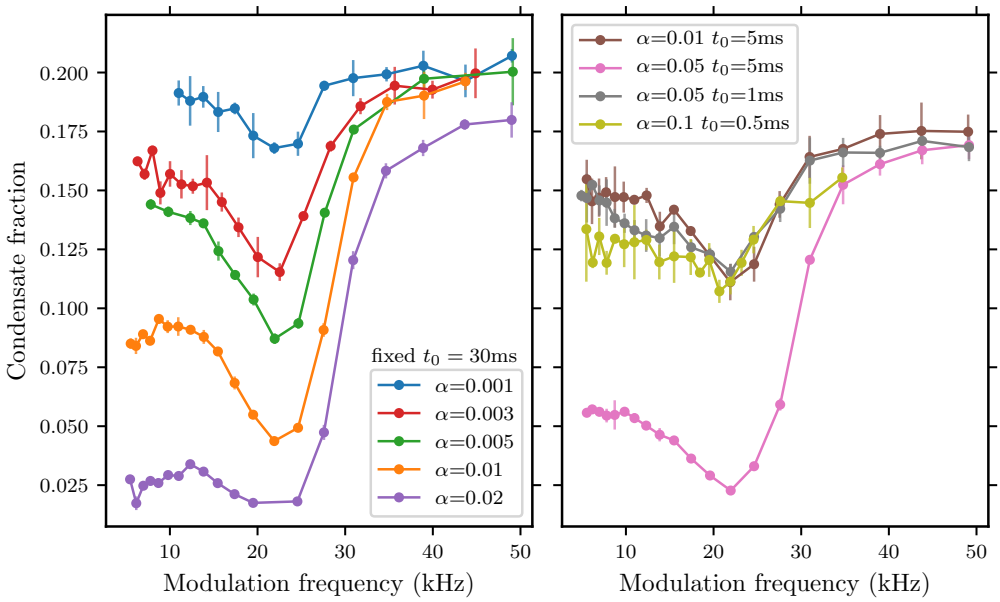

Figure 7.9: Spectra taken at 910 G, corresponding to $1/k_F a \approx -0.43$, for varying α and t_0. The spectra will be discussed in detail in Section 7.5. For the left figure the t_0 is fixed at 30 ms, as α is increased the signal strength increases, however, it is possible to fully deplete the condensate fraction at large α. For the right figure both the α and t_0 are varied to see whether the signal is still visible for very small $t_0 \approx 0.5$ ms. At $\alpha = 0.005$ it was found that the FWHM of the signal did not decrease for t_0 longer than 30 ms. Error bars show the standard deviation of approximately four repetitions.

$t_0 = 30$ ms, we have confirmed that we can still measure spectral signals at significantly higher α and shorter t_0, albeit with worse signal to noise. Several spectra measured at 910 G are shown in Fig. 7.9 for varying α and t_0. This shows a reasonable signal measured with $\alpha = 0.1$, $t_0 = 500\,\mu$s, which opens the possibility of performing these spectral measurements during slow dynamics of the system.

7.5 Measuring the Gap

At this point, it was possible to see if there was a specific frequency at which the condensate fraction was reduced more rapidly during the RF drive at constant α for fixed duration time, t_0. By repeating this method at different magnetic fields, varying the $1/k_F a$, the shift of this response frequency could be examined. Firstly, let us review the experimental sequence for this measurement. The cloud was prepared as described in Chapter 5 by evaporating the ^{6}Li atoms in the dipole trap at 795 G, close to the $|12\rangle$ Feshbach resonance, to a temperature of approximately $T/T_F = 0.07 \pm 0.02$. The magnetic field was then slowly (200 ms) ramped to a chosen field, B_0, in the BEC-BCS crossover,

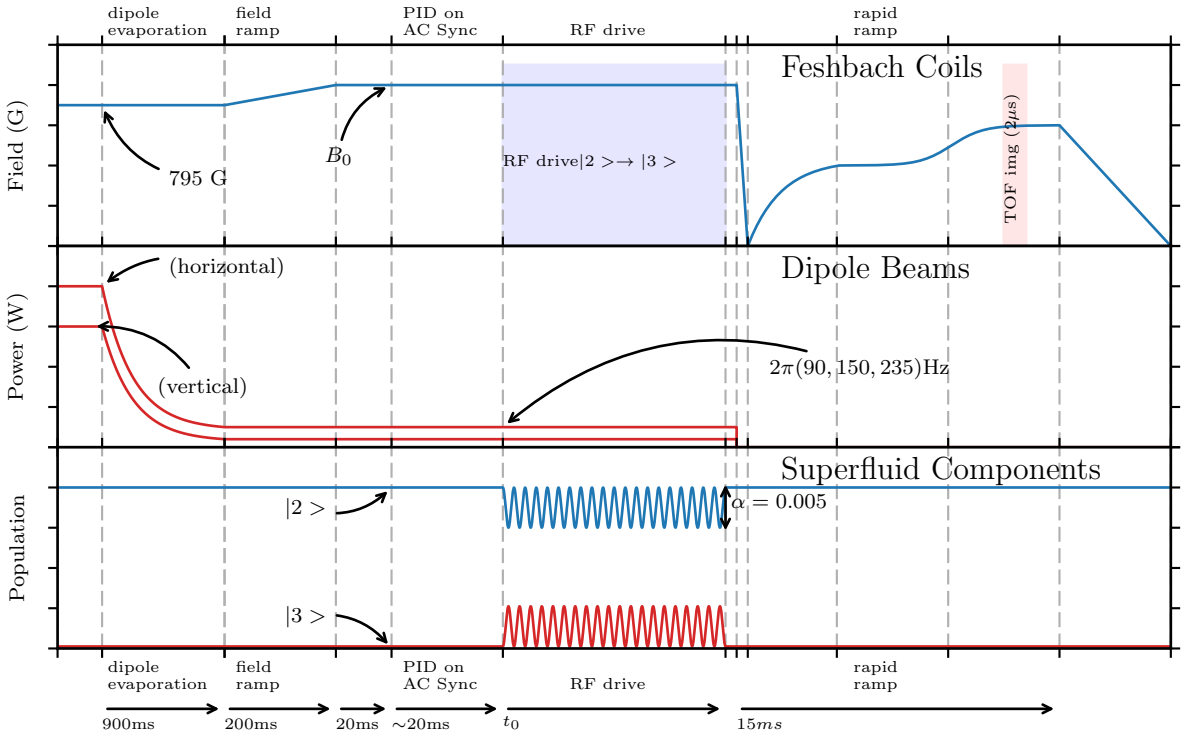

Figure 7.10: Summary of the experiment sequence for the measurement of the gap. Note that the time axis is non-linear to show all important steps. The cloud is evaporated in the two-beam dipole trap giving final frequencies as shown. After evaporation the field is ramped to B_0 in the BEC-BCS crossover and the PID and AC synchronization are turned on to regulate the field. The RF drive discussed is applied for a duration t_0, with a detuning δ and RF power chosen to give a modulation frequency Ω_{eff} and population transfer α. This causes the population of the $|2\rangle$ and $|3\rangle$ state to oscillate as shown. The population of the $|1\rangle$ state remains unchanged. The rapid ramp technique is performed after the RF drive.

defining the $1/k_F a$. The field is then allowed to stabilize and the coils are changed to the PID regulation circuit after which the AC line is synchronized (as described in Section 6.3.2). The RF driving pulse was then applied for a duration time t_0 with a chosen red-detuned frequency and power to give the chosen (constant) α and (variable) modulation frequency. Immediately after the RF drive, the rapid ramp was performed and the resulting absorption image fitted with a bimodal distribution. The calibrated final trap frequencies[1] were $2\pi \times (91, 151, 235)$Hz. For each field, the atom number was calibrated by performing time-of-flight on the $|2\rangle$ without the RF flip and without the rapid ramp, and using the calibration method described in Section 6.1.3. The atom number was approximately 2×10^6 for all fields. Some additional measurements to ensure the total atom number remained constant and to quantify pair breaking were also performed and are discussed later.

[1]Initially the spectra were observed with the elongated trapping geometry and frequencies $2\pi \times (16, 70, 166)$Hz, however, it was thought that the elongated shape and large spatial extent may introduce complexities into the analysis so the more symmetric geometry above was chosen.

In Fig. 7.11 some example spectra are shown for varying magnetic fields which varied the $1/k_Fa$ value as shown in the legend. Take for example the curve with $1/k_\mathrm{F}a = -0.3$, which was taken at 880 G. At high drive frequencies, there is little reduction in the condensate fraction after the RF drive of $t_0 = 30\,\mathrm{ms}$. However, around some lower modulation frequency (here 26 kHz) there is a resonance for which the condensate fraction is significantly reduced. The resonance has a noticeable asymmetry, with the condensate fraction not fully recovering at low drive frequencies. These spectra show a clear resonance for all $1/k_Fa < 0$ up to $1/k_Fa \approx -1$, which is the limiting value we can reach given our maximum magnetic field. Note that as $1/k_Fa$ is varied, the background condensate fraction changes as Δ and T_c change according to Eqs. (2.44) and (2.46), even though the temperature is constant. One difficulty in the analysis is the asymmetry of the resonance and without a model for this asymmetry, a Gaussian fit is used for the high frequency side of the spectrum, with a fraction of the width included on the low frequency side around the minimum. This provides a very good fit to the high frequency side of the spectrum and region surrounding the minimum, deviating only at lower frequencies. Examples of the fits are also shown in Fig. 7.11. The fitted Gaussian gives a resonance frequency and a characteristic full-width at half maximum (FWHM), which increases as $1/k_Fa$ increases from negative to positive values. Notably, on the BEC side of the crossover, the spectrum has become extremely broad and by $1/k_Fa \approx 1$ the signal is not visible and the condensate fraction noticeably reduced even at very high drive frequencies. In Fig. 7.15 for each spectrum there is an associated vertical dashed line which marks the frequency of the atomic transition relative to the $\delta = 0$ frequency found from the calibrations described in Section 7.3. These lines show that for all the $1/k_Fa$ values analyzed the resonance occurs red-detuned both from the $\delta = 0$ and atomic transition resonance. This point will be discussed in more detail later when discussing pair breaking.

By taking many of these spectra at various $1/k_Fa$, the dataset can be combined into a three-dimensional plot as shown in Fig. 7.12. Here the color scale represents the condensate fraction after the RF drive. For each $1/k_Fa$ (B_0) value the limiting condensate fraction at the highest modulation frequency has been normalized to one. The black dots in Fig. 7.12 represent measured data points and the blue dots are the fitted resonance frequencies (connected by straight lines). Note that since the atom number and trap frequencies were accurately calibrated (Chapter 6), the E_F (Eq. (2.12)) for each spectrum is known. Thus, the modulation frequency axis can be given in units of E_F. If it is assumed that this modulation has a similar mechanism to the field modulation proposed in [73], an interpretaion of these spectra would be that the modulation excites the Higgs mode of Δ and this excitation leads to a reduction in the time-averaged value of Δ, with maximum

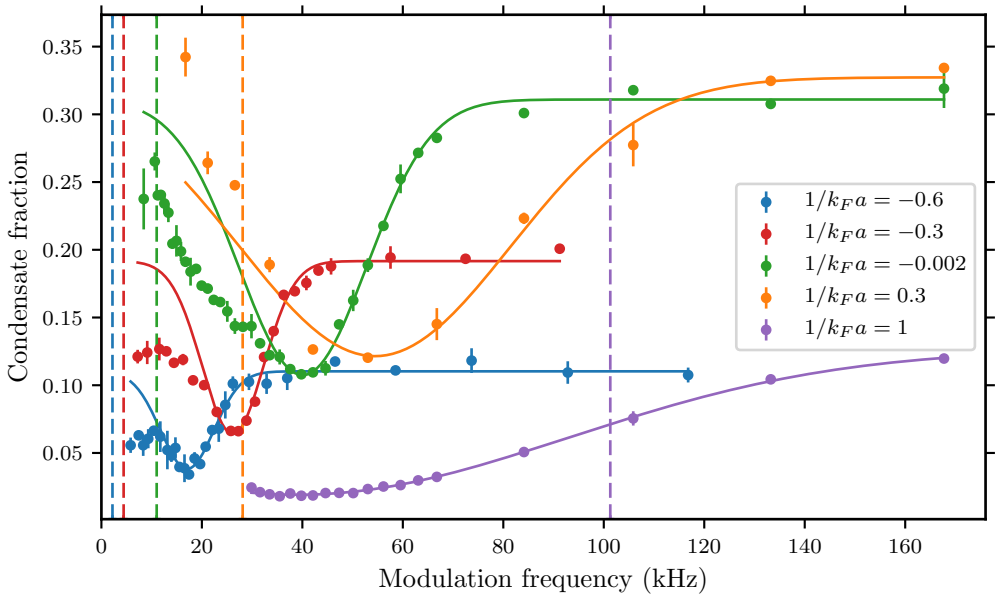

Figure 7.11: Response of the condensate fraction to an RF drive of fixed duration (30 ms) for several $1/k_Fa$ (see legend) which is changed by B_0. For all values except $1/k_Fa = 1$ (BEC regime), a clear resonance is visible at some modulation frequency that decreases as $1/k_Fa$ goes from BEC to BCS. The error bars on each data point represent the standard deviation of the condensate fraction from four repetitions. The solid lines are a Gaussian fit to each resonance on the high frequency side, clearly showing the asymmetry of the spectra at low frequencies. From these fits, a center frequency (used in Fig. 7.13) and width (used in Fig. 7.14) can be extracted. The dashed vertical line shows where the modulation frequency crosses the RF frequency of the atomic transition. Increasing modulation frequency corresponds to decreasing RF frequency (i.e. red-detuned). Note that the drive frequencies (x-axis) shown here in kHz can be converted to E_F units using the tabulated E_F values shown in Table 7.1.

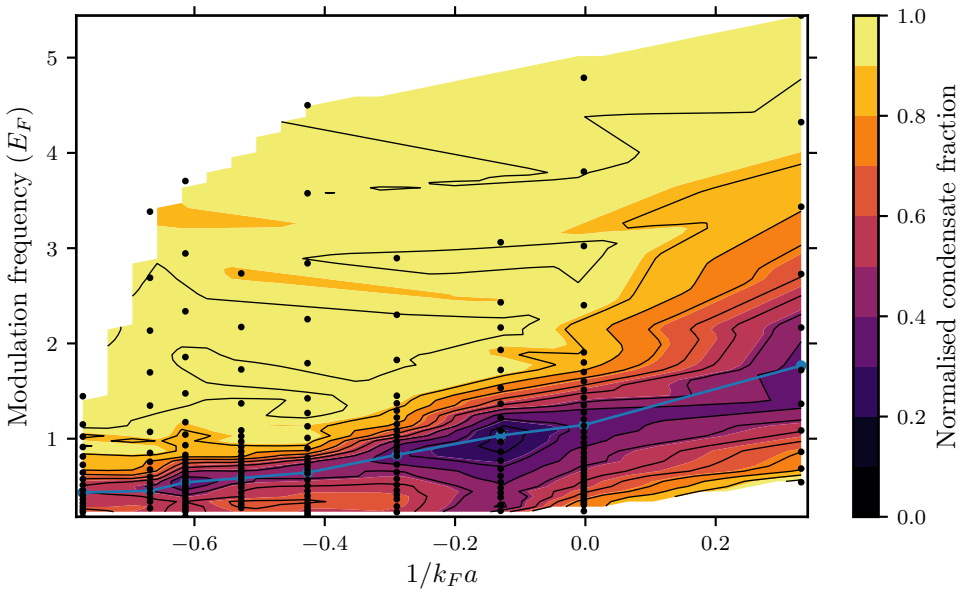

Figure 7.12: Many spectra like that shown in Fig. 7.11 can be taken and combined into a three-dimensional plot, where the colorbar represents the remaining condensate fraction after the modulation. The background condensate fractions at high drive frequencies have been normalized to one. The drive frequency axis has been converted to E_F units using the E_F values tabulated in Table 7.1. Black dots correspond to measured points and the blue dots (connected by straight lines) are the fitted center frequency.

excitation and reduction when driving at a frequency $2\Delta_{\text{gap}}/\hbar$. This would be the first observation of the amplitude/Higgs mode in Fermi gases. Preliminary theoretical studies in the group of Corinna Kollath have shown that this RF modulation does indeed permit the excitation of the Higgs mode. With this insight, it was instructive to assume that the resonance frequency was at $2\Delta_{\text{gap}}/\hbar$ and plot the quantity Δ_{gap}/E_F against $1/k_Fa$. This is shown in Fig. 7.13 and Table 7.1 and is compared to the results from mean-field theory (Eq. (2.46)), quantum Monte Carlo simulations [75,216,217], particle-hole channel analysis [218], and previous measurements of the gap [207]. The error bars in Fig. 7.13 include the standard error in the fitted resonance frequency, derived from the diagonal terms of the covariance matrix, as well as the uncertainty in the trap frequencies and atom number. On the BCS side the error is dominated by the uncertainty in the atom number, set at $\delta N/N = 0.25$; fortunately, the scaling of E_F and k_F with N is very weak (Eq. (2.12)). Far on the BEC side, the error in the fitted resonance frequency becomes more significant as the spectra get significantly broader. This measurement provides a method very similar to that proposed in [73], by which a measure of the spectral gap can be obtained through the entire BEC-BCS crossover, by excitation of the Higgs mode.

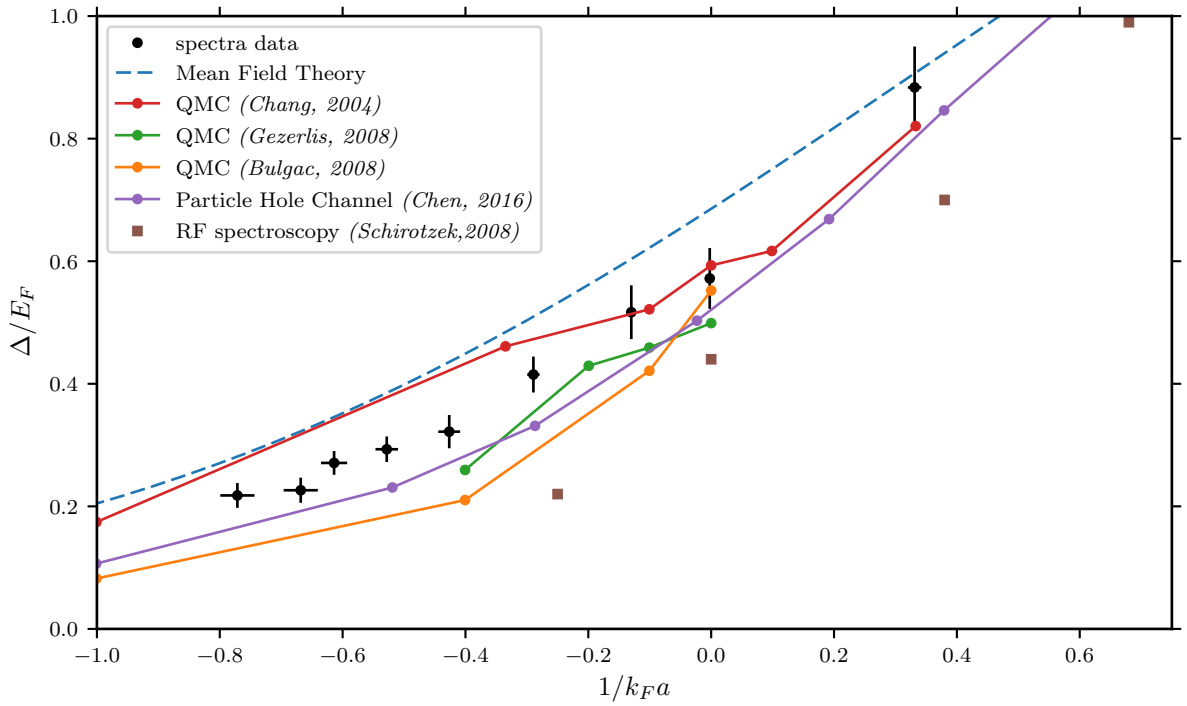

Figure 7.13: Following the interpretation of [73] the resonance frequency should occur at $2\Delta_{\text{gap}}/\hbar$. The black point in this figure shows how the extracted Δ_{gap} would vary with $1/k_Fa$ based on this interpretation. The dashed blue line shows the mean-field gap calculated with Eq. (2.46) and the additional series are quantum Monte Carlo and particle-hole channel theories taken from [75, 216–218], for comparison with the measurement. The brown squares show the measured values from [207] by performing RF spectroscopy on an imbalanced superfluid.

Table 7.1: Tabulated results for the measurement of the gap. The resonant frequencies, f_0, is extracted from the Gaussian fits shown in Fig. 7.11. The calibrated atom number, N, is measured with the method described in Section 6.1.3. The Δ/E_F value is then calculated as $f_0/(2(E_F/h))$. The geometric mean of the trap frequency is $\bar{\omega} = 2\pi \times 148\,\text{Hz}$. Note that the $1/k_Fa_{12} = 1.03$ value is not fitted well.

B-field (G)	N (10^6)	$1/k_Fa_{12}$	E_F/h (kHz)	f_0 (kHz)	Δ/E_F	FWHM (kHz)
1000.0	1.7	-0.77	32.2	14.0	0.22	14.0
974.3	2.1	-0.67	34.5	15.6	0.23	13.4
950.6	1.6	-0.61	31.5	17.1	0.27	12.5
929.2	1.6	-0.53	31.5	18.5	0.29	12.1
910.6	2.1	-0.43	34.5	22.2	0.32	13.1
879.7	1.6	-0.29	31.5	26.2	0.42	14.4
853.6	1.9	-0.13	33.4	34.5	0.52	21.3
834.5	2.2	0.00	35.0	40.1	0.57	30.0
795.2	1.5	0.33	30.8	54.5	0.88	63.6
739.3	1.5	1.03	30.8	39.0	0.63	127.1

There are several effects that could affect the measurement of the gap with this method. Firstly, the finite temperature may play a role in the small discrepancy between the measurements and various theories, which assume zero temperature. However, within the temperature range of the experiment, $T/T_{\mathrm{F}} \approx 0.07 \pm 0.02$, the temperature dependence of the gap at such low temperatures should be small. The harmonic confinement and trap geometry may play a role. The local density in the trap varies in space, which means that E_F, k_F and Δ are spatially varying and different to the peak values used in Fig. 7.11. Some analysis was performed locally by analyzing elliptical rings through the bimodal distribution (similar to the analysis used for atom number calibration in Section 6.1.3) and seeing if certain regions of the condensate decayed differently. No resolvable shift was seen for different regions, however, given the long t_0, an atom may explore a significant region of the trap during the pulse leading to an averaging effect. The role of the harmonic confinement was considered in the context of the Higgs mode in [73, 90, 219] and [73] argued it should have a small effect on the position of the peak. We are still analysing the effects of the harmonic confinement on these spectra ourselves. There could also be issues from the RF pulse addressing a certain sub-region of the cloud. This was the main reason why the more symmetric final trap frequencies were chosen for this measurement. The small curvature of the B-field means that the change in B-field over the size of the cloud is small, however, density variations will lead to a spatially varying interaction shift, changing the experienced modulation frequency and α away from the center of the trap. The fact that it is possible to achieve $\alpha \approx 1$ with a short pulse, changing the spin state of all atoms in the trap, would imply this issue is not so significant. However, when conducting experiments in the elongated geometry ($> 10:1$ aspect ratio), by performing blue-detuned RF inversions, it was possible to create spatial structures in the condensed component, which are most likely similar to those observed in [206]. These structures are not fully understood and are a potential topic for future investigation, but are not significant when using the symmetric trapping frequencies and red-detuned RF.

As was seen in Figs. 7.11 and 7.12, the spectra became broader as the system moved from the BCS to the BEC regime, becoming almost flat by $1/k_F a \approx 1$. This is quantified in Fig. 7.14, which shows the fitted FWHM in units of E_F against $1/k_F a$. In an ideal system, the width should be limited by the finite lifetime of the Higgs mode. However, experimental factors such as t_0 and α will affect the width, as will finite size and harmonic confinement, as discussed above. A discussion of the lifetime of the Higgs mode in the context of solid state BCS superconductors can be found in [220], where a bandwidth from the lifetime $\approx 0.35\Delta$ is calculated, which can be compared to our minimum FWHM

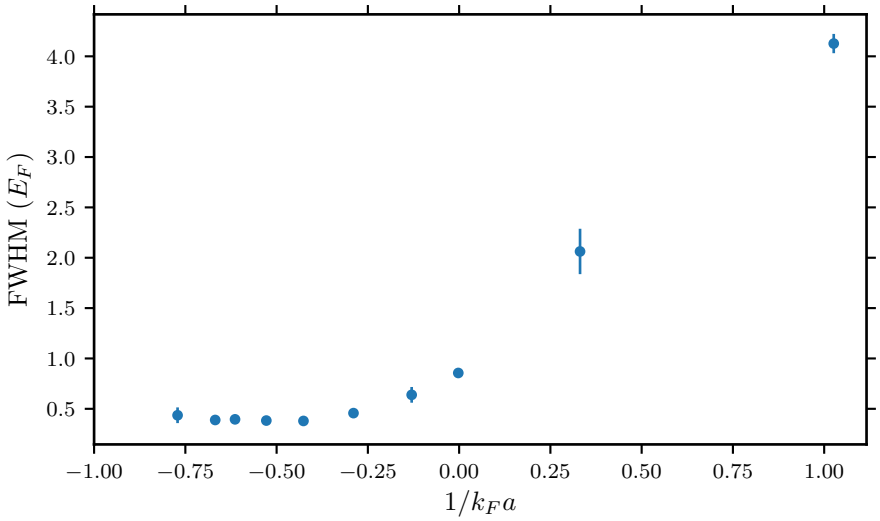

Figure 7.14: Fitted full-width at half maximum (FWHM) against $1/k_Fa$ extracted from the Gaussian fits to the high frequency side of the spectra, as shown in Fig. 7.11. The FWHM is in units of E_F.

of 0.55Δ at $1/k_Fa = -0.29$. The broadening and eventual disappearance of the signal, as the unitarity and the BEC regime are approached, is interesting. In the BCS regime a width smaller than E_F was observed, which implies that the mode has a lifetime longer than $\hbar/E_F$. In the BEC limit, the mode is not long-lived or well-defined. The earlier discussion of the Higgs mode showed that particle-hole symmetry was required to give the effective Lorentz invariance. The Lorentz invariance is gradually lost as the system leaves the BCS regime, and the amplitude (Higgs) mode and phase (Goldstone) mode become coupled. In 2016, a theoretical study [91] of the Higgs mode in the BEC-BCS crossover calculated the spectral weight of the amplitude and phase modes. It was found that they are strongly coupled in the unitarity and BEC regimes, and their calculated spectral weights show a significant broadening in these regions. In addition, they state that in the unitarity and BEC regime the Higgs mode can become strongly coupled to quasiparticle excitations and become overdamped [91]. This broadening and damping mechanism provides one interpretation for the measured widths of the spectra. It is possible that the inhomogeneous density in the trap may also play a role in the width and asymmetry of the spectra. The value of the gap decreases away from the center, which may lead to a slowing decaying tail at lower drive frequencies. The spatial variation of the gap would not explain the broadening as the BEC regime is approached.

Several measurements were taken to help understand the results of this investigation. From the same data set, the total atom number (condensed+thermal) and a measure of the temperature, extracted from the Gaussian waist of the bimodal fit, could be obtained.

For all data sets, there was no significant change in the total atom number with the drive frequency, except at some low drive frequencies $\ll 10\,\mathrm{kHz}$, which for most of the spectra is significantly lower than the measured resonance frequency. One reason for this might be that, at low frequencies, the requirement that the drive is faster than the t_F and t_Δ is no longer met. This means that during the RF drive, decoherence and three-body recombination could lead to atom loss and possibly heating, which would cause the atom number and condensate fraction to decrease. Furthermore, at low frequencies it should be possible to drive single-particle excitations, which can lead to atom loss. An alternative interpretation could be the large spectral weight of the Goldstone mode at low frequencies [91], however, we do not yet have an experimental method to clarify this. With regards to the temperature, one must be careful using the Gaussian waist, as immediately after the drive on resonance, the system is not in equilibrium and there are further complications as the TOF is performed in the weak harmonic confinement of the Feshbach coils. Nevertheless, the fitted temperature should give a measure of energy absorbed during the drive. The fitted temperatures are shown overlaid on the spectra in Fig. 7.15. A measurable but very small increase in the fitted temperature can be seen when driving on resonance even in the BCS regime, however, it becomes noticeably larger at unitarity and in the BEC regime. This increase can be explained by the energy absorption during the RF drive, which would be largest when exciting the collective mode on resonance. Again the increase at unitarity and in the BEC regime is most probably due to the coupling to the phase mode leading to more significant damping, however, this observation is not quantitatively understood.

An additional measurement was performed to better characterize the state of the system directly after the excitation by modulation. By adding a variable hold time after the RF modulation but before the imaging, it was possible to examine how the condensate fraction recovered over time after the excitation. This was of interest as the final state after the excitation is predicted to be a non-equilibrium asymptotic state characterized by an asymptotic order parameter. This measurement is shown for 880 G in Fig. 7.16 for hold times of up to 600 ms. Initially the spectrum is clear, with a reduced condensate fraction around 30 kHz. The system then slowly recovers back to an equilibrium state where the condensate fraction is independent of the drive frequency. During this time the atom number reduces (approximately a factor of 2 in 600 ms) and evaporation occurs, which could explain the recovery in the condensate fraction. This shows that there is some energy absorption when driving the system on resonance. The system can then thermalize and cool at later times.

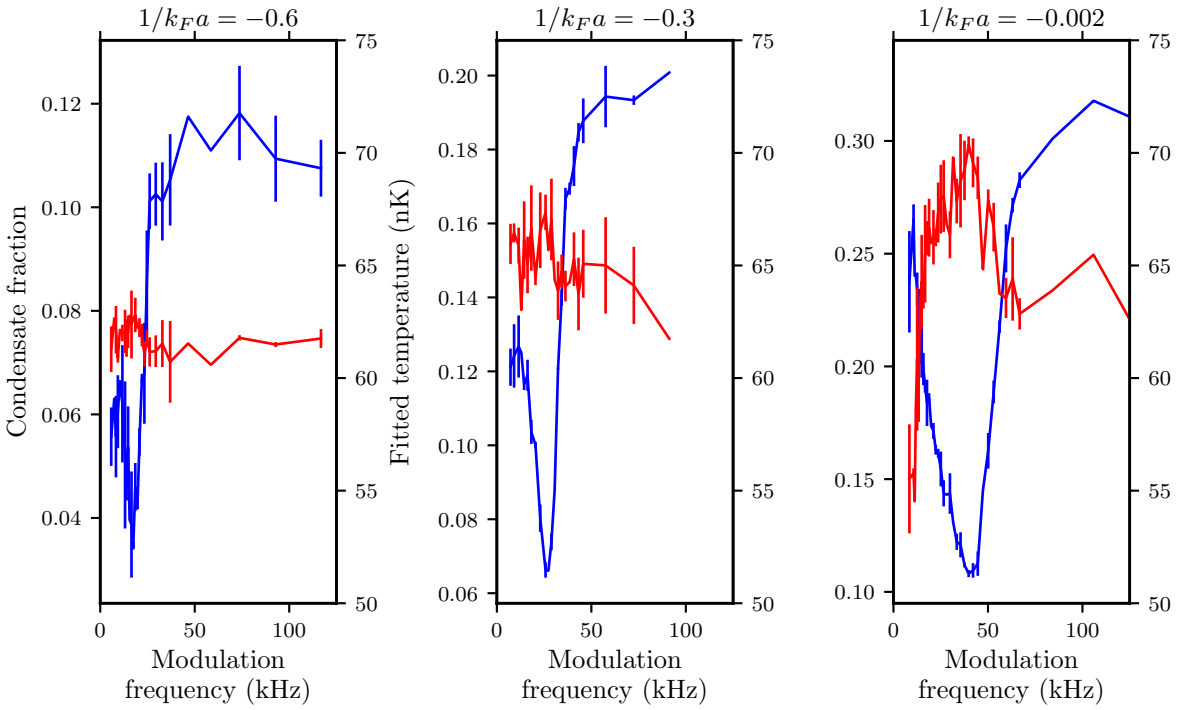

Figure 7.15: Each plot shows the condensate fraction (blue) and fitted temperature (nK) (red) against drive frequency for a selection of $1/k_Fa$ values (see text on sub figures). Note that the drive frequency and temperature scales are the same in the different plots but that the condensate fraction axis differs to make the spectra clearer.

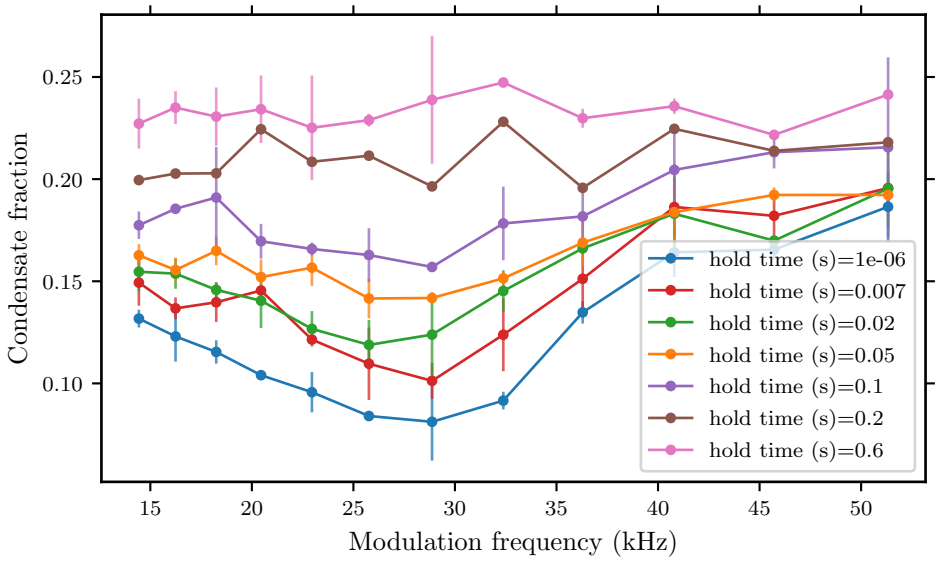

Figure 7.16: Immediately after the RF modulation the system could be held for some variable time, as shown by the legend, before performing the rapid ramp technique and imaging. The spectral signal is clear at early times. As system slowly thermalizes and atoms evaporate, the spectrum signal disappears.

It is important to understand if this investigation distinguishes the collective Higgs mode from the energetically degenerate quasiparticle excitations. There is a difference between the experimental method implemented here and that of traditional RF spectroscopy [50], in which a long RF pulse is applied and the transfer from $|2\rangle \rightarrow |3\rangle$ is measured for different absolute frequencies. Here, the modulation frequency of the population between states $|2\rangle$ and $|3\rangle$ is varied by detuning the RF. This RF is always red-detuned with respect to the paired peak and (except far in the BEC regime) always red-detuned to the atomic transition. In this picture it would not be expected that one can break pairs or probe the single-particle excitation spectrum. The preliminary numerical simulations in the group of Kollath have also shown that the modulation of a single component to a third state, modeled by Eq. (7.2), should provide a mechanism to couple to the Higgs mode. Although the microscopic mechanism for the excitation of the Higgs mode is different to the direct $1/k_F a$ modulation proposed in [73], it would seem reasonable that the response of the system would be the same. To further quantify the effects of single-particle excitation spectrum and pair breaking, the rapid ramp technique was adapted such that the final imaging field occurred far in the BEC regime at 450 G, where the pairs form deeply bound molecules and are not detected in absorption imaging. Here only a weak signal of unpaired atoms can be observed, which in the typical evaporation sequences is around 2 % to 4 % of the total number. By measuring the unpaired atom number after the RF drive, it is possible to see if there is significant single-particle excitation during the spectrum measurement. An example of this measurement is shown in Fig. 7.17. It was found that there was no significant increase in the unpaired number when red-detuned from the $\delta = 0$ reference. However, when blue-detuned, it was found that there was a significant increase in the unpaired atom number which increased for higher driving frequencies, which correspond to higher RF frequencies. This was interpreted as the RF, blue-detuned from both the $\delta = 0$ resonance and the atomic transition, being able to break pairs and excite them into the continuum of states.

In conclusion, a method was developed to use the RF to modulate the population of one component of a two-component superfluid over the BEC-BCS crossover. This modulation is thought to excite the Higgs mode and the experiment is qualitatively similar to the $1/k_F a$ modulation proposed in [73]. After careful calibration of the modulation frequency and population transfer amplitude, spectra were taken where the modulation frequency was varied with a fixed drive time. Resonances were seen in these spectra at specific frequencies. Following the analysis of [73], these could be interpreted as an excitation of the Higgs mode with a resonance frequency of $2\Delta_{\mathrm{gap}}/\hbar$. This technique provides a method to measure Δ_{gap} and compare it to recent theoretical predictions. Whilst the data shown

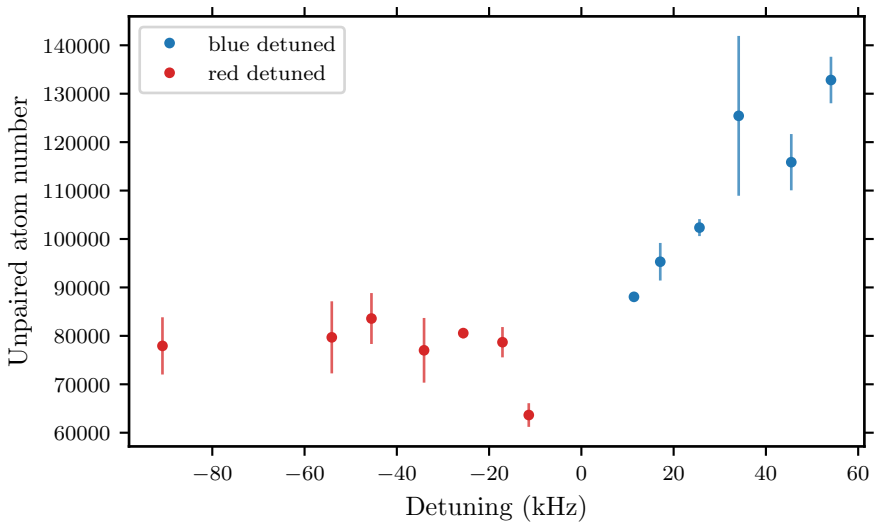

Figure 7.17: Number of unpaired atoms after the RF drive for varying drive frequencies, measured by imaging at 450 G after the rapid ramp. A negative frequency corresponds to red-detuning relative to the $\delta = 0$ reference. There was no significant increase in the unpaired atoms while red-detuned. If the frequency was blue-detuned a noticeable increase was measured.

uses a drive time of 30 ms, we have been able to measure a signal with larger α and drive times as short as 500 µs. This opens the possibility for using this technique to time-resolve slow changes in Δ.

Chapter 8

Quenches and Non-Equilibrium in the BEC-BCS Crossover

8.1 Introduction

Whilst over the last decade many of the equilibrium properties of Fermi gases have been characterized, out-of-equilibrium systems have been more challenging to investigate. Nevertheless, non-equilibrium transport properties and dynamics are of great significance in condensed matter physics (for example the transport properties of superconductors [221]), but also in fields as diverse as self-assembly in Biology [222] and the modelling of traffic flow [223]. Taking the system far from equilbrium can also lead to novel effects; recent experiments have used pulsed lasers to drive metals out of equilibrium to induce superconductivity at very high temperatures [82, 83], albeit only for very short time scales ($\sim$10 ps). Quenches far from equilibrium also allow us to address several fundamental and long-standing questions in physics. The process of how quantum many-body systems eventually equilibrate is still not well understood and it is not clear how the macroscopic quantum statistical mechanics can be derived from the local dynamics of microscopic laws [78]. Recent experiments studying integrable systems that do not satisfy ergodicity [224] have provided a way to test several different theories. Non-equilibrium physics also plays a role in very small systems where standard equilibrium physics no longer applies [77], which has led to the development of quantum fluctuation theorems [225]. This has enhanced our understanding of how a system responds to a perturbation from which much information about the state and properties of the system can be derived. Ultracold atoms provide an ideal platform to study many-body quantum systems out of equilib-

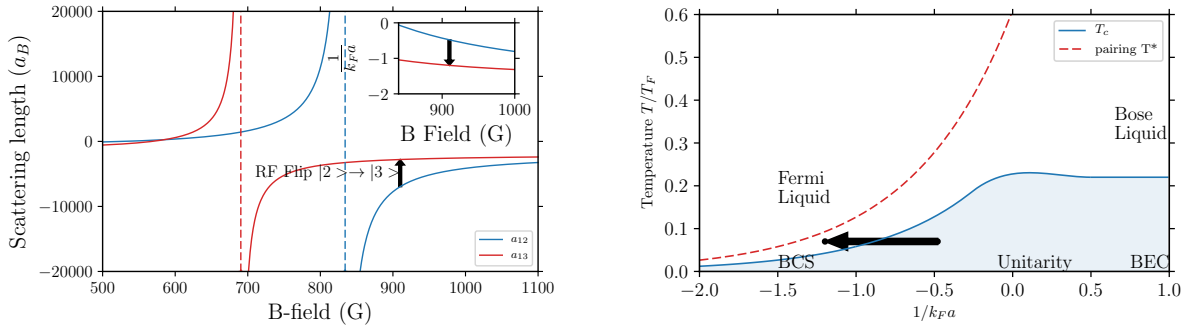

(a) Feshbach resonances **(b)** Critical temperature

Figure 8.1: Feshbach resonances of the $|13\rangle$ and $|12\rangle$ mixture (Fig. 8.1a) and superfluid phase diagram in the BEC-BCS crossover (Fig. 8.1b). The black arrow represents the RF drive $|2\rangle \rightarrow |3\rangle$ converting the mixture from $|12\rangle \rightarrow |13\rangle$, changing the $1/k_F a$ and hence the Δ and the T_c.

rium [226]. However, despite much theoretical interest and discussion, until now there has been little experimental investigation of non-equilibrium Fermi gases [227] because the timescales on which the system must be perturbed were too small.

In this chapter RF pulses are used to perform rapid quenches of the scattering length, and hence of the order parameter, in the BEC-BCS crossover. Whilst in Chapter 7, the RF was used to continuously drive a single component of the superfluid, the investigations in this chapter rapidly transfer the entire population of a single component to a new third state, by using the fast RF π pulse previously discussed. The different Feshbach resonances between $|12\rangle$ and $|13\rangle$ show that the superfluid, after the quench, has a Δ that is far from the equilibrium value for the new component configuration. These fast global quenches provide an ideal situation for studying the rich non-equilibrium dynamics in Fermi gases that have previously been inaccessible experimentally [78]. The quench process is highlighted in Fig. 8.1. Here the black arrow represents the RF pulse $|12\rangle \rightarrow |13\rangle$, which changes the scattering length and hence the $1/k_F a$ and equilibrium Δ parameter (Fig. 8.1a). Thus, the superfluid may now be far from equilibrium, being in a regime where it would normally not have a condensed component (Fig. 8.1b). Similarly, the cloud can be prepared in the $|13\rangle$ state and the reverse quench performed. This brings the gas suddenly to a $1/k_F a$ value where, in equilibrium, it should have a superfluid component and the emergence of quantum coherence can be observed.

In 1974, Volkov and Kogan [67] were one of the first to investigate the response of a superconductor to perturbations[1] in the order parameter, Δ. Working with the BCS Hamiltonian, they showed that a small perturbation in Δ led to oscillations in $|\Delta|$ with

[1]Other early studies include: [66, 228].

frequency $2|\Delta|/\hbar$, which decayed in time according to a power law, $t^{-1/2}$. This led to many further studies which verified these results, even with noticeably different models being used [71]. Additionally, it was found that undamped oscillations could be excited for particular large perturbations of $|\Delta|$ and certain non-equilibrium states [68, 90, 229]. At this time, ultracold Fermi gases had recently been shown as an excellent system for investigating the BEC-BCS crossover and changing the $1/k_F a$ parameter was recognised as a possible method for perturbing Δ. Several studies investigated the response of the superfluid to different quenches in the crossover regime [69, 91, 204, 219, 230]. Many of these findings are summarized and combined in [72] where quenches of Δ in the BEC-BCS crossover are thought to lead to three possible dynamical regimes, depending on the initial (Δ_{0i}) and final (Δ_{0f}) equilibrium order parameters. This *phase diagram* is shown in Fig. 8.2 and defines three regimes (separated by black lines): **I**, where Δ vanishes exponentially [231]; **II**, where Δ goes to a non-zero constant with some decaying oscillations; and **III**, where Δ oscillates persistently. From the known properties of the Feshbach resonance[1] (Section 2.2) and using the mean-field gap equation (Eq. (2.46)), it is possible to show which regions of this phase diagram can be explored using quenches between the lowest three hyperfine states of ^{6}Li. These are shown as solid colored lines with the colored points being values that we have investigated so far. Note that the $|23\rangle \rightarrow |12\rangle$ curve is not allowed by the selection rules, however, it has been implemented by performing two RF transitions simultaneously[2]. As we go to higher magnetic fields, the quenches approach the diagonal line in the quench diagram, which is the limit of a weak quench where $\Delta_{0i} \approx \Delta_{0f}$. The lines accessible to the experiment can be changed slightly by varying the atom number and trap frequencies to change $1/k_F a$. Of course, this phase diagram is at $T = 0$ and the finite temperature will have a noticeable effect. Importantly, for some of the quenches investigated, the start (or end) point is normal (i.e. $\Delta = 0$) in equilibrium. Additionally, the study of [72] does not focus on quenches to or from the unitarity regime (see for example [90]), which are within the parameter range of the experiment.

The dynamic process of superfluid state formation is of great interest with the emergence, timescales and evolution of long-range order deeply related to the concept of spontaneous symmetry breaking and non-equilibrium phase transitions [232]. However, the formation process in quantum gases has been challenging to investigate both experimentally and theoretically. The earliest quench experiments involved suddenly changing the trap

[1] For the results in Chapters 7 and 8 the precisely characterized Feshbach resonances tabulated in [100] are used.

[2] $|2\rangle \rightarrow |3\rangle$ and $|1\rangle \rightarrow |2\rangle$. Note that the quench is slower as RF power at each frequency is approximately halved.

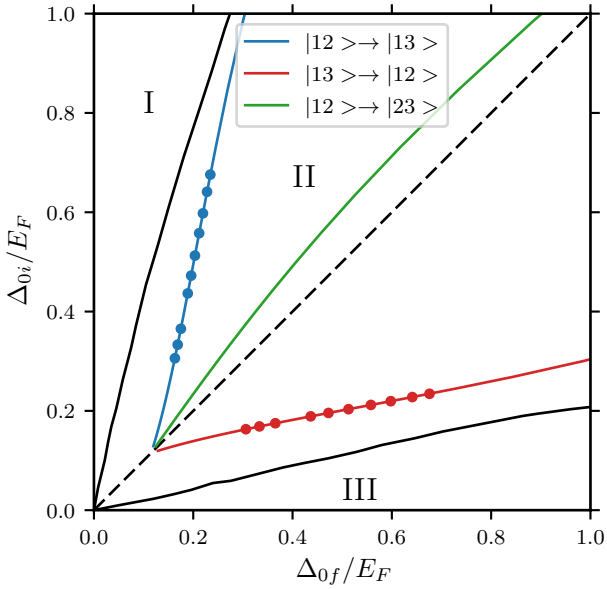

Figure 8.2: *Phase diagram* of quantum quenches in BEC-BCS crossover, adapted from [72], in terms of the initial and final order parameter, Δ_{0i} and Δ_{0f}. The solid black lines mark the transition to the different regimes **I**, **II** and **III** (see text or [72]). The colored lines show the regions accessible by rapidly changing a single component of the two-component superfluid using the broad Feshbach resonances of ^{6}Li (see legend). These colored lines were calculated using mean-field theory (Eq. (2.46)). The lines can be shifted slightly by adjusting the atom number or trap frequencies. The diagonal line is the limit of weak perturbations where $\Delta_{0i} \approx \Delta_{0f}$.

depth [233], applying a RF drive to perform evaporation [234] or using a dimple trap to modulate the phase space density [235] and observing the dynamics of the emerging condensate fraction. Simultaneously, many theoretical models arose to describe the BEC formation dynamics, including [236–238], with an overview of the methods summarized in [232]. Most of these approaches involved using the quantum Boltzmann equation to model the quasiclassical regime and one cause of discrepancy between experiment and theory was the evaporation dynamics of the thermal atoms [232]. Nevertheless, BEC formation experiments have helped understand a range of quantum phenomena, including topological structures studying the Kibble-Zurek mechanism [239], originally introduced in the context of cosmological models of the early universe.

The dynamics of superfluid formation in the context of fermions in the BEC-BCS crossover have not been investigated in as much detail as for bosons. In the works of Leggett [203] and Levitov [68], they study the response of a system where the BCS interaction parameter is suddenly turned on, and the dynamics from a normal to superfluid system. These works show that the initial quench leads to oscillations in the order parameter which in the long time limit (with damping) tends to an asymptotic value less than the equilibrium value. Without damping, they show that the order parameter should oscillate persistently. The formation dynamics and time scales were extended to include finite temperature effects in [70]. The main result shows that the oscillations are rapidly damped if the initial state is normal, however, they should persist for much longer if the initial state is superfluid. The experiments in this chapter thus provide an interesting testing ground for these theoretical models and can be compared with the formation dynamics found in bosonic systems.

For these measurements several different times scales play a role as shown in Fig. 8.3. The dynamical gap time [68] $t_\Delta = h/\Delta$, varies considerably from 40 µs to 140 µs, depending on the $1/k_F a$ where the quench is performed. Similarly, the quasiparticle relaxation time [68, 240], $t_\epsilon = (E_F/\Delta)t_\Delta$ varies from 60 µs to 700 µs. The unitarity-limited collision time [241] may also play a role $t_{\mathrm{col}} = 0.2hT_F/(TE_F) \approx 590\,\mu\mathrm{s}$, as may the trapping period $t_{\mathrm{trap}} = 2\pi/\bar{\omega} = 6.7\,\mathrm{ms}$. While t_Δ defines the timescale for coherent evolution of the wave function, t_ϵ defines the timescale for incoherent dynamics.

The investigations in this chapter are split into two sections. In Section 8.2 a $|12\rangle$ superfluid in the strongly interacting regime is quenched to much weaker interactions and the dynamics of the condensate fraction are observed. Qualitatively this probes regions **I** and **II** of the quench *phase diagram*. In Section 8.3 a $|13\rangle$ is prepared with very weak interactions in the normal phase and quenched to very strong interactions. The emergence

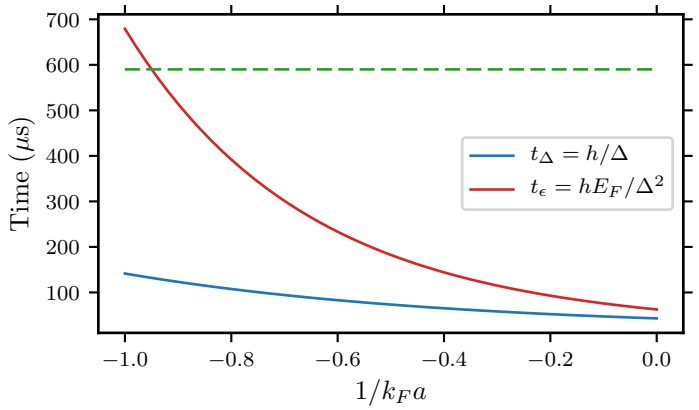

Figure 8.3: Different time scales that play a role in the dynamics of the order parameter using our experimental parameters. The dynamical gap time [68] is $t_\Delta = h/\Delta$, the quasiparticle relaxation time [68, 240], $t_\epsilon = (E_F/\Delta)t_\Delta$. The unitarity-limited collision time [241] $t_{\mathrm{col}} = 0.2hT_F/(TE_F)$ is shown by a dashed green line. Δ was calculated as a function of $1/k_F a$ using mean-field theory (Eq. (2.46)).

of the superfluid in the BEC-BCS crossover is then observed.

8.2 Quenches from Unitarity to BCS: Vanishing of Order

In this section the evolution of the condensate fraction of a $|12\rangle$ superfluid, with $T/T_F \approx 0.07$, rapidly transferred to the $|13\rangle$ mixture is investigated. The initial $|12\rangle$ superfluid is prepared at various fields from unitarity to the BCS regime, changing the Δ_{12}, the $1/k_F a_{12}$ and slightly the $1/k_F a_{13}$. An example is shown in Fig. 8.4 for a large quench, where initially there is a large condensate fraction in $|12\rangle$ at unitarity (Fig. 8.4a). The RF pulse drives the $|2\rangle \rightarrow |3\rangle$ creating a $|13\rangle$ mixture in 50 µs, which still has a visible condensate fraction (Fig. 8.4b). In equilibrium at this $1/k_F a_{13}$, the $|13\rangle$ should have a much smaller condensate fraction. The condensate fraction rapidly decays in less than 100 µs and the mixture becomes normal (Fig. 8.4c). These dynamics are clearly much faster than the $t_{\rm trap} = (7\,\text{ms})$ and $t_{\rm col} \approx (590\,\mu\text{s})$. When the initial regime is unitarity, $t_\epsilon \sim t_\Delta$; however, as the initial condition moves further to the BCS regime, $t_\epsilon \gg t_\Delta$ and there may be a change in the dynamics. This experiment provides the first realization of fast quenches in the BEC-BCS crossover and examination of the dynamics proposed first in [71, 231].

For each initial condition, the decay in the condensate fraction is measured in time after the RF pulse, as shown in Fig. 8.5. For each $1/k_F a_{12}$, a time scale for the vanishing of order can be extracted from an exponential fit. Furthermore, the initial condensate fraction in $|13\rangle$ (CF_{13}), immediately after the RF pulse, can be compared to the condensate fraction in $|12\rangle$ (CF_{12}) before the quench, and the quantity $\text{CF}_{13}/\text{CF}_{12}$ can be calculated. For these measurements, it has been confirmed that the RF pulse has a high $|2\rangle \rightarrow |3\rangle$ transfer efficiency ($> 96\,\%$), which is attributed to the short pulse time, meaning the RF pulse is broad in frequency space (FWHM = 38 kHz) and can address the entire cloud. Furthermore, it was confirmed that there is no significant change of atom number during the quench, and that the decay in the condensate can also be seen as increase in the thermal background. The different $1/k_F a_{12}$ can be converted into a gap, Δ_{12}, which plays the role of the initial order parameter, Δ_{i0}. This allows the values where the quench is performed to be shown on a phase diagram, adapted from [72], as shown in Fig. 8.2. The quenches from unitarity go from a large Δ_{i0} to a smaller Δ_{f0} in the BCS regime. This is close to the boundary between region **I** and **II** in the phase diagram. As the $1/k_F a_{12}$ is increased, the change in Δ from the quench becomes smaller and the diagonal line, representing a weak perturbation, is approached. Since the theoretical model in [72] does not consider quenches from unitarity, this limit should be more appropriate for comparison

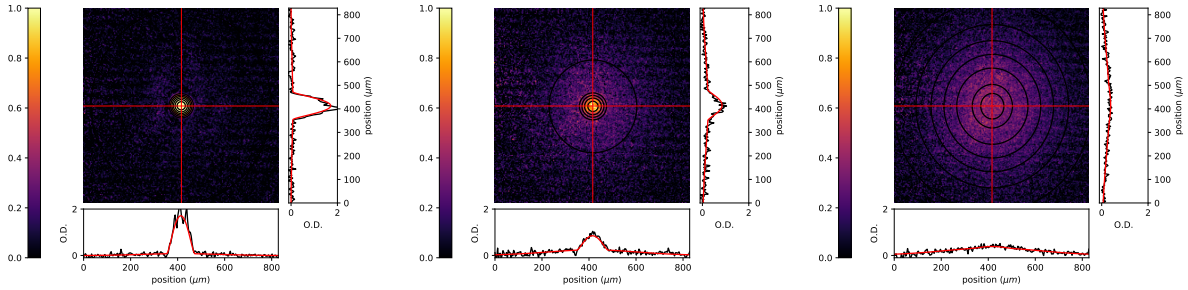

(a) $|12\rangle$ before quench **(b)** $|13\rangle$ after quench **(c)** $|13\rangle$ 100 µs after quench

Figure 8.4: Example images of the atom cloud after the rapid ramp technique, with a bimodal fit. **Fig. 8.4a** shows the atoms before the quench in the $|12\rangle$ state. **Fig. 8.4b** shows the $|13\rangle$ non-equilibrium superfluid immediately after the quench. **Fig. 8.4c** shows the $|13\rangle$ state 100 µs after the quench when the condensate fraction is no longer visible. These images are taken from the quench at 835 G corresponding to $1/k_F a_{12} = 0$ and $1/k_F a_{13} = -0.9$.

with theory. Furthermore, as this region is approached it may be possible to see damped oscillations in the decay of Δ, which would be a direct method to observe the Higgs mode [71].

Fig. 8.6 compares the initial CF_{13} with CF_{12} before the quench. As expected (see Fig. 5.18) the CF_{12} decays as $1/k_F a_{12}$ decreases due to a reduction in Δ_{12} (see Eq. (2.46)). The evolution of CF_{13} is more complex. It could be expected that as the weak perturbation limit is approached where, $1/k_F a_{12} \to 1/k_F a_{13}$, that $CF_{13} \to CF_{12}$. This is observed as the BCS regime is approached with $CF_{13}/CF_{12} > 70\,\%$. In the other limit of a stronger quench, $(1/k_F a_{12} = 0 \to 1/k_F a_{13} = -0.9)$, the CF_{13}/CF_{12} is much smaller. It was thought this effect could be understood by analyzing the overlap of the BCS wave function (Eq. (2.43)) between two different $1/k_F a$ values. In a simple picture this may be some measure of how many $|12\rangle$ pairs can be projected to $|13\rangle$ pairs. The quantity $\langle \psi_{\mathrm{BCS}}(1/k_F a_{12}) \,|\, \psi_{\mathrm{BCS}}(1/k_F a_{13}) \rangle$ was calculated using Eq. (2.43) (black line Fig. 8.6) for the specific quenches in the experiment and shows the correct trend. However, it usually predicts too large a conversion. Following the analyses of Altman [187] and Ho [242], this discrepancy may be due to the different conversion efficiencies of the rapid ramp technique for the different pairs, which have different $1/k_F a$ values. In the limit of the weak quenches, the $1/k_F a$ values are similar and the effect of the rapid ramp should be the same for both $|12\rangle$ and $|13\rangle$ pairs, as shown by the good agreement of the $\langle \psi_{\mathrm{BCS}}(1/k_F a_{12}) \,|\, \psi_{\mathrm{BCS}}(1/k_F a_{13}) \rangle$ calculation at $1/k_F a_{12} \approx -0.75$. This effect does not play a significant role in the observed non-equilibrium time dynamics as it should simply lead to a scale factor for the condensate fraction measured.

In Fig. 8.7 the fitted time constants, τ, assuming an exponential decay in the CF_{13} of

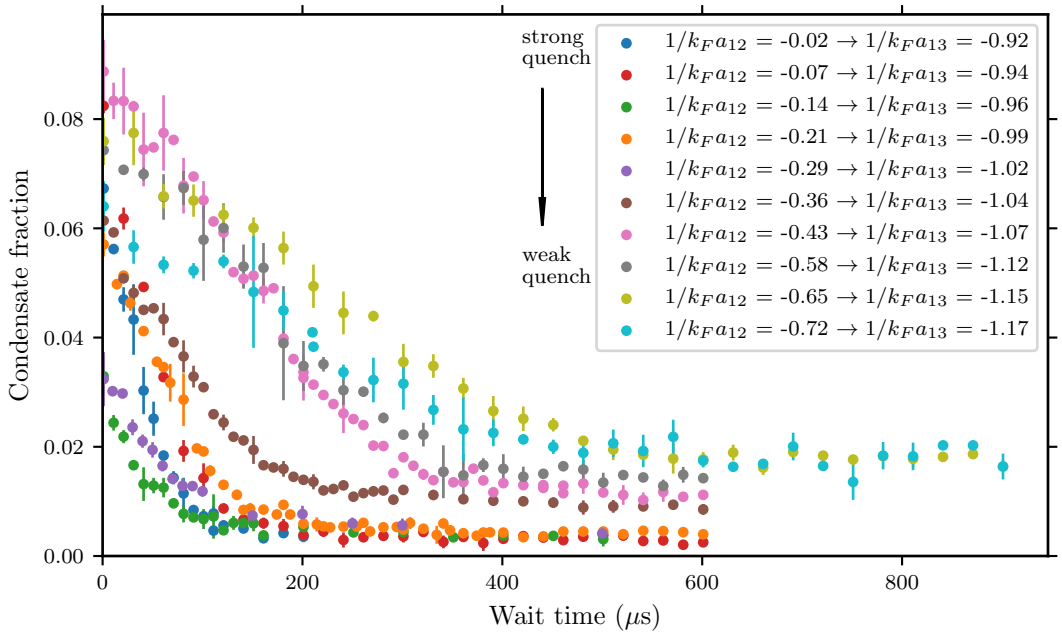

Figure 8.5: Evolution in time (µs) of the $|13\rangle$ out-of-equilibrium condensate fraction immediately after the quench, for various quench parameters (see legend). The initial condensate fraction and timescale of the dynamics changes for different quenches. The error bars represent the standard deviation of approximately four repetitions.

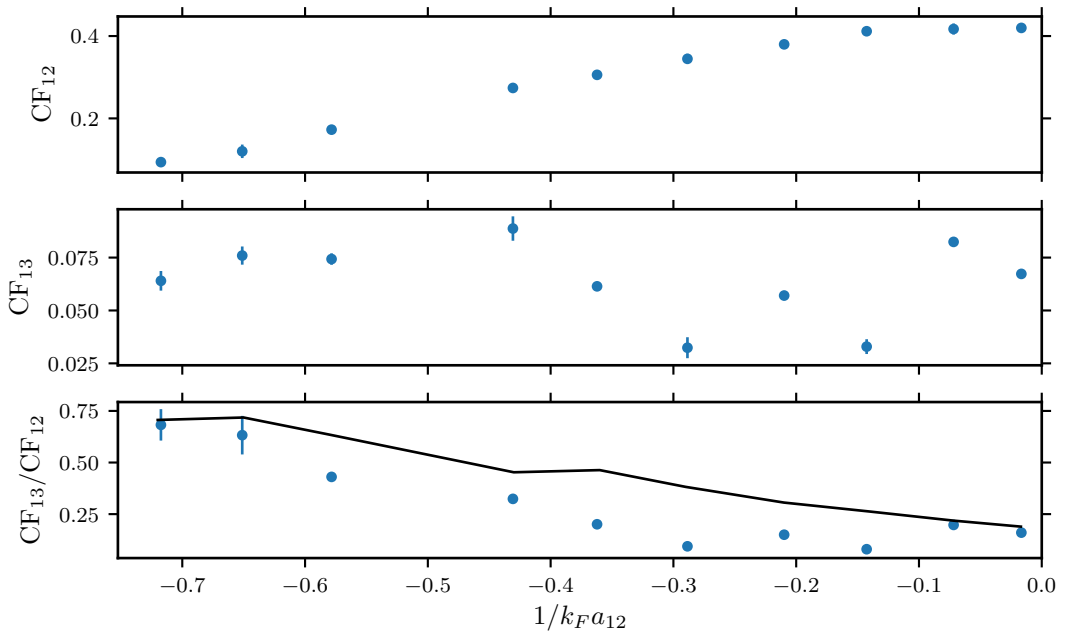

Figure 8.6: Comparison of the initial condensate fraction in the out-of-equilibrium $|13\rangle$ superfluid (CF_{13}), compared to the typical in-equilibrium condensate fraction of the $|12\rangle$ mixture immediately before the quench, (CF_{12}). The *conversion efficiency* from the equilibrium $|12\rangle$ to the out-of-equilibrium $|13\rangle$, CF_{13}/CF_{12} is also shown. Error bars are the standard deviation of approximately four repetitions. The black line is the calculated quantity $\langle\psi_{\mathrm{BCS}}(1/k_Fa_{12})\,|\,\psi_{\mathrm{BCS}}(1/k_Fa_{13})\rangle$ for the specific quench parameters, which should give some measure of the conversion efficiency.

the form $Ae^{-t/\tau} + B$, are shown in units of µs and compared to the values of t_Δ and t_ϵ. In absolute time, the decay is most rapid at unitarity ($< 50\,\mu s$), slowing down by approximately a factor of six in the BCS regime. From Fig. 8.7 it is seen that the decay time for the larger quenches from unitarity is comparable to t_Δ. For the weaker quenches the decay is significantly slower than t_Δ and well matched by t_ϵ. Following the theoretical work for quenches to lower interaction strengths [71, 231], the initial time dynamics of Δ after the quench can be approximated as:

$$\frac{\Delta(t)}{\Delta_i} = A(t)e^{-2\alpha\Delta_i t} + B(t)e^{-2\Delta_i t} \quad \text{Region } \mathbf{I} \tag{8.1}$$

$$\frac{\Delta(t)}{\Delta_\infty} = 1 + a\frac{\cos(2\Delta_\infty t + \pi/4)}{\sqrt{\Delta_\infty t}} \quad \text{Region } \mathbf{II} \tag{8.2}$$

where $\Delta_\infty \approx \Delta_f$ is the asymptotic value of $\Delta(t)$ after the quench and α, a, $A(t)$ and $B(t)$ are constant or functions whose definitions can be found in [231][1]. The important predictions from Eqs. (8.1) and (8.2) are that region **I** is dominated by an exponential decay in Δ to zero on a timescale comparable to t_Δ, whereas in region **II** there is a power law decay in Δ to an asymptotic value with some weak oscillations at a frequency of $2\Delta_\infty/\hbar$. For these equations, the effects of relaxation are not considered, and one would expect that Δ also shows a decay on the timescale of the quasiparticle relaxation time, t_ϵ, which should define the timescale for the dissapearance of the non-equilibrium fermionic condensate [68, 240]. The timescales for the decay of Δ shown in Fig. 8.7 agree qualitatively with the predicted behavior in Eqs. (8.1) and (8.2) and the dramatic change in time scales, shown in Fig. 8.7, provides strong evidence that the quenches cross from region **I** to **II**. It is difficult to confirm that region **II** shows a power-law decay as opposed to an exponential decay, especially with the added decay rate from relaxation effects. It should also be noted that the condensate fraction is measured, which is not a direct measure of Δ. For the weaker quenches, there is also the possibility of seeing fast oscillatory dynamics on a time scale, t_Δ, within the time of the *slow* decay, which will be discussed at the end of this section. Note that the weaker quenches in the BCS regime satisfy the condition that $t_{\text{quench}} \ll t_\Delta \ll t_\epsilon$ well, as required in the theoretical discussion of the quench [68,71,72]. A simplistic thermodynamic argument for the different behavior in region **I** and **II** is given in [231]. Immediately after the quench, the system has a higher energy than the ground state with order parameter Δ_f, which in equilibrium would correspond to some new temperature, T_0. As Δ_f decreases (i.e. the quench gets

[1]Note that in Eqs. (8.1) and (8.2) $\hbar = 1$ to follow the definitions in [71].

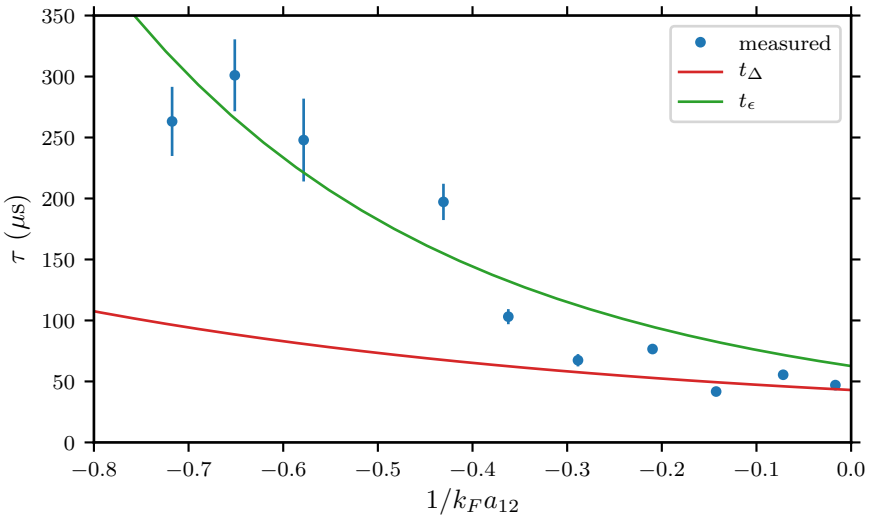

Figure 8.7: Decay time constant, τ of the $|13\rangle$ out-of-equilibrium superfluid against the initial gap in the $|12\rangle$ superfluid, Δ_{12}/E_F. The time constant is extracted by fitting an exponential decay of the form $Ae^{-t/\tau} + B$. The gap time, $t_\Delta = h/\Delta$, (red line) and the quasiparticle relaxation time, $t_\epsilon = (E_F/\Delta)t_\Delta$ (green line) are shown for comparison. Note that the red and the green line are calculated and not fitted.

larger), the T_c decreases, but T_0 grows. For a sufficiently large quench, the additional energy of the system is enough to drive the transition to the normal phase, which is why in region **I**, $\Delta \to 0$.

From the data in Fig. 8.5, it can be seen that the weaker quenches, further into the BCS regime, seem to show a higher final value of the condensate fractions at times $t > t_\epsilon$. This was surprising as the final state was further into the BCS regime and in equilibrium a smaller condensate fraction would be expected at the same temperature. In Fig. 8.8a, the evolution of the condensate fraction is shown for considerably longer times and a clear revival in the condensate fraction is seen for the weaker quenches at times $t \gg t_\epsilon$. Dynamics very similar to this were also predicted in [71, 231] where they show that, following a sudden change of the BCS coupling constant, the system recovers to a non-stationary steady state and the order parameter tends to a finite value. For the larger quenches in region **I** the Δ decays to zero without revival. Fig. 8.8 can be directly compared to the inset of Figure 2 in [231]. This would imply that as the quenches become weaker, the boundary between the **I** and **II** regions of the phase diagram shown in [72] is crossed. This would not match the calculated Δ_{0i}/Δ_{0f} values in [72], however, our quenches start close to unitarity and we calculate the Δ_{0i}/Δ_{0f} using mean-field theory, which may explain this discrepancy. This revival would provide evidence of the non-equilibrium asymptotic state after the quench, that persists for times much larger than t_ϵ as predicted in [231]. The observed time scale for the revival was approximately $30t_\Delta$,

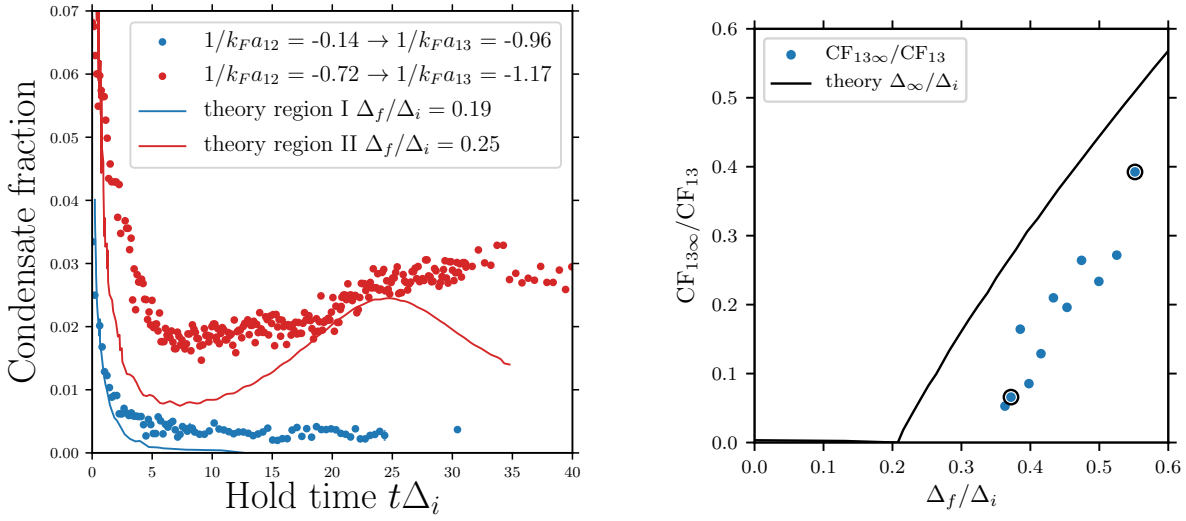

(a) Revival in the time domain.

(b) Final state after revival.

Figure 8.8: Revival of the condensate fraction after certain quenches. **Fig. 8.8a** shows the condensate fraction against time for two different quenches. For the larger quench, no revival is seen (blue), however, for weaker quenches the revival becomes clear (red). Theoretical simulations of the response of the order parameter for similar quenches were calculated in [231]. The theoretical data from the inset of Figure 2 in [231] is shown in Fig. 8.8a for comparison. The theoretically simulated $\Delta(t)/\Delta_i$ has been linearly scaled to give the same initial value as the corresponding condensate fraction data. The shape and timescales of the decay and revival qualitatively match, however, quantitative matches are not expected as the simulation does not use our exact quench conditions. Additionally, it is not simple to convert the simulated order parameter into a measured condensate fraction. Similarly to Fig. 8.5, it can be seen that the larger quench also has a faster initial decay. Note that the time is in units of the initial t_Δ (calculated using mean-field theory) so as to be directly comparable to [231]. **Fig. 8.8b** shows the asymptotic condensate fraction (measured always at 4 ms) for various initial and final state quench conditions. These can be compared to the theoretical asymptotic non-equilibrium gap values (solid black line) computed in [231]. The blue points compare the asymptotic condensate fraction to that initially in the $|13\rangle$ state immediately after the quench. The circled points correspond to the quenches shown in Fig. 8.8a. The quench parameters $1/k_Fa_{12} \rightarrow 1/k_Fa_{13}$ have been converted to a ratio of the final and initial equilibrium order parameter (Δ_f/Δ_i) using mean-field theory, to be directly compared to theoretical simulation in [231].

comparable to the theoretical predictions [231]. In Fig. 8.8b the condensate fraction after revival (i.e. in the long time limit) is shown as a function of the quench conditions. Here, this quantity is compared to the theoretical non-equilibrium asymptotic gap value, first calculated in [231]. Note that this time scale is still less than t_{trap} and the atom number remains constant during the evolution, implying that no evaporation and cooling occurs. This observation would provide evidence for the predicted coherent dynamics of far from equilibrium fermionic condensates. Furthermore, it is predicted that these non-equilibrium states have a finite superfluid density but are gapless [231], similar to the gapless superconductivity observed in some metals [205]. However, measuring this feature with our system may be challenging.

It would be interesting to perform a quench where there was a large condensate fraction in both the initial and final equilibrium states. For the $|13\rangle$ fermionic condensate this involves working at fields 580 G to 790 G, close to the resonance. However, these fields are all in the BEC regime for the $|12\rangle$ Feshbach resonance. It was attempted to perform the quench at 790 G, however, it was found that after the quench the $|3\rangle$ atoms were rapidly expelled from the trap. At this field, the binding energy of the $|12\rangle$ molecules is 9 kHz (400 nK), which may lead to energy transfer and heating of the $|3\rangle$ state. Furthermore, this transition involves starting from the BEC regime of $|12\rangle$, where the pairs have formed weakly bound molecules, and quenching to the BCS regime of the $|13\rangle$. The transformation of the $n(k)$ from bosonic to fermionic behavior may also cause a significant change in the energy distribution. For this reason, a quench from a clear equilibrium superfluid state to another has not yet been achieved. The $|23\rangle$ Feshbach resonance is quite similar to the $|12\rangle$ and with this quench the regime of weak perturbation from superfluid states could easily be performed. Unfortunately, the required $|1\rangle \rightarrow |3\rangle$ transition is forbidden. Whether it is possible to drive a simultaneous $|2\rangle \rightarrow |3\rangle$, $|1\rangle \rightarrow |2\rangle$ transition is currently being investigated.

Finally, it is interesting to consider if any dynamics can be seen on the time scale of t_Δ, as predicted in many of the theoretical studies [68, 72, 73]. This would provide a direct signal for the excitation of the Higgs mode in the time domain. Consider the quench close to the weak perturbation limit, where the $\Delta_{0i} = 0.31 \rightarrow \Delta_{0f} = 0.16$. This gives a t_Δ of 95 µs, which is well within the regime that can be resolved. However, the predicted amplitude of these dynamics is very small [72, 73] and it is not clear if it could be resolved in the condensate fraction signal averaged over the finite size cloud or if the signal would dephase for different experiment cycles. Nevertheless, some preliminary data of the fast dynamics is shown in Fig. 8.9. Here a very weak signal, indicative of heavily damped oscillations on the rapid decay, is visible with a period of approximately 80 µs. To resolve this signal, each point was averaged five times and the error bars show the standard error in the mean of the measured condensate fractions. An additional difficulty is that when working at 1000 G, over a time scale of several hours, the vacuum chamber slowly begins to magnetize, which causes some of the early RF sweeps in the experiment to be less efficient, reducing the overall atom number. This occurs even with the demagnetization routine implemented as described in Chapter 5. This prevents us from averaging the signal for even longer, as the systematic drift in condensate fraction and atom number becomes significantly larger than the signal strength. The fast dynamics and potential observation of the predicted oscillations in Δ are still being investigated.

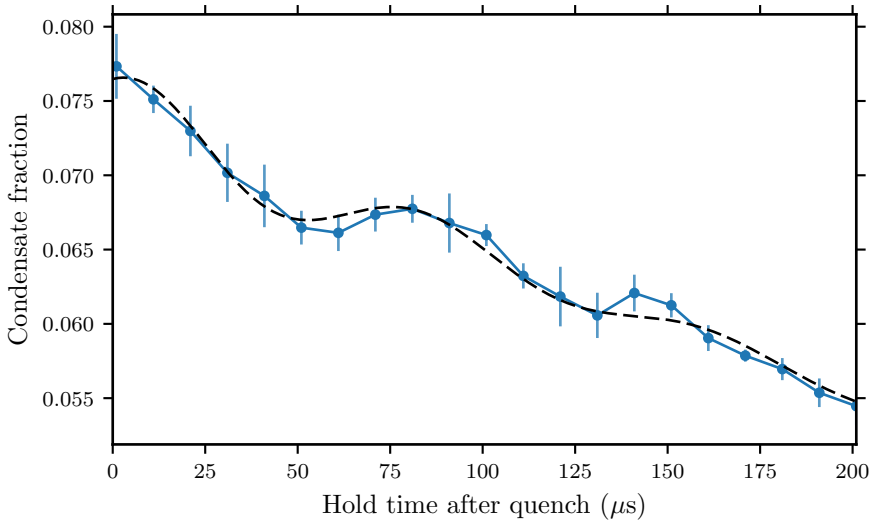

Figure 8.9: High resolution of the time dynamics of the decaying $|13\rangle$ out-of-equilibrium superfluid at 1000 G. This corresponds to $1/k_F a_{12} = -0.7 \rightarrow 1/k_F a_{13} = -1.2$. There appear to be heavily damped oscillations on a time scale comparable to t_Δ as predicted in region **II** in [72]. The error bars represent the standard error in the mean condensate fraction from five repetitions. These dynamics can also be seen in the original data (Fig. 8.5) with lower time resolution. The dashed black line is a fit of an exponentially decaying sine-wave with a linear background. The frequency from this fit is 12.8 kHz which can be compared to the value of the resonance frequency found in the gap measurement (Table 7.1) of 14.0 kHz.

8.3 Quenches from BCS to Unitarity: Emergence of Order

In this section the formation of the superfluid in the BEC-BCS crossover is investigated by quenching the (attractive) interaction parameter from a very weak value, where the system is normal, to a much stronger interaction, where in equilibrium the system should condense. This quench is performed by rapidly transferring one spin component to a third state, which gives rise to a much larger scattering length due to the broad Feshbach resonances in ^{6}Li (see Fig. 8.1). These quenches have the advantage that they do not change the trap depth, geometry or density and do not involve evaporation which can lead to changes in atom number and temperature that affect the dynamics and interpretation.

The experimental routine for this investigation is similar to that discussed in Section 8.2, however, the atoms are now prepared in the $|13\rangle$ state and evaporated on the $|13\rangle$ Feshbach resonance[1]. The field is then adiabatically ramped to 790 G–1000 G where the Δ_{13} is

[1]This involves performing an additional Landau-Zener sweep from state $|2\rangle \rightarrow |3\rangle$ before ramping to the $|13\rangle$ Feshbach resonance at 680 G.

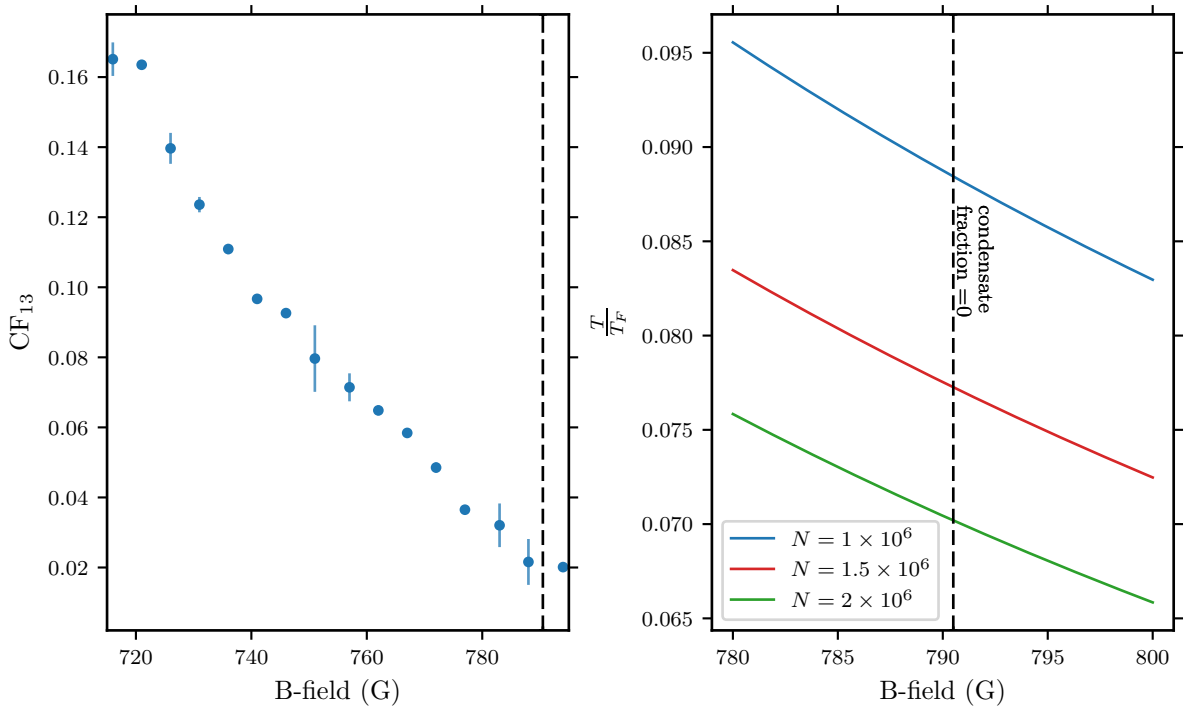

Figure 8.10: Technique for the calibration of temperature. The $|13\rangle$ mixture is adiabatically ramped to different B-field values before performing the rapid ramp technique. At some field, B, the condensate fraction will go to zero when $T = T_c$. The T_c far on the BCS side is closely related to the gap and for this analysis the Gor'kov-Melik-Barkhudarov correction is used [113], giving $T_c \approx 0.277 E_F \mathrm{e}^{-\frac{\pi}{2k_F|a_{13}|}}$. The left plot shows the reduction in condensate with B. The right figure shows the calculated T_c for various atom numbers (see legend). The field at which the condensate fraction reaches zero was found to be 790.5 G as shown by the black dashed line. The condensate fraction is extracted from the bimodal fit and won't go exactly to zero as the least squares fitting algorithm will always prefer a small value for the parabola amplitude. The zero reference is usually taken to be where no condensate fraction can be seen by eye, or when the fitted waists of the parabola begin to vary significantly from shot to shot. The calibrated atom number was measured as 1.5×10^6 (red curve) giving a T/T_F of 0.077. A condensate fraction was still visible at 787 G which provides an upper bound to the temperature. Even a factor of two uncertainty in the atom number only changes the T/T_F from 0.07 to 0.09.

small enough that $T = 0.07 T_F > T_c$. The RF π pulse then creates a $|12\rangle$ mixture in 50 µs bringing the atoms to a $1/k_F a_{12}$ value, where at equilibrium, they would have a condensate fraction. The emergence of the condensate is observed by measuring the condensate fraction after the rapid ramp technique. An additional hold time (300 ms to 500 ms) was used before the quench to ensure that evaporation had finished and it was confirmed that the temperature and atom number before the quench were approximately constant for all quenches. The temperature calibration is performed by finding the critical field at which the $|13\rangle$ has no condensate fraction after the adiabatic ramp. At this point $T = T_c$, which can be estimated using the GMB approximation (Eq. (2.44)) as shown in Fig. 8.10.

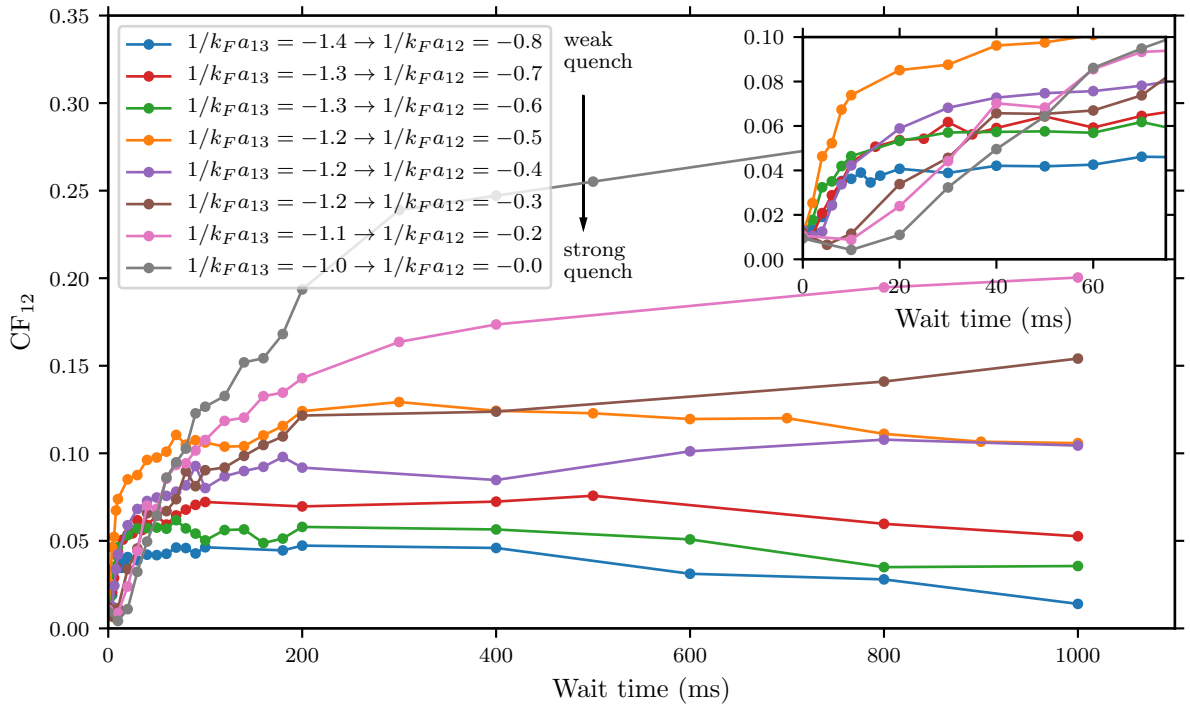

Figure 8.11: Appearance of the $|12\rangle$ condensate fraction after a quench from the normal $|13\rangle$ mixture. The inset figure shows the same data but zoomed in on the initial time range 0 ms to 75 ms.

The time domain data set for these quenches is shown in Fig. 8.11, where the inset figure shows the same data in the initial 75 ms of dynamics. From these data, two immediate observations can be made. Firstly, for all the quenches, in the long time limit, a superfluid is the final state as would be expected for the final $1/k_F a$ and T/T_F. Secondly, the time scale for the dynamics changes considerably for the quenches to different $1/k_F a$, and this time scale is several orders of magnitude slower than those observed in Section 8.2. For a coarse analysis, a constrained exponential decay of the form $A(1 - \mathrm{e}^{-t/\tau})$ can be fitted to each quench, which gives a reasonable approximation for the final condensate fraction, $\mathrm{CF}_{12}(t \to \infty)$ and the decay time constant τ.

The final condensate fractions are shown in Fig. 8.12 where they are compared to the typical condensate fractions when the $|12\rangle$ superfluid is prepared directly (without a quench). The general trend of $\mathrm{CF}_{12}(t \to \infty)$ follows that of the standard $|12\rangle$ superfluid, which implies that in the long time limit the equilibrium state is reached. The agreement is, however, noticeably better in the BCS regime with a significant discrepancy at unitarity. This may be related to the change in energy of the system as a result of the sudden change in $1/k_F a$, which is larger for the quenches to unitarity. The change in total energy of the system as a result of the quench can be calculated from the universal Tan rela-

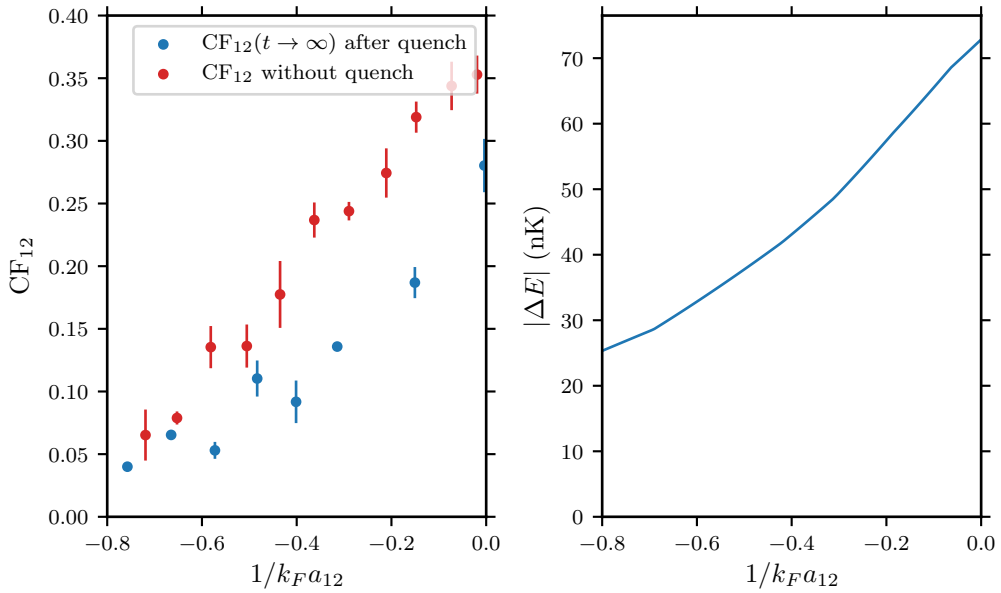

Figure 8.12: The final condensate fraction in the $|12\rangle$ superfluid ($\mathrm{CF}_{12}(t \to \infty)$) is shown on the left for quenches to various $1/k_F a_{12}$ (blue points). This is compared to the equilibrium $|12\rangle$ condensate fraction without a quench (red points). The discrepancy between the values at unitarity may be explained by the change in total energy of the system ΔE (nK) as a result of the quench. From Eq. (8.3) a measure of the change in energy of the system as a result of the quench can be calculated, as shown in the figure on the right. Qualitatively, it is clear that the larger quenches correspond to a larger change in energy, which may explain the difference in condensate fraction. This calculation used the values for Tan's contact from [245]. The error bars show the standard deviation of approximately four repetitions.

tions [35, 243], briefly discussed earlier, which should be highly applicable at these values of $1/k_F a$ and also given that the initial state has no condensate fraction:

$$\Delta E = \frac{-\hbar^2}{4\pi m}\left(\frac{1}{a_{12}} - \frac{1}{a_{13}}\right) C \tag{8.3}$$

where C is the initial Tan's contact parameter [243], which has been calculated theoretically as a function of $1/k_F a$ [244, 245]. This quantity will be larger for the quenches where $1/k_F a_{12}$ approaches unitarity, and this additional total energy leads to a lower condensate fraction. The ΔE for the quenches performed by the $|13\rangle \to |12\rangle$ flip have been calculated and are also shown in Fig. 8.12. The slight measured peak at $1/k_F a \approx -0.5$ is repeatable and not understood, but may relate to the fact that $1/k_F a_{13}$ is also changing slowly as the B field is varied, changing the scattering length before the quench.

The time scale for the formation of the superfluid is shown in Fig. 8.13, highlighting several interesting properties. The time scale for the formation is always much slower than that for the $|12\rangle \to |13\rangle$ quenches, which were on the order of t_ϵ =50 µs to 350 µs. For the $|13\rangle \to |12\rangle$ quenches discussed here, the initial state is normal with $\Delta = 0$ and the initial

t_ϵ is not well defined. Not only is the time scale much slower, but it also varies by almost an order of magnitude (5 ms to 200 ms) for the range of $1/k_F a$ investigated and, quite surprisingly, the formation dynamics are slower when quenching into unitarity. Naively, one would expect that the formation dynamics would be dominated by the collision time, which should be fastest at unitarity. It is interesting to consider this in comparison to Fig. 8.7 of the $|12\rangle \rightarrow |13\rangle$ quench. There it was found that the condensate fraction persisted for the longest time out of equilibrium when the BCS and weak perturbation regime was approached. For the opposite quenches it was found that, in the BCS and weak perturbation regime, the condensate fraction formed the fastest. These timescales can be compared to those predicted in [68,203]. During these quenches no large amplitude oscillations from normal to superfluid state were observed, as predicted in [68]. However, it was also shown that a small damping term significantly reduced the amplitude of the oscillations. Furthermore, the finite temperature effects discussed in [70] should lead to rapid damping of the oscillations if the initial state is normal. They also argue that each time the quench is performed, the initial condition of Δ is selected and when measuring in our system the oscillations may rapidly dephase. The time scales predicted to reach the asymptotic gap value with damping in [68, 203] are 50 to 300 t_Δ ($\approx$5 ms to 30 ms). These are similar to the time scales we have measured in the BCS limit. Leggett predicts in [203] that the approach to the asymptotic state is faster for larger quenches, however, we have observed the opposite trend. This may be due to effects at unitarity that are not considered in these works. It would be very interesting to perform these simulations with the quench conditions used in the experiment and compare the time scales and amplitude of the predicted (but unobserved) oscillations. Furthermore, the predicted envelope of the evolution is not a simple exponential decay and could be more closely compared to the experimental data. Notably, when quenching from unitarity the initial shape looks noticeably different with the condensate fraction initially growing very slowly as can be seen in the inset of Fig. 8.5.

The fact that the timescale for formation is fastest in the case of the weaker perturbations (i.e. where the $1/k_F a$ does not change as much) could be an indirect observation of preformed pairs in the $|13\rangle$ mixture, even though no superfluid order is present. If the preformed pairs were present, then in the case of a weak perturbation, the size of the pairs would be approximately correct for the size of Cooper pairs in the $|12\rangle$ superfluid state, meaning the ordered state could form on faster timescales. When quenching to unitarity, the preformed pairs would not have the correct size for the condensed pairs at unitarity, meaning the dynamics of the formation would occur more slowly, even though the collision time should be much faster. It should be stressed that this would only be

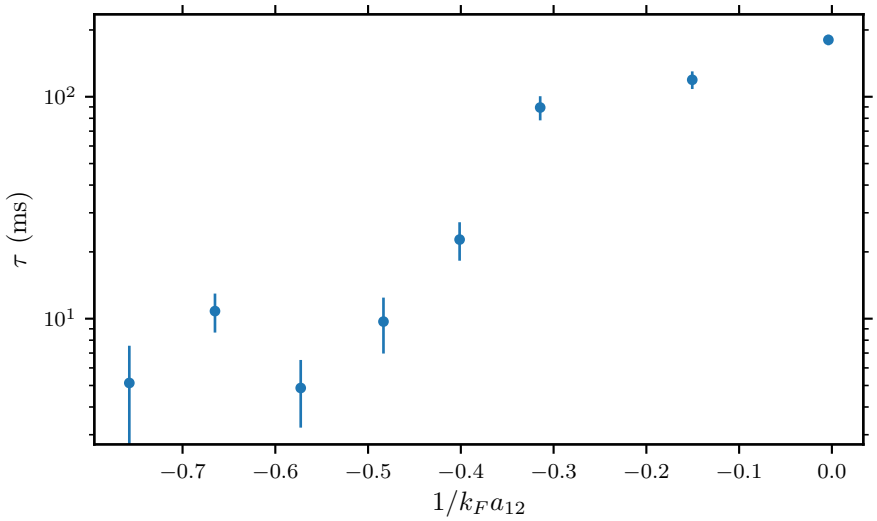

Figure 8.13: Fitted exponential decay time constant τ for the appearance of the condensate fraction against the final quench parameter $1/k_F a_{12}$. Note that τ changes by over an order of magnitude and is largest (slowest) at unitarity. The error bar represents the uncertainty in the fitted τ from the diagonal terms of the covariance matrix.

an indirect measurement and requires further theoretical investigation. It is also possible that some of the damping mechanisms associated with the collective modes may play a role, as the damping would be stronger at unitarity [91]. However, it is unlikely that the collective modes still play a role at such long time scales.

An additional measurement was performed to quantify how the formation dynamics depended on temperature. Parametric heating was used to vary the temperature of the cloud, with each temperature calibrated individually using the method shown in Fig. 8.10. The additional heating causes the atom number to be reduced slightly with a factor of two difference in the atom number between the minimum and maximum temperatures measured. The variation in the time constant with temperature is shown in Fig. 8.14 and shows an increase in τ with T/T_F. Note that the GMB mean-field method for calculating T/T_F should systematically over estimate the temperature, which explains why a small condensate fraction was still visible at a $T/T_F \approx 0.16$. Since the temperature is known to play a role in the time scales for bosonic superfluid formation, this data set may be of interest for theoretical models of fermionic superfluid formation.

Due to the surprisingly slow dynamics of the formation, the idea of combining the spectra, used to measure the gap in Section 7.5, with the rapid quenches discussed here was proposed. By using a larger value of $\alpha \approx 0.1$ and shorter $t_0 \approx 1\,\text{ms}$ it would be possible to measure the dynamics of the gap with a resolution of approximately $t_0 \ll \tau$. This

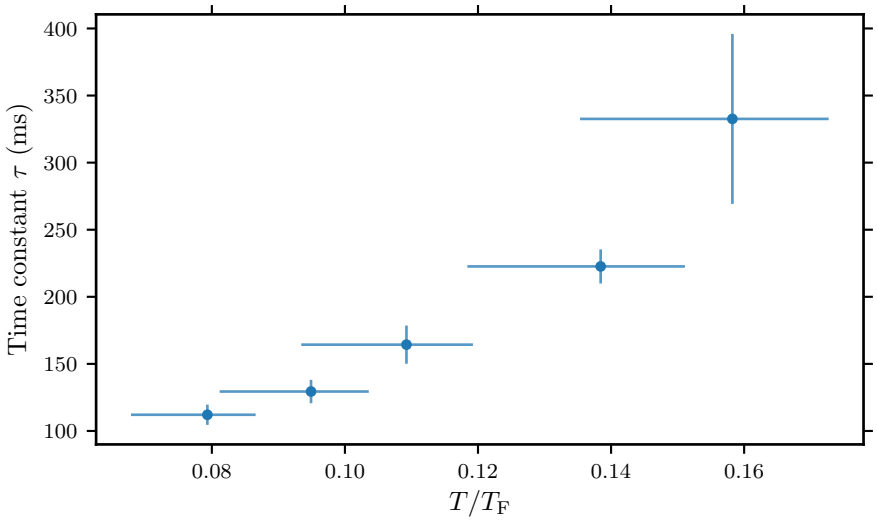

Figure 8.14: Variation in the exponential decay time constant τ for the appearance of the condensate fraction against the temperature of the initial cloud. The temperature is controlled via parametric heating and measured with the method shown in Fig. 8.10. Due to the heating, the atom number changes by a factor of two between $T/T_F = 0.08$ and $T/T_F = 0.16$. This data set was taken at 850 G corresponding to $1/k_F a_{13} = -0.95 \rightarrow 1/k_F a_{12} = -0.12$. The temperature error bars are limited by the uncertainty in the atom number. The uncertainty in τ is from the diagonal terms of the covariance matrix of the fitted parameters.

could answer many interesting questions about the emergence and evolution of the non-equilibrium gap and existence of preformed pairs. This is currently under investigation with the experiment.

Chapter 9

Summary and Outlook

This thesis has described the construction and operation of a new Bose-Fermi mixture quantum gas experiment, capable of producing molecular BECs of ^{6}Li with over 5×10^6 atoms per spin state at temperatures $T = 0.07 \pm 0.02 T_F$. There are currently over 30 quantum gas machines worldwide using ^{6}Li and the atom numbers and temperatures in our experiment are comparable to the best numbers that have been achieved. An advantage of our system is that bosonic ^{23}Na is initially used to sympathetically cool the fermionic ^{6}Li. This allows us to transfer very large numbers of ^{6}Li atoms to a high power crossed-beam dipole trap, where they can be evaporated very efficiently using a Feshbach resonance. Additionally, the broad Feshbach resonances of ^{6}Li make it ideal for investigating the BEC-BCS crossover. This regime connects the BCS superfluid to a BEC of bound molecules through the unitarity regime, where the strongly interacting many-body system is still not fully understood theoretically. We have implemented a new technique to quench or perturb the fermionic system using fast RF flips. This opened the possibility to study many non-equilibrium phenomena that have not been investigated before. These investigations are briefly summarized below before discussing the future outlook of the experiment.

Measuring the gap in the BEC-BCS crossover

An RF drive was used to modulate the population of one component of the two-component condensate in the BEC-BCS crossover. This modulation is thought to couple to the amplitude/Higgs mode of the superfluid order parameter. By continuous modulation, the Higgs mode was excited and the condensate fraction decreased depending on the drive frequency of the modulation. Following the interpretation of Stringari et. al. in [73], the

excitation of the Higgs mode should have a resonance frequency at twice the equilibrium gap. By interpreting the resonance frequency of the excitation in this way, the gap could be measured in the BEC-BCS crossover. This measurement was compared to mean-field theory and recent quantum Monte Carlo simulations. The signal for the resonance became broader as the BEC-regime was approached, implying that the lifetime of the Higgs mode decreases. By $1/k_{\mathrm{F}}a \approx 1$, it was not possible to measure a clear signal. This broadening is thought to be caused by damping of the Higgs mode and coupling to the phase mode as the unitarity and BEC regimes are approached. It is also possible that the harmonic trapping potential plays a role in the gap measurement and the asymmetric shape of the resonance, as the local gap will be smaller near the edges of the cloud.

Non-equilibrium dynamics in the BEC-BCS crossover

The RF modulation can be tuned such that the entire population of one component is transferred to a different third component in less than 30 µs. This is less than the dynamical gap time, t_Δ, and quasiparticle relaxation time, t_ϵ. The broad Feshbach resonances in the three lowest hyperfine states of ^{6}Li mean that the fast π pulses act like a quench in the scattering length and hence, a quench of the interaction $(1/k_{\mathrm{F}}a)$ parameter. By varying the field and initial spin state configuration, a wide range of initial and final $1/k_{\mathrm{F}}a$ parameters can be accessed.

Starting with a $|12\rangle$ superfluid state and driving the $|2\rangle \rightarrow |3\rangle$ transition, a $|13\rangle$ mixture can be created that has much weaker interactions. Immediately after the quench, a condensate in the $|13\rangle$ state is visible, however, in equilibrium this mixture should be normal or only have a very small condensate fraction because of the weak interactions. This non-equilibrium, transient $|13\rangle$ superfluid is seen to decay on timescales comparable to t_ϵ. For weak perturbations in the BCS limit, some preliminary evidence of decaying, fast oscillations on top of the overall decay has been observed. These fast oscillations have a frequency comparable to twice the gap value, although the signal is very weak. Additionally, a revival of the condensate fraction was observed for weaker quenches and it was found that in the long time limit there is a small but finite condensate fraction. This revival has been theoretically predicted [231] and can be interpreted as a non-stationary steady state, characterized by an asymptotic order parameter.

Alternatively, starting with a normal $|13\rangle$ mixture and driving the $|1\rangle \rightarrow |2\rangle$ transition, a $|12\rangle$ mixture can be created that has much stronger interactions. Immediately after the quench, the system is still normal, but in equilibrium this $|12\rangle$ mixture should condense

due to the larger equilibrium gap value. The emergence of the superfluid occurs on very different timescales (5 to 200 ms) depending on the initial and final $1/k_{\mathrm{F}}a$. Surprisingly, the growth of the order parameter was slowest when making the largest quenches to the unitarity regime, and fastest when the quenches were weaker and into the BCS regime. No large amplitude oscillations in the condensate fraction were seen, as predicted, which was attributed to damping and finite temperature effects. These measurements provide a new test-bed for theories on the non-equilibrium emergence of quantum order in Fermi gases.

Outlook

These investigations have provided unique insights into non-equilibrium dynamics in the BEC-BCS crossover. Whilst the order parameter far in the BCS regime is well understood theoretically, the properties of the strongly correlated system at unitarity is much more complex. By investigating these systems, it may be possible to better understand unconventional systems such as high temperature superconductors. The Higgs mode has not previously been observed in ultracold Fermi gases and this experiment would provide a new technique for exciting the collective mode in superfluid Fermi systems. Besides providing a possible way of measuring the gap in the BEC-BCS crossover, the Higgs mode is of well known importance in particle physics and many spontaneous symmetry breaking processes. Whilst the Higgs mode has previously been observed in superconducting systems, our experiments with quantum gases have the advantage of being more easily tuned and probed. So far, we have only implemented these techniques on spin-balanced systems. One potential future investigation would be to attempt to excite the Higgs mode and measure the gap in the BEC-BCS crossover as a function of spin-imbalance. Fermionic superfluidity with imbalanced spin populations has already been observed in [45] and it is expected that the imbalance should decrease the gap as a smaller fraction of the atoms can be involved in the many-body pairing mechanism [210, 246, 247]. This is related to finite momentum (FFLO) superconductivity, where different sub-regions of the Fermi surfaces take part in the pairing mechanism. It could also be relevant to perform the rapid RF flips on an imbalanced mixture and see if it is possible to excite new dynamics related to the Higgs mode [246, 247]. Furthermore, it should be possible to perform an RF flip such that three strongly interacting states are present simultaneously, and examine the non-equilibrium dynamics before the time-scale of three-body loss. These strongly interacting Fermi gases with three states have been proposed as a potential system for studies on quantum chromodynamics [15, 34, 248].

The rapid quenches in the interaction parameter using the RF transitions provide a novel method for perturbing the system in times comparable to $\hbar/E_F$, which has not been previously achieved. Whilst several of the observed dynamics as a result of the quenches match theoretical predictions, some of our observations remain unexplained. The time scales for the emergence of a condensate from a normal mixture have not been investigated in detail and our results could provide an interesting test-bed for new theoretical investigations. Additionally, we have not yet observed the predicted persistent large amplitude oscillations in the order parameter associated with the direct excitation of the Higgs mode. This may be due to damping mechanisms or finite temperature effects that are not well understood.

Now that the equilibrium properties of Fermi gases have become well-characterized by experiments over the last decade, it is likely that more attention will turn to their rich non-equilibrium properties and dynamics. This experiment provides an excellent system to study these phenomena, and furthermore, future enhancements, such as reducing the dimensionality or using the ^{23}Na to create a Bose-Fermi mixture, provide several exciting routes for investigations of non-equilibrium systems.

Appendix A

Breit-Rabi Diagrams

A.1 Atomic Physics

This appendix shows the Breit-Rabi diagrams for the hyperfine states of ^{23}Na (Fig. A.1) and ^{6}Li (Fig. A.2) referred to throughout the thesis. See [138] for an overview of atomic physics, [124] for atomic properties of ^{23}Na and [126] for atomic properties of ^{6}Li. Numerical expressions (six-significant figures) for the ^{23}Na and ^{6}Li ground state and D2 excited state Breit-Rabi shifts are given in Eqs. (A.1) to (A.4) as a function of the B-field, B. These equations were formulated by diagonalizing the magnetic field dependent hyperfine Hamiltonian. With these equations it is possible to calculate the required frequencies for different hyperfine transitions and also the imaging frequencies at high fields. The energy shifts for some states can only be expressed as the solutions to a polynomial equation, in terms of the frequency, f. All energy shifts and frequencies are in MHz and all B-fields are in G. The different states are numbered by their order in the high field limit. These expressions were used to create Figs. A.1 and A.2 and have been used to accurately predict hyperfine and imaging transitions in the experiment.

For ^{23}Na, the ground state shift ΔE_{gs} (MHz) and D2 manifold shift ΔE_{D2} (MHz) can be expressed as:

$$\Delta E_{\text{gs}} = \begin{cases} -0.978686\left(\sqrt{2.04356B^2+1293.87B+819214.}-0.00115064B+226.276\right) & |1\rangle \\ -0.978687\left(\sqrt{2.04355B^2+819213.}+226.276\right) & |2\rangle \\ -0.978686\left(\sqrt{2.04356B^2-1293.87B+819214.}+0.00115064B+226.276\right) & |3\rangle \\ 664.36-1.40131B & |4\rangle \\ 0.978686\left(\sqrt{2.04356B^2-1293.87B+819214.}-0.00115064B-226.276\right) & |5\rangle \\ 0.978687\left(\sqrt{2.04355B^2+819213.}-226.276\right) & |6\rangle \\ 0.978686\left(\sqrt{2.04356B^2+1293.87B+819214.}+0.00115064B-226.276\right) & |7\rangle \\ 1.40131B+664.36 & |8\rangle \end{cases} \tag{A.1}$$

$$\Delta E_{\text{D2}} = \begin{cases} -272195.+633.267B^2+1.00000B^4+(-23857.1-19.5731B^2)f+(-60.7154-1.27774B^2)f^2+13.4163f^3+0.146935f^4=0 & |1\rangle,|6\rangle,|10\rangle,|13\rangle \\ -12509.9-768.426B+15.3758B^2-1.00000B^3+(-826.811+17.0578B-0.354721B^2)f+(9.48442+1.15089B)f^2+0.410894f^3=0 & |2\rangle,|7\rangle,|9\rangle \\ -1.30859\left(\sqrt{0.507817B^2+0.46356B+451.454}+1.42695B-10.3623\right) & |3\rangle \\ 41.6164-2.80094B & |4\rangle \\ -12509.9+768.426B+15.3758B^2+1.00000B^3+(-826.811-17.0578B-0.354721B^2)f+(9.48442-1.15089B)f^2+0.410894f^3=0 & |5\rangle,|11\rangle,|14\rangle \\ 1.30859\left(\sqrt{0.507817B^2+0.46356B+451.454}-1.42695B+10.3623\right) & |8\rangle \\ -1.30859\left(\sqrt{0.507817B^2-0.46356B+451.454}-1.42695B-10.3623\right) & |12\rangle \\ 1.30859\left(\sqrt{0.507817B^2-0.46356B+451.454}+1.42695B+10.3623\right) & |15\rangle \\ 2.80094B+41.6164 & |16\rangle \end{cases} \tag{A.2}$$

and for ^{6}Li:

$$\Delta E_{\text{gs}} = \begin{cases} -0.979913\left(\sqrt{2.041B^2+110.902B+13558.6}+0.00031973B+38.8139\right) & |1\rangle \\ -0.979913\left(\sqrt{2.041B^2-110.902B+13558.6}-0.00031973B+38.8139\right) & |2\rangle \\ 76.0684-1.399B & |3\rangle \\ 0.979913\left(\sqrt{2.041B^2-110.902B+13558.6}+0.00031973B-38.8139\right) & |4\rangle \\ 0.979913\left(\sqrt{2.041B^2+110.902B+13558.6}-0.00031973B-38.8139\right) & |5\rangle \\ 76.0684+1.399B & |6\rangle \end{cases} \tag{A.3}$$

$$\Delta E_{\text{D2}} = \begin{cases} -2.79862B-1.72 & |1\rangle \\ -1.30509\left(1.\sqrt{0.511507B^2-0.350724B+1.23495}+1.42967B+0.206882\right) & |2\rangle \\ 2.32075-1.80354B-0.0354570B^2-1.00000B^3+(-1.51625-0.825931B-0.357878B^2)f+(-0.926483+1.14755B)f^2+0.409948f^3=0 & |3\rangle,|5\rangle,|9\rangle \\ 2.32075+1.80354B-0.0354570B^2+1.00000B^3+(-1.51625+0.825931B-0.357878B^2)f+(-0.926483-1.14755B)f^2+0.409948f^3=0 & |4\rangle,|8\rangle,|12\rangle \\ 1.30509\left(\sqrt{0.511507B^2-0.350724B+1.23495}-1.42967B-0.206882\right) & |6\rangle \\ -1.30509\left(\sqrt{0.511507B^2+0.350724B+1.23495}-1.42967B+0.206882\right) & |7\rangle \\ -1.72+2.79862B & |10\rangle \\ 1.30509\left(\sqrt{0.511507B^2+0.350724B+1.23495}+1.42967B-0.206882\right) & |11\rangle \end{cases} \tag{A.4}$$

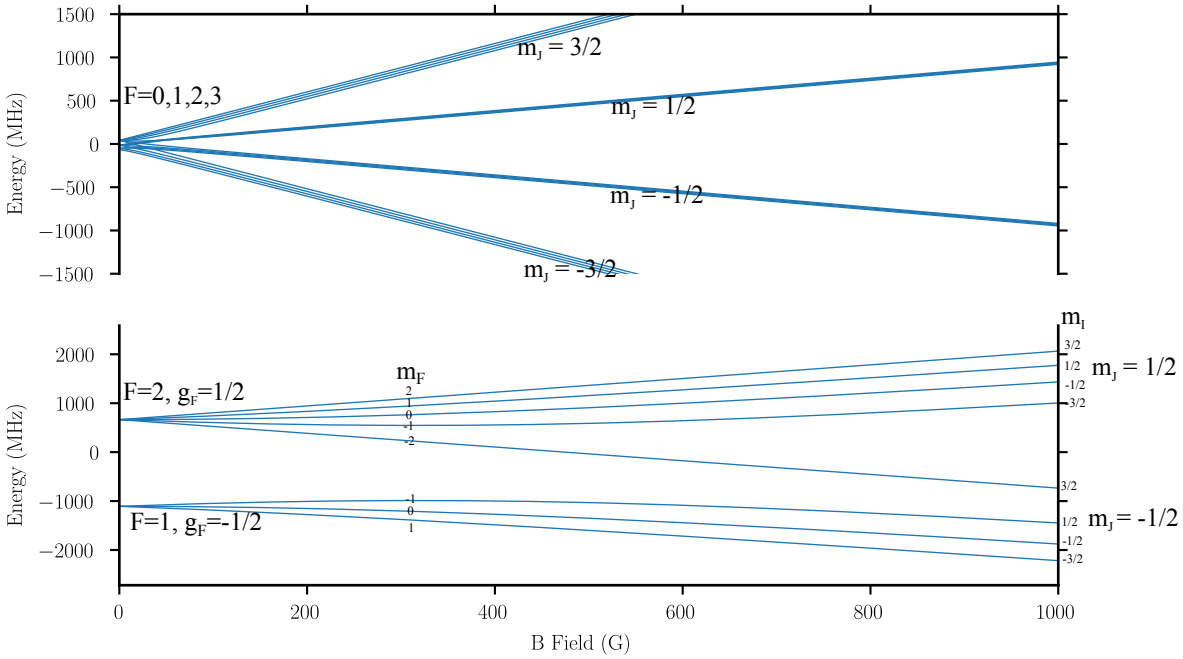

Figure A.1: Breit-Rabi diagram for the $3^2S_{1/2}$ (lower) and $3^2P_{3/2}$ (upper) manifolds of ^{23}Na. The zero references in the lower and upper plots are separated by the D2 line: 508.848 716 2 THz. The nuclear spin of ^{23}Na is $I = 3/2$. The properties of ^{23}Na are tabulated in [124].

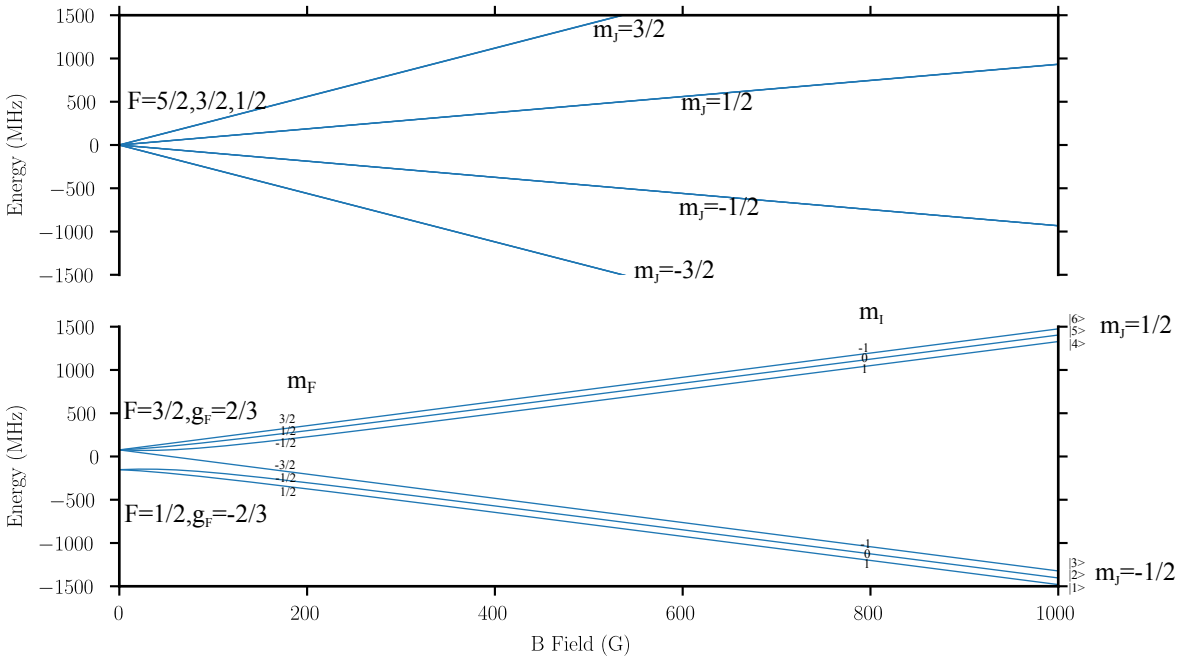

Figure A.2: Breit-Rabi diagram for the $2^2S_{1/2}$ (lower) and $2^2P_{3/2}$ (upper) manifolds of ^{6}Li. The zero references in the lower and upper plots are separated by D2 line: 446.799 677 THz. The nuclear spin of ^{6}Li is $I = 1$. The properties of ^{6}Li are tabulated in [126].

Appendix B

Experimental Setup

B.1 Vacuum System Bake-out

In order to reach ultra high vacuum (UHV), corresponding to pressures less than 1×10^{-11} mbar, several different vacuum pumps and stages must be used. Using basic roughing and turbo pumps to remove the volume of gas, and assuming there are no leaks, quickly leads to the pressure being limited by outgassing of the vacuum material. This outgassing primarily occurs from surface contaminants[1] adsorbed to the vacuum walls which slowly desorb [120, 121] and lead to a limiting pressure. Tabulated outgassing rates can be found in many vacuum textbooks for different materials [120, 121]. For a stainless steel vacuum chamber, the outgassing will initially be dominated by water and, at lower pressures, hydrogen. Heating the vacuum system to high temperatures ($> 120\,^{\circ}\mathrm{C}$), such that contaminants desorb much more rapidly and can be pumped away, is crucial to reaching UHV. Typically, the higher the temperature the better the *bake-out*, leading to a lower final pressure that is reached faster. Using too high a temperature, however, can damage windows, the vacuum knife edges and vacuum components.

The first stage of the bake-out involved sealing only the main Kimball chamber and pumping tower with blanks instead of windows. The system was heated to very high temperatures ($350\,^{\circ}\mathrm{C}$) and the titanium sublimation pump was fired several times over the course of 7 d. The purpose of this initial bake-out was to ensure that we can reach the minimum possible pressure in the main Kimball chamber, even if the bake-out temperature cannot be so high once the windows are attached. Baking out at this high temperature can also have a significant effect on the outgassing of the hydrogen from stainless steel

[1] Outgassing can also occur from diffusion through the bulk material.

[249].

Once the vacuum system had been constructed, the system was pumped, firstly with the roughing pumps, and then, at pressures less than 1×10^{-2} mbar, with the turbo pumps. The entire system was wrapped in aluminum foil and several temperature sensors were added. The entire system was wrapped in heating tapes and another layer of foil. Finally, the system was covered in fiber glass for thermal insulation. Since vacuum windows can easily be damaged by temperature gradients or rapid changes, the main Kimball chamber temperature was controlled by a PID and ramped to 150 °C over 10 h. The other heating tapes were controlled manually with transformers and any area without windows was heated to approximately 300 °C. As the system is heated the pressure rapidly increases, then rapidly drops, and finally exponentially decays as shown in Fig. B.1.

After baking out for approximately 1 week, the four ion pumps connected to the experiment were turned on. The temperature was kept high during the turn-on procedure (250 °C). The ion pumps were initially turned on with the minimum voltage (3000 V) and increased to maximum voltage (7000 V) over 30 min. It should be noted that Ion Pump 1, which is closest to the atomic oven, had several warnings about arcing and high currents during the turn-on procedure. After the pressure dropped, these warnings stopped. Once all ion pumps were on full voltage, each of the four filaments in the three Titanium sublimation pumps (TSP) were fired for 2 min at 40 A to degas. The first firing of the TSPs caused the pressure to drop by approximately a factor of three within a few minutes.

The non-evaporable getters (NEGs) inside the main Kimball chamber were activated with a current of 5.2 A for 10 min. Note that it was important to activate all NEGs simultaneously and that the pressure increased substantially during the activation process. No significant pressure drop was recorded after their activation.

During the bake-out, the ^{23}Na and ^{6}Li ovens were maintained at 300 °C and the mixing and exit nozzle at 400 °C. Some groups have reported that ^{6}Li can be contaminated with hydrogen during the manufacturing process, leading to out-gassing during the experiment lifetime [250]. To attempt to prevent this, a very high temperature bake-out of the ^{6}Li oven to 500 °C for 10 min was performed, before ramping back to 300 °C. During this high temperature bake-out of ^{6}Li the pressure in the oven rose and fell dramatically several times suggesting that some contaminants may have been released. A residual gas analyzer was attached to the turbo pump during the bake-out and during the high temperature bake-out of ^{6}Li the partial pressure of hydrogen increased by a factor of five.

After baking out for two weeks, the temperature of the system was ramped down to

room temperature over approximately 12 h. During this time the pressure, measured with the ion gauge, dropped to approximately 1×10^{-10} mbar. Pressures of less than 1×10^{-11} mbar were then obtained by firing the TSPs several times over the 24 h.

After the cooldown, it was noticed that the pressure measured from the current of the ion pumps did not decrease similarly to the pressure measured by the ion gauge and was 1 to 2 orders of magnitude higher[1]. However, after direct discussion with Gamma Vacuum the cause of the problem was identified. Ion pumps measure pressure directly from the discharge current and voltage across them. The discharge current should be linear with the operating voltage and can be converted into a pressure. There can, however, be several spurious currents that are not due to the discharge current [251, 252]:

- Secondary electron currents can occur when electrons are ejected from cathode plates by colliding ions. This current increases with increasing operating voltage as the ion energy increases.
- Leakage current flows across resistive elements e.g. high voltage cables or feedthroughs. This current increases with ion pump age.
- Field emission current is caused by a high voltage gradient and depends on the operating voltage, distance to nearby surfaces and geometry.

By plotting the ion pump's current against the operating voltage (see Fig. B.2), it was found that the ion pumps in our system were not measuring the discharge current. Communications with Gamma Vacuum concluded this was most likely due to field emission current from depositions in the ion pump which leads to an exponential increase in current with voltage. Sputtering during bake-out can create depositions with sharp, small features that lead to large field emission currents. It is interesting that the effect is worst at the ion pump nearest the oven and gets better with increasing distance from the oven. This would imply the ^{23}Na or ^{6}Li oven is the primary source of the sputtered material. This problem was relatively well known to the manufacturer and they have a Hi-Pot feature built into the ion pump controller that applies a large voltage for a short time. Since the field emission current scales exponentially with the voltage, the high voltage gives a very high current which can burn off depositions. The effect of the Hi-Pot was dramatic, reducing the current in one ion pump from 800 nA to 20 nA and after this, the derived pressure approximately matched the reading on the ion gauge. Unfortunately, the ion pump controller was not able to provide a large enough current to Hi-Pot the ion pump closest to the oven, where the pressure is highest. This does not affect the performance

[1] This led to us checking for leaks near all the ion pumps and eventually we began the bake-out again.

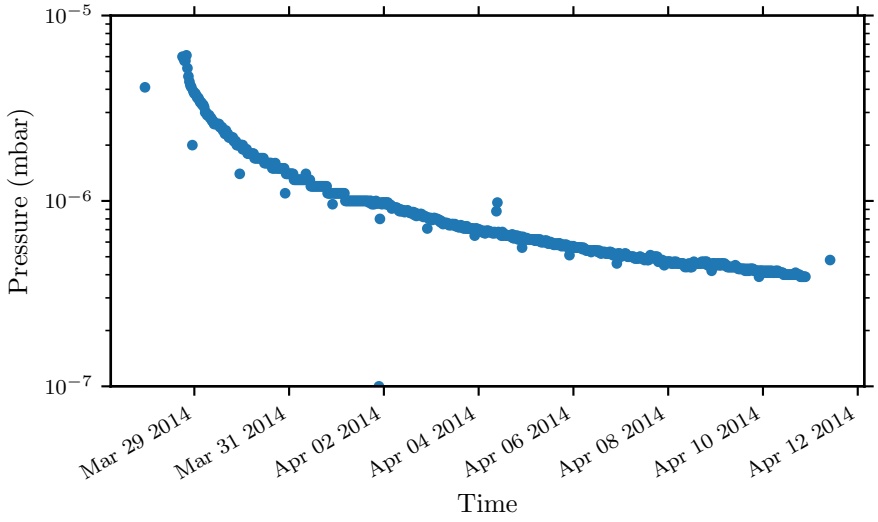

Figure B.1: Pressure from the ion gauge during the first week of the bake-out. Note the logarithmic scale on the pressure axis. After approximately one week, we turned on the ion pumps and degassed the TSPs and NEGs. Before cooling down the vacuum system, the pressure was 4×10^{-8} mbar.

of the ion pump, it only means that the pressure reading is not accurate. As a rule of thumb, the best estimate of the pressure can be obtained by going to the lowest operating voltage where all the additional sources of currents are minimized. It is still not clear why the ion pumps in our experiment suffered from field emission currents substantially more than has been reported in similar experiments. Hopefully, this description and Fig. B.2 will allow other experiments to diagnose field emission currents in their ion pumps.

After the final ramp down and resolving the issues with the ion pump pressure measurements, the pressure gauge and ion pumps 2, 3 and 4 measured pressures of 1×10^{-11} mbar (the minimum they can measure). Ion pump 1 measured a pressure of 1.8×10^{-9} mbar in the oven, which provides an estimate to the pressure in the oven. At the time of writing, the vacuum system has been sealed for nearly 3 years. The oven has been open once to replace and clean out the ^{23}Na. The ion gauge was turned off soon after the bake-out finished and the pressure is read out using the ion pumps. Every few months, if the pressure has increased by a factor of three or more, the TSPs are fired again, which reduces the pressure over 48 h as shown in Fig. B.3. The pumps can also re-use the Hi-Pot feature which has a noticeable effect on the pressure reading, however, this is done less frequently as it shortens the lifetime of the pumps and doesn't reduce the real pressure.

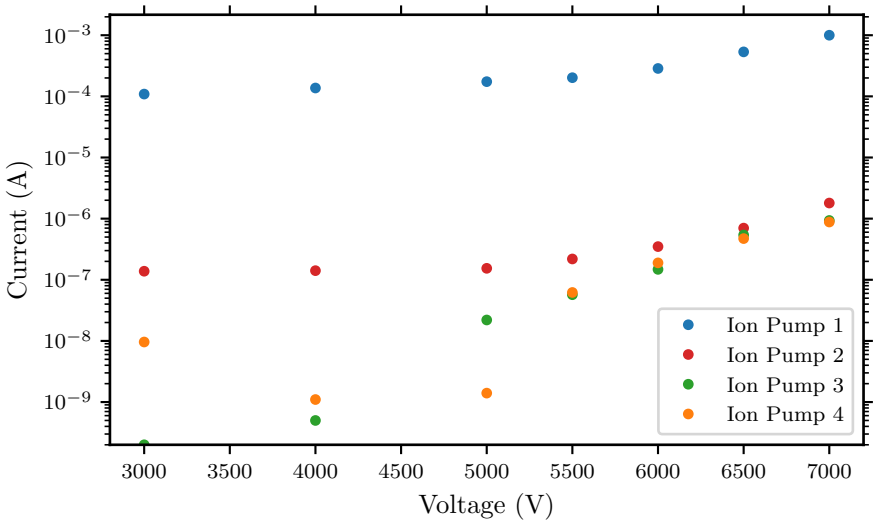

Figure B.2: The operating voltage of each of the ion pumps is changed and the total current measured by the controller is plotted. For an ideal ion pump where there is only discharge current, the current should be linearly proportional to the voltage [251, 252]. A clear non-linear behavior is observed, caused by the field emission current scaling exponentially with voltage. A reasonable upper limit to the pressure can be obtained by using the minimum operating voltage which brings us far from the non-linear regime. Using the Hi-Pot feature dramatically reduced the measured current at high voltages.

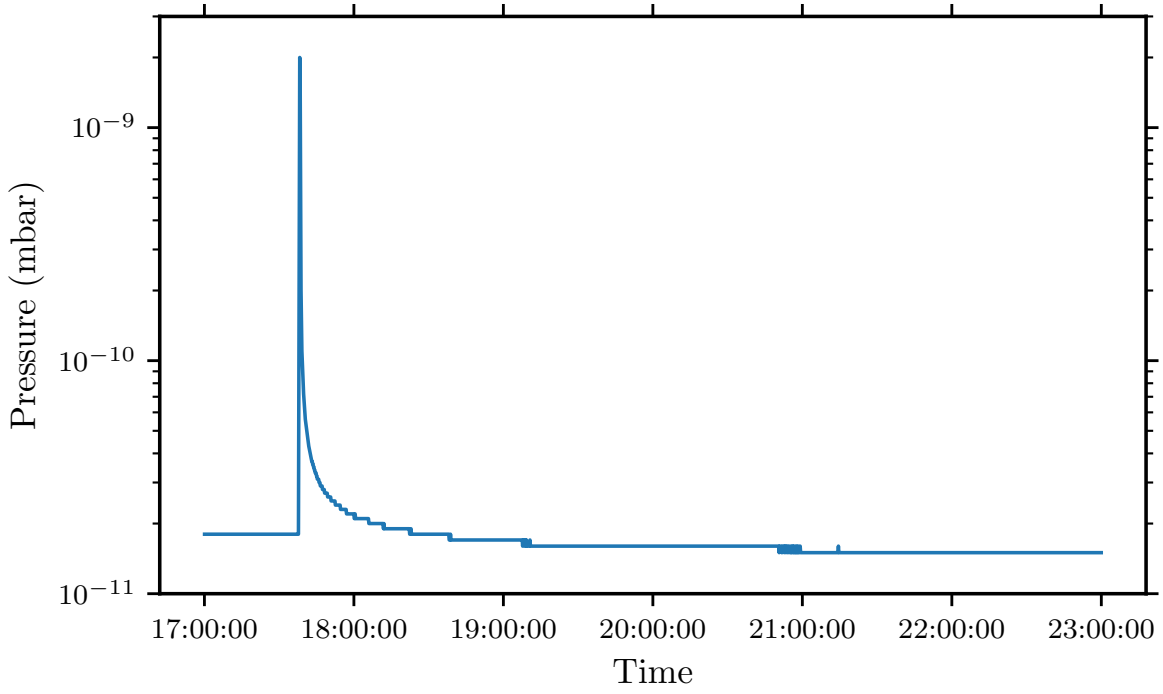

Figure B.3: This figure shows the typical use case for firing the titanium sublimation pumps in the UHV vacuum chamber. After several months of operation, the pressure in the main chamber (measured using the ion pump current) is slightly higher than normal. The TSP pump is activated by running it at 45 A for 60 s. During this time the pressure increases by more than two orders of magnitude due to the increase in temperature and degassing. However, after the current is slowly decreased the pressure begins to drop. A stable and lower pressure is reached after approximately 6 h, however, the TSP can continue to pump for 100 h or more if the pressure is sufficiently low.

B.2 ^{23}Na and ^{6}Li Oven

The ^{23}Na and ^{6}Li oven is based on the Ketterle group (MIT) design presented in [253–255]. This involves a ^{23}Na and ^{6}Li reservoir connected in series by the mixing nozzle (diameter 2 mm). Both species then leave through the exit nozzle (diameter 4 mm, length 2 mm). Inside the main oven chamber, a copper cup is placed directly after the exit, which is water cooled using a feed through. The copper cup aims to capture the atomic flux with at large solid angles, which will condense on the cold cup, reducing the pressure and preventing the reactive ^{23}Na and ^{6}Li coating large regions of the oven chamber. A hole in the center of the cold cup allows the desired atomic flux to pass and a slightly adjustable skimmer plate, attached to the cold cup, can be used to define the collimated atomic beam. Directly after the cold cup is a rotary shutter, which can be rotated from outside the vacuum chamber using a magnetic feed through. The purpose of this shutter is to block the atomic flux except when loading the MOT, reducing the pressure, increasing the lifetime and preventing ^{23}Na and ^{6}Li from coating the Zeeman slower window. After the first ^{23}Na exchange (see Appendix B.2.1), several pieces of ^{23}Na fell into the rotary feed through, meaning the rotation is no longer smooth and the shutter cannot be used[1]. No significant change in the pressure or the lifetime of the degenerate gases was measured after this change.

Two heating bands are attached to each of the ^{23}Na and ^{6}Li resevoirs, with an additional band on both the mixing and exit nozzle. Each region has two high temperature sensors attached. A temperature controller[2] is used to control and regulate the temperature of the ^{23}Na reservoir, ^{6}Li reservoir, mixing nozzle and exit nozzle independently. The controllers can communicate over the network and a user interface was made to allow the temperature and ramp speed of each channel to be controlled remotely and automatically. In normal operation the ^{23}Na and ^{6}Li resevoirs are run at 330 °C and 390 °C, respectively. The nozzles are run at 485 °C to prevent ^{23}Na or ^{6}Li condensing in the nozzles. The ^{6}Li temperature should always be substantially higher than the ^{23}Na temperature to prevent ^{23}Na condensing in the ^{6}Li cup. Further details on the filling, exchanging and cleaning of the oven can be found in Appendix B.2.1.

[1] In general the rotary shutter feed through should always come from the side or above, not from the bottom, to prevent debris falling into the feed through.

[2] CAL 9400 Dual Display Autotune Temperature Controller (pulse width modulation).

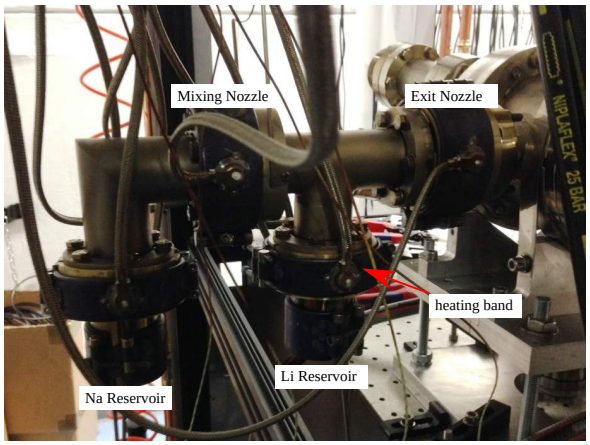

(a) Oven resevoirs with heating bands

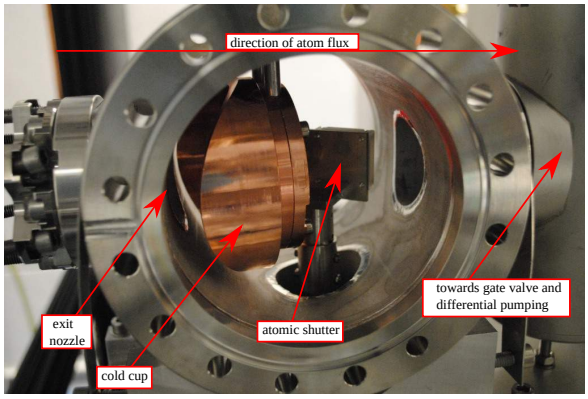

(b) Inside the oven chamber

Figure B.4: Fig. B.4a shows the different oven resevoirs and nozzles with the heating bands attached. **Fig. B.4b** shows the inside of the oven chamber. Atoms leaving the resevoirs through the exit nozzle must pass through the skimmer and cold cup creating a reasonably collimated atomic beam. Atoms with larger solid angles condense on the water cooled cold cup. The rotary shutter was designed to block the atomic beam when the MOT was not being loaded

B.2.1 ^{23}Na and ^{6}Li Replacement

Detecting ^{23}Na Depletion

The dual species oven was originally filled with approximately 21 g of ^{23}Na[1] and 12 g of ^{6}Li[2]. The large flux of ^{23}Na limits the lifetime of the oven. It was noticed that the ^{23}Na oven was running low when the ^{23}Na atom number dropped rapidly[3]. There are many reasons that could cause a low ^{23}Na atom number and it is vital to rule these out before concluding the depletion of the oven. A low ^{23}Na atom number can be seen in either the MOT fluorescence or by observing the initial ^{23}Na number after magnetic transport. On the day the ^{23}Na oven was depleted a 40 % drop in the MOT fluorescence was observed and the fitted number of atoms in the initial magnetic trap was reduced by a factor of three. These continued to drop steadily throughout the next few hours of operation. To rule out other issues, one should:

- check the powers and the frequency of the MOT beams and Zeeman slower beams to confirm there are no optical problems.

[1] Originally used Sigma Aldrich product number 282065-50G. Now use: STREM, prescored ampule under argon, model number: MFCD00085307.

[2] Originally 95 % enriched ^{6}Li under oil was used (Sigma Aldric product number 340421-SPEC). In the future, glass ampules under argon will be used.

[3] If a sequence is used that only observes the ^{6}Li cloud, then this will be observed indirectly by being unable to load a ^{6}Li large cloud in the dipole trap.

- check for major misalignment of the MOT beams (minor misalignment has a much smaller effect).
- check if the ^{6}Li MOT fluorescence is normal or higher than usual. This rules out electronics, coil or sequence issues.
- check the current in the Zeeman slower and MOT coils directly with an amp clamp
- check the predicted consumed ^{23}Na on the oven controller user interface. The controller logs the temperatures every 10 s and estimates the flux giving a reasonable prediction of how much ^{23}Na and ^{6}Li have been consumed in the oven.

For final confirmation, the atom number can be monitored while increasing the oven temperature[1]. A rapid increase in the ^{23}Na atom number with oven temperature followed by steady decline is the signature of a depleted oven as shown in Fig. B.5.

Refill procedure

Refilling the ^{23}Na involves opening the vacuum chamber, however, replacing the resevoir is a simple process that was prepared and completed within 6 h of first detecting depletion. The vacuum was only opened for 30 min during this routine. The procedure is very similar to that described in [254]. Firstly, the UHV gate valve connecting the oven chamber to the main experiment is closed and the oven is cooled down. The additional valve in the oven is connected to a turbo pump and the oven is flushed with high grade argon[2] to slightly higher than atmospheric pressure. The minimum amount of insulation is removed to provide access to the ^{23}Na cup but ensuring that the fiber glass is kept back to prevent contamination with the vacuum. Note that the screws on the heating band and the vacuum screws are prone to locking, having been under many extreme thermal cycles. The ^{23}Na cup was removed and was found to be completely empty. The new ^{23}Na source (25 g in a glass vessel under inert gas) was wrapped in aluminum foil and then cloth, and cracked thoroughly with a hammer. The cloth and foil was quickly removed and the ^{23}Na was placed into a new oven cup with the remaining broken, surrounding glass. The cup was then reconnected to the oven and the vacuum was sealed. The argon flushing was stopped and the turbo pump was turned on. The pressure had reached normal levels of operation within 3 h.

[1] Both the ^{23}Na and ^{6}Li oven temperatures should be increased, as the ^{23}Na may be condensed in the ^{6}Li cup.

[2] Using nitrogen is not advisable as it may react with ^{6}Li to form Lithium Nitride which has a very high melting point.

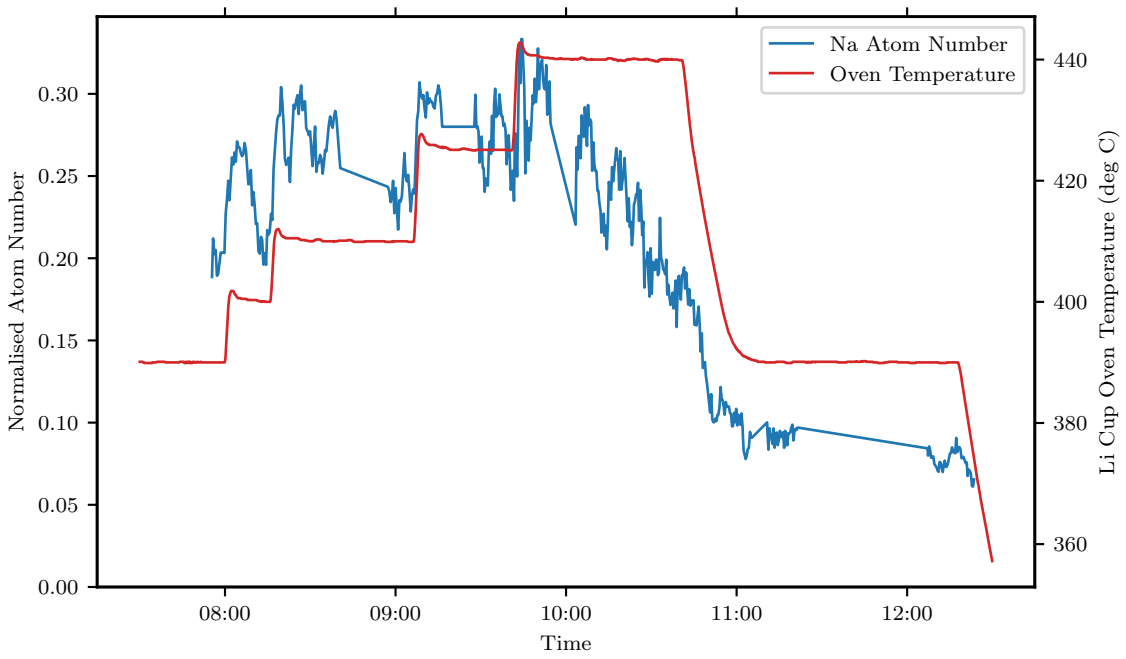

Figure B.5: This figure shows the atom number in the initial magnetic trap (blue) against the temperature of the ^{6}Li cup in the dual species oven (red) as ^{23}Na depletion was diagnosed for the first time. The typical atom number for ^{23}Na on this scale is 1. The temperature of the ^{6}Li cup was increased periodically in steps and always caused a sudden increase in the atom number initially and was followed by a slow decline. This effect is caused by the remaining ^{23}Na condensed in the ^{6}Li cup being evaporated leading to an increase in flux. As there is very little remaining ^{23}Na, the increase is short lived, compared to when the oven is operating normally. The oscillations observed were considerably larger than during normal operation and were probably also related to the depletion. Increasing the ^{23}Na oven temperature had no effect implying all remaining ^{23}Na was condensed in the ^{6}Li cup. Towards the end of the graph we began to cool down the oven in preparation for refilling the ^{23}Na.

Estimating the depletion time

The oven controller records the temperature of the ^{23}Na and ^{6}Li cup (and the nozzles) every 10 s. This large data set can be used to estimate the depletion rate of ^{23}Na and ^{6}Li. The ^{23}Na oven was run at 330 °C for 3500 h which accounts for the majority of the atom loss. Given that we approximately had 21 g of ^{23}Na, this would predict a loss rate of 6 mg h^{-1}. For the sake of comparison the theoretical loss rate can be calculated using the thermodynamic result for the total flux, F [256, 257]:

$$F = \frac{1}{4}\kappa n v A \tag{B.1}$$

where n is the density, v is the average thermal velocity, A is the aperture area and κ is a correction accounting for the finite length of the aperture. κ can be approximated as $\kappa = \frac{4d}{3l}$ [257], where d is the aperture diameter and l is the aperture length. Both n and v depend on the partial pressure of the atomic species which is defined by the temperature, T. Hence, for a given T one can estimate the loss rate in a given time.

By integrating the data set to calculate the time spent at a specific temperature one can estimate the mass lost. This assumes that all ^{23}Na that enters the ^{6}Li reservoir then leaves via the exit nozzle. The analysis of this data predicts that 20.5 g of ^{23}Na and 1 g of ^{6}Li have been consumed during the operation of the oven over a 2 year period. This number is in good agreement with the estimated 21 g originally inserted and confirms that there are no immediate concerns of running out of ^{6}Li. Since the prediction described above accurately calculated the depletion time of the oven, the flux calculation was built into the oven controller such that the software tracks how many seconds the oven has been run at a certain temperature and calculates the consumed mass of ^{23}Na and ^{6}Li.

Cleaning the Oven

After depleting the first 21 g of ^{23}Na the cold cup was filled and the hole partially clogged meaning the oven needed to be cleaned. Initially, a 50 W infrared beam was sent into the oven incident on the cold cup to try and heat it to melt the ^{23}Na. Whilst this did melt the ^{23}Na, which ran out of the cold cup onto the bottom of the oven chamber, it did not successfully clear the skimmer hole attached to the cold cup and it was necessary to open the oven and clean the system. After closing the oven gate valve, the system was opened and flushed continuously with argon. The large lumps of ^{23}Na were scraped out of the oven chamber in small pieces. Note that scraping too hard or vigorously was dangerous

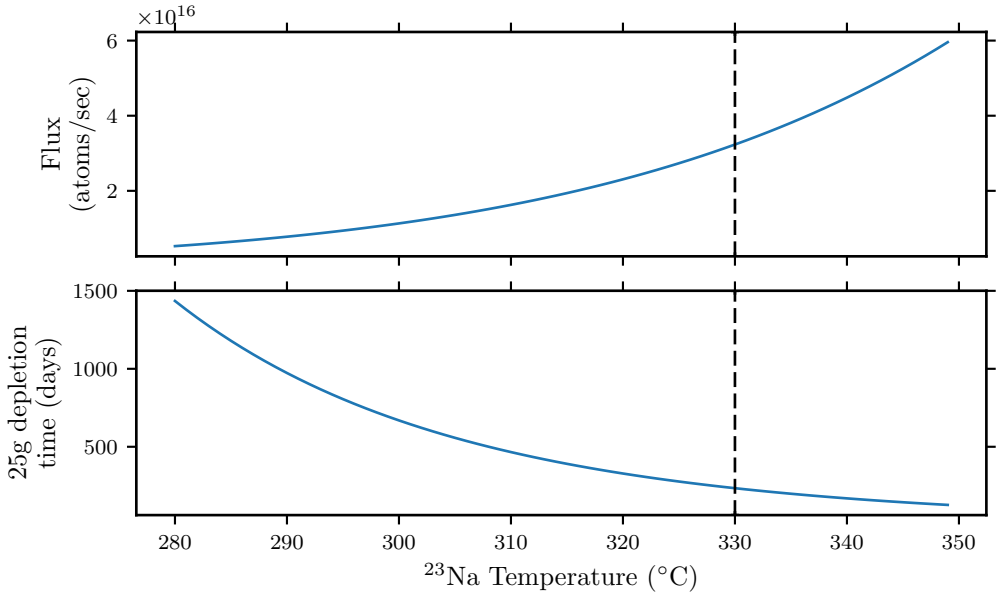

Figure B.6: This figure shows the calculated depletion time for 25 g of ^{23}Na in the oven and the associated atomic flux at a specific temperature. Increasing the temperature increases the flux and correspondingly shortens the lifetime of the oven. The operating temperature of 330 °C is shown by the black dashed line and the measured depletion time is in agreement with the prediction.

as the chunks of ^{23}Na could combust. The cold cup was carefully removed and cleaned separately, firstly by removing the large pieces of ^{23}Na and eventually by spraying it with water from a distance. Unfortunately, several pieces of ^{23}Na had fallen into the rotary atomic shutter, which means that it no longer rotates smoothly and cannot be used. Fig. B.8 shows the oven before and after cleaning. Some additional copper sheets were inserted so that in the future the collected ^{23}Na can easily be removed. After cleaning, the vacuum system was reconnected and pumped down. No ^{6}Li deposits were visible in the oven chamber, as expected from the much lower ^{6}Li flux.

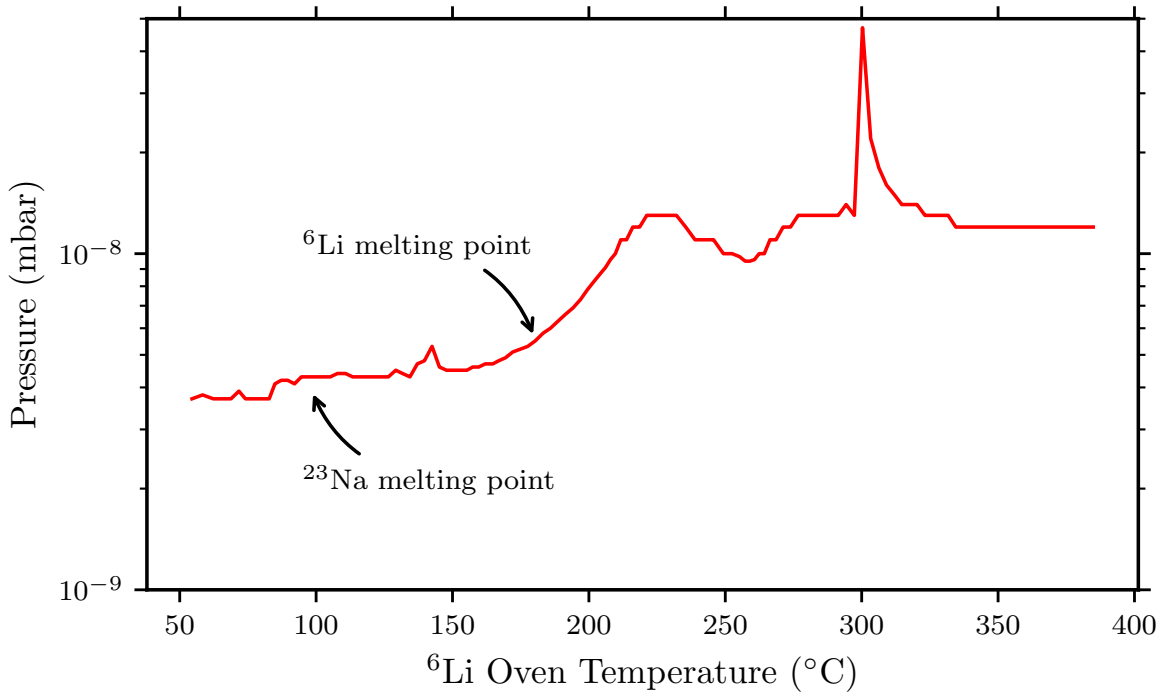

Figure B.7: This figure shows the increase in pressure measured on the ion pump attached to the oven chamber as the ^{6}Li reservoir is heated. A rapid increase in pressure is seen when the melting point of ^{6}Li is reached. The same increase in pressure is not seen for the ^{23}Na cup. The spike at higher temperatures is most likely caused by some contaminants (e.g. hydrogen) being released as the ^{6}Li is heated.

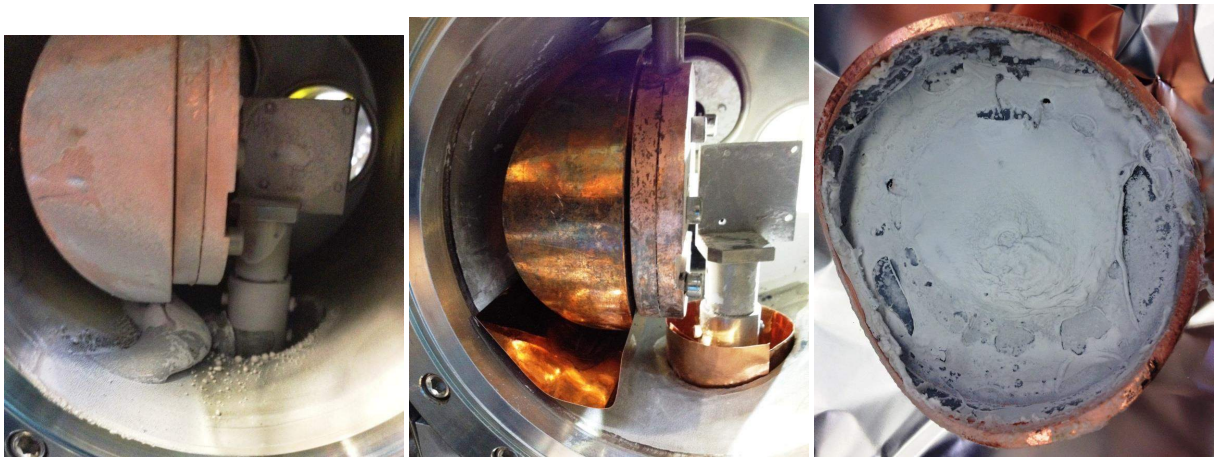

(a) Before cleaning **(b)** After cleaning **(c)** Cold cup

Figure B.8: Images of the oven chamber before and after cleaning. Note the additional copper sheets which should make it easier to remove the ^{23}Na in the future. The image on the right shows the removed cold cup, filled with ^{23}Na.

B.3 Electronics Configurations

Mini-MOSFET Box

The Mini-MOSFET box has four MOSFET channels each with a single sub-channel. It uses STP16NF06L MOSFETs capable of 16 A continuous use or 64 A pulsed. It can operate in *BNC mode* where a TTL signal directly drives the gate or in *on-mode* where an internal 9 V battery drives the gate continuously. Each channel has a 30 V clamping varistor snubber circuit across the output. It is used for low current applications in the experiment and is often connected to the Delta 15 A 10 V power supplies used for compensation fields.

MOSFET Box 1

MOSFET Box 1 was re-used from an old experiment in the research group. It has three channels each with five sub-channels. The different channels use either STE180NE10 or IXFN230N10 MOSFETs mounted to a large aluminum heat sink[1]. To allow channels from this MOSFET box to be used with other boxes and power supplies, a high current (300 A) diode (BYV255V) was added to each channel. MOSFET Box 1 had a safety circuit to prevent MOSFETs being on or off for too long using a 74HC/HCT221 multivibrator. This feature caused many problems as the chip is specified for time constants of µs to ms and was unreliable when the time constant was set to several seconds as required for a typical coil in the experiment. This malfunction meant that sometimes the MOSFETs would close during operation in the sequence[2]. The MOSFETs are driven by an optocoupled (HCPL2400) TTL input signal. Each channel has a 0.5 Ω power resistor with diode snubber circuit across the output. Only one of the channels of MOSFET Box 1 is still used and it is connected to the Delta 100 A 60 V, which drives the MOT coils (during the MOT phase), the compensation field in the Y' direction and the optional L1L2 Anti-Helmholtz compensation coil. All channels on MOSFET Box 1 are slowly being migrated to MOSFET Box 2.

[1] One channel is mounted on the underside of the heat sink. To access this the box must be turned upside down.

[2] To improve this the minimum time capacitor was replaced with a short circuit to set the minimum time to zero and the case of the box was milled such that the 74HC/HCT221 was accessible and one can use the pins to check the maximum on time constant.

Table B.1: Table describing which boxes and power supplies each coil is connected to.

Coil	Box	Power Supply
Big Zeeman slower	IGBT Box 1	Lambda 400 A 25 V
Small Zeeman slower	Direct	Delta 40 A 6 V (1)
Zeeman slower compensation X2	MOSFET Box 2	Delta 40 A 6 V (2)
unused compensation X1	—	—
X'A compensation coil	Mini MOSFET Box MOSFET Box 2	Delta 10 A 15 V (1) Delta 40 A 6 V (2)
X'B compensation coil	Mini MOSFET Box	Delta 10 A15 V (2)
Y'A compensation coil	Mini MOSFET Box MOSFET Box 1	Delta 10 A 15 V (3) Delta 100 A 60 V
Y'B compensation coil	Mini MOSFET Box	Delta 10 A 15 V (4)
MOT coils	MOSFET Box 1 IGBT Box 1	Delta 100 A 60 V Lambda 400 A 25 V
3 layer Feshbach	H Bridge Box 1	Delta 600 A30 V
L1 L2 combination	MOSFET Box 1	Delta 600 A30 V
magic layer	MOSFET Box 2	Delta 10 A 15 V (5) Delta 40 A 6 V (2)
gradient lines X' Y'	MOSFET Box 2	Delta 40 A 6 V (2)

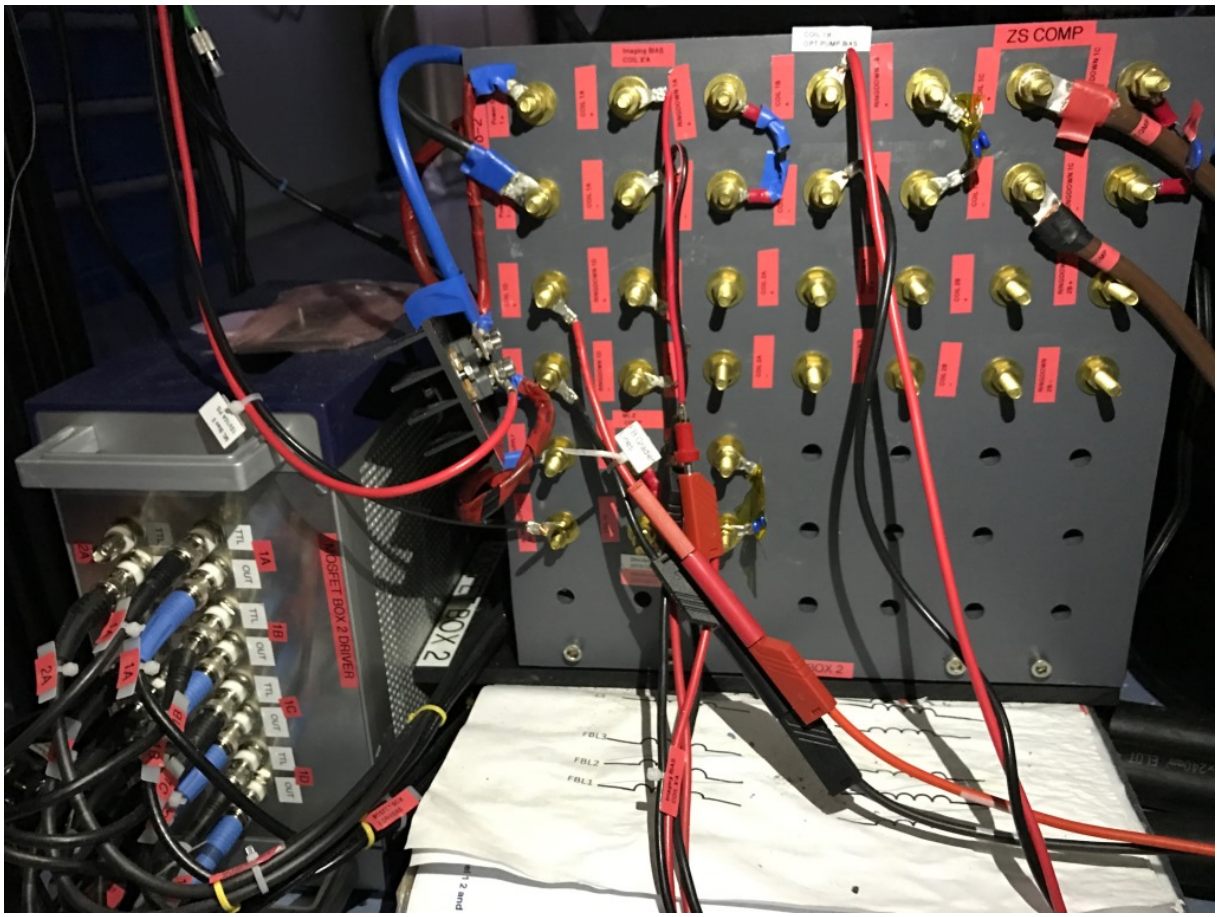

Figure B.9: Image of MOSFET Box 2 driver box (left) and connection board (right). The brass screws in the plastic connection board connect through to copper blocks and wires on the reverse side that connect to the MOSFETs and diodes. Each sub-channel can have its own snubber circuit (e.g. varistor or diodes) connected as can be seen in the image.

MOSFET Box 2

MOSFET Box 2 is similar to MOSFET Box 1 with four channels each with two to four sub channels. It uses STE180NE10 or IXFN230N10 MOSFETs with a high current (300 A) diode (BYV255V) on each channel. It does not use the 74HC/HCT221 safety circuit and instead has a separate dedicated MOSFET driver box with optocoupled TTL inputs and TC4422 high speed MOSFET drivers. The MOSFETs and diodes are mounted to an aluminum heat sink. All connections to the power supplies and coils are made from a separate plastic board with brass screw connections that are easily accessible. Copper blocks and wires make all the necessary connections to the MOSFETs, diodes and drivers on the reverse side of the plastic board. Each sub-channel can have its own snubber circuit via the brass screw connections (see Fig. B.9).

Figure B.10: IGBT Box 1 has 4 channels (each with a single sub-channel). The IGBT modules are the black structures towards the back of the image. The white components in the center are the 600 A diodes. The PCBs visible at the bottom of the image are the IGBT driver boards. The wires at the bottom go directly to the coils and connections at the back of the box go to the power supplies. The plate at the bottom is water cooled.

IGBT Box 1

IGBT Box 1 is composed of four channels each with one sub-channel. Each channel uses a single 1MBI600U4B-120 Fuji Electronic IGBT module capable of 600 A 1200 V continuous and 600 A diode. Each channel has a dedicated IGBT Gate Driver board (VLA500K-01R). The modules are mounted on a water cooled aluminum plate. A 360 V clamping varistor (B72210S0141K101 Epcos) is connected across the collector-emitter to protect the modules. IGBT Box 1 is used for the big Zeeman slower coil and the magnetic transport with the MOT coils both using the Lambda 400 A 25 Vpower supply. It is also used to rapidly discharge the Delta 600 A 30 V hybrid power supply. A picture of IGBT Box 1 is shown in Fig. B.10.

H-Bridge Box

The H-Bridge box contains two h-bridges (only one of which is currently in use). Each H-bridge is composed of two half bridge 900 A 1200 V IGBT modules (2MBI900VXA-120E-50 Fuji Electric). They are driven by an AgileSwitch IGBT Driver (AS1-HPM Fiber Series). The h-bridge channel is used to rapidly turn off the current in the 3 layer Feshbach coils and for switching these coils from anti-Helmholtz (magnetic trap) to Helmholtz (Feshbach field) configuration. The IGBT modules are mounted on a water cooled aluminum plate. Several 360 V clamping varistor (B72210S0141K101 Epcos) are connected across the collector-emitter connections to protect the modules. An ITN 600-s Ultrastab current transducer is built into the first collector connection such that the current can accurately be measured for regulation. The PID and current stabilisation will be discussed in Section 6.3. An image of the connections in the H-Bridge box is shown in Fig. B.11.

Temperature Interlock Box

Two temperature interlock boxes are used to turn off power supplies (and high power lasers) if temperatures cross a threshold value. The temperature interlock box uses a single MAX31865 resistance-to-digital converter chip. This chip is multiplexed to 16 different PT100 temperature sensors. An Arduino (with Ethernet) is used to read the temperature from the chip and compares it to the stored threshold value. Relays are used to provide either a short or open circuit to the interlock control of the power supplies and lasers. Additionally, the box accepts a TTL signal that triggers the alarm state, which is used if the heat exchanger or water pumps turn off. The threshold can be set via remote communication with the Arduino. The current temperatures can be read over the network and are logged every 10 seconds.

Temperature Monitoring Box

For non-critical temperature monitoring, a different box is used. This box uses many DSB1820+ digital temperature sensors, which are read out with a Raspberry Pi. These sensors are used on the optics tables, water pipes and in the air conditioning units. If their values leave a threshold region, a warning email is sent.

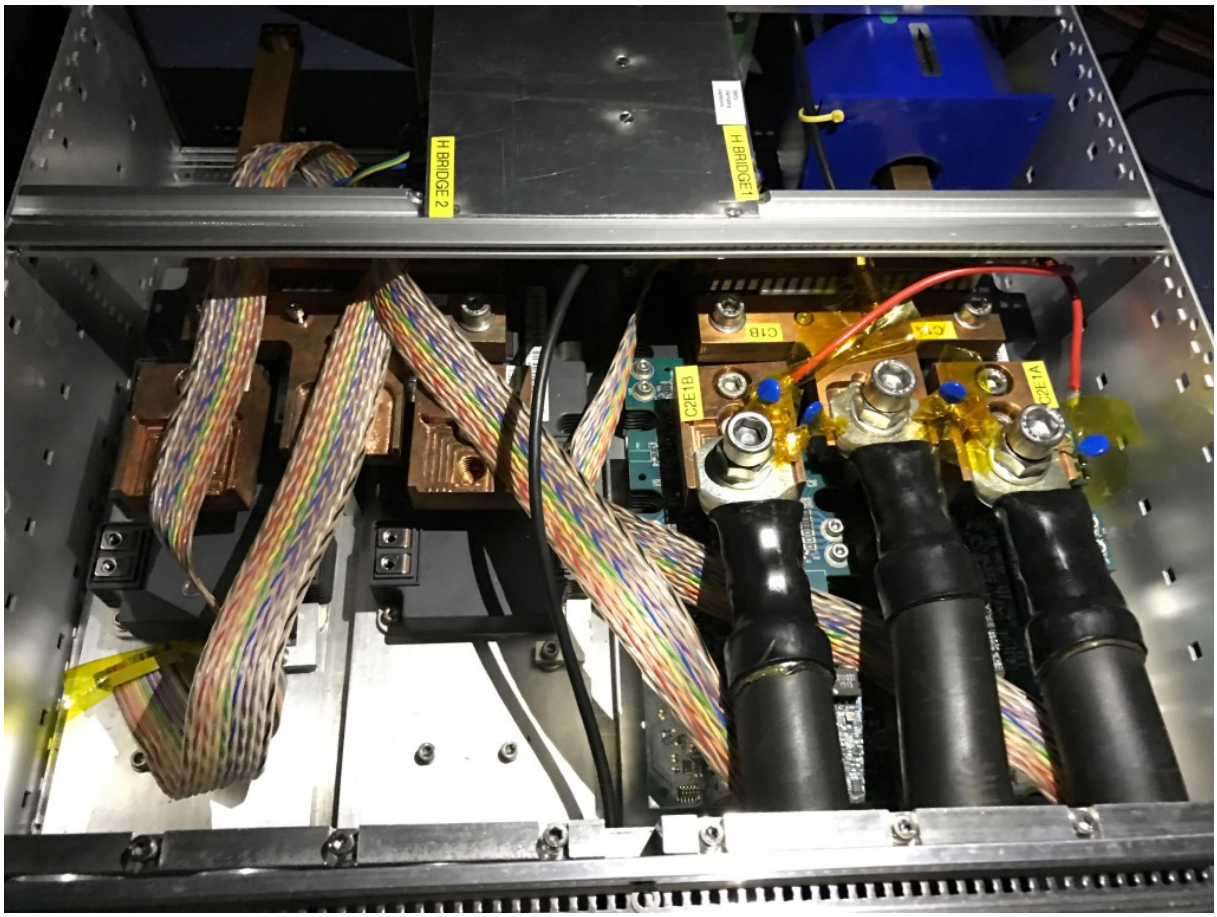

Figure B.11: The H-Bridge Box contains two h-bridges only one of which is in use (right). The high current 240 mm^2 cables are used (H07RN Lappkabel). The IGBT drivers are under the metal plate (center-top) and connect to the IGBT modules via the rainbow ribbon cable. Varistors (blue) are connected between all collector-emitter connections to protect the modules. A current transducer (top-right)is used for current regulation. The modules are mounted on a water cooled aluminum plate.

RPi ADC Box

For low accuracy logging of voltage signals a box was made that contains a MCP3008 (10-bit) analog-to-digital converter chip that is read out using a Raspberry Pi. This box logs voltage signals, such as the ^{23}Na and ^{6}Li MOT fluorescence and the dipole and plug laser beam powers. The voltage signals are displayed live on a monitor and provide several useful diagnosis signals for debugging the experiment.

B.4 Schematics and Diagrams

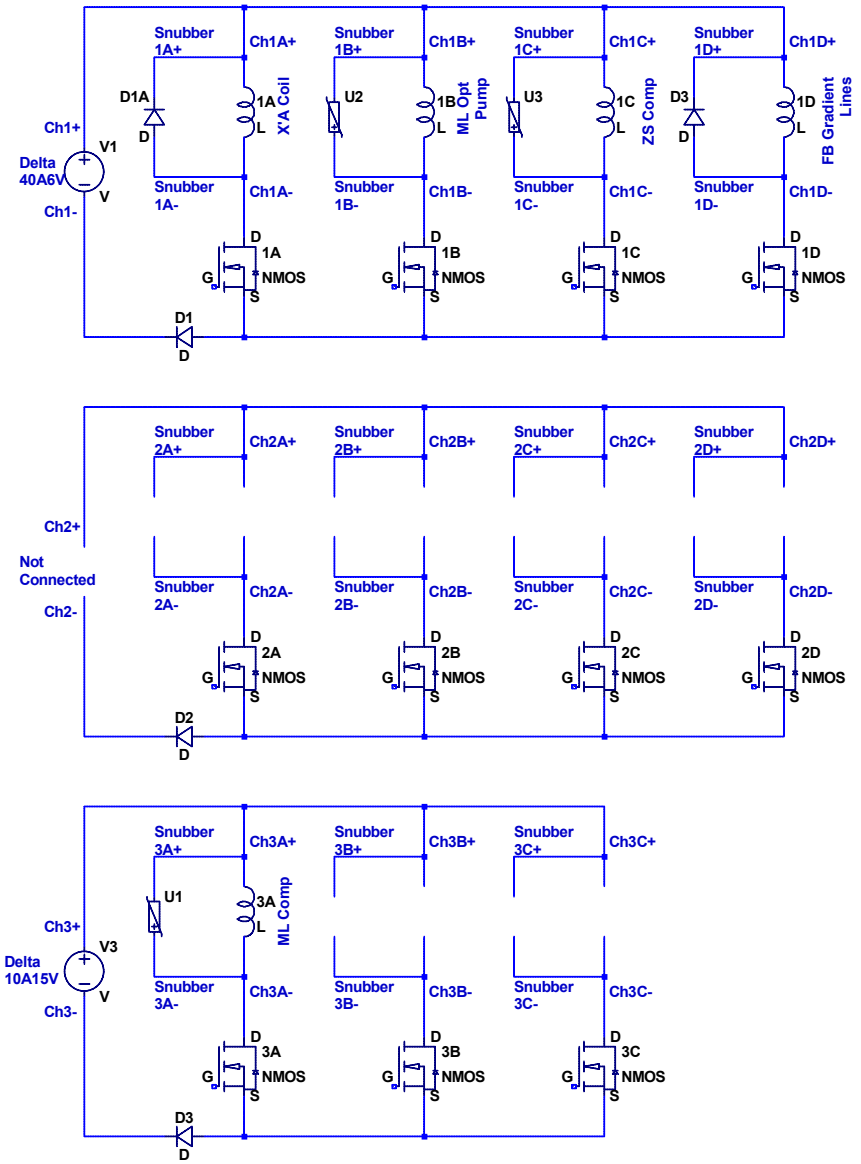

Figure B.12: Schematic of MOSFET Box 2. Three Channels each with a different power supply connect to three or four sub-channels allowing the power supply to drive different coils. All coils in a channel share the same positive terminal connected to the power supply. The labeled blue text represents connections on the plastic connection board (see Fig. B.9. MOSFETs are STE180NE10, high current diodes are BYV255V and varistors/diodes in the snubber circuits vary depending on the requirements for that coil.

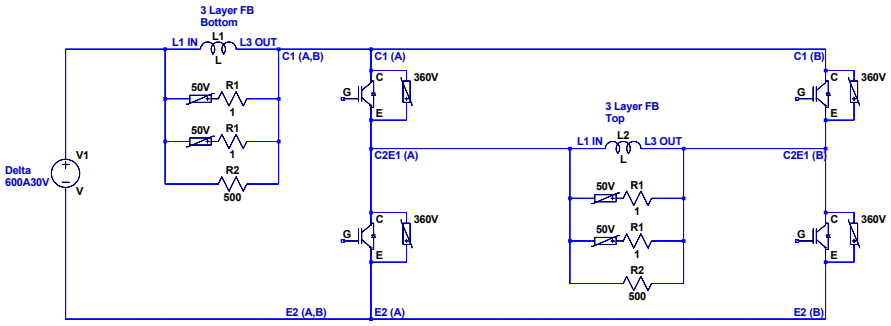

Figure B.13: Schematic of the H-Bridge Box and how it is configured to allow the 3 layer Feshbach coils to operate in anti-Helmholtz (for magnetic trapping) and Helmholtz (for the Feshbach field). The current in the bottom coils is always in the same direction, however, the direction of the current in the top can be reversed. IGBT half bridge modules are 2MBI900VXA-120E-50 Fuji Electric, 360 V clamping varistors are placed across all collector-emitter connections. Directly across the coil are the snubber circuits described in Section 3.4.5.

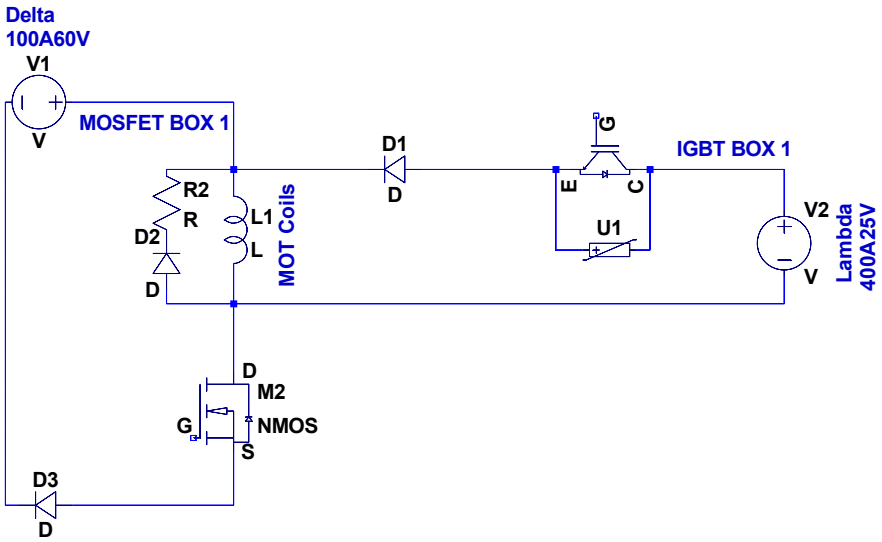

Figure B.14: Schematic of how the MOT coils are connected to allow the MOT current and also the magnetic transport current from different power supplies. At the beginning of the sequence the MOT coils are driven at around 20 A by the Delta 100 A 60 V power supply while the Lambda 400 A 25 Vpower supply drives the big Zeeman slower at 400 A. After the MOT phase, the Lambda 400 A 25 Vis free to be used to drive the MOT coils at high current for magnetic transport (see Section 5.3). The schematic shows how two different power supplies can be connected to the same coil using different channels on different boxes and the necessary diodes. Other sub-channels have been removed from the schematic for clarity. Several coils in the experiment use a similar configuration.

B.5 Experiment Control and Software

This section presents an overview of how the experiment is controlled and the software and hardware used to implement this. The control splits into two parts: Experiment Wizard (Appendix B.5.1) and Experiment Snake (Appendix B.5.2). The analysis and processing of data is handled by Experiment Eagle and Log File Plots (Appendix B.5.3). For this section, several terms are defined below:

- A **sequence** is defined as a single run of the experiment going from loading atoms in the MOT to imaging a degenerate cloud.
- A **loop** is a collection of sequences often (but not always) with one or more parameters varying for each sequence.
- A **log** is a data store associated with one or more **loops** which includes:
  - the original file used to run the first sequence in the log.
  - a folder with all the images taken.
  - a CSV file where each row corresponds to a **sequence**. The row contains all the experiment parameters used as well as all fitted and derived parameters calculated by Experiment Eagle.
  - description text and saved plots that are also automatically saved to the OneNote lab book.

B.5.1 Experiment Wizard

Experiment Wizard was originally developed by Thilo Stöferle in ETH Zurich [258] and a version is now maintained internally within our research group. Experiment Wizard is split into 3 parts: Experiment Runner, Experiment Control and Camera Control. These three applications can (and usually are) run on three individual machines. There can be several instances of Experiment Control and Camera Control running on a single experiment, however, there can only be one Experiment Runner they communicate with.

Experiment Control is the sequence design interface which defines a matrix of channels and timing events. A given position in the matrix then defines an event that occurs on a specific channel at a specific time. The visual user interface view of the sequence can be converted into an XML file by experiment control which contains all the information necessary to run the sequence. The detailed structure of this XML file goes beyond the

scope of this section, but is necessary to know when making software such as Experiment Eagle/Experiment Snake that utilize the sequence data to perform actions or analyze the data. Experiment Control also allows for the definition of variables which can be used in the control of analog channels, definitions of timing edges or to control external hardware using Experiment Snake. Experiment Control can setup basic loops that iterate over the value of a variable, changing the sequence each time. More complex loops (e.g looping many variables in parallel or varying a parameter to optimize a measured quantity) can be done with additional software.

Experiment Runner controls time-synchronized hardware in the experiment and also broadcasts the XML file of the sequence that is currently being run, allowing other software to know the details of the current sequence. Experiment Runner can control digital and analog cards and in the experiment two Viewpoint DIO-64 cards (giving 128 digital channels) with 100 ns resolution and three National Instruments PCI-6733 cards (giving 24 analog channels) with 100 µs resolution are used. The DIO-64 cards are connected to a breakout box which isolates (optocouples) the digital channels in groups of four and the analog channels are connected to home made analog isolation boxes. A Rubidium oscillator atomic clock[1] provides a 10 MHz signal which can be distributed to many devices around the laboratory. It is connected directly to one of the DIO-64 cards and synchronized with the other cards via RTSI. The Experiment Runner PC is also connected to a National Instruments analog input card (NI 6224) which has 32 analog inputs and can be used for logging analog signals for a given sequence (e.g. laser powers or magnetic field values).

B.5.2 Experiment Snake

Experiment Runner can control accurately time synchronized digital and analog channels, however, for many pieces of hardware in the experiment, synchronization with the atomic clock is not necessary. Furthermore, many pieces of hardware require complicated programming instructions that might change significantly depending between sequences and can simply be triggered to perform their task by a TTL signal from the synchronized DIO-64 cards. Experiment Snake can perform actions with a time accuracy of 100 ms by synchronizing to the time broadcast by Experiment Runner during the sequence. It implements a flexible Python interface that allows arbitrary hardware to be controlled and actions to be executed at a set time in the sequence[2]. It connects with Experiment

[1] Model LPRO, manufacturer Datum.

[2] The time an action is executed can, in principle, also be a sequence variable.

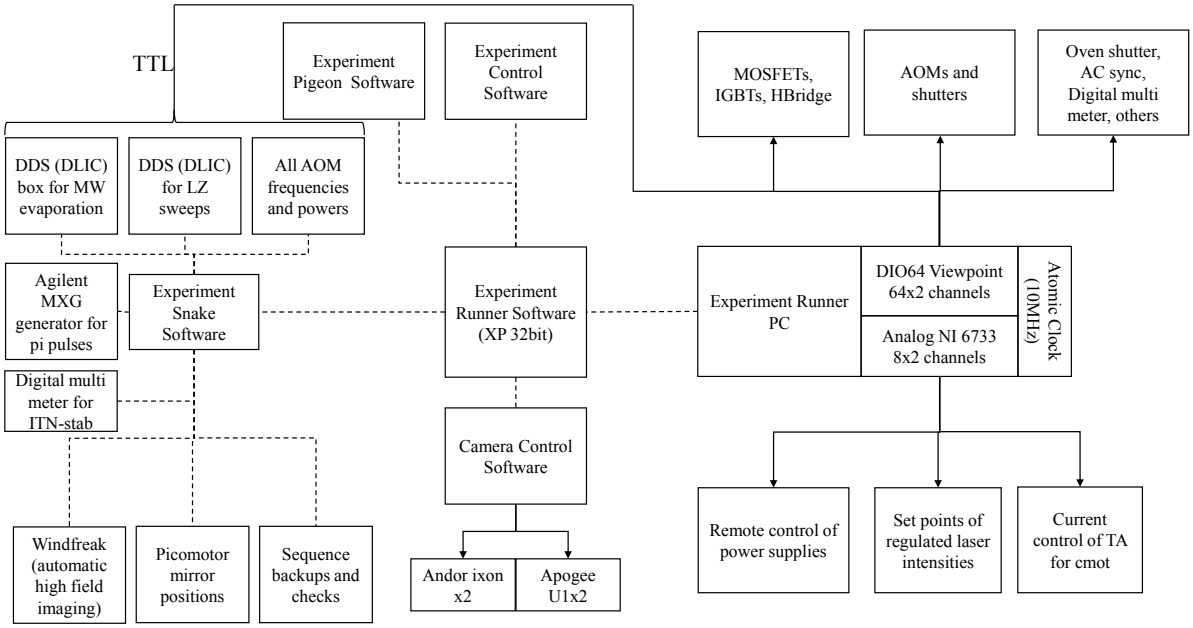

Figure B.15: Communication of devices that control the experiment system. Solid lines represent physical cables carrying analog or TTL signals and dashed lines represent communication over the lab network (Ethernet cables). Experiment Runner PC is the central device of the experiment control system. Digital and Analog cards are physically connected to it and synchronized via an atomic clock. The Experiment Runner Software controls the digital and analog cards and executes the sequence designed in the UI Experiment Control Software. All other hardware is distributed throughout the lab and controlled/programmed over the network via Experiment Snake. Experiment Snake has all the information of the sequence and hence all hardware can depend on variables or timings defined in the Experiment Control UI.

Runner and hence knows all the properties of a sequence (variables, timing edges etc.) which the action can depend on. Experiment Snake is used to control all the AOM drivers in the ^{23}Na and ^{6}Li optics system such that their frequency and power can be changed in the sequence. The devices used for RF sweeps and pulses are all controlled via Experiment Snake. It also can control the picomotor mirrors for alignment of the plug and dipole trap, as well as many other pieces of hardware. Fig. B.15 sketches how the different control hardware is connected in the experiment.

B.5.3 Experiment Eagle and Log Files

Almost every sequence produces one or more absorption images that are the primary data source for the experiment (see Section 6.1). To extract quantitative information from the absorption images, they must be analyzed, usually by fitting some function to the two-dimensional data. Experiment Eagle automatically opens images taken by camera control or other camera software. It performs the necessary manipulation to convert the raw image into the desired form (usually an optical density) as described in Section 6.1.2. It can then perform a wide variety of fitting functions to the image (e.g. Gaussian or bimodal) or automatically perform more complex custom analysis via Python scripts (e.g. analyzing individual rings around the atom cloud as performed in Section 6.1.3). The majority of analysis described in this experiment used Experiment Eagle and Log File Plots.

Experiment Eagle is also used to create logs. When a new log is created, it saves the full sequence data to a file and then saves a backup of every image recorded as part of that log. For each sequence which is fitted and analyzed as part of that log a new row in the CSV log file is created, with all experiment variables and all fitted or analyzed quantities derived from the image. These log folders are how data and the sequences produced in the experiment are saved and recorded. A separate program called Log File Plots can then be used to interactively visualize the data recorded in the log file. This implements several different types of plots and is connected to the OneNote lab book such that comments about the data and images of the plots can be saved for future reference. Many instances of Experiment Eagle can be running at the same time to analyze images from different cameras, or to analyze the same image differently. Log File Plots can be running simultaneously meaning the plots can be updated live with the progress of a loop. The data in Log File Plots can also be fitted with a collection of standard (or custom) functions. Most of the figures in this thesis showing experimental data were produced using Log File Plots.

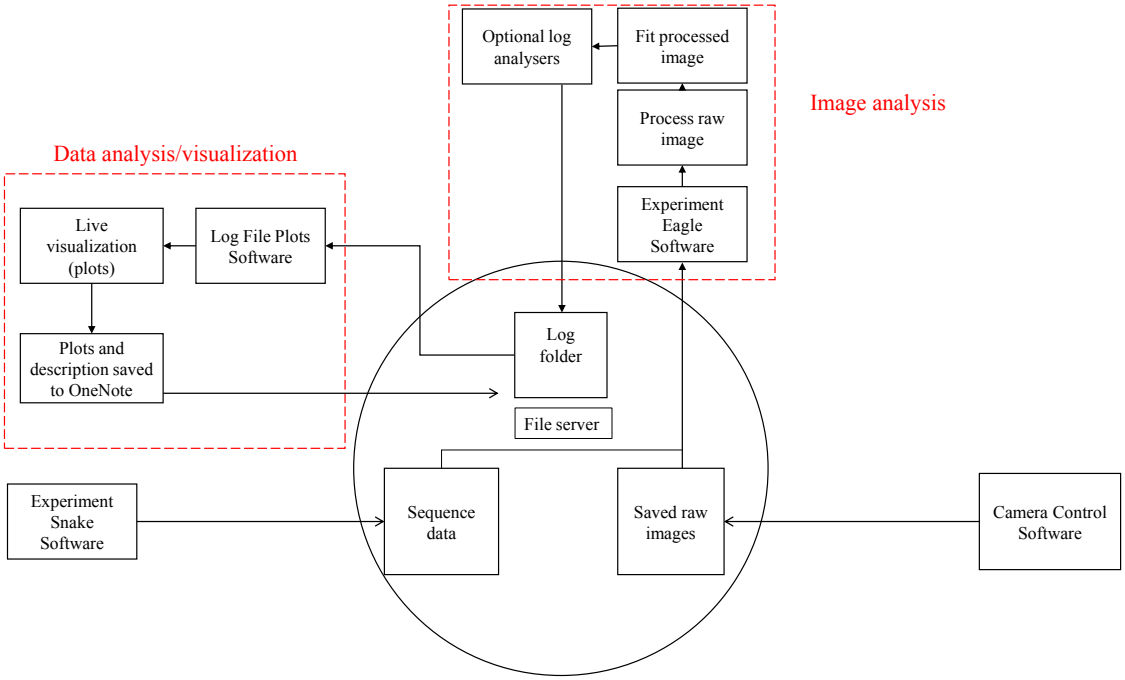

Figure B.16: Overview of how the data from a log (one or more sequence loops) is stored. A copy of the complete sequence data is stored with a copy of all the raw images. The log file is a CSV file which lists for every sequence run: the image file, all experimental parameters, all fitted parameters of the image, all additional analyzed quantities. Experiment Eagle is responsible for processing the image and writing the appropriate data to the file. It is able to fit many standard functions (e.g. Gaussian/bimodal) to an image and custom functions can also be defined. After fitting the image, an optional additional script can be run (a log analyzer) that can be used to perform more experiment specific analysis. Log File Plots software can be used to plot the data in a log file and can easily be refreshed to update the plots as new data is processed.

B.5.4 Additional Software

Many additional pieces of software were written to help control the experiment and produce sequences. Notably, a small python package, known as Experiment Pigeon, was developed that provided a Python interface to the XML sequence data. This meant several operations on a sequence could be performed, such as complex loops where several parameters are changed in parallel. This has allowed the experiment to perform optimization tasks where algorithms (e.g. differential evolution) are used to optimize some measured observable (e.g. atom number after evaporation) by varying many parameters (e.g. evaporation times and powers). This has led to several stages in the experiments being improved. Another package was made that visualizes the entire experiment sequence, and can also compare two different sequence files for debugging.

B.6 Technical Improvements

There are several technical improvements that could be made in the future, which may aid with investigations or simply the speed and stability of the experiment.

- The improvements to the PID regulation suggested in Section 6.3.2 should be implemented. This should allow us to reach B-field stability $\sim 1 \times 10^{-6}$ which would allow investigations driving the $|1\rangle \rightarrow |6\rangle$ transition of ^{6}Li.
- Currently, the sequence has a 7 s cooling period at the end of every cycle due to heating of the big Zeeman slower coil. Improving the water cooling or design such that this wasn't required could allow the cycle time to be reduced to less than 15 s.
- It is currently thought that the ^{6}Li molecular BEC is limited by the number of atoms that can be transferred into the dipole trap. Increasing the power of the dipole beams would increase the trapping volume and depth. The horizontal PCF fiber has been tested up to 30 W and if both beams could be increased in power it is likely the ^{6}Li number would be further increased. Additionally, a two stage regulation would be required, using a different photodiode for the high power (initial) and low power (final) regulation.
- The high loss rate of ^{6}Li in the magnetic trap is not understood and increases noticeably at low temperature. The most likely cause is spin exchange collisions with unwanted hyperfine states due to inefficient optical pumping of ^{23}Na or ^{6}Li. This could be better quantified by imaging the different hyperfine states in the initial

and final magnetic trap. Improving the optical pumping would require higher laser powers.

- The RF coils were crucial to the investigations performed in this thesis. Even though they were optimized theoretically, it would be interesting to measure the properties of any new coils in place using a vector network analyzer. With this, it may be possible to improve the RF coupling further and reduce the time required to perform the quenches in the experiment.
- The initial oven design had several flaws. The cold cup was at an angle leading to the atomic beam being angled with respect to the Zeeman slower, which was corrected by twisting the oven. Additionally, the rotary atomic shutter enters from the bottom oven, and after the first ^{23}Na exchange, a large quantity of ^{23}Na fell into the rotary shutter such that it can longer be easily rotated. In the future, the oven may be redesigned to correct these problems.

Bibliography

[1] E. Schrödinger, *Statistical Thermodynamics: A Course of Seminar Lectures Delivered in January-March 1944, At the School of Theoretical Physics, Dublin Institute For Advanced Studies*, Cambridge University Press (1946).

[2] T. Hänsch and A. Schawlow, *Cooling of gases by laser radiation*, Optics Communications **13**, 68 (jan 1975).

[3] W. D. Phillips, *Nobel Lecture: Laser cooling and trapping of neutral atoms*, Reviews of Modern Physics **70**, 721 (jul 1998).

[4] C. N. Cohen-Tannoudji, *Cohen-Tannoudji*, Rev. Mod. Phys. **70**, 707 (jul 1998).

[5] S. Chu, *Nobel Lecture: The manipulation of neutral particles*, Reviews of Modern Physics **70**, 685 (jul 1998).

[6] W. D. Phillips and H. Metcalf, *Laser deceleration of an atomic beam*, Physical Review Letters **48**, 596 (mar 1982).

[7] E. L. Raab, M. Prentiss, A. Cable, S. Chu and D. E. Pritchard, *Trapping of Neutral Sodium Atoms with Radiation Pressure*, Physical Review Letters **59**, 2631 (1987).

[8] A. L. Migdall, J. V. Prodan, W. D. Phillips, T. H. Bergeman and H. J. Metcalf, *First observation of magnetically trapped neutral atoms*, Physical Review Letters **54**, 2596 (jun 1985).

[9] T. W. Hijmans, O. J. Luiten, I. D. Setija and J. T. M. Walraven, *Optical cooling of atomic hydrogen in a magnetic trap*, Journal of the Optical Society of America B **6**, 2235 (nov 1989).

[10] S. N. Bose, *Wärmegleichgewicht im Strahlungsfeld bei Anwesenheit von Materie*, Zeitschrift für Physik **27**, 392 (1924).

[11] M. H. Anderson, J. R. Ensher, M. R. Matthews, C. E. Wieman and E. A. Cornell, *Observation of Bose-Einstein Condensation in a Dilute Atomic Vapor*, Science **269**, 198 (jul 1995).

[12] K. B. Davis, M. O. Mewes, M. R. Andrews, N. J. Van Druten, D. S. Durfee, D. M. Kurn and W. Ketterle, *Bose-Einstein condensation in a gas of sodium atoms*, Physical Review Letters **75**, 3969 (nov 1995).

[13] C. C. Bradley, C. A. Sackett, J. J. Tollett and R. G. Hulet, *Evidence of Bose-Einstein condensation in an atomic gas with attractive interactions*, Physical Review Letters **75**, 1687 (aug 1995).

[14] Q. Chen, J. Stajic, S. Tan and K. Levin, *BCS-BEC crossover: From high temperature superconductors to ultracold superfluids* (jun 2005).

[15] M. G. Alford, A. Schmitt, K. Rajagopal and T. Schäfer, *Color superconductivity in dense quark matter*, Reviews of Modern Physics **80**, 1455 (nov 2008).

[16] A. G. Truscott, K. E. Strecker, W. I. Mcalexander, G. B. Partridge and R. G. Hulet, *Observation of Fermi Pressure in a Gas of Trapped Atoms*, Science **291**, 2570 (mar 2001).

[17] L. Salasnich, *Fermionic condensation in ultracold atoms, nuclear matter and neutron stars*, Journal of Physics: Conference Series **497**, 012026 (apr 2014).

[18] B. DeMarco and D. S. Jin, *Onset of Fermi Degeneracy in a Trapped Atomic Gas*, Science **285**, 1703 (sep 1999).

[19] Z. Hadzibabic, C. A. Stan, K. Dieckmann, S. Gupta, M. W. Zwierlein, A. Görlitz and W. Ketterle, *Two-species mixture of quantum degenerate Bose and Fermi gases.*, Physical review letters **88**, 160401 (apr 2002).

[20] F. Schreck, L. Khaykovich, K. L. Corwin, G. Ferrari, T. Bourdel, J. Cubizolles and C. Salomon, *Quasipure Bose-Einstein condensate immersed in a Fermi sea*, Physical Review Letters **87**, 804031 (aug 2001).

[21] K. H. Onnes, *research notebooks, 56,57, Kammerlingh Onnes Archive, Boerhaave Museum*, Tech. rep., Leiden, Netherlands (1987).

[22] H. K. Onnes, *The resistance of pure mercury at helium temperatures*, Comm. Leiden **119b** (1911).

[23] H. K. Onnes, *The disappearance of the resistivity of mercury*, Comm. Leiden (1911).

[24] F. London, *The λ-Phenomenon of Liquid Helium and the Bose-Einstein Degeneracy*, Nature **141**, 643 (apr 1938).

[25] L. Landau, *Theory of the superfluidity of helium II*, Physical Review **60**, 356 (aug 1941).

[26] J. Bardeen, L. N. Cooper and J. R. Schrieffer, *Microscopic Theory of Superconductivity*, Physical Review **106**, 162 (apr 1957).

[27] J. G. Bednorz and K. A. Müller, *Perovskite-type oxidesThe new approach to high-Tc superconductivity* (jul 1988).

[28] V. L. Ginzburg, *Nobel Lecture: On superconductivity and superfluidity (what I have and have not managed to do) as well as on the physical minimum at the beginning of the XXI century**, Reviews of Modern Physics **76**, 981 (dec 2004).

[29] D. J. Scalapino, *A common thread: The pairing interaction for unconventional superconductors*, Reviews of Modern Physics **84**, 1383 (oct 2012).

[30] E. Dagotto, *Correlated electrons in high-temperature superconductors*, Reviews of Modern Physics **66**, 763 (jul 1994).

[31] C. A. R. Sá De Melo, *When fermions become bosons: Pairing in ultracold gases*, Physics Today **61**, 45 (2008).

[32] U. Fano, *Effects of Configuration Interaction on Intensities and Phase Shifts*, Physical Review **124**, 1866 (dec 1961).

[33] P. Nikolić and S. Sachdev, *Renormalization-group fixed points, universal phase diagram, and 1/N expansion for quantum liquids with interactions near the unitarity limit*, Physical Review A - Atomic, Molecular, and Optical Physics **75**, 033608 (mar 2007).

[34] E. Braaten and H. W. Hammer, *Universality in few-body systems with large scattering length* (jun 2006).

[35] S. Tan, *Energetics of a strongly correlated Fermi gas*, Annals of Physics **323**, 2952 (dec 2008).

[36] S. Tan, *Large momentum part of a strongly correlated Fermi gas*, Annals of Physics **323**, 2971 (dec 2008).

[37] K. M. O'Hara, S. L. Hemmer, M. E. Gehm, S. R. Granade and J. E. Thomas, *Observation of a Strongly Interacting Degenerate Fermi Gas of Atoms*, Science (2002).

[38] J. Kinast, A. Turlapov, J. E. Thomas, Q. Chen, J. Stajic and K. Levin, *Heat Capacity of a Strongly Interacting Fermi Gas*, Science **307**, 1296 (2005).

[39] C. A. Regal, M. Greiner and D. S. Jin, *Observation of resonance Condensation of Fermionic Atom Pairs*, Physical Review Letters **92**, 040403 (jan 2004).

[40] J. T. Stewart, J. P. Gaebler, C. A. Regal and D. S. Jin, *Potential energy of a 40K Fermi gas in the BCS-BEC crossover*, Physical review letters **97**, 220406 (nov 2006).

[41] J. T. Stewart, J. P. Gaebler and D. S. Jin, *Using photoemission spectroscopy to probe a strongly interacting Fermi gas.*, Nature **454**, 744 (aug 2008).

[42] M. Zwierlein, C. Stan, C. Schunck, S. Raupach, A. Kerman and W. Ketterle, *Condensation of Pairs of Fermionic Atoms near a Feshbach Resonance*, Physical Review Letters **92**, 120403 (mar 2004).

[43] M. W. Zwierlein, J. R. Abo-Shaeer, A. Schirotzek, C. H. Schunck and W. Ketterle, *Vortices and superfluidity in a strongly interacting Fermi gas*, Nature **435**, 1047 (jun 2005).

[44] C. H. Schunck, M. W. Zwierlein, A. Schirotzek and W. Ketterle, *Superfluid expansion of a rotating fermi gas*, Physical Review Letters **98**, 050404 (feb 2007).

[45] M. W. Zwierlein, A. Schirotzek, C. H. Schunck and W. Ketterle, *Fermionic Superfluidity with Imbalanced Spin Populations*, Science **311**, 492 (jan 2006).

[46] T. Bourdel, J. Cubizolles, L. Khaykovich, K. M. F. Magalhães, S. J. J. M. F. Kokkelmans, G. V. Shlyapnikov and C. Salomon, *Measurement of the Interaction Energy near a Feshbach Resonance in a 6Li Fermi Gas*, Physical Review Letters **91**, 020402 (jul 2003).

[47] T. Bourdel, L. Khaykovich, J. Cubizolles, J. Zhang, F. Chevy, M. Teichmann, L. Tarruell, S. J. J. M. F. Kokkelmans and C. Salomon, *Experimental study of the BEC-BCS crossover region in lithium 6*, Physical Review Letters **93**, 050401 (jul 2004).

[48] G. B. Partridge, K. E. Strecker, R. I. Kamar, M. W. Jack and R. G. Hulet, *Molecular probe of pairing in the BEC-BCS crossover*, Physical Review Letters **95**, 020404 (jul 2005).

[49] G. B. Partridge, W. Li, Y. A. Liao and R. G. Hulet, in *Journal of Low Temperature Physics*, vol. 148, pp. 323–330. Kluwer Academic Publishers-Plenum Publishers (jun 2007).

[50] C. Chin, M. Bartenstein, A. Altmeyer, S. Riedl, S. Jochim, J. H. Denschlag and R. Grimm, *Observation of the pairing gap in a strongly interacting Fermi gas.*, Science (New York, N.Y.) **305**, 1128 (2004).

[51] M. Bartenstein, A. Altmeyer, S. Riedl, S. Jochim, C. Chin, J. H. Denschlag and R. Grimm, *Collective Excitations of a Degenerate Gas at the BEC-BCS Crossover*, Physical Review Letters **92**, 203201 (may 2004).

[52] M. J. Wright, S. Riedl, A. Altmeyer, C. Kohstall, E. R. S. Guajardo, J. H. Denschlag and R. Grimm, *Finite-temperature collective dynamics of a fermi gas in the BEC-BCS crossover*, Physical Review Letters **99**, 150403 (oct 2007).

[53] C. Kohstall, M. Zaccanti, M. Jag, A. Trenkwalder, P. Massignan, G. M. Bruun, F. Schreck and R. Grimm, *Metastability and coherence of repulsive polarons in a strongly interacting Fermi mixture*, Nature **485**, 615 (may 2012).

[54] N. Strohmaier, Y. Takasu, K. Günter, R. Jördens, M. Köhl, H. Moritz and T. Esslinger, *Interaction-controlled transport of an ultracold fermi gas*, Physical Review Letters **99**, 220601 (nov 2007).

[55] M. Feld, B. Frohlich, E. Vogt, M. Koschorreck and M. Kohl, *Observation of a pairing pseudogap in a two-dimensional Fermi gas*, Nature **480**, 75 (dec 2011).

[56] E. Vogt, M. Feld, B. Fröhlich, D. Pertot, M. Koschorreck and M. Köhl, *Scale invariance and viscosity of a two-dimensional fermi gas*, Physical Review Letters **108**, 070404 (feb 2012).

[57] M. Koschorreck, D. Pertot, E. Vogt, B. Frohlich, M. Feld and M. Kohl, *Attractive and repulsive Fermi polarons in two dimensions*, Nature **485**, 619 (may 2012).

[58] A. Sommer, M. Ku, G. Roati and M. W. Zwierlein, *Universal spin transport in a strongly interacting Fermi gas*, Nature **472**, 201 (apr 2011).

[59] T. Yefsah, A. T. Sommer, M. J. H. Ku, L. W. Cheuk, W. Ji, W. S. Bakr and M. W. Zwierlein, *Heavy solitons in a fermionic superfluid*, Nature **499**, 426 (jul 2013).

[60] G. Valtolina, A. Burchianti, A. Amico, E. Neri, K. Xhani, J. A. Seman, A. Trombettoni, A. Smerzi, M. Zaccanti, M. Inguscio and G. Roati, *Josephson effect in fermionic superfluids across the BEC-BCS crossover*, Science **350** (2015).

[61] W. Weimer, K. Morgener, V. P. Singh, J. Siegl, K. Hueck, N. Luick, L. Mathey and H. Moritz, *Critical velocity in the BEC-BCS crossover*, Physical Review Letters **114**, 095301 (mar 2015).

[62] M. Ries, A. Wenz, G. Zürn, L. Bayha, I. Boettcher, D. Kedar, P. Murthy, M. Neidig, T. Lompe and S. Jochim, *Observation of Pair Condensation in the Quasi-2D BEC-BCS Crossover*, Physical Review Letters **114**, 230401 (jun 2015).

[63] I. Boettcher, L. Bayha, D. Kedar, P. A. Murthy, M. Neidig, M. G. Ries, A. N. Wenz, G. Zuern, S. Jochim and T. Enss, *Equation of State of Ultracold Fermions in the 2D BEC-BCS Crossover Region*, Physical Review Letters **116**, 045303 (jan 2016).

[64] L. P. Gor 'kov, *On the Energy Spectrum of Superconductors*, J. Exptl. Theoret. Phys. (U.S.S.R.) **34**, 735 (1958).

[65] P. W. Anderson, *Random-Phase Approximation in the Theory of Superconductivity*, Physical Review **112**, 1900 (dec 1958).

[66] V. P. Galaiko, *Kinetic Equations for Relaxation Processes in Superconductors*, SOVIET PHYSICS JETP **34** (1972).

[67] A. F. Volkov and S. M. Kogan, *Collision less relaxation of the energy gap in superconductors*, Journal of Experimental and Theoretical Physics **38**, 1018 (1974).

[68] R. A. Barankov, L. S. Levitov and B. Z. Spivak, *Collective Rabi Oscillations and Solitons in a Time-Dependent BCS Pairing Problem*, Physical Review Letters **93**, 160401 (oct 2004).

[69] A. V. Andreev, V. Gurarie and L. Radzihovsky, *Nonequilibrium Dynamics and Thermodynamics of a Degenerate Fermi Gas Across a Feshbach Resonance*, Physical Review Letters **93**, 130402 (sep 2004).

[70] E. A. Yuzbashyan and O. Tsyplyatyev, *Dynamics of emergent Cooper pairing at finite temperatures*, Physical Review B - Condensed Matter and Materials Physics **79** (2009).

[71] E. A. Yuzbashyan, O. Tsyplyatyev and B. L. Altshuler, *Relaxation and persistent oscillations of the order parameter in fermionic condensates*, Physical Review Letters **96**, 097005 (mar 2006).

[72] E. A. Yuzbashyan, M. Dzero, V. Gurarie and M. S. Foster, *Quantum quench phase diagrams of an s -wave BCS-BEC condensate*, Physical Review A **91**, 033628 (mar 2015).

[73] R. G. Scott, F. Dalfovo, L. P. Pitaevskii and S. Stringari, *Rapid ramps across the BEC-BCS crossover: A route to measuring the superfluid gap*, Physical Review A **86**, 053604 (nov 2012).

[74] M. W. Zwierlein, C. H. Schunck, C. A. Stan, S. M. F. Raupach and W. Ketterle, *Formation dynamics of a fermion pair condensate*, Physical Review Letters **94**, 180401 (may 2005).

[75] A. Gezerlis and J. Carlson, *Strongly paired fermions: Cold atoms and neutron matter*, Physical Review C - Nuclear Physics **77**, 032801 (mar 2008).

[76] A. Bulgac, *Time-Dependent Density Functional Theory and the Real-Time Dynamics of Fermi Superfluids*, Annu. Rev. Nucl. Part. Sci **63**, 97 (2013).

[77] A. Klopper, *Topics in non-equilibrium physics*, Nature Physics **11**, 103 (feb 2015).

[78] J. Eisert, M. Friesdorf and C. Gogolin, *Quantum many-body systems out of equilibrium*, Nature Physics **11**, 124 (feb 2015).

[79] S. R. Manmana, S. Wessel, R. M. Noack and A. Muramatsu, *Time evolution of correlations in strongly interacting fermions after a quantum quench*, Physical Review B - Condensed Matter and Materials Physics **79** (2009).

[80] T. W. B. Kibble, *Topology of cosmic domains and strings*, Journal of Physics A: Mathematical and General **9**, 1387 (aug 1976).

[81] W. H. Zurek, *Cosmological experiments in superfluid helium?*, Nature **317**, 505 (oct 1985).

[82] D. Fausti, R. I. Tobey, N. Dean, S. Kaiser, A. Dienst, M. C. Hoffmann, S. Pyon, T. Takayama, H. Takagi and A. Cavalleri, *Light-induced superconductivity in a stripe-ordered cuprate.*, Science (New York, N.Y.) **331**, 189 (jan 2011).

[83] M. Mitrano, A. Cantaluppi, D. Nicoletti, S. Kaiser, A. Perucchi, S. Lupi, P. Di Pietro, D. Pontiroli, M. Riccò, S. R. Clark, D. Jaksch and A. Cavalleri, *Possible light-induced superconductivity in K3C60 at high temperature.*, Nature **530**, 461 (feb 2016).

[84] P. B. Littlewood and C. M. Varma, *Amplitude collective modes in superconductors and their coupling to charge-density waves*, Physical Review B **26**, 4883 (1982).

[85] P. W. Higgs, *Broken Symmetries and the Masses of Gauge Bosons*, Physical Review Letters **13**, 508 (oct 1964).

[86] M. Endres, T. Fukuhara, D. Pekker, M. Cheneau, P. Schauβ, C. Gross, E. Demler, S. Kuhr and I. Bloch, *The Higgs' amplitude mode at the two-dimensional superfluid/Mott insulator transition*, Nature **487**, 454 (jul 2012).

[87] R. Sooryakumar and M. V. Klein, *Raman Scattering by Superconducting-Gap Excitations and Their Coupling to Charge-Density Waves*, Physical Review Letters **45**, 660 (aug 1980).

[88] R. Matsunaga, Y. I. Hamada, K. Makise, Y. Uzawa, H. Terai, Z. Wang and R. Shimano, *Higgs Amplitude Mode in the BCS Superconductors Nb 1 x Ti x N Induced by Terahertz Pulse Excitation*, Physical Review Letters **111**, 057002 (jul 2013).

[89] R. Matsunaga, N. Tsuji, H. Fujita, A. Sugioka, K. Makise, Y. Uzawa, H. Terai, Z. Wang, H. Aoki and R. Shimano, *Light-induced collective pseudospin precession resonating with Higgs mode in a superconductor*, Science **345** (2014).

[90] A. Bulgac and S. Yoon, *Large Amplitude Dynamics of the Pairing Correlations in a Unitary Fermi Gas*, Physical Review Letters **102**, 085302 (feb 2009).

[91] X. Han, B. Liu and J. Hu, *Observability of Higgs mode in a system without Lorentz invariance*, Physical Review A - Atomic, Molecular, and Optical Physics **94**, 033608 (sep 2016).

[92] B. Liu, H. Zhai and S. Zhang, *Evolution of the Higgs mode in a fermion superfluid with tunable interactions*, Physical Review A - Atomic, Molecular, and Optical Physics **93**, 033641 (mar 2016).

[93] S. Giorgini and S. Stringari, *Theory of ultracold atomic Fermi gases*, Reviews of Modern Physics **80**, 1215 (oct 2008).

[94] C. Chin, R. Grimm, P. Julienne and E. Tiesinga, *Feshbach resonances in ultracold gases*, Reviews of Modern Physics **82**, 1225 (apr 2010).

[95] C. N. Cohen-Tannoudji, *Quantum Mechanics Vol. 1 & 2* (1977).

[96] C. J. Pethick and H. Smith, *Bose Einstein Condensation in Dilute Gases* (2001).

[97] J. Walraven, *Quantum Gases - Collisions and Statistics - Lecture Notes* (2013).

[98] I. Bloch, J. Dalibard and W. Zwerger, *Many-body physics with ultracold gases*, Reviews of Modern Physics **80**, 885 (jul 2008).

[99] W. Zwerger, M. Randeria and M. Zwierlein, pp. 1–32, Springer (2012).

[100] M. Bartenstein, A. Altmeyer, S. Riedl, R. Geursen, S. Jochim, C. Chin, J. H. Denschlag, R. Grimm, A. Simoni, E. Tiesinga, C. J. Williams and P. S. Julienne, *Precise Determination of Li 6 Cold Collision Parameters by Radio-Frequency Spectroscopy on Weakly Bound Molecules*, Physical Review Letters **94**, 103201 (mar 2005).

[101] G. Zürn, T. Lompe, A. N. Wenz, S. Jochim, P. S. Julienne and J. M. Hutson, *Precise Characterization of Li 6 Feshbach Resonances Using Trap-Sideband-Resolved RF Spectroscopy of Weakly Bound Molecules*, Physical Review Letters **110**, 135301 (mar 2013).

[102] D. S. Petrov, *Three-body problem in Fermi gases with short-range interparticle interaction*, Physical Review A **67**, 010703 (jan 2003).

[103] D. S. Petrov, C. Salomon and G. V. Shlyapnikov, *Weakly Bound Dimers of Fermionic Atoms*, Physical Review Letters **93**, 090404 (aug 2004).

[104] D. S. Petrov, C. Salomon and G. V. Shlyapnikov, *Diatomic molecules in ultracold Fermi gasesnovel composite bosons*, Journal of Physics B: Atomic, Molecular and Optical Physics **38**, S645 (may 2005).

[105] P. Pieri and G. C. Strinati, *Trapped Fermions with Density Imbalance in the Bose-Einstein Condensate Limit*, Physical Review Letters **96**, 150404 (apr 2006).

[106] C. A. R. Sá de Melo, M. Randeria and J. R. Engelbrecht, *Crossover from BCS to Bose superconductivity: Transition temperature and time-dependent Ginzburg-Landau theory*, Physical Review Letters **71**, 3202 (nov 1993).

[107] E. J. Mueller, *Pseudogaps in strongly interacting Fermi gases*, arXiv preprint **14853** (jan 2017).

[108] H. Fröhlich, H. Pelzer and S. Zienau, *XX. Properties of slow electrons in polar materials*, The London, Edinburgh, and Dublin Philosophical Magazine and Journal of Science **41**, 221 (mar 1950).

[109] H. Frohlich, *Interaction of Electrons with Lattice Vibrations*, Proceedings of the Royal Society of London A: Mathematical, Physical and Engineering Sciences **215** (1952).

[110] H. Fröhlich, *Electrons in lattice fields*, Advances in Physics **3**, 325 (jul 1954).

[111] P. L. P. L. Taylor and O. Heinonen, *A quantum approach to condensed matter physics*, Cambridge University Press (2002).

[112] M. Ueda, *Fundamentals and New Frontiers of Bose-Einstein Condensation*, WORLD SCIENTIFIC (jul 2010).

[113] L. P. Gor 'kov and T. K. Melik-Barkhudarov, *Contribution to the theory of superfluidity to in an imperfect Fermi gas* **40**, 1452 (1961).

[114] J. Carlson, S.-Y. Chang, V. R. Pandharipande and K. E. Schmidt, *Superfluid Fermi Gases with Large Scattering Length*, Physical Review Letters **91**, 050401 (jul 2003).

[115] G. Wlazłowski, P. Magierski, J. E. Drut, A. Bulgac and K. J. Roche, *Cooper Pairing Above the Critical Temperature in a Unitary Fermi Gas*, Physical Review Letters **110**, 090401 (feb 2013).

[116] M. Randeria, W. Zwerger and M. Zwierlein, pp. 1–32 (2012).

[117] A. J. Leggett, in *Pękalski A., Przystawa J.A. (eds) Modern Trends in the Theory of Condensed Matter. Lecture Notes in Physics, vol 115. Springer, Berlin, Heidelberg*, pp. 13–27, Berlin, Heidelberg (1980), Springer Berlin Heidelberg.

[118] W. Ketterle and M. W. Zwierlein, *Making, probing and understanding ultracold Fermi gases* p. 206 (jan 2008).

[119] S. Crane and C. R. Ekstrom, in *Proceedings of the 37th Annual Precise Time and Time Interval Systems and Applications Meeting*, pp. 297–300 (2005).

[120] J. F. O'Hanlon, *A user's guide to vacuum technology*, Wiley-Interscience (2003).

[121] K. K. Jousten, *Handbook of vacuum technology* (2016).

[122] P. A. Franken, A. E. Hill, C. W. Peters and G. Weinreich, *Generation of Optical Harmonics*, Physical Review Letters **7**, 118 (aug 1961).

[123] H.-M. Meyer, *A Laser System for Trapping and Cooling of Ytterbium-Ions*, Ph.D. thesis (2010).

[124] D. Steck, *Properties of Sodium 23Na*, Tech. rep., University of Oregon (2008).

[125] C. Linse, *Construction of a 6Li spectroscopy cell and Doppler-free spectroscopy* (2014).

[126] M. E. Gehm, *Properties of 6Li*, Tech. rep. (2003).

[127] J. Andrijauskas, *Master Thesis*, Ph.D. thesis, University of Bonn (2015).

[128] NKT, *Private Communications* (2015).

[129] D. J. Detroye and R. J. Chase, *The Calculation and Measurement of Helmholtz Coil Fields*, Tech. rep. (1994).

[130] D. O. Sabulsky, C. V. Parker, N. D. Gemelke and C. Chin, *Efficient continuous-duty Bitter-type electromagnets for cold atom experiments*, Review of Scientific Instruments **84**, 104706 (oct 2013).

[131] I. Ferrier-Barbut, M. Delehaye, S. Laurent, A. T. Grier, M. Pierce, B. S. Rem, F. Chevy and C. Salomon, *A mixture of Bose and Fermi superfluids.*, Science (New York, N.Y.) **345**, 1035 (aug 2014).

[132] W. Weimer, *Probing superfluid properties in strongly correlated Fermi gases with high spatial resolution*, Ph.D. thesis (2014).

[133] P. A. Murthy, D. Kedar, T. Lompe, M. Neidig, M. G. Ries, A. N. Wenz, G. Zürn and S. Jochim, *Matter-wave Fourier optics with a strongly interacting two-dimensional Fermi gas*, Physical Review A **90**, 043611 (oct 2014).

[134] S. C. Bell, M. Junker, M. Jasperse, L. D. Turner, Y.-J. Lin, I. B. Spielman and R. E. Scholten, *A slow atom source using a collimated effusive oven and a single-layer variable pitch coil Zeeman slower*, Review of Scientific Instruments **81**, 013105 (jan 2010).

[135] C. L. G. Alzar, P. G. Petrov, D. Oblak, J. H. Mueller and E. S. Polzik, *Compensation of eddy-current-induced magnetic field transients in a MOT*, arXiv p. 14 (2007).

[136] A. Ayorinde, S. Adekola and A. Ike Mowete, *Performance Characteristics of Loop Antennas above a Ground Plane of Finite Extent*, Progress In Electromagnetics Research Symposium Proceedings p. 769 (2013).

[137] C. Zipkes, S. Palzer, C. Sias and M. Köhl, *A trapped single ion inside a Bose-Einstein condensate.*, Ph.D. thesis (2011).

[138] C. J. Foot, *Atomic physics*, Oxford University Press (2005).

[139] S. A. Hopkins, K. Butler, A. Guttridge, S. Kemp, R. Freytag, E. A. Hinds, M. R. Tarbutt and S. L. Cornish, *A versatile dual-species Zeeman slower for caesium and ytterbium*, Review of Scientific Instruments **87**, 043109 (apr 2016).

[140] K. J. Günter, *Design and implementation of a Zeeman slower for 87 Rb*, Tech. rep. (2004).

[141] W. Ketterle, K. B. Davis, M. A. Joffe, A. Martin and D. E. Pritchard, *High densities of cold atoms in a dark spontaneous-force optical trap*, Physical Review Letters **70**, 2253 (apr 1993).

[142] M.-O. Mewes, G. Ferrari, F. Schreck, A. Sinatra and C. Salomon, *Simultaneous magneto-optical trapping of two lithium isotopes*, Physical Review A **61**, 011403 (dec 1999).

[143] P. M. Duarte, *Observation of antiferromagnetic correlations in the Fermi-Hubbard model*, Ph.D. thesis (2014).

[144] M. Okano, H. Hara, M. Muramatsu, K. Doi, S. Uetake, Y. Takasu and Y. Takahashi, *Simultaneous magneto-optical trapping of lithium and ytterbium atoms towards production of ultracold polar molecules*, Applied Physics B **98**, 691 (mar 2010).

[145] P. D. Lett, R. N. Watts, C. I. Westbrook, W. D. Phillips, P. L. Gould and H. J. Metcalf, *Observation of Atoms Laser Cooled below the Doppler Limit*, Physical Review Letters **61**, 169 (jul 1988).

[146] J. Dalibard and C. Cohen-Tannoudji, *Laser cooling below the Doppler limit by polarization gradients: simple theoretical models*, Journal of the Optical Society of America B **6**, 2023 (nov 1989).

[147] D. S. Durfee, *Dynamic Properties of Dilute Bose-Einstein Condensates*, Ph.D. thesis (1999).

[148] P. M. Duarte, R. A. Hart, J. M. Hitchcock, T. A. Corcovilos, T.-L. Yang, A. Reed and R. G. Hulet, *All-optical production of a lithium quantum gas using narrow-line laser cooling*, Physical Review A **84**, 061406 (dec 2011).

[149] W. Setiawan, *Fermi Gas Microscope A dissertation presented* (2012).

[150] P. Hamilton, G. Kim, T. Joshi, B. Mukherjee, D. Tiarks and M. Holger, *Sisyphus Cooling of Lithium* pp. 1–5 (2013).

[151] A. T. Grier, I. Ferrier-Barbut, B. S. Rem, M. Delehaye, L. Khaykovich, F. Chevy and C. Salomon, Λ *-enhanced sub-Doppler cooling of lithium atoms in D 1 gray molasses*, Physical Review A **87**, 063411 (jun 2013).

[152] A. Burchianti, G. Valtolina, J. A. Seman, E. Pace, M. De Pas, M. Inguscio, M. Zaccanti and G. Roati, *Efficient all-optical production of large Li 6 quantum gases using D 1 gray-molasses cooling*, Physical Review A **90**, 043408 (oct 2014).

[153] F. Sievers, N. Kretzschmar, D. R. Fernandes, D. Suchet, M. Rabinovic, S. Wu, C. V. Parker, L. Khaykovich, C. Salomon and F. Chevy, *Simultaneous sub-Doppler laser cooling of fermionic Li 6 and K 40 on the D 1 line: Theory and experiment*, Physical Review A **91**, 023426 (feb 2015).

[154] A. Burchianti, G. Valtolina, J. A. Seman, E. Pace, M. De Pas, M. Inguscio, M. Zaccanti and G. Roati, *Efficient all-optical production of large Li 6 quantum gases using D 1 gray-molasses cooling*, Physical Review A **90**, 043408 (oct 2014).

[155] S.-J. Deng, P.-P. Diao, Q.-L. Yu and H.-B. Wu, *All-Optical Production of Quantum Degeneracy and Molecular Bose-Einstein Condensation of 6 Li*, Chinese Physics Letters **32**, 053401 (may 2015).

[156] G. Colzi, G. Durastante, E. Fava, S. Serafini, G. Lamporesi and G. Ferrari, *Sub-Doppler cooling of sodium atoms in gray molasses*, Physical Review A **93**, 023421 (feb 2016).

[157] K. B. Davis, M. O. Mewes, M. R. Andrews, N. J. van Druten, D. S. Durfee, D. M. Kurn and W. Ketterle, *Bose-Einstein Condensation in a Gas of Sodium Atoms*, Physical Review Letters **75**, 3969 (nov 1995).

[158] D. G. Fried, T. C. Killian, L. Willmann, D. Landhuis, S. C. Moss, D. Kleppner and T. J. Greytak, *Bose-Einstein Condensation of Atomic Hydrogen*, Physical Review Letters **81**, 3811 (nov 1998).

[159] K. M. R. van der Stam, E. D. van Ooijen, R. Meppelink, J. M. Vogels and P. van der Straten, *Large atom number Bose-Einstein condensate of sodium*, Review of Scientific Instruments **78**, 013102 (jan 2007).

[160] M. Houbiers, H. T. C. Stoof, W. I. McAlexander and R. G. Hulet, *Elastic and inelastic collisions of 6 Li atoms in magnetic and optical traps*, Physical Review A **57**, R1497 (mar 1998).

[161] W. Ketterle and N. J. V. Druten, *Evaporative Cooling of Trapped Atoms*, Advances in Atomic, Molecular and Optical Physics **37**, 181 (1996).

[162] W. Ketterle, D. S. Durfee and D. M. Stamper-Kurn, *Making, probing and understanding Bose-Einstein condensates* (1999).

[163] E. Majorana, *Atomi Orientati Incampo Magnetico Variabile.*, Nuovo Cimento **9**, 43 (feb 1932).

[164] C. Sukumar and D. Brink, *Spin-flip transitions in a magnetic trap*, Physical Review A **56**, 2451 (sep 1997).

[165] D. M. Brink and C. V. Sukumar, *Majorana spin-flip transitions in a magnetic trap*, Physical Review A - Atomic, Molecular, and Optical Physics **74**, 035401 (sep 2006).

[166] W. Petrich, M. H. Anderson, J. R. Ensher and E. A. Cornell, *Stable, Tightly Confining Magnetic Trap for Evaporative Cooling of Neutral Atoms*, Physical Review Letters **74**, 3352 (apr 1995).

[167] S. Gov and H. T. S. Shtrikman, *1D toy model for magnetic trapping*, Am. J. Phys. **68 (4), 33**, N (2000).

[168] R. Grimm, M. Weidemüller and Y. B. Ovchinnikov, *Optical Dipole Traps for Neutral Atoms*, Advances in Atomic, Molecular and Optical Physics **42**, 95 (feb 2000).

[169] C. Cohen-Tannoudji, C. Cohen-Tannoudji, J. Dupont-Roc, J. Dupont-Roc, G. Grynberg and G. Grynberg, *Photons and Atoms - Introduction to Quantum Electrodynamics (Wiley Professional)* (1997).

[170] C.-Y. Shih, *Characterizing Single Atom Dipole Traps for Quantum Information Applications Characterizing Single Atom Dipole Traps*, Ph.D. thesis (2013).

[171] E. Hecht, *Optics*, Addison-Wesley (2002).

[172] C. Zener, *Non-Adiabatic Crossing of Energy Levels*, Proceedings of the Royal Society A: Mathematical, Physical and Engineering Sciences **137**, 696 (sep 1932).

[173] S. Jochim, *Bose-Einstein Condensation of Molecules*, Ph.D. thesis (2003).

[174] E. Cocchi, *Analogue Qantum Simulation of the Two-Dimensional Hubbard Model with Ultracold Fermions*, Ph.D. thesis (2016).

[175] L. A. Miller, *Ultracold Fermions in Two-Dimensional Optical Lattices : Quantum Simulation of the Hubbard Model* (2016).

[176] T. Leuteritz, *High Resolution Imaging of an Ultracold Fermi Gas*, Ph.D. thesis (2016).

[177] R. Campbell, *Thermodynamic properties of a Bose gas with tuneable interactions*, Ph.D. thesis, University of Cambridge (2011).

[178] G. Reinaudi, T. Lahaye, Z. Wang and D. Guéry-Odelin, *Strong saturation absorption imaging of dense clouds of ultracold atoms*, Optics Letters **32**, 3143 (nov 2007).

[179] L. Chomaz, *Coherence and superfluidity of Bose gases in reduced dimensions : from harmonic traps to uniform fluids*, Ph.D. thesis (2015).

[180] S. Stringari, *Collective Excitations of a Trapped Bose-Condensed Gas*, Physical Review Letters **77**, 2360 (sep 1996).

[181] Y. Castin and R. Dum, *Bose-Einstein Condensates in Time Dependent Traps*, Physical Review Letters **77**, 5315 (dec 1996).

[182] S. Riedl, E. R. S. Guajardo, C. Kohstall, A. Altmeyer, M. J. Wright, J. H. Denschlag, R. Grimm, G. M. Bruun and H. Smith, *Collective oscillations of a Fermi gas in the unitarity limit: Temperature effects and the role of pair correlations* (2008).

[183] Y.-H. Hou, L. P. Pitaevskii and S. Stringari, *Scaling solutions of the two-fluid hydrodynamic equations in a harmonically trapped gas at unitarity*, Physical Review A **87**, 033620 (mar 2013).

[184] V. Makhalov, K. Martiyanov, T. Barmashova and A. Turlapov, *Precision measurement of a trapping potential for an ultracold gas*.

[185] DELTAELEKTRONIKA, *SM 6000-Series 6000W DC Power Supplies - Data Sheet*, Tech. rep. (2017).

[186] R. A. Barankov, *Dynamical Pairing States in Cold Gases*, Ph.D. thesis (2006).

[187] E. Altman and A. Vishwanath, *Dynamic projection on feshbach molecules: A probe of pairing and phase fluctuations*, Physical Review Letters **95**, 110404 (sep 2005).

[188] S. Matyjaśkiewicz, M. H. Szymańska and K. Góral, *Probing fermionic condensates by fast-sweep projection onto Feshbach molecules*, Physical Review Letters **101**, 150410 (oct 2008).

[189] S. Giorgini and S. Stringari, *Theory of ultracold atomic Fermi gases*, Reviews of Modern Physics **80**, 1215 (oct 2008).

[190] J. Goldstone, *Field theories with Superconductor solutions*, Il Nuovo Cimento **19**, 154 (jan 1961).

[191] J. Goldstone, A. Salam and S. Weinberg, *Broken Symmetries*, Physical Review **127**, 965 (aug 1962).

[192] T. Lancaster and S. Blundell, *Quantum Field Theory for the Gifted Amateur* (2014).

[193] F. Englert and R. Brout, *Broken symmetry and the mass of gauge vector mesons*, Physical Review Letters **13**, 321 (aug 1964).

[194] G. S. Guralnik, C. R. Hagen and T. W. B. Kibble, *Global conservation laws and massless particles*, Physical Review Letters **13**, 585 (nov 1964).

[195] P. W. Anderson, *Plasmons, gauge invariance, and mass*, Physical Review **130**, 439 (apr 1963).

[196] P. B. Littlewood and C. M. Varma, *Gauge-Invariant Theory of the Dynamical Interaction of Charge Density Waves and Superconductivity*, Physical Review Letters **47**, 811 (1981).

[197] U. Bissbort, S. Götze, Y. Li, J. Heinze, J. S. Krauser, M. Weinberg, C. Becker, K. Sengstock and W. Hofstetter, *Detecting the amplitude mode of strongly interacting lattice bosons by Bragg scattering*, Physical Review Letters **106**, 205303 (may 2011).

[198] D. Pekker and C. Varma, *Amplitude/Higgs Modes in Condensed Matter Physics*, Annual Review of Condensed Matter Physics **6**, 269 (mar 2015).

[199] N. N. Bogoljubov, V. V. Tolmachov and D. V. Širkov, *A New Method in the Theory of Superconductivity*, Fortschritte der Physik **6**, 605 (1958).

[200] K. Kadowaki, I. Kakeya, M. Gaifullin, T. Mochiku, S. Takahashi, T. Koyama and M. Tachiki, *Longitudinal Josephson-plasma excitation in Bi2Sr2CaCu2O8+δ: Direct observation of the Nambu-Goldstone mode in a superconductor*, Physical Review B **56**, 5617 (sep 1997).

[201] S. Sachdev, *Universal relaxational dynamics near two-dimensional quantum-critical points*, Physical Review B **59**, 45 (jun 1998).

[202] D. Podolsky and S. Sachdev, *Spectral functions of the Higgs mode near two-dimensional quantum critical points*, Physical Review B - Condensed Matter and Materials Physics **86**, 054508 (aug 2012).

[203] G. L. Warner and A. J. Leggett, *Quench dynamics of a superfluid Fermi gas*, Physical Review B **71**, 134514 (apr 2005).

[204] B. Liu, H. Zhai and S. Zhang, *Evolution of the Higgs mode in a fermion superfluid with tunable interactions*, Physical Review A **93**, 033641 (mar 2016).

[205] P. A. Lee, N. Nagaosa and X. G. Wen, *Doping a Mott insulator: Physics of high-temperature superconductivity*, Reviews of Modern Physics **78**, 17 (jan 2006).

[206] Y. Shin, C. H. Schunck, A. Schirotzek and W. Ketterle, *Tomographic rf spectroscopy of a trapped fermi gas at unitarity*, Physical Review Letters **99**, 090403 (aug 2007).

[207] A. Schirotzek, Y. I. Shin, C. H. Schunck and W. Ketterle, *Determination of the superfluid gap in atomic fermi gases by quasiparticle spectroscopy*, Physical Review Letters **101**, 140403 (oct 2008).

[208] M. Greiner, C. A. Regal and D. S. Jin, *Probing the excitation spectrum of a Fermi gas in the BCS-BEC crossover regime*, Physical Review Letters **94**, 070403 (feb 2005).

[209] C. K. Chung and C. K. Law, *Short-time dynamics of an ultracold Fermi gas in radio-frequency spectroscopy*, Physical Review A - Atomic, Molecular, and Optical Physics **79**, 043611 (apr 2009).

[210] C. K. Chung and C. K. Law, *Pairing and coherence order parameters in a three-component ultracold Fermi gas*, Physical Review A - Atomic, Molecular, and Optical Physics **82**, 033620 (sep 2010).

[211] P. Pieri, A. Perali, G. C. Strinati, S. Riedl, M. J. Wright, A. Altmeyer, C. Kohstall, E. R. Sánchez Guajardo, J. Hecker Denschlag and R. Grimm, *Pairing-gap, pseudogap, and no-gap phases in the radio-frequency spectra of a trapped unitary Li6 gas*, Physical Review A - Atomic, Molecular, and Optical Physics **84**, 011608 (jul 2011).

[212] S. Basu and E. J. Mueller, *Final-state effects in the radio frequency spectrum of strongly interacting fermions*, Physical Review Letters **101**, 060405 (aug 2008).

[213] M. Punk and W. Zwerger, *Theory of rf-spectroscopy of strongly interacting fermions*, Physical Review Letters **99**, 170404 (oct 2007).

[214] A. Perali, P. Pieri and G. C. Strinati, *Competition between final-state and pairing-gap effects in the radio-frequency spectra of ultracold fermi atoms*, Physical Review Letters **100**, 010402 (jan 2008).

[215] Y. He, C. C. Chien, Q. Chen and K. Levin, *Temperature and final state effects in radio frequency spectroscopy experiments on atomic fermi gases*, Physical Review Letters **102**, 020402 (jan 2009).

[216] S. Y. Chang, V. R. Pandharipande, J. Carlson and K. E. Schmidt, *Quantum Monte Carlo studies of superfluid Fermi gases* (oct 2004).

[217] A. Bulgac, J. E. Drut and P. Magierski, *Quantum Monte Carlo Simulations of the BCS-BEC Crossover at Finite Temperature*, Physical Review A **78**, 24 (mar 2008).

[218] B. G.-g. Chen, B. Liu, A. A. Evans, J. Paulose, I. Cohen, V. Vitelli and C. D. Santangelo, *Topological Mechanics of Origami and Kirigami*, Physical Review Letters **116**, 135501 (mar 2016).

[219] S. Hannibal, P. Kettmann, M. D. Croitoru, A. Vagov, V. M. Axt and T. Kuhn, *Quench dynamics of an ultracold Fermi gas in the BCS regime: Spectral properties and confinement-induced breakdown of the Higgs mode*, Physical Review A **91**, 043630 (apr 2015).

[220] N. Tsuji and H. Aoki, *Theory of Anderson pseudospin resonance with Higgs mode in superconductors*, Physical Review B - Condensed Matter and Materials Physics **92** (2015).

[221] N. Kopnin, *Theory of Nonequilibrium Superconductivity*, Oxford Scholarship Online (2001).

[222] Editorial, *Self-assembling life*, Nature Nanotechnology **11**, 909 (nov 2016).

[223] S. Çolak, A. Lima and M. C. González, *Understanding congested travel in urban areas.*, Nature communications **7**, 10793 (mar 2016).

[224] T. Kinoshita, T. Wenger and D. S. Weiss, *A quantum Newton's cradle*, Nature **440**, 900 (apr 2006).

[225] P. Hänggi and P. Talkner, *The other QFT*, Nature Physics **11**, 108 (feb 2015).

[226] T. Langen, R. Geiger and J. Schmiedmayer, *Ultracold Atoms Out of Equilibrium*, Annual Review of Condensed Matter Physics **6**, 201 (mar 2015).

[227] A. Roy, *Nonequilibrium dynamics of ultracold Fermi superfluids* (jul 2013).

[228] P. W. Anderson, *Random-Phase Approximation in the Theory of Superconductivity*, Physical Review **112**, 1900 (dec 1958).

[229] R. A. Barankov and L. S. Levitov, *Synchronization in the BCS Pairing Dynamics as a Critical Phenomenon*, Physical Review Letters **96**, 230403 (jun 2006).

[230] G. E. Astrakharchik, J. Boronat, J. Casulleras, Giorgini and S., *Equation of State of a Fermi Gas in the BEC-BCS Crossover: A Quantum Monte Carlo Study*, Physical Review Letters **93**, 200404 (nov 2004).

[231] E. A. Yuzbashyan and M. Dzero, *Dynamical vanishing of the order parameter in a fermionic condensate*, Physical Review Letters **96**, 230404 (jun 2006).

[232] M. Davis, T. Wright and T. Gasenzer, *Formation of Bose-Einstein condensates*, arXiv preprint arXiv: ... pp. 1–15 (jan 2016).

[233] H. Miesner, D. Stamper-Kurn, A. M. R., D. D. S., I. S. and K. W, *Bosonic Stimulation in the Formation of a Bose-Einstein Condensate*, Science **279**, 1005 (feb 1998).

[234] M. Köhl, M. J. Davis, C. W. Gardiner, T. W. Hänsch and T. Esslinger, *Growth of Bose-Einstein condensates from thermal vapor.*, Physical review letters **88**, 080402 (feb 2002).

[235] D. M. Stamper-Kurn, H. J. Miesner, A. P. Chikkatur, S. Inouye, J. Stenger and W. Ketterle, *Reversible formation of a Bose-Einstein condensate*, Physical Review Letters **81**, 2194 (sep 1998).

[236] M. J. Davis, C. W. Gardiner and R. J. Ballagh, *Quantum kinetic theory. VII. The influence of vapor dynamics on condensate growth*, Physical Review A - Atomic, Molecular, and Optical Physics **62**, 063608 (nov 2000).

[237] M. J. Bijlsma, E. Zaremba and H. T. C. Stoof, *Condensate growth in trapped Bose gases*, Physical Review A - Atomic, Molecular, and Optical Physics **62**, 063609 (nov 2000).

[238] M. J. Davis and C. W. Gardiner, *Growth of a Bose-Einstein condensate: a detailed comparison of theory and experiment*, Journal of Physics B: Atomic, Molecular and Optical Physics **35**, 733 (feb 2002).

[239] G. Lamporesi, S. Donadello, S. Serafini and G. Ferrari, *Compact high-flux source of cold sodium atoms.*, The Review of scientific instruments **84**, 063102 (jun 2013).

[240] R. A. Barankov and L. S. Levitov, *Atom-molecule coexistence and collective dynamics near a Feshbach resonance of cold fermions*, Physical Review Letters **93**, 130403 (sep 2004).

[241] M. E. Gehm, S. L. Hemmer, K. M. O'Hara and J. E. Thomas, *Unitarity-Limited Elastic Collision Rate in a Harmonically-Trapped Fermi Gas*, Physical Review A - Atomic, Molecular, and Optical Physics **68**, 4 (jul 2003).

[242] R. B. Diener and T.-L. Ho, *Projecting Fermion Pair Condensates into Molecular Condensates*, arXiv preprint cond-mat/0404517v1 p. 4 (apr 2004).

[243] S. Tan, *Large momentum part of fermions with large scattering length*, arXiv: cond-mat/0508320v2 **60637** (2005).

[244] R. Haussmann, M. Punk and W. Zwerger, *Spectral functions and rf response of ultracold fermionic atoms*, Physical Review A - Atomic, Molecular, and Optical Physics **80**, 063612 (dec 2009).

[245] J. T. Stewart, J. P. Gaebler, T. E. Drake and D. S. Jin, *Verification of universal relations in a strongly interacting fermi gas*, Physical Review Letters **104**, 235301 (jun 2010).

[246] A. Tomadin, M. Polini, M. P. Tosi and R. Fazio, *Nonequilibrium pairing instability in ultracold Fermi gases with population imbalance*, Physical Review A - Atomic, Molecular, and Optical Physics **77**, 033605 (mar 2008).

[247] A. Nahum and E. Bettelheim, *Dissipationless BCS dynamics with large branch imbalance*, Physical Review B - Condensed Matter and Materials Physics **78** (2008).

[248] A. Adams, L. D. Carr, T. Schaefer, P. Steinberg and J. E. Thomas, *Strongly Correlated Quantum Fluids: Ultracold Quantum Gases, Quantum Chromodynamic Plasmas, and Holographic Duality*, New Journal of Physics **14** (may 2012).

[249] S. Avdiaj and B. Erjavec, *Outgassing of hydrogen from a stainless steel vacuum chamber*, Materials and Technology **46**, 161 (2012).

[250] W. Gunton, M. Semczuk and K. W. Madison, *Realization of BEC-BCS-crossover physics in a compact oven-loaded magneto-optic-trap apparatus*, Physical Review A **88**, 023624 (aug 2013).

[251] G. Vacuum, *Ion Pumps Users Manual*, Tech. rep. (2008).

[252] G. Vacuum, *Private Communications with Gamma Vacuum*, Tech. rep. (2013).

[253] C. A. Stan and W. Ketterle, *Multiple species atom source for laser-cooling experiments*, Review of Scientific Instruments **76**, 063113 (jun 2005).

[254] C. A. Stan, *Experiments with Interacting Bose and Fermi Gases*, Ph.D. thesis (2005).

[255] Z. Hadzibabic, *Studies of a Quantum Degenerate Fermionic Lithium Gas* (2003).

[256] D. O. SABULSKY, *A Cesium-133 effusive oven for ultracold atomic experiments*, Ph.D. thesis (2014).

[257] K. J. Ross and B. Sonntag, *High temperature metal atom beam sources*, Review of Scientific Instruments **66**, 4409 (sep 1995).

[258] T. Stoeferle, *Exploring Atomic Quantum Gases in Optical Lattices*, Ph.D. thesis (2005).